Magnetohydrodynamic Relaxation in Astrophysical Plasmas

A Thesis

submitted for the Award of Ph.D. degree of

MOHANLAL SUKHADIA UNIVERSITY

in the

Faculty of Science

By

Sanjay Kumar

Under the supervision of

Dr. Ramitendranath Bhattacharyya
Associate Professor
Udaipur Solar Observatory
Physical Research Laboratory
Udaipur, India

DEPARTMENT OF PHYSICS
FACULTY OF SCIENCE
MOHANLAL SUKHADIA UNIVERSITY
UDAIPUR (RAJ)

Year of submission: 2016

DECLARATION

I, **Mr. Sanjay Kumar**, S/o Mr. Fakir Chand, resident of C-2, USO staff quarters, Badi road, Udaipur-313001, hereby declare that the research work incorporated in the present thesis entitled, **"Magnetohydrodynamic Relaxation in Astrophysical Plasmas"** is my own work and is original. This work (in part or in full) has not been submitted to any University for the award of a Degree or a Diploma. I have properly acknowledged the material collected from secondary sources wherever required. I solely own the responsibility for the originality of the entire content.

Date:

Sanjay Kumar

(Author)

CERTIFICATE

I feel great pleasure in certifying that the thesis entitled, **"Magnetohydrodynamic Relaxation in Astrophysical Plasmas"** embodies a record of the results of investigations carried out by **Mr. Sanjay Kumar** under my guidance. He has completed the following requirements as per Ph.D regulations of the University.

(a) Course work as per the university rules.

(b) Residential requirements of the university.

(c) Regularly submitted six monthly progress reports.

(d) Presented his work in the departmental committee.

(e) Published minimum of one research papers in a referred research journal.

I recommend the submission of thesis.

Date:

Dr. Ramitendranath Bhattacharyya
(Thesis Supervisor)
Associate Professor, USO,
Physical Research Laboratory,
Udaipur - 313 001.

Countersigned by

Head of the Department

To

My Family

Acknowledgements

I would like to start by expressing my sincere and deep gratitude to my supervisor Dr. Ramitendranath Bhattacharyya for his invaluable guidance, encouragement and support throughout my PhD tenure. I immensely benefited from his insight and expertise in the subject. Discussions with him were a great pleasure as he always gave importance to my views and was patient with me. I thank him for the patience and confidence that he showed in me. Apart from being my thesis supervisor, I also felt that he is my true teacher who introduced me to the joy of doing science, especially physics. Moreover, he treated me as a younger brother which enables me to share my personal problems with him and he always helped me to overcome them.

I further extend my special thanks to Prof. Piotr K. Smolarkiewicz for helping me in various ways whenever I got stuck with the numerical models. I also acknowledge his constant support to enhance the presentation as well as the academic content of the work presented in the thesis.

I also express my gratitude to the academic committee of PRL for reviewing my progress in research periodically. I am grateful to my thesis experts Prof. Jitesh Bhatt and Dr. Bhuwan Joshi for throughly reviewing my thesis. I thank the faculty members of USO, Prof. Ashok Ambastha, Prof. Nandita Srivastava, Prof. Shibu K. Mathew, Dr. Brajesh Kumar and Dr. Raja Bayanna for their generous helps and encouragements throughout my research endeavor. I also convey my sincere thanks to Prof. P. Venkatakrishnan for his continuous encouragement to do good work. A very special thanks to all other staff members of USO, Mr. Raju Koshy, Ms. Ramya Bireddy, Mr. Rakesh Jaroli, Mr. Naresh Jain, Mr. Mukesh M. Saradava and all the trainees for their help and support in various ways during my stay at USO.

My special thanks goes to all the staff members of the computer center of PRL for providing uninterrupted computing facility which helps me to complete computations in time. The computations presented in the thesis are performed using the High Performance Computing (HPC) cluster and the 100 TF cluster

Vikram-100 at Physical Research Laboratory, India. I also wish to acknowledge the visualisation software VAPOR (www.vapor.ucar.edu) for generating relevant graphics.

I must express my sincere gratitude to my seniors at USO; Dr. Anand D. Joshi, Dr. Vema Reddy Panditi, Dr. Suruchi Goel, Dr. Wageesh Mishra, Dr. Dinesh Kumar, Dr. Upendra Kushwaha, Dr. Sajal Dhara, and Dr. Avijeet Prasad for helping me at various stages of the thesis work. I also thank all the seniors at PRL for being supportive whenever I visited PRL. I would like to thank all my batch-mates; Alok Ranjan, Arun Pandey, Guru Kadam, Girish Kumar, Manu George, Ikshu Gautam, Sharadha Band, Tanmoy Mondal, Gaurava Jaiswal, Abhaya, Chithrabhanu, Kuldeep Suthar, and my junior Rahul Yadav for making my stay at PRL/USO comfortable and enjoyable. I extend my thank to my college and university friends Prashant, Dinesh Mahala, Pawan, Mahipal, Akhil, Pooja, Neha, Swati, Anmol and many others who have been always supportive.

I would like to take this opportunity to thank all the family members at USO colony Mrs. Usha Venkatakrishnan, Mrs. Saraswati, Mrs. Mahima, and Mrs. Bharti for inviting me for lunches and dinners on various occasions. I especially thank to Mrs. Uhsa Venkatakrishanan for arranging get-together and making the environment of colony homely.

Finally, I owe my deepest gratitude to my parents who have given me the freedom necessary to concentrate on my research. I convey my gratitude for their constant support, encouragement and unconditional love. I am also thankful to other family members, in particular, grandparents, uncles, aunties, siblings and cousins for their wholehearted love. It was extremely pleasurable to spend time with my nephews, Vineet, Viren and Akshat whenever I visited home. I must say, that being away from home, I have missed many opportunities to be with my family members. But, they have always been by my side all the time.

Sanjay Kumar

ABSTRACT

The astrophysical plasmas in general, and the solar corona in particular, are described by the non-diffusive limit of magnetohydrodynamics. The reason for the achievement of this limit is the large length scales and high temperatures inherent to such plasmas, making magnetic Reynolds number ($R_M = vL/\lambda$, in usual notations) extremely high. These high R_M plasmas satisfy the Alfvén theorem of flux-freezing, resulting in tying magnetic field lines with fluid parcels during an evolution. In such plasmas, small scales in magnetic field, or equivalently current sheets develop spontaneously in accordance with the Parker's magnetostatic theorem. These current sheets are the locations where the plasma becomes locally diffusive because of a local reduction in R_M. The consequent magnetic reconnections convert the magnetic energy into heat and kinetic energy of mass outflow along with a topological rearrangement of magnetic field lines. With reconnections, the current sheets decay and magnetic field lines frozen with the mass outflows push onto other magnetic field lines and, under favorable conditions may lead to secondary current sheets and second generation reconnections. These reconnections are expected to repeat in time until the plasma relaxes to a terminal state characterized by an allowable minimum of the magnetic energy. Consequently, a scenario is proposed where the magnetohydrodynamic relaxation, maintained by the repeated magnetic reconnections, provides an autonomous mechanism which governs the creation and dynamics of coherent structures in relaxing astrophysical plasmas.

With the above scenario of magnetohydrodynamic relaxation in astrophysical plasmas, in the thesis, we first numerically explore the physics of spontaneous formation of current sheets and assess the important of magnetic field lines topology in the generation. For the purpose, we employ a novel approach of describing the plasma evolution in terms of magnetic flux surfaces instead of the vector magnetic field. The approach provides a direct visualization of the current sheet formation which is helpful in understanding the governing dynamics. The presented computations confirm spontaneous development of current

sheets through favorable contortions of magnetic flux surfaces where two oppositely directed parts of either the same or different field line(s) come to close proximity while the plasma undergoes a topology-preserving viscous relaxation from an initial non-equilibrium state with interlaced magnetic field lines. Importantly, these current sheet are distributed throughout the computational volume with no preference for favorable sites like magnetic nulls or field reversal layers. However for magnetic field with less interlaced magnetic field lines, the simulations show the development of current sheets only at the favorable sites. These current sheets originate as two sets of anti-parallel complimentary magnetic field lines press onto each other.

Further, we explore the ceaseless regeneration of current sheets. For the purpose, we advect vector magnetic field since the flux surface description is valid till onset of magnetic reconnections. Notably with a fixed grid resolution, the magnetic reconnections described in the thesis are related to under-resolved scales—generated by an unbounded increase of magnetic field gradient. The performed computations are then in the spirit of implicit large eddy simulations which regularize the under-resolved scales through simulated reconnections which are concurrent and collocated with developing current sheets. The spontaneous generation of current sheets is ensured by congruency of the computations with the magnetostatic theorem. An important finding of the thesis is the establishment of the comparative scaling of peak current density with spatial resolution for current sheets developing near and away from different magnetic nulls. The results document the current sheets near two dimensional magnetic nulls to have larger strength while exhibiting a stronger scaling than the current sheets close to three dimensional magnetic nulls or away from any magnetic null. The comparative scaling points to a scenario where the energetics of the secondary reconnections is determined by the magnetic topology near a developing current sheet.

Finally, we explore magnetohydrodynamic relaxation with magnetic field line geometry similar to the solar corona. In particular, through numerical simulations we identify the relaxation as an autonomous mechanism for creating a magnetic flux-rope from initial bipolar magnetic field lines and, subsequently, for triggering and maintaining its ascend via reconnections that occur below the rope. The revealed morphology of the evolution process including onset and ascend of the rope, reconnection locations and the associated topology of the magnetic field lines agrees with observations, and thus substantiates physical realizability of the advocated mechanism. The computations support the scenario where repeated reconnections can generate observed magnetic structures in any high R_M plasma.

Keywords : Magnetohydrodynamics, MHD relaxation, Current sheets, Magnetic reconnections, EULAG

LIST OF PUBLICATIONS

1. *Formation of magnetic discontinuities through viscous relaxation*, **Sanjay Kumar**, R. Bhattacharyya, and P. K. Smolarkiewicz, Physics of Plasmas, **21**, 052904 (2014).

2. *On the role of topological complexity in spontaneous development of current sheets*, **Sanjay Kumar**, R. Bhattacharyya, and P. K. Smolarkiewicz, Physics of Plasmas, **22**, 082903 (2015).

3. *Continuous development of current sheets near and away from magnetic nulls*, **Sanjay Kumar** and R. Bhattacharyya, Physics of Plasmas, **23**, 044501 (2016).

4. *On the Role of Repetitive Magnetic Reconnections in Evolution of Magnetic Flux-Ropes in Solar Corona*, **Sanjay Kumar**, R. Bhattacharyya, Bhuwan Joshi, and P. K. Smolarkiewicz, The Astrophysical Journal (*accepted*).

Contents

List of Figures

Chapter 1

Introduction

Observations document presence of extreme ultra-violet (EUV) and X-rays in the electromagnetic spectrum of most stars and correspond to very high temperatures $\approx 10^6$-10^7K (Parker 1994; Aschwanden 2005). Under such high temperatures, the neutral gases in these stars get ionized and are in plasma state – the so called "fourth state" of matter. Standardly, the macroscopic behavior of plasmas can be described by the magnetohydrodynamics (MHD) approximation which treats the plasma as a hydromagnetic fluid obeying Maxwell's equations (cf. chapter 2). Because of the high temperature, the magnetic diffusivity of astrophysical plasmas is small (Aschwanden 2005). In addition to the small magnetic diffusivity λ, the involved large length scales make the corresponding magnetic Reynolds number $R_M = vL/\lambda$—where L and v are the characteristic length and speed of the system—very large. For example, the solar corona with a length scale $L \approx 10^7$m, flow speed $v \approx 10^4$m/s, and magnetic diffusivity $\lambda \approx 1\text{m}^2/\text{s}$, have $R_M \approx 10^{11}$ (Aschwanden 2005). For such R_M ($R_M >> 1$), the MHD attains its non-diffusive limit. Consequently, magnetic field lines (MFLs) are tied to fluid parcels—a condition referred to as the "flux-freezing" (Alfvén 1942). Because of the flux-freezing, it is possible to infer the observed plasma structures to be the manifestations of corresponding magnetic structures. For instance, under the flux-freezing the observed plasma loops in the solar corona (Figure 1.1) suggest the corresponding MFLs to be also in the form of loops (Priest 2014).

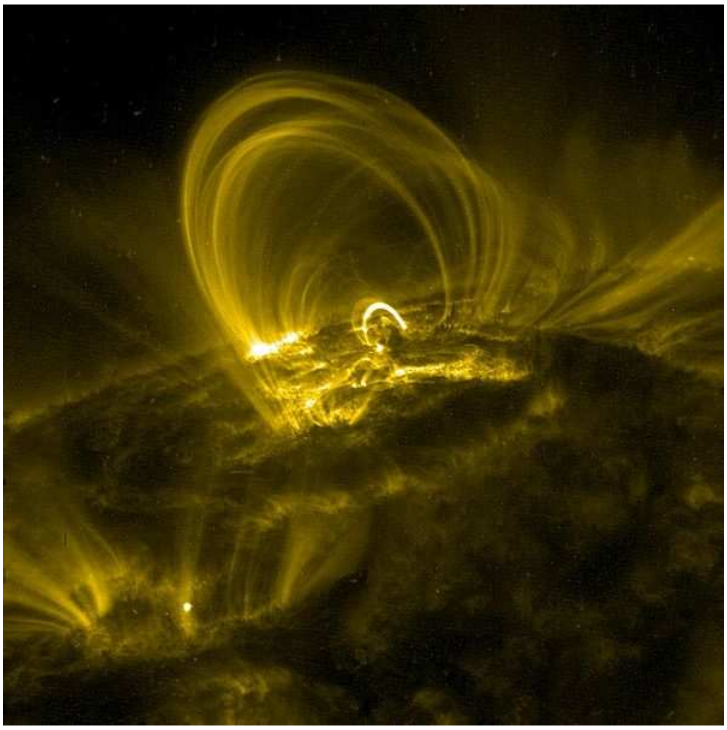

Figure 1.1: Typical solar coronal loops observed by the Transition Region And Coronal Explorer (TRACE). This image was taken at 171Å, which is around the border of the X-ray and the Ultraviolet parts of the electromagnetic spectrum. Approximate temperature of these loops is one million Kelvin. These plasma loops replicate the magnetic structures in the corona.

Interestingly, the astrophysical plasmas and in particular the solar corona, exhibit various eruptive phenomena which release energy $\approx 10^{32}$ergs in the form of heat and mass motion on a time scale (τ_e) which varies from few seconds to minutes (Poletto et al. 1988; Aschwanden 2005). However a simple diffusion time scale calculated using

$$\tau_D = \frac{L^2}{\lambda}, \tag{1.0.1}$$

is 10^{14}s ($\approx 3 \times 10^8$yr) for the solar corona. Notable is the inference $\tau_D >> \tau_e$, whereas an eruptive phenomena requires $\tau_D \approx \tau_e$ (Priest and Forbes 2006; Priest 2014). A viable way to achieve the τ_e is by reducing L, i.e., by developing small scales in the magnetic field. This effectively decreases the R_M locally and the dynamics of plasma in this localized region is governed by diffusive limit of MHD. The condition of flux-freezing then breaks down and MFLs undergo magnetic reconnection (MR) where magnetic energy gets converted into heat and kinetic energy of mass outflow (Priest and Forbes 2006). After reconnection, the small scales decay out from the system and the flux-freezing is restored. Consequently, the mass outflow expunges MFLs from the reconnection site. These expunged MFLs are expected to press a separate set of MFLs located elsewhere in the plasma, and under favorable pressing, create a second generation of the small scales which lead to further MRs. These MRs—intermittent in space and time—facilitate MHD relaxation by decreasing the magnetic energy of the plasma. The relaxation process is expected to continue until an allowable lower limit of the magnetic energy is achieved. The lower limit is determined by the constraint applied on the dynamics (cf. chapter 2). Therefore a scenario is possible where MHD relaxation, sustained by spontaneous reconnections which repeat in time, shapes up the dynamics of the observed structures. The works presented in the thesis mainly focus on the objective to understand this interesting and ubiquitous coupling between the large scales (where the flux-freezing is valid) and the small scales (where the diffusion dominates) with particular emphasis in field line topologies similar to the solar corona because of the availability of a wealth of observational data with sufficiently high temporal and spatial resolution. Towards achieving the objective, we note that an analytical study of the dynamics of MHD relaxation is formidable because of the inherent non-linearity and coupled nature of MHD equations, and therefore we employ suitable numerical simulations by formulating relevant initial value problems.

To initiate, following is a brief introduction to the mechanism behind the origin of small scales from the large scales. We also present some of the observational signatures of reconnections in astrophysical plasmas. The details are in chapters 3 and 4.

1.1 Formation of small scales in magnetic field

For understanding the formation of small scales, notable is the Parker's magnetostatic theorem (Parker 1972, 1988, 1994, 2012). The theorem establishes the

L to become zero in an equilibrium plasma having infinite electrical conductivity and interlaced MFLs, rendering the magnetic field discontinues. From Ampere's law, the corresponding volume current density diverges and is contained in a surface across which the field is discontinuous. Because of their two dimensional appearances, such volume current densities are called current sheets (CSs). In presence of small but non-zero λ, these CSs are the sites with reduced L (and hence, R_M) where reconnections occur.

Astrophysical plasmas with high R_M are suitable candidates to support the magnetostatic theorem. To appreciate this, we note the solar corona to have low plasma-β (the ratio of thermodynamic pressure to magnetic pressure), in general, with Lorentz force dominating all other forces (Low 1996; Gary 2001; Wiegelmann and Sakurai 2012). With quasi-steady evolution, the coronal magnetic field is then in equilibrium which corresponds to zero Lorentz force (Low 1996; Wiegelmann and Sakurai 2012). Under the flux-freezing, both ends of the corresponding bipolar field lines are firmly rooted on the photosphere and the photospheric motions cause the MFLs to get interlaced (cf. chapter 3). The CSs then develop voluntarily by the interlaced MFLs in accordance with the magnetostatic theorem and lead to MRs in presence of non-zero magnetic diffusivity (Parker 1988, 1994).

1.2 Reconnections in astrophysical systems

The manifestations of CS formation and subsequent reconnection are ubiquitous in astrophysical plasmas. The recent multi-wavelength space-based observations from Yohkoh (Masuda et al. 1994; Tsuneta 1996), Solar and Heliospheric Observatory (SoHO) (Kohl et al. 1997), TRACE (Golub et al. 1999), Ramaty High Energy Solar Spectroscopic Imager (RHESSI) (Lin et al. 2003) and Solar Dynamics Observatory (SDO) (Pesnell 2010) satellites have generated a near consensus about the existence of reconnection in the solar atmosphere. Presently, the magnetic reconnection is believed to be the fundamental mechanism responsible for the occurrence of explosive phenomena likes flares and coronal mass ejections (CMEs) (Golub and Pasachoff 1997; Aschwanden 2005); cf. chapter 4 for details. The observations also suggest the creation of a magnetic flux-rope through repeated reconnections occurring in the corona (Cheng et al. 2011). For instance, activation of a flux-rope is shown in Figure 1.2. The rope appears as a bright blob of hot plasma in the corona and ascends from the source region while stretching the overlying field lines. Observed intense localized brightenings below the rising flux-rope (Fig. 1.2) indicate the spatio-temporal correlation between intermittent energy release and ascend of the rope which imply a causal connection between MRs and the rise (Cho et al. 2009; Cheng et al. 2011; Kushwaha et al. 2015; Kumar et al. 2016).

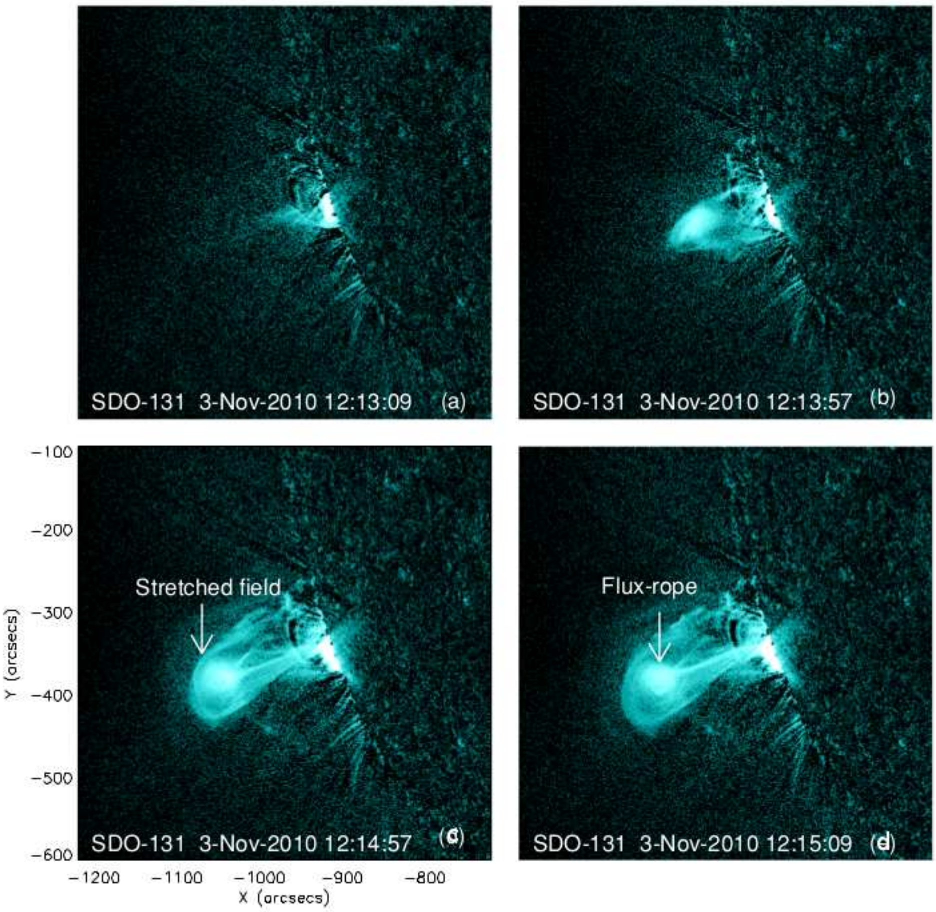

Figure 1.2: The Atmospheric Imaging Assembly (AIA) 131Å($\approx$ 11MK) images of the solar eruption on 3 November 2010. Notable is the appearance of a blob of plasma first appeared above the solar limb (panels a and b). Such a plasma blob is generally accepted as an observational signature of the flux-rope. Stretched overlying magnetic field lines and the flux-rope are indicated in panels c and d respectively. The figure is adapted from (Cheng et al. 2011).

Moreover, the Parker's nanoflare model (Parker 1988, 1994) for explaining the heating of the solar corona to million degrees Kelvin temperature is based on reconnection events—nanoflares—distributed throughout the coronal volume. Notably, although the underlying mechanism (i.e., magnetic reconnection) for eruptive events (flares and CMEs) and nano-flares is identical but the energy release in nanoflares is expected to be small $\approx 10^{23} - 10^{25}$ergs (Parker 1994) whereas the eruptive events are characterized by comparatively larger energy releases $\approx 10^{32}$ergs (Aschwanden 2005).

Furthermore, we note that magnetic reconnection is proposed to be a crucial in many other astrophysical processes. For example, the flare events are also observed in many other stars. The stellar flares can release 10^4 to 10^6 times the amount of energy of a large solar flare (Gershberg 1983; Poletto et al. 1988). The analyses of stellar flares suggest that they are identical to solar flares expect for the larger energy release, indicating towards the importance of MRs in generation of stellar flares (Mullan 1986). It has also been suggested that magnetic reconnection may provide the energy required to develop jets from active galactic nuclei and gamma-ray bursts (Romanova and Lovelace 1992; Drenkhahn and Spruit 2002; Giannios 2010). Moreover, analogous to the solar corona, MRs have been put forward as a possible heating mechanism for the coronae of different stars and the warm ionized medium of galaxies (Reynolds et al. 1999). Another system in which MR is thought to play a key role is in accretion disks (Verbunt 1982). The reconnection in the disks is believed to be responsible for the flare-like outbursts generated within the disks.

1.3 Reconnections in the interplanetary medium

Magnetic reconnection play an important role in the interaction between the interplanetary magnetic field (IMF) of the solar wind (expanding solar corona) and the earth's dipole field (Dungey 1961; Lang 2006; Raeder 2006). The shape and size of the earth's magnetic field envelop, known as the magnetosphere, is controlled by the solar wind. A simplified picture of the reconnection in magnetosphere is as follows (Figure 1.3). If IMF is oppositely directed (southward) to the earth's magnetic field, reconnections occur in the dayside. Reconnected field lines then get dragged by the solar wind to the nightside and enhances the magnetic pressure across the magnetotail. The enhanced magnetic pressure compresses two lobes of the magnetotail towards each other. Since the magnetic fields are oppositely directed in these two lobes, the compression results in reconnection at the nightside. With reconnection, solar wind particles are allowed to enter the earth's atmosphere and create auroras (Lang 2006). Moreover, these particles also contribute to the ring current, an electric current flowing toroidally around the earth (Daglis et al. 1999). Occasionally, fast solar wind or earth directed CMEs with their larger IMF may generate stronger reconnections. The consequent enhancement of the ring current can weaken the geomagnetic field which leads to various geomagnetic activities (Pulkkinen 2007).

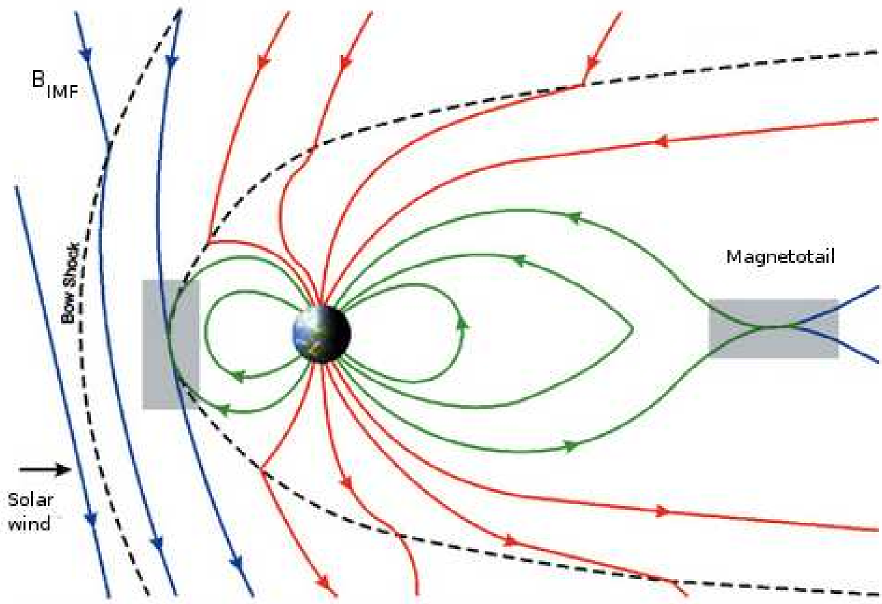

Figure 1.3: Schematic of the occurrence of magnetic reconnection in the earth's magnetosphere. The probable reconnections sites are marked by shaded regions. Image source: http://www.nap.edu.

1.4 Objectives and organization of the thesis

From the above discussion, noteworthy is the development of secondary current sheets and resultant repeated reconnections in MHD relaxation for high R_M astrophysical plasmas. Therefore, it is plausible that the repeated reconnections can be responsible to dynamically shape up the magnetic topology of astrophysical plasmas. In the backdrop of the above plausibility, the specific objectives of the thesis are outlined below:

- To perform suitable MHD simulations with infinite electrical conductivity to explore the physics of current sheet formation.
- To assess the role of topological complexity in spontaneous generation of current sheets.
- To establish the development of secondary current sheets by conducting MHD simulations with an apt magnetic diffusivity.
- To demonstrate repetitive spontaneous reconnections, and hence MHD relaxation, as a viable mechanism to generate and sustain observed magnetic structures.

For completeness we first formally introduce MHD relaxation, and follow with the computations carried out to accomplish the above objectives. Based on this planning, rest of the thesis is organized into seven chapters. The chapters 2-4 are kept introductory to realize the relevant analytical and observational requirements for a successful numerical demonstration of MHD relaxation in astrophysical plasmas. The numerical models used to perform MHD simulations are described in chapter 5 and the new results of the simulations are presented in chapters 6-7. A brief summary of each chapter is given below.

Chapter 2: Magnetohydrodynamics Relaxation

This chapter focuses on the theoretical aspects of MHD relaxation. To lay out ideas, we start the chapter with a brief introduction of the MHD model. Then, Taylor's theory for MHD relaxation is discussed which highlights the requirement of spontaneously developed CSs and subsequent MRs.

Chapter 3: Astrophysical Plasmas: Current Sheet and Magnetic Reconnection

Here we provide the details of Parker's magnetostatic theorem to develop a specific guideline for computations presented in the thesis. Further, the standard two-dimensional models for steady state reconnections are introduced.

Chapter 4: Solar Corona as a Prototype Example

In this chapter, we revisit various physical conditions of the solar corona along with the possibility of CS formation and highlight different observational signatures of magnetic reconnection.

Chapter 5: Numerical Models

This chapter provides the numerical models EULAG-MHD and EULAG-EP utilized in this thesis to solve MHD equations. We also discuss the important features of the advection scheme used in the models.

Chapter 6: Initial Value Problems: Current Sheet Formations

In this chapter, we numerically demonstrate the process of current sheet formation and assess the importance of field line complexity in the process. Importantly, the computations presented in this chapter provide a new physics of spontaneous CS formation through contortions of magnetic flux surfaces. Also, the CSs develop away from magnetic nulls or any other favorable sites. Further, a different set of computations relate the above CSs with the complexity (or interlacing) of the magnetic field lines. Important is the finding that, for more interlaced field lines CSs form away from the favorable site and are distributed throughout the computational volume—in accordance with the magnetostatic theorem and the general expectation of nanoflares occurring throughout the solar corona.

Chapter 7: Initial Value Problems: Magnetic Reconnections

Here we undertake simulations to establish the generation of secondary CSs as a consequence of reconnections occurring at initially developed CSs. Importantly, we establish a scaling between intensity of CSs with resolution which helps to link energetics of magnetic reconnection to the proximity of the corresponding current sheet with the favorable location. The findings are in overall agreement with the expectation that the energy yield in eruptive events are larger than the same in nanoflares. Further, we explore the role of secondary MRs in generating observable structures. For the purpose, simulations are reported to identify repeated MRs as an autonomous mechanism to generate and sustain the ascend of a magnetic flux-rope.

Chapter 8: Summary and Future Works

Here we summarize the thesis by highlighting major findings. Lastly, we discuss the scope for the future work.

Chapter 2

Magnetohydrodynamic Relaxation

2.1 Introduction

The signatures of magnetohydrodynamic relaxation are ubiquitous in astrophysical as well as laboratory plasmas. Particularly, the relaxed or self-organized states, in general, show some form of long-range ordering and spontaneity in onset. In this chapter, we formally introduce MHD relaxation and present its fundamental physics. Towards that, we initiate the chapter with a brief discussion on MHD and its important properties. A detailed description of MHD can be found in (Goldston and Rutherford 1995; Bellan 2008). We further identify calculus of variation as a relevant analytical tool and revisit Taylor's theory (Taylor 1974) to have a general physical understanding of MHD relaxation.

2.2 Magnetohydrodynamics

Plasma is a collection of charged and neutral particles which obeys the condition of quasi-neutrality and exhibits collective behavior in presence of self-consistent electromagnetic field (Goldston and Rutherford 1995; Bellan 2008). A direct understanding of dynamics of these charged particles is difficult because of the self-consistent nature of the involved electromagnetic force (Bellan 2008).

An apt simplification is provided by a fluid (continuum) approximation where an individual particle looses its identity. Under this approximation, for sufficiently large time and length scales the plasma can be treated as a magnetized fluid or magnetofluid (Goldston and Rutherford 1995; Choudhuri 1998). The dynamics of the fluid is then described by magnetohydrodynamics equations, which are generically similar to the Navier-Stokes equations complemented by the Maxwell's equations in their non-relativistic limit. The MHD equations (in cgs units) are

$$\rho\left[\frac{\partial \mathbf{v}}{\partial t}+(\mathbf{v}\cdot\nabla)\,\mathbf{v}\right]=-\nabla p+\frac{1}{4\pi}(\nabla\times\mathbf{B})\times\mathbf{B}+\mu\nabla^2\mathbf{v}+\rho\mathbf{g}, \tag{2.2.1}$$

$$\frac{\partial \rho}{\partial t}+\nabla\cdot(\rho\mathbf{v})=0, \tag{2.2.2}$$

$$\mathbf{E}+\frac{\mathbf{v}\times\mathbf{B}}{c}=\eta\mathbf{J}, \tag{2.2.3}$$

$$\nabla\times\mathbf{E}=-\frac{1}{c}\frac{\partial \mathbf{B}}{\partial t}, \tag{2.2.4}$$

$$\nabla\times\mathbf{B}=\frac{4\pi}{c}\mathbf{J}, \tag{2.2.5}$$

$$\nabla\cdot\mathbf{B}=0, \tag{2.2.6}$$

$$\frac{d}{dt}\left(\frac{p}{\rho^{\gamma}}\right)=0, \tag{2.2.7}$$

in standard notations, where electrical resistivity η and dynamic viscosity μ are assumed to be constant. Equations (2.2.1) and (2.2.2) are momentum transport and continuity equations which are natural laws of motion and mass conservation. Ohm's law, Faraday's law and Ampere's law are represented by equations (2.2.3), (2.2.4), and (2.2.5), respectively. The displacement current $\frac{1}{c}\frac{\partial \mathbf{E}}{\partial t}$ is absent in the Ampere's law because of the non-relativistic limit (Goldston and Rutherford 1995). Notably, the fluid description of plasma is achieved by taking moments of the Vlasov equation (Goldston and Rutherford 1995; Choudhuri 1998; Bellan 2008). In this process the nth moment, for any arbitrary n, always contains a term involving (n+*1*)th moment. This forbids the corresponding continuum equations to get closed and necessitates the requirement of an ad hoc closure. Typically an equation of state, usually utilized in thermodynamics, is assumed to formally close the MHD equations. The equation (2.2.7) is one such closure relating thermodynamic pressure and mass density.

Importantly, the MHD equations are always non-linear. To appreciate the non-linearity, we substitute electric field $\mathbf{E}$ from the Ohm's law (2.2.3) to equation (2.2.4) and then plug the current density $\mathbf{J}$ from equation (2.2.5) to arrive at the induction equation,

$$\frac{\partial \mathbf{B}}{\partial t} = \nabla \times \mathbf{v} \times \mathbf{B} + \lambda \nabla^{\mathbf{2}} \mathbf{B}, \tag{2.2.8}$$

where $\lambda = \dfrac{\eta c^2}{4\pi}$ is constant magnetic diffusivity. Notably, the induction equation and the momentum transport equation reveal $\mathbf{B}$ and $\mathbf{v}$ to be coupled, making the MHD equations inherently non-linear through the presence of $\nabla \times \mathbf{v} \times \mathbf{B}$ term. The induction equation maintains the solenoidal condition $\nabla \cdot \mathbf{B} = 0$ for all later times if the initial $\mathbf{B}$ is divergence-free.

Relevantly, the magnetic field $\mathbf{B}$ can be represented by magnetic field lines. A magnetic field line is a space-curve which is everywhere tangential to a given magnetic field $\{\mathbf{B} = B_x, B_y, B_z\}$ and is described by the ordinary differential equations (ODEs):

$$\frac{dx}{ds} = \frac{B_x}{\mid \mathbf{B} \mid}, \tag{2.2.9}$$

$$\frac{dy}{ds} = \frac{B_y}{\mid \mathbf{B} \mid}, \tag{2.2.10}$$

$$\frac{dz}{ds} = \frac{B_z}{\mid \mathbf{B} \mid}, \tag{2.2.11}$$

in Cartesian coordinates (x, y, z), where ds is the invariant length and $\mid \mathbf{B} \mid$ is the magnitude of $\mathbf{B}$. Field lines are obtained by integrating ODEs (2.2.9)-(2.2.11). The topology of the magnetic field $\mathbf{B}$ is determined by the linkage and knottdness of magnetic field lines which do not change under continuous deformations (Berger and Field 1984; Priest 2014).

To further scrutinize the importance of the induction equation in magnetofluid evolution, notable is the competition between the non-linearity ($\nabla \times \mathbf{v} \times \mathbf{B}$) and the diffusion ($\lambda\nabla^2\mathbf{B}$), making up the right hand side of the induction equation. From an order of magnitude estimation, the ratio of non-linearity to diffusion yields magnetic Reynolds number

$$R_M = \frac{vL}{\lambda}. \tag{2.2.12}$$

The value of R_M determines the effectiveness of the non-linearity over the diffusion in an evolving magnetofluid. For instance, if $R_M >> 1$, the non-linearity dominates over the diffusion. Whereas for $R_M << 1$, the magnetofluid becomes predominantly diffusive.

In the limit of $R_M >> 1$, for all practical purposes the induction equation reduces to

$$\frac{\partial \mathbf{B}}{\partial t} = \nabla \times \mathbf{v} \times \mathbf{B}, \tag{2.2.13}$$

and the magnetofluid satisfies the Alfvén's theorem of flux-freezing (Alfvén 1942), which ascertains the MFLs to be tied with fluid parcels as the whole system evolves in time. As a consequence, the magnetic flux across an arbitrary fluid surface, physically identified by the material elements lying on it, remains conserved in time (Choudhuri 1998; Priest 2014). Importantly, the otherwise abstract magnetic field lines attain physicality as the flux-freezing allows them to be identified with fluid parcels, which are real. A proof of the flux-freezing is as follows. Let us consider an arbitrary fluid surface S enclosed by a curve C, moving with fluid velocity $\mathbf{v}$. The magnetic flux passing through the surface S is given by,

$$\Phi = \int_S \mathbf{B} \cdot d\mathbf{S}. \tag{2.2.14}$$

The rate of change of Φ is

$$\frac{d\Phi}{dt} = \int_S \frac{\partial \mathbf{B}}{\partial t} \cdot d\mathbf{S} + \oint_C \mathbf{B} \cdot \mathbf{v} \times d\mathbf{l}, \tag{2.2.15}$$

where $d\mathbf{l}$ is the line element along C and $\mathbf{v} \times d\mathbf{l}$ is the area swept out by $d\mathbf{l}$ per unit time (Priest 2014). Hence, the total rate of change of Φ includes two terms; the first term is due to the change in $\mathbf{B}$ over the surface S and the second term is due to the variation in area spanned by the S as the boundary C moves in space. Employing Stokes' theorem in equation (2.2.15), we get

$$\frac{d\Phi}{dt} = \int_S \left[\frac{\partial \mathbf{B}}{\partial t} - \nabla \times (\mathbf{v} \times \mathbf{B})\right] \cdot d\mathbf{S}. \tag{2.2.16}$$

Using equation (2.2.13) in above equation, we obtain

$$\frac{d\Phi}{dt} = 0, \tag{2.2.17}$$

stating the Φ to be conserved across the fluid surface S. As a consequence, depending on the topology of magnetic field, a subset Γ of fluid surfaces can be identified such that the loci of magnetic field lines are entirely contained on Γ. It is then imperative that the magnetic flux passing through the Γ surfaces is zero. The Γ surfaces are called magnetic flux surfaces (MFSs) in literature (Choudhuri 1998; Priest 2014). Under the condition of flux-freezing, the Γ surfaces retain zero magnetic flux during the evolution which ensures the MFLs to remain always tangential to these surfaces. Consequently, if a fluid surface is identified as a flux surface, then under flux-freezing, this identity is maintained throughout the evolution. An important consequence of flux-freezing on the dynamics is that, if two fluid parcels are connected by a field line at time $t = 0$ then they will always remain connected by the same field line. The preservation of such connectivities warrants the corresponding magnetic topolology to be invariant. For example, if two field lines are linked n times at $t = 0$ then they must retain the same number of linkages at all times (Choudhuri 1998; Priest 2014).

2.3 Magnetohydrodynamic relaxation

From the induction equation, high R_M plasmas are strongly non-linear. It is generally observed that such plasmas tend to spontaneously evolve towards relaxed states that possess coherent structures (Hasegawa 1985; Ortolani and Schnack 1993). These states are found to be relatively independent of their initial conditions, or the way in which the system was prepared. In general these states are remarkably robust, insensitive to any local perturbations and relatively long-lived. The dynamical process responsible for development of relaxed state is called the magnetohydrodynamic relaxation (Taylor 1986; Ortolani and Schnack 1993).

Instances of MHD relaxation are known in laboratory plasmas, particularly in context of different magnetic confinement schemes: Spheromaks (Dasgupta et al. 2002), Field Reversed Configurations (FRCs) (Bhattacharyya et al. 2003) and Reversed Field Pinches (RFPs) (Bhattacharyya et al. 2000; Sarff et al. 2005)—relevant to controlled thermonuclear fusion. In all these configurations, a common notable feature is that plasma constantly tends to relax into a more quiescent state through global self-organization of the magnetic field. For instance, the spheromak is an axisymmetric compact toroid with simply connected geometry (Figure 2.1) where the toroidal field is generated primarily by internal plasma currents. It is characterized by the presence of both toroidal and poloidal fields of nearly equal intensity. The spheromak is observed to form naturally as a detached plasma blob supported by self-generated magnetic field. In RFP, a toroidal configuration of multiply connected geometry, the toroidal field at the edge is reversed with respect to that at the center (Ortolani and Schnack 1993; Sarff et al. 2005). With sufficient applied toroidal voltage the field reversed state is achieved spontaneously without the necessity of any externally applied poloidal voltages and survives over time scales longer than the resistive diffusion time (Ortolani and Schnack 1993; Sarff et al. 2005). All these observations indicate that these configurations are terminal states of a MHD relaxation process.

The astrophysical plasmas with their inherently large R_M are also prone to sustain MHD relaxation (Ortolani and Schnack 1993). For instance, the solar coronal loops are observed to have lifetimes varying from few hours to days (Foukal 1976). Whereas, from the ideal MHD stability analysis it is known that any cylindrical or toroidal magnetofluid is expected to become unstable

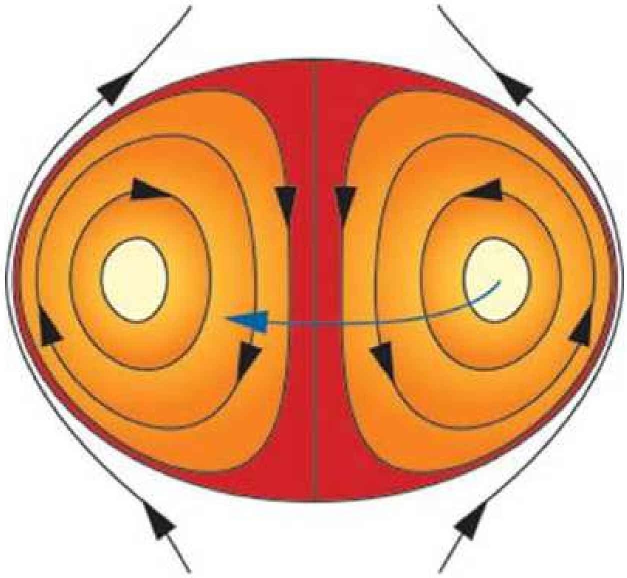

Figure 2.1: Schematic of field line configuration for spheromak. The field line in color blue represents the toroidal magnetic field while field lines in color black mark the poloidal magnetic field. In absence of a hole in the middle, the figure confirms the magnetic configuration to be simply connected. Image source http://www.llnl.gov/str/September05/Hill.html.

on the Alfvén time scale $\tau_a = L/v_a$ (Goedbloed and Hagebeuk 1972; Chiuderi et al. 1977) where L is the characteristic length of the structure and v_a is the Alfvén speed—the speed at which the magnetic disturbances travel in a plasma (Choudhuri 1998). For typical coronal parameters, this time scale is of the order of few seconds, making a loop relatively long-lived. The long-lived property of coronal loops is an indication of possible MHD relaxation in the solar corona. Moreover, the formations of large scale structures like magnetic flux-ropes and occurrence of solar flares can also be thought as possible manifestations of MHD relaxation operating in the corona (Kusano et al. 1994, 2004).

An analytical theory of MHD relaxation was proposed by Taylor (Taylor 1974, 1986). This theory qualitatively, and in some cases quantitatively, describes observed properties of both laboratory and astrophysical plasmas. Taylor's theory essentially originates from the Woltjer's work (Woltjer 1958) which is described in the following.

2.3.1 The Woltjer invariants and relaxed state

To demonstrate the idea, we consider an isolated magnetofluid with a perfectly conducting boundary. Moreover, the magnetofluid is assumed to have infinite electrical conductivity. In absence of any plasma flow, the total energy for such a system is given by

$$W = \int_{V_0} \left(\frac{B^2}{8\pi} + \frac{p}{\gamma - 1} \right) dV, \tag{2.3.1}$$

where the integration is over total plasma volume V_0. For such a system, an infinite set of integrals,

$$K_l = \int_{V_l} \mathbf{A} \cdot \mathbf{B} \, dV, \tag{2.3.2}$$

were proposed by Woltjer (Woltjer 1958; Ortolani and Schnack 1993) where $l = 1, 2, 3 ... \infty$ and integrals are taken over the volume V_l of the lth flux tube. In the expression of K_l, $\mathbf{A}$ is vector potential which evolves according to equation,

$$\frac{\partial \mathbf{A}}{\partial t} = \mathbf{v} \times \mathbf{B} + \nabla \xi, \tag{2.3.3}$$

with ξ as an arbitrary gauge. K_l is known as the magnetic helicity for lth flux tube and is related to its magnetic topology. The time derivative of equation (2.3.2) is,

$$\frac{dK_l}{dt} = \int_{V_l} \frac{\partial \mathbf{A}}{\partial t} \cdot \mathbf{B} \, dV \; + \int_{V_l} \mathbf{A} \cdot \frac{\partial \mathbf{B}}{\partial t} \, dV \; + \oint_{s_l} (\mathbf{A} \cdot \mathbf{B}) \mathbf{v} \cdot \hat{n} \, da, \tag{2.3.4}$$

where s_l represents the closed surface, bounding the volume V_l. The last term on the right hand side appears because the surface of flux tube is moving with a velocity $\mathbf{v}$. Using equations (2.2.13) and (2.3.3), the above equation takes the form of

$$\frac{dK_l}{dt} = \int_{V_l} (\nabla\xi) \cdot \mathbf{B}\, dV \ + \int_{V_l} \mathbf{A} \cdot \nabla \times (\mathbf{v} \times \mathbf{B})\, dV \ + \oint_{s_l} (\mathbf{A} \cdot \mathbf{B})\mathbf{v} \cdot \hat{n}\, da, \quad (2.3.5)$$

Utilizing vector identities and Guass's divergence theorem,

$$\frac{dK_l}{dt} = \oint_{s_l} \xi\mathbf{B} \cdot \hat{n}\, da \ + \oint_{s_l} (\mathbf{v} \times \mathbf{B} \times \mathbf{A}) \cdot \hat{n}\, da \ + \oint_{s_l} (\mathbf{A} \cdot \mathbf{B})\mathbf{v} \cdot \hat{n}\, da \quad (2.3.6)$$

$$= \oint_{s_l} (\xi - \mathbf{A} \cdot \mathbf{v})\mathbf{B} \cdot \hat{n}\, da. \quad (2.3.7)$$

By definition of a flux tube the surface s_l is a MFS and hence, the flux tube satisfies the boundary condition $\mathbf{B} \cdot \hat{n} = 0$ (Woltjer 1958). Therefore

$$\frac{dK_l}{dt} = 0, \quad (2.3.8)$$

showing the K_l for each flux tube to be invariant for a magnetofluid with infinite electrical conductivity. Realizing that in a volume filling magnetic field there are infinite number of such flux tubes, eventually we have infinite number of ideal invariants for the magnetofluid.

To elucidate the physical significance of magnetic helicity, we consider two interconnected flux tubes that follow two closed contours C_1 and C_2, containing magnetic fluxes Φ_1 and Φ_2 with volumes V_1 and V_2, as depicted in Figure 2.2. We further assume no magnetic field exists outside these flux tubes. Then, the magnetic helicity integral for first flux tube C_1

$$K_1 = \int_{V_1} \mathbf{A} \cdot \mathbf{B} dV, \quad (2.3.9)$$

replacing $\mathbf{B}dV$ by $\Phi_1 d\mathbf{l}$ and using Stokes's theorem we obtain

$$K_1 = \Phi_1 \oint_{C_1} \mathbf{A} \cdot d\mathbf{l} = \Phi_1\Phi_2. \quad (2.3.10)$$

Similarly for the second flux tube C_2, we have

$$K_2 = \int_{V_2} \mathbf{A} \cdot \mathbf{B} dV = \Phi_2 \oint_{C_2} \mathbf{A} \cdot d\mathbf{l} = \Phi_1 \Phi_2. \tag{2.3.11}$$

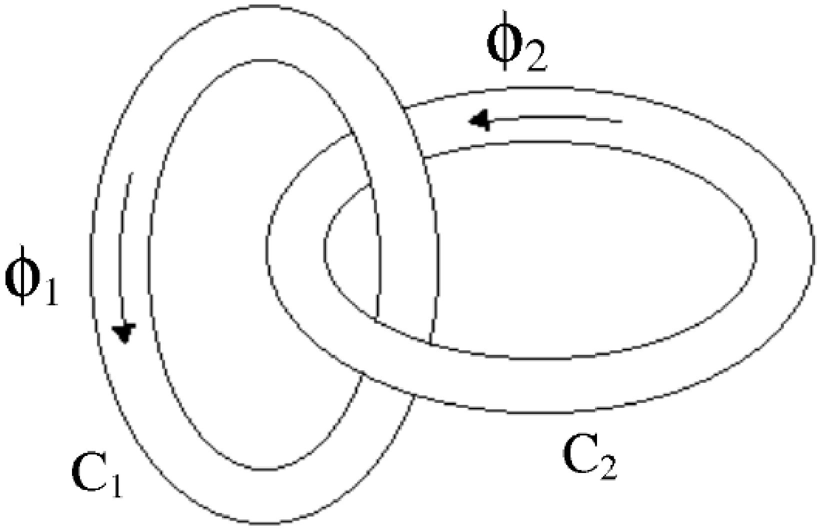

Figure 2.2: Two interconnected magnetic flux tubes.

Thus, K_1 and K_2 measure the linkage of the two tubes of fluxes. It can easily be demonstrated that if these two flux tubes are not interlinked then $K_1 = K_2 = 0$. While, if these tubes are linked N times, the magnetic helicity would be given by $K_1 = K_2 = \pm N \Phi_1 \Phi_2$, with sign determined by the handedness of the linkage. Hence, the magnetic helicity is directly related to the field line topology. The preservation of magnetic helicity then ascertains that the magnetic field lines are allowed to attain only those configurations for which the initial topology remains unchanged.

Towards obtaining the Woltjer relaxed state, we further assume the internal energy of the magnetofluid to be negligible compared to its magnetic energy i.e. plasma-$\beta << 1$. The total energy W is given by,

$$W = \int_{V_0} \left(\frac{\mathbf{B}^2}{8\pi} \right) dV. \tag{2.3.12}$$

The Woltjer variational problem minimizes the W while keeping the magnetic helicity of each flux tube invariant (Woltjer 1958). The relaxed state is then governed by the Euler-Lagrange equation

$$\nabla \times \mathbf{B} = \alpha(r)\mathbf{B}. \tag{2.3.13}$$

where the coefficient $\alpha(r)$ is Lagrange undetermined multiplier. The solenoidality of $\mathbf{B}$ further restricts $\alpha(r)$ to obey

$$\mathbf{B} \cdot \nabla\alpha(r) = 0, \tag{2.3.14}$$

confirming that $\alpha(r)$ does not vary along a given magnetic field line (or infinitesimal flux-tube). Notably, the relaxed state is non-linear and the corresponding Lorentz force ($\mathbf{J} \times \mathbf{B}$) is zero, leading to the nomenclature of the relaxed state as "non-linear force-free state". As mentioned above, for an ideal magnetofluid ($\lambda = 0$), we can associate a different K_l with each field line (or flux tube). Therefore, in principle, we can relate the value of $\alpha(r)$ with the K_l for each flux tube, which is determined by the initial magnetic configuration of the system. In other words, the function $\alpha(r)$ directly depends on the details of the initial conditions. But this contradicts the properties of relaxed state, which are observed to be independent of the initial conditions. Mathematically then, the infinite set of constraints over-determines the system and a reduction to a smaller set of constraints is desirable.

2.3.2 Presence of finite resistivity

The above difficulty can be resolved by realizing that the invariance of an individual K_l is a mathematical idealization yielded by the assumption of infinite electrical conductivity. In nature, no magnetofluid is ideal but has some finite electrical resistivity. Under such circumstance, it can easily be shown that the magnetic helicity integrals are no more invariants but decay with a rate,

$$\frac{dK_l}{dt} = -2\eta \int_{V_l} \mathbf{J} \cdot \mathbf{B}\, dV \; - \eta \oint_{s_l} (\mathbf{J} \times \mathbf{A}) \cdot \hat{n}\, da. \tag{2.3.15}$$

The principal effect of non-zero resistivity, even infinitesimal, is then to loosen the Woltjer's infinite number of invariants and allows all the helicity integrals to decay. Notably, in absence of any invariants, a direct minimization of W leads to the trivial state $\mathbf{B} = 0$, pointing towards the requirement of additional physically relevant constraints.

2.3.3 Taylor's hypothesis

A relevant constraint for the minimization of the W was put forward by J. B. Taylor in 1974 (Taylor 1974, 1986, 2000). For the purpose, he considered a plasma with very small electrical resistivity (characterized by high R_M) and plasma-$\beta << 1$, surrounded by a perfectly conducting boundary. In presence of the resistivity, the field lines break and reconnect (cf. chapter 3) and hence, the individual helicities K_l are not constant during an evolution. In such a plasma, Taylor hypothesized that total or global magnetic helicity (the sum of all K_l's), expressed as

$$\sum_{l=1}^{\infty} K_l = K_0 = \int_{V_0} \mathbf{A} \cdot \mathbf{B} \, dV \tag{2.3.16}$$

with the integral over the total plasma volume V_0, remains preserved during the evolution. With K_0 being invariant, it is possible to formulate a variational problem in which the magnetic energy is minimized while keeping the global magnetic helicity invariant. Then, the action integral is

$$I = W - \lambda_0 K_0 = \int_{V_0} \left(\frac{\mathbf{B}^2}{8\pi}\right) dV \; - \lambda_0 \int_{V_0} \mathbf{A} \cdot \mathbf{B} \, dV, \tag{2.3.17}$$

with constant λ_0 representing the Lagrange undetermined multiplier. I is minimized to obtain the relaxed state following

$$\delta I = \delta W - \lambda_0 \delta K_0 = 0, \tag{2.3.18}$$

$$\int_{V_0} \frac{\mathbf{B} \cdot \delta \mathbf{B}}{4\pi} dV \; - \lambda_0 \int_{V_0} (\delta \mathbf{A} \cdot \mathbf{B} + \mathbf{A} \cdot \delta \mathbf{B}) \, dV \; = 0. \tag{2.3.19}$$

Notably, the first order variation is sufficient to conclude that the achieved state is the relaxed (minimum magnetic energy) state as the decay of magnetic energy is assured by the physical properties of the magnetofluid. Using $\delta\mathbf{B} = \nabla \times \delta\mathbf{A}$ and vector identity $\nabla \cdot (\mathbf{Q} \times \mathbf{R}) = \mathbf{R} \cdot \nabla \times \mathbf{Q} - \mathbf{Q} \cdot \nabla \times \mathbf{R}$, equation (2.3.19) modifies as,

$$\int_{V_0} \delta\mathbf{A} \cdot \left(\frac{\nabla \times \mathbf{B}}{4\pi} - 2\lambda_0 \mathbf{B} \right) dV \; + \oint_{S_0} \delta\mathbf{A} \times \left(\frac{\mathbf{B}}{4\pi} - \lambda_0 \mathbf{A} \right) \cdot \hat{n} dS \; = 0. \quad (2.3.20)$$

boundary S_0 being a perfect conductor, the tangential component of $\delta\mathbf{A}$ vanishes at the boundary and we have

$$\int_{V_0} \delta\mathbf{A} \cdot \left(\frac{\nabla \times \mathbf{B}}{4\pi} - 2\lambda_0 \mathbf{B} \right) dV \; = 0, \quad (2.3.21)$$

which leads to relaxed state,

$$\nabla \times \mathbf{B} = \alpha_0 \mathbf{B} \quad , \quad (2.3.22)$$

where $\alpha_0 = 8\pi\lambda_0$ is constant throughout the plasma volume. Since during every reconnection, the participating magnetic field lines lose their identity, the terminal relaxed state is expected to be independent of the initial configuration. The Taylor relaxed state is linear and corresponds to zero Lorentz force. Therefore, the state is known as linear force-free state. The relaxed state does not have any thermodynamic pressure gradient because of low plasma-β. Also the way relaxation process is envisioned in the Taylor-relaxation, a force-free state (2.3.22) is a natural outcome. The relaxation process is assumed to proceed by spontaneous reconnections of magnetic field lines and, during reconnections the pressure can equalize itself so that the relaxed state is a state of uniform pressure.

2.3.4 Requirement of small scales for relaxation

Noteworthy in the Taylor's theory is the crucial requirement of spontaneous occurrence of magnetic reconnections to lower the magnetic energy. Notably, the dynamics of a high R_M magnetofluid is governed by the non-diffusive limit of the induction equation. Whereas magnetic reconnection being a diffusive process requires the $\lambda\nabla^2\mathbf{B}$ term of the induction equation to be effective (Priest and Forbes 2006). This leads to the necessity of spontaneous generations of small scales in the magnetic field or current sheets which amount to steep gradients in $\mathbf{B}$. R_M is then reduced locally to make the otherwise negligible diffusion to be effective. Noticeably, for an ideal magnetofluid ($\eta = 0$) these CSs are the current layers with zero thickness having unbounded but integrable current density. For a high R_M fluid with small electrical resistivity η, the CSs have finite thickness fixed by η and magnetic field lines are frozen to the fluid everywhere but at the CSs. Thus, the CSs are the potential sites where magnetic reconnections occur. The details of spontaneous development of CS constitute the next chapter.

Importantly, the existence of the small scales in $\mathbf{B}$ or CSs also validates Taylor's postulate of preservation of global magnetic helicity K_0 during the relaxation. To demonstrate, we calculate the decay rates of magnetic energy W and magnetic helicity K_0. The decay rates are

$$\frac{dW}{dt} = -\eta \int_{V_0} \mathbf{J}^2 \, dV, \tag{2.3.23}$$

$$\frac{dK_0}{dt} = -2\eta \int_{V_0} \mathbf{J}\cdot\mathbf{B} \, dV. \tag{2.3.24}$$

From an order of magnitude estimation, the ratio of magnetic energy decay rate to magnetic helicity decay rate $\approx 1/L$. Notably, the diffusion is only operative in the vicinity of CSs which corresponds to small L ($L << 1$). Therefore, the decay rate of W is expected to be much larger than that of K_0 under magnetic reconnections. This asserts the magnetic helicity to be relatively invariant in comparison to magnetic energy during the relaxation.

2.3.5 Taylor's theory for open systems

For a closed system with the boundary condition $\mathbf{B}\cdot\hat{n} = 0$, the global magnetic helicity K_0 given by equation (2.3.16) is gauge invariant and hence, is a physically meaningful parameter associated with complexity of field lines. For an open system where $\mathbf{B}\cdot\hat{n} \neq 0$, i.e. the magnetic field lines penetrate the boundary, the

K_0 is no more physically meaningful because of its dependence on an arbitrary gauge. However, a gauge invariant form of helicity, denoted as relative magnetic helicity

$$K_R = \int_{V_0} (\mathbf{A} \cdot \mathbf{B} - \mathbf{A_r} \cdot \mathbf{B_r})\, dV, \tag{2.3.25}$$

can be defined, with a reference magnetic field $\mathbf{B}_r = \nabla \times \mathbf{A}_r$ satisfying the boundary condition $\mathbf{B}_r \cdot \hat{n} = \mathbf{B} \cdot \hat{n}$ (Berger and Field 1984). In general, a current-free or potential field—satisfying the equation (2.3.13) with $\alpha(r) = 0$—is chosen as a reference field in context of the solar physics. Utilizing this relative magnetic helicity K_R, Heyvaerts and Priest (Heyvaerts and Priest 1984) extended Taylor's theory to open systems like the solar corona to explain the coronal heating. According to their model, solar flares can also be conceived as an explosive relaxation towards a Taylor-Heyvarts-Priest relaxed state. It also attempts to explain the quiescent prominences as a Taylor-Heyvarts-Priest minimum energy state (Demoulin et al. 1989; Amari and Aly 1990, 1992). Some observational studies (Nandy et al. 2003, 2004) show the possible signature of Taylor-type relaxation process in the magnetic fields of flare productive solar active regions.

The above discussion documents a general nature of standard analytical theories for MHD relaxation. Notable is the use of variational calculus in these theories to achieve the relaxed state. Although they are successful in predicting relaxed state. But, being of a variational nature, they do not provide any information of underlying dynamical processes which are responsible for the generation of the relaxed state. For instance, they do not shed light on how a current sheet develops and decays through magnetic reconnection. This is expected since an analytical study of the relaxation dynamics is a formidable task due to inherent non-linear and coupled nature of MHD equations. Therefore, numerical computations of MHD equations are required to explore the dynamics of MHD relaxation.

2.4 Summary

In this chapter, plasma is treated as an electrically conducting fluid which evolves according to MHD equations. The relative prevalence of non-linearity and diffusion in MHD equations is determined by magnetic Reynolds number. Generally, the astrophysical as well as some laboratory plasmas are characterized by very large magnetic Reynolds number. Such plasmas are highly non-linear and prone to exhibit MHD relaxation. As an analytical model for MHD relaxation, we have presented the Taylor's theory. It is shown that for a perfectly electrical conducting plasma, dynamics is constrained by infinite number of constraints in the form of magnetic helicity of individual magnetic field lines. In presence of a small but non-zero magnetic diffusivity, as in high R_M plasmas, all these constraints are removed and only the global magnetic helicity remains approximately preserved during an evolution. The relaxed state is then obtained by formulating a variational problem in which magnetic energy is minimized while keeping global magnetic helicity invariant. The Taylor's theory can be extended to open systems—like solar corona—by utilizing the concept of relative magnetic helicity. It has been argued that MHD relaxation inherently requires autonomous generation of current sheets for lowering of magnetic energy while approximately preserving magnetic helicity. This is achieved by magnetic reconnections. In the next chapter, we discuss the analytical theory of such autonomous formation of current sheets.

.

Chapter 3

Astrophysical Plasmas: Current Sheet Formation and Magnetic Reconnection

3.1 Introduction

From chapter 2, noteworthy is the crucial requirement of autonomous generation of current sheets and spontaneous magnetic reconnections for MHD relaxation to occur in astrophysical plasmas. For elucidating the autonomous development of CSs, this chapter provides the details of the magnetostatic theorem proposed by Parker (Parker 1972, 1988, 1994, 2012). The chapter concludes with a discussion on standard two-dimensional reconnection models.

3.2 Magnetostatic theorem

According to the magnetostatic theorem, formation of current sheets is inevitable in an equilibrium magnetofluid with infinite electrical conductivity and complex magnetic topology. The inevitability is attributed to a general failure of magnetic field in achieving equilibrium with simultaneous preservation of its topology while being spatially continuous everywhere. Extended to a dynamical scenario, such CSs are expected to develop in a magnetofluid undergoing topology preserving evolution towards an equilibrium.

For an illustration of the theorem, we revisit the example presented by Parker (Parker 1972, 1994). In the example, a uniform magnetic field $\mathbf{B} = B_0 \hat{e}_z$ passes through an incompressible, viscous magnetofluid with infinite electrical conductivity which is confined between boundary planes $z = 0$ and $z = L_0$, as shown in Figure 3.1 (a). The magnetic field exerts no Lorentz force on the fluid and magnetic field lines are tied to fluid parcels because of the flux-freezing. A random and continuous two-dimensional fluid motion is applied at the boundaries which moves the footpoints—the points at which the magnetic field lines intersect the $z = 0$ and $z = L_0$ boundary planes. In response, the initial MFLs evolve under ideal induction equation (2.2.13).

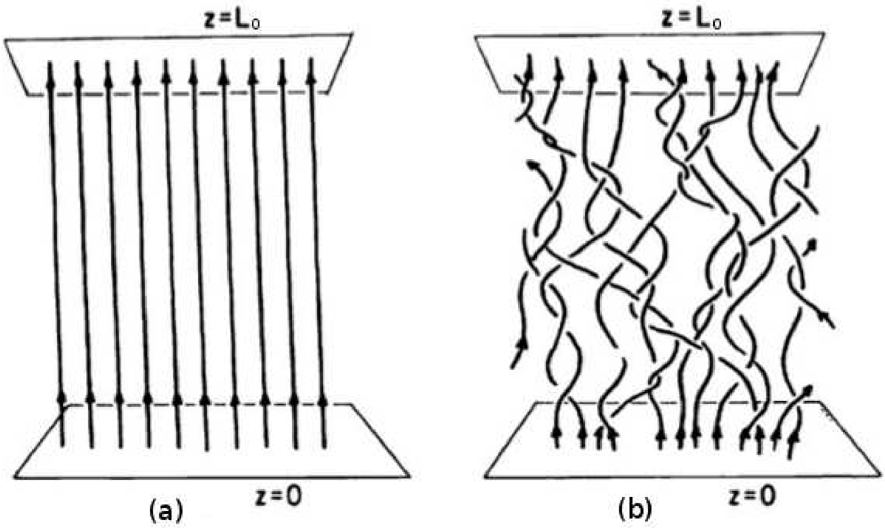

Figure 3.1: Schematic of the magnetic field lines of a uniform field (left panel) and a complex field (right panel). The complex field is generated by randomly moving the footpoints of the uniform field at boundary planes $z = 0$ and $z = L_0$. Notable is the interlaced MFLs of the complex field. The figure is adapted from (Parker 1994).

After a time t, it is expected that different field lines located at the neighborhood of a given field line will be wrapped around it. An extension of this wrapping to every field line leads to interlaced field lines, which can be identified as a measure of the topological complexity of the corresponding magnetic field. Thus, at time t, the MFLs are strongly interlaced and randomly intermixed (panel b, Fig.

3.1). Notably, the field $\mathbf{B}$ is devoid of any discontinuities because the prescribed boundary flows are smooth and continuous. An initial state is identified by switching off the fluid motions at t while making the footpoints of $\mathbf{B}$ motionless. If released from this initial state, the fluid is free to relax towards a minimum energy state in response to unbalanced forces while being confined in the domain $z \in \{0, L_0\}$. The flux-freezing guarantees the preservation of interlacing of MFLs during the relaxation. The magnetofluid then settles down to an equilibrium state where the Lorentz force is balanced by the thermodynamic pressure gradient (neglecting gravity) and satisfies the magnetostatic equation

$$4\pi\nabla p = (\nabla \times \mathbf{B}) \times \mathbf{B}, \tag{3.2.1}$$

with p as thermodynamic pressure. The scalar product of $\mathbf{B}$ with equation (3.2.1) yields the condition

$$\mathbf{B} \cdot \nabla p = 0, \tag{3.2.2}$$

rendering p to be constant along each MFL. It is readily seen that a specification of uniform pressure ($p = p_0$) at the boundaries ascertains the p to become constant (p_0) throughout the domain $z \in \{0, L_0\}$. Then, the equilibrium is determined by

$$(\nabla \times \mathbf{B}) \times \mathbf{B} = 0, \tag{3.2.3}$$

implementing a balance between forces of magnetic tension $(\mathbf{B} \cdot \nabla)\mathbf{B}/4\pi$ and magnetic pressure -$\nabla[B^2/(8\pi)]$ (Priest and Forbes 2006). As a consequence, the $\mathbf{B}$ satisfies the non-linear free equation (2.3.13) with $\alpha(r)$ constant along each MFL. The $\alpha(r)$ can be physically interpreted in terms of local magnetic circulation around a small closed contour C encircling any given flux bundle with infinitesimal cross-sectional area S. The circulation is defined as,

$$\omega = \oint_C \mathbf{B} \cdot d\mathbf{l}. \tag{3.2.4}$$

Utilizing Stokes's theorem in the above equation we get

$$\omega = \int_S \nabla \times \mathbf{B} \cdot d\mathbf{S}. \tag{3.2.5}$$

Using equation (2.3.13),

$$\omega = \int_S \alpha(r)\mathbf{B} \cdot d\mathbf{S}. \tag{3.2.6}$$

With the assumption that $\alpha(r)$ and $\mathbf{B}$ vary smoothly across the flux bundle, for an infinitesimal S we have

$$\omega = \alpha(r) \int_S \mathbf{B} \cdot d\mathbf{S}. \tag{3.2.7}$$

Then

$$\alpha(r) = \frac{\oint_C \mathbf{B} \cdot d\mathbf{l}}{\int_S \mathbf{B} \cdot d\mathbf{S}}, \tag{3.2.8}$$

representing the magnetic circulation per unit flux (Parker 1994). Since both $\alpha(r)$ and magnetic flux $\int_S \mathbf{B} \cdot d\mathbf{S}$ are constant along the bundle, equation (3.2.7) confirms that magnetic circulation is also constant along the flux bundle.

The equilibrium magnetic field $\mathbf{B}$ satisfying (2.3.13) with interlaced MFLs, is expected to have flux bundles that wrap clockwise around their neighboring flux bundles at a given location and wrap counterclockwise at another location (cf. panel b, Fig. 3.1). Consequently, the magnetic circulation is generally not of a fixed sign along a given flux bundle. Equation (3.2.8) then implies that the $\alpha(r)$ is not fixed along the flux bundle but it varies. This variation of $\alpha(r)$ is incompatible with equation (2.3.14) which demands the invariance of $\alpha(r)$ along each flux bundle. According to the magnetostatic theorem, this contradiction is avoided when the field $\mathbf{B}$ becomes discontinuous and develops current sheets across which the direction of the magnetic field changes abruptly. These CSs are the surfaces which occupy no volume, and on these surfaces the magnetic field is undefined. In essence, a magnetofluid under equilibrium accommodates the arbitrary interlacing of MFLs by spontaneously developing CSs.

3.3 The Optical Analogy

To further confirm the development of CSs, Parker proposed that the streaming of MFLs of a potential field $\mathbf{B}_p$ is identical to the streaming of optical rays in a medium of refractive index $\mid \mathbf{B}_p \mid$. The proposal is called the optical analogy (Parker 1989a,b,c, 1990, 1994). To fix ideas we note that the potential field $\mathbf{B}_p$ being curl-free, can be expressed as

$$\mathbf{B}_p = -\nabla\phi_p, \tag{3.3.1}$$

with scalar potential ϕ_p. The corresponding field lines equations are

$$B_p \frac{dx}{ds} = -\frac{\partial\phi_p}{\partial x}, \tag{3.3.2}$$
$$B_p \frac{dy}{ds} = -\frac{\partial\phi_p}{\partial y}, \tag{3.3.3}$$
$$B_p \frac{dz}{ds} = -\frac{\partial\phi_p}{\partial z}, \tag{3.3.4}$$

where we have employed Cartesian coordinates with $ds = \sqrt{dx^2 + dy^2 + dz^2}$ as the invariant length, and the magnitude B_p satisfies

$${B_p}^2 = \mid \nabla\phi_p \mid^2 . \tag{3.3.5}$$

Notable is the resemblance of equations (3.3.2)-(3.3.4) with equations of optical ray paths in a medium with refractive index $n = B_p$ and eikonal ϕ_p; where (3.3.5) represents the equivalent eikonal equation (Born and Wolf 1975; Parker 1989b). Therefore, the trajectories of MFLs of $\mathbf{B}_p$ will be identical to the optical rays in a medium with refractive index B_p and hence, follow Fermat's principle (Parker 1994). The principle provides the path taken by an optical ray between two points P and Q as the curve which minimizes the optical path length $\int_P^Q B_p dl$, i.e.

$$\delta \int_P^Q B_p dl = 0. \tag{3.3.6}$$

Further analysis concludes that a field line tends to deflect away from a sufficiently local maximum in B_p since the optical path length is shorter around the maximum compared to the one which is over the top of the maximum (Parker 1994).

Importantly, the optical analogy also applies to a non-potential vector field $\mathbf{F}$ (i.e., $\nabla \times \mathbf{F} \neq 0$). This applicability comes from the fact that non-potential field $\mathbf{F}$ can be represented as the gradient of a scalar potential in any local surface S which contains field lines of both $\mathbf{F}$ and $\nabla \times \mathbf{F}$ (Parker 1994). That is to say, in two-dimensional space of the surface S, the field $\mathbf{F}$ is curl-free. Then the optical analogy is applicable for field lines of $\mathbf{F}$ tangential to S and the corresponding streaming of field lines follows optical ray paths in a medium with refractive index $\mid \mathbf{F} \mid$. To demonstrate formally, we consider the force-free magnetic field $\mathbf{B}$ satisfying equation (2.3.13). It is clear from the equation (2.3.13) that every local magnetic flux surface S_f of $\mathbf{B}$ also carries the field lines of $\nabla \times \mathbf{B}$. Hence, on the flux surface S_f the magnetic field $\mathbf{B}$ can be expressed as,

$$\mathbf{B} = -\nabla\phi_f, \tag{3.3.7}$$

where ϕ_f is a scalar potential. Without any lose in generality (Parker 1989b, 1994), we further assume the S_f to be a flat surface, tangential to z-constant planes of a Cartesian domain. The equations for field lines that are tangential to S_f are,

$$B\frac{dx}{ds} = -\frac{\partial \phi_f}{\partial x}, \tag{3.3.8}$$
$$B\frac{dy}{ds} = -\frac{\partial \phi_f}{\partial y}, \tag{3.3.9}$$

where $ds = \sqrt{dx^2 + dy^2}$ and the magnitude $B = B(x, y)$ is expressed as,

$$B^2 = \left(\frac{\partial \phi_f}{\partial x}\right)^2 + \left(\frac{\partial \phi_f}{\partial y}\right)^2. \tag{3.3.10}$$

It follows that the MFLs of $\mathbf{B}$ on S_f stream similar to the optical rays associated with the eikonal equation (3.3.10) with B as the effective refractive index of the medium. Fermat's principle is then applicable to these streaming MFLs, making them deflect away from regions with locally intense B. To illustrate, in Figure 3.2(a), we show a schematic of the flux surface S_f having locally enhanced B in the domain D (cross hatched). Notable is the concave deflections of a bunch of MFLs towards the domain D which generate a gap or a zone of exclusion on the flux surface co-located to the region where $B \approx B_{max}$ (panel a).

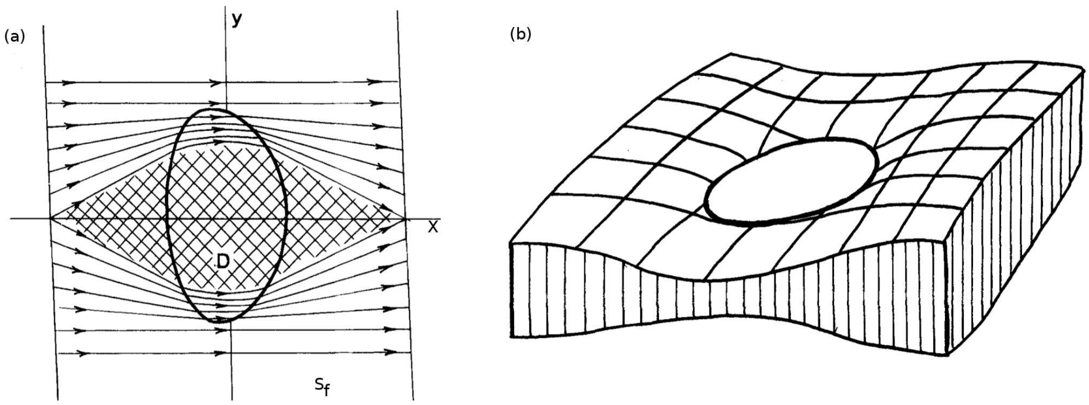

Figure 3.2: Panel a depicts a schematic of MFLs pattern in the flux surface S_f. The domain D (cross hatched) represents the region of $B \approx B_{max}$. The MFLs are concave towards the domain D and hence develop a gap in the surface S_f. In a stack of the flux surfaces of finite thickness, the gap appears as a hole as shown in panel b. Panels a and b are taken from (Parker 1989b, 1994).

Continued in three dimensions, a local region enclosing a volume can be made of a stack of magnetic flux surfaces similar to the S_f. Then, the gaps generated on the flux surfaces create a hole in the stack, as sketched in Figure 3.2(b). A possibility then opens up where separate MFLs located on either side of the stack intrude into the hole and become arbitrarily close. In general the field lines on both sides of the stack are non-parallel and hence their arbitrary closeness can generate CSs. Similar to the force-free field, it is easy to demonstrate the applicability of optical analogy to the magnetostatic field satisfying the equation (3.2.1). In this case, both $\mathbf{B}$ and $\nabla \times \mathbf{B}$ lie on the surface of constant thermodynamic pressure p. The optical analogy then applies to these isobaric surfaces and CSs are generated.

3.4 Magnetic Reconnection

In contrast to the zero thickness of CSs in an infinitely conducting plasma, CSs developed in large R_M fluids have finite thickness as the non-zero magnetic diffusivity forces a local destruction of the flux-freezing and allows field lines to diffuse out. The resulting slippages of field lines through the fluid parcels initiate magnetic reconnections where magnetic energy gets converted into heat and kinetic energy of mass flow along with a local rearrangement of field line topology.

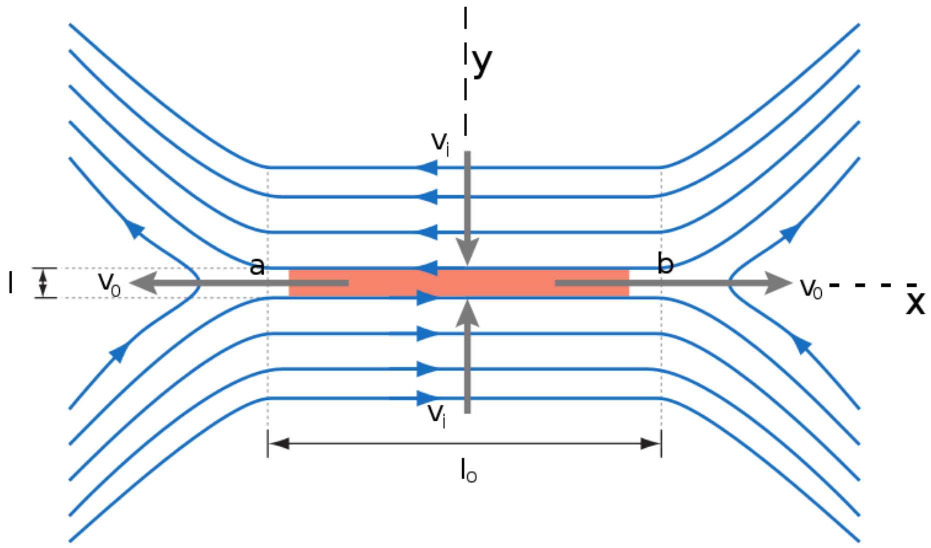

Figure 3.3: The schematic shows current sheet (shaded area) with thickness l and width l_0, in xy plane. The field lines are oppositely directed in the vicinity of the CS. The figure is adapted from (Zweibel and Yamada 2009).

One of the traditional reconnection models, known as the Sweet-Parker model, was proposed by Sweet and Parker (Parker 1957; Sweet 1958). The Sweet-Parker model describes the steady state magnetic reconnection across a CS by approximately solving MHD equations in a two-dimensional Cartesian geometry. To discuss the essential features of the model, we consider an incompressible magnetofluid with mass density ρ and magnetic diffusivity λ. The assumed magnetic field configuration contains a current sheet situated around $y = 0$ plane with a finite thickness l and a width l_0, as shown in Figure 3.3. The figure also plots a schematic of MFLs of two oppositely directed magnetic fields, $\pm B$, in the vicinity of the current sheet. We assume that the oppositely directed MFLs are pushed towards the CS from each side (over the length l_0) with an inflow speed v_i (Fig. 3.3). In response to this inflow, the fluid squeezes out sideways through the regions a and b (Fig. 3.3). We consider this outflow speed to be v_o. Under steady state assumption, an approximate form of mass conservation yields

$$l_0 v_i \approx l v_o. \tag{3.4.1}$$

Since the Lorentz force is responsible for the generation of the outflow, we expect that the kinetic energy associated with the outflow should be comparable to the magnetic energy stored in the current sheet. Therefore, we have

$$\frac{1}{2}\rho {v_o}^2 \approx \frac{B^2}{8\pi}, \tag{3.4.2}$$

$$v_o \approx \frac{B}{\sqrt{4\pi\rho}} = v_a, \tag{3.4.3}$$

revealing that the outflow speed v_o is almost equal to the Alfvén speed v_a. Further with the steady state approximation, the induction equation (2.2.8) is

$$\nabla \times (\mathbf{v} \times \mathbf{B}) + \lambda \nabla^2 \mathbf{B} = 0, \tag{3.4.4}$$

stating that the magnetic field is dissipated (via the $\lambda\nabla^2\mathbf{B}$ term) as rapidly as it is convected towards the current sheet at a speed v_i (via the $\nabla \times \mathbf{v} \times \mathbf{B}$ term). An order of magnitude estimation for these two terms leads to,

$$\frac{v_i B}{l} \approx \frac{\lambda B}{l^2}, \tag{3.4.5}$$

$$v_i \approx \frac{\lambda}{l}. \tag{3.4.6}$$

From equations (3.4.1) and (3.4.3) we have $l = v_i l_0 / v_a$. Plugging l into equation (3.4.6) yields

$$v_i \approx \frac{\lambda v_a}{v_i l_0} \approx \frac{v_a}{\sqrt{S}}, \tag{3.4.7}$$

$$l = \frac{l_0}{\sqrt{S}}, \tag{3.4.8}$$

where $S = v_a l_0/\lambda$ is known as the Lundquist number. Hence, the fields reconnect at a speed given by equation (3.4.7). This rate is known as the Sweet-Parker reconnection rate. Utilizing this rate, the characteristic diffusion time scale τ_d is

$$\tau_d = \frac{l_0}{v_i} = \tau_a \sqrt{S}, \tag{3.4.9}$$

where $\tau_a = l_0/v_a$ is the characteristic Alfvén time scale.

Observations reveal the occurrence of sudden energy release in the form of solar and stellar flares in astrophysical plasmas. For example, in a large solar flare, an energy of the order of 10^{32}ergs is released within a few minutes (Aschwanden 2005). In a magnetically dominated solar corona, it is believed that magnetic reconnection is the process responsible for such eruptions. With the typical solar coronal parameters (Aschwanden 2005): Alfvén speed $v_a \approx 10^6$m/s, the characteristic length scale $l_0 \approx 10^7$m (typical height of magnetic loops) and magnetic diffusivity (calculated using Spitzer resistivity) $\lambda \approx 1\text{m}^2$/s; the Lundquist number S and Alfvén crossing time τ_a are 10^{13} and 10s. Following Sweet-Parker model, the reconnection rate v_i and the characteristic reconnection time τ_d are approximately 0.3m/s and 3×10^6s respectively. The τ_d is clearly much larger than the observed flaring time—inferring the model to be inadequate to account for solar flares.

In an attempt to increase the reconnection rate, Petschek (Petschek 1964) assumed a two-dimensional current sheet where $l_0 \approx l$. Further physical arguments lead to a reconnection rate given by

$$v_i = v_a \ln S, \tag{3.4.10}$$

which is known as the Petschek reconnection rate. Noticeably, for a given S, the Petschek reconnection rate is much faster compared to the Sweet-Parker reconnection rate. Furthermore, Priest and Forbes (Priest and Forbes 1986) proposed an unified model where the Sweet-Parker and Petschek rates appear as special cases.

3.5 Summary

The magnetostatic theorem provides an analytical frame-work for spontaneous development of current sheets in magnetofluids with infinite electrical conductivity. The development of CSs is argued in a magnetofluid undergoing topology preserving evolution towards an equilibrium with interlaced MFLs. The optical analogy further supports the spontaneous formation of CSs. The analogy takes the advantage of the fact that MFLs in any local magnetic flux surface trace the path of optical rays in a medium with refractive index given by the intensity of the magnetic field. A locally intense magnetic field then causes a bifurcation of field lines, developing a hole in a stack of magnetic flux surfaces. The hole then permits otherwise separated non-parallel field lines to come arbitrarily close and generate CSs. In astrophysical magnetofluids, the field lines across the CS undergo reconnections. To explain reconnection, the Sweet-Parker model is discussed. In the following chapter, we present observational signatures of reconnections in the solar corona.

Chapter 4

Solar Corona as a Prototype Example

4.1 Introduction

Sun, being nearest to the earth, serves as a natural laboratory involving astronomical time and length scales (Choudhuri 2010) and provides an ideal testbed to evaluate various ideas related to MHD relaxation. From the last few decades, space and ground-based observatories have been supplying a wealth of data in different wavelengths which provide us the opportunity to explore the physics of the solar atmosphere. Standardly, based on the physical properties such as density and temperature, the solar atmosphere is subdivided into three layers: the photosphere, the chromosphere and the corona (Figure 4.1). The density decreases monotonically from the photosphere to the corona. However, the temperature decreases until it reaches a minimum located at the base of the chromosphere. Above the base, the temperature starts to increase slowly throughout the chromosphere (upto around 20000K) followed by a steep enhancement in the narrow transition region upto around a few million degrees Kelvin in the corona. It is widely believed that the dissipation of magnetic energy is one of the possible causes for the temperature enhancement (Kuperus et al. 1981; Parker 1994; Priest 2014). The precise physical mechanism through which the magnetic energy gets dissipated in the corona is still debatable (Priest 2014) and is an open research problem. Notably, the ubiquitous generation of current sheets and subsequent relaxation through magnetic reconnections provide a possible mechanism to heat the corona (Parker 1972, 1988, 1994; Klimchuk 2006). Moreover, observations suggest repetitive magnetic reconnections to be responsible for various eruptive phenomena and large scale structure formations in the corona (Chen 2011; Shibata and Magara 2011) and hence point towards a possible occurrence of MHD relaxation. In the following section, we briefly discuss various properties of the corona to highlight plausible observational signatures of MHD relaxation.

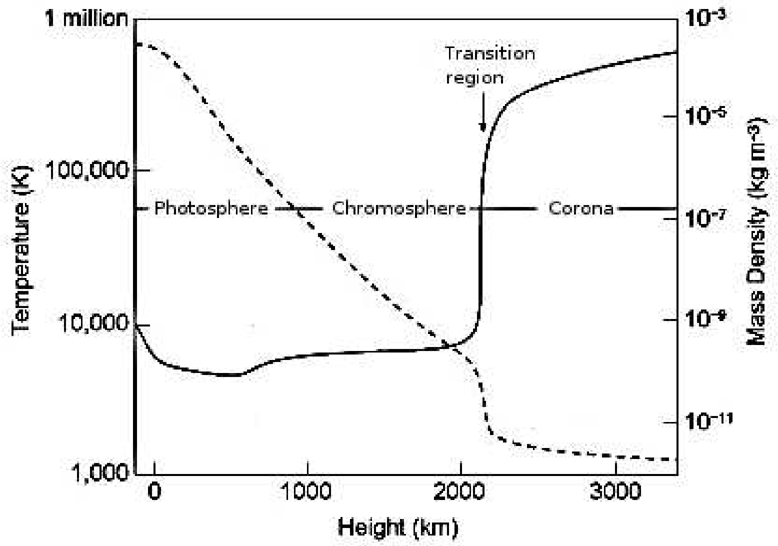

Figure 4.1: The figure plots profiles of mass density (dashed line) and temperature (solid line) in the solar atmosphere (courtesy of Eugene Avrett, Smithsonian Astrophysical Observatory).

4.2 Solar corona

At million degrees Kelvin, the solar corona primarily emits in ultra-violet (UV) and X-ray region of the electromagnetic spectrum (Golub and Pasachoff 1997; Aschwanden 2005). When observed in these bands, the corona appears highly structured. For example, we show an X-ray image of the corona in Figure 4.2. The image shows bright coronal regions with a variety of complex plasma loops from where the most of X-ray emissions are produced. These bright regions are known as coronal active regions. Noticeably, a direct comparison between

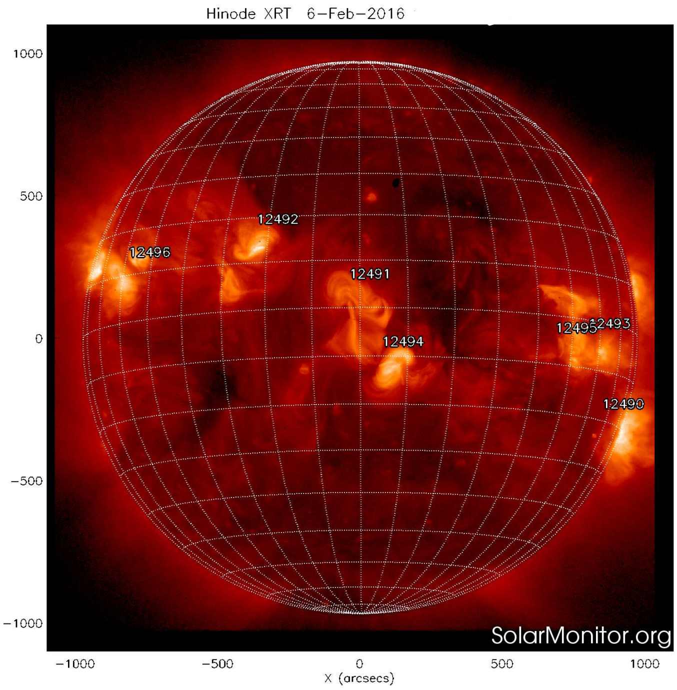

Figure 4.2: An X-ray image of the corona on 6 February 2016, taken from soft X-ray telescope (SXT) on board Hinode. The bright complex regions represent the coronal active regions which are numbered by NOAA. Image source: https://www.solarmonitor.org.

the X-ray emissions in the solar corona and underlying photospheric magnetic field (Figure 4.2 and Figure 4.3) shows a strong correlation between intensity of the X-ray emissions and strength of the magnetic field. Therefore, these coronal active regions are generally associated with the underlying strong magnetic field regions (sunspots) on the photosphere (Aschwanden 2005). Further the Spitzer magnetic diffusivity (Spitzer 1962) is approximately $10^9 T^{-3/2}\mathrm{m}^2/\mathrm{s}$ which amounts to a magnetic diffusivity $\lambda \approx 1\mathrm{m}^2/\mathrm{s}$ for the million degree corona (Aschwanden 2005). With a small magnetic diffusivity and large length scales (typical loop height is $\approx 10^7$m), coronal plasma satisfies the condition of flux-freezing. Standardly, under the flux-freezing, the plasma loops traces the associated magnetic field lines characterized by a field strength of $\approx 10^2$G (Golub and Pasachoff 1997; Wiegelmann and Solanki 2004) and connect two opposite polarity sunspots. Being closed, the loops confine plasma with higher particle density ($\approx 10^{16}$particles/m^3) in comparison to the surroundings ($\approx 10^{14}$particles/m^3) (Golub and Pasachoff 1997).

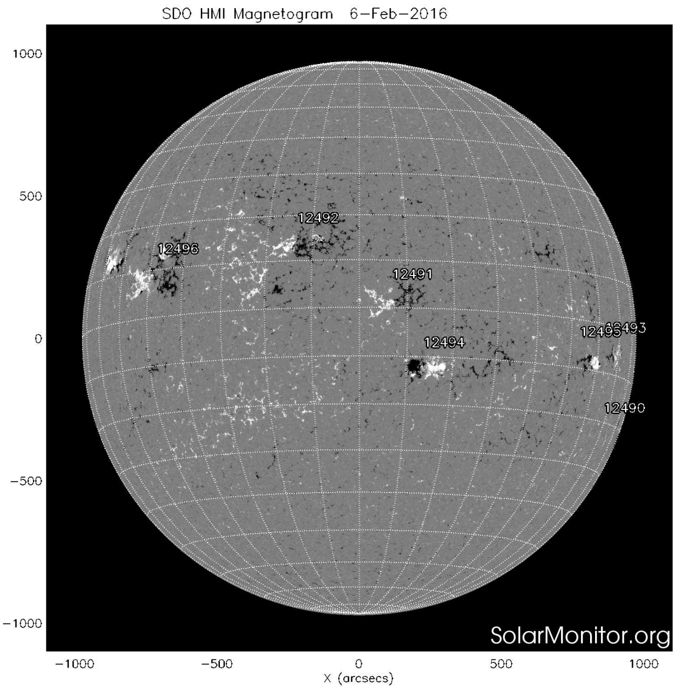

Figure 4.3: Maps of photospheric magnetic field on 6 February 2016, recorded with Helioseismic and Magnetic Imager (HMI) on board SDO. White and black colors indicate positive and negative magnetic polarity of the sunspots respectively. Image source: https://www.solarmonitor.org.

From the above discussion, it is imperative that magnetic field plays an important role in structuring the coronal plasma. Therefore, in the thesis, we focus on the field line topology of the coronal magnetic field to understand overall dynamics of the coronal plasma. Notably, the photospheric magnetic field is routinely measured by exploiting the Zeeman effect (del Toro Iniesta 2003). Since coronal magnetic field is small in amplitude, the corresponding polarization is also small and limits the accuracy of coronal field measurements (del Toro Iniesta 2003). Therefore, the coronal magnetic field is usually extrapolated from the photospheric magnetic measurements using three-dimensional magnetic field models (Wheatland 1999; Carcedo et al. 2003; Wiegelmann and Sakurai 2012).

The standard modeling of the field makes certain assumptions regarding the coronal plasma (Carcedo et al. 2003; Wiegelmann and Sakurai 2012). To demonstrate them, we approximately calculate each term of the momentum transport equation (2.2.1). For the purpose, let us assume that L, v_0 and L/v_0 are characteristic values for length scale, plasma flow speed and time scale in the corona, respec-

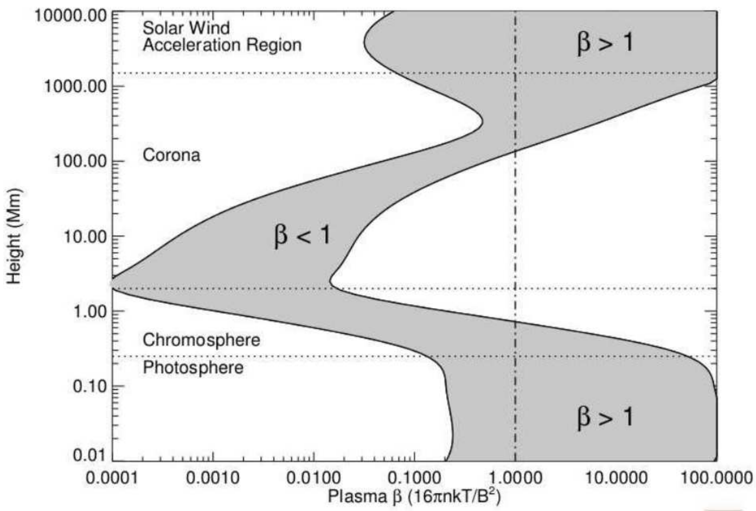

Figure 4.4: Change in plasma-β with height in the solar atmosphere. Notably, a region with plasma-$\beta << 1$ is sandwiched between the photosphere and the upper corona, where plasma-β is about unity or larger. The figure is taken from (Gary 2001).

tively. For the typical density ρ_0, pressure p_0, magnetic field B_0, and kinematic viscosity ν_0, we compare the order of magnitude estimations of Lorentz force with other forcing terms in equation (2.2.1). The ratios are

$$\frac{(\nabla\times\mathbf{B})\times\mathbf{B}}{4\pi\nabla p}\approx\frac{2}{\beta},\quad \frac{(\nabla\times\mathbf{B})\times\mathbf{B}}{4\pi\rho\mathbf{g}}\approx\frac{2H}{L\beta},\quad \frac{(\nabla\times\mathbf{B})\times\mathbf{B}}{4\pi\mu\nabla^2\mathbf{v}}\approx\frac{{v_a}^2 R_F}{{v_0}^2}, \tag{4.2.1}$$

where β is the plasma-β, while $H = kT/g$, $R_F = v_0 L/\nu_0$ and $v_a = B_0/\sqrt{4\pi\rho_0}$ are pressure scale height, fluid Reynolds number and Alfvén speed respectively. Figure 4.4 illustrates the variation of plasma-β with height in the solar atmosphere (Gary 2001). The figure documents $\beta << 1$ in lower and middle corona. For a typical coronal parameter set: $v_a \approx 10^6$m/s, $v_0 \approx 10^4$m/s, $H \approx 100$Mm, $L \approx 10$Mm and $R_F \approx 100$ (Aschwanden 2005), it is clear from equation (4.2.1) that Lorentz force dominates over all other forces in the lower and middle corona where $\beta << 1$. Moreover the ratio of Lorentz force to $\rho\frac{dv}{dt}$, LHS of equation (2.2.1), is approximately ${v_a}^2/{v_0}^2$ which is much greater than one. Therefore, the coronal magnetofluid can be assumed to be in the force-free equilibrium (3.2.3). The equilibrium is satisfied either by a potential field which is devoid of current;

or by force-free fields satisfying equations (2.3.13) and (2.3.22). The potential field is the simplest assumption for the coronal magnetic field. But, this field does not support twisted field lines. In contrast, the observations evince the presence of twist in the coronal field, rendering the force-free fields to better approximate the corona (Wiegelmann and Sakurai 2012).

4.3 Current sheet and magnetic reconnection in the corona

Under the flux-freezing, the coronal magnetic field is non-diffusive and hence the topology of field lines are expected to be preserved. Nevertheless, observations reveal the occurrence of various eruptive phenomena which are diffusive in nature and involve reconfiguration of coronal loops (Shibata and Magara 2011). This alludes to the development of current sheets and consequent magnetic reconnections (Parker 1994).

Towards exploring the possibility of CS formation in the corona, we note that the footpoints of the coronal magnetic field lines remain rooted to the photosphere (Parker 1994, 2005). The photospheric flows are then expected to shuffle these footpoints. For instance, a typical convective cell of length $l = 3 \times 10^5$m with speed $v = 10^3$m/s shuffles the footpoint on a time scale $\tau = l/v \approx 300$s. Notably $\tau > \tau_a$ with $\tau_a \equiv L/v_a \approx 10$s, where L is typical height of coronal loops. This suggests that the coronal magnetic fields adjust quasi-statically in response to the photospheric flows (Parker 2005). The flows being random, are expected to slowly mix and swirl the footpoints. Consequently, the coronal MFLs get interlaced, and have more magnetic energy in comparison to non-interlaced MFLs. With these interlaced MFLs, the CSs develop spontaneously according to the Parker's magnetostatic theorem. The theorem further asserts that the Maxwell stresses always operate in a way to sharpen magnetic field gradients and hence, decrease thicknesses of developing CSs. In presence of non-zero coronal magnetic diffusivity, these current sheets are dissipated by MRs as their thicknesses fall below a threshold.

4.3.1 Potential sites for current sheet formation

Notably, the potential sites for development of CSs in the corona can pre-exist in the form of magnetic nulls—the points in space where $\mathbf{B} = 0$ (Longcope and Parnell 2009). Generally the field line topology near a magnetic null is favorable for CS generation. For instance, in two-dimensional (2D) geometry, the field line structure in the vicinity of magnetic nulls is either "X" type or "O" type, leading to their nomenclatures X-type or O-type nulls (cf. Figure 4.5). A favorable pressing of these nulls readily originates extended CSs, as shown in Figure 3.3. Noticeably, in the case of X-type null, the reconnection may also occur at the null point without developing a CS if the favorable pressing is absent.

Figure 4.5: Panels a and b plot MLFs in the neighborhood of X-type and O-type null respectively.

A three-dimensional (3D) null is characterized by the presence of a spine axis along which field lines approach (or recede from) the null, and a fan surface along which field lines recede from (or approach) the null; see Figure 4.6(a). The fan is a separatrix surface that divides the local volume into two topologically distinct regions with respect to the MFLs connectivity. From the Figure 4.6(a), it is straightforward that a pair of MFLs belonging to one end of the spine axis (and hence close to each other) can end up at altogether separate regions on the fan plane. The corresponding connectivity is then discontinuous (Pontin 2012). The 3D nulls and their associated separatrix surfaces and separators (MFLs joining a pair of 3D null) are proposed as potential locations for the CS formation (Lau and Finn 1990; Priest and Titov 1996; Priest et al. 2002; Pontin 2012). In addition to magnetic nulls, other proposed potential sites are the regions where connectivity of MFLs between a pair of boundaries changes drastically (Priest and Démoulin 1995; Démoulin 2006). Such regions are called quasi-separatrix layers (QSLs) and Figure 4.6 (b) depicts an example.

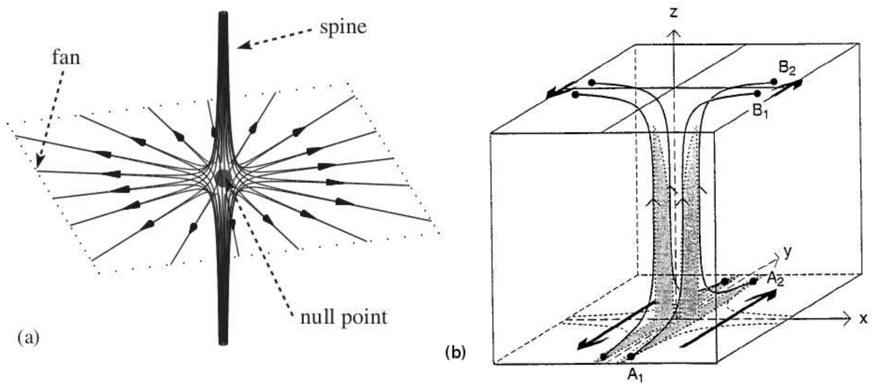

Figure 4.6: Panel a shows the MLFs in the vicinity of a 3D null . Panel b illustrates QSLs (shaded area). The panel documents the connectivity of two set of MFLs. The bifurcation of the MFLs, with the footpoints B_1 and B_2 are in close proximity while footpoints A_1 and A_2 are very far, depicts a change in field line connectivity. Panel a is from (Pontin 2012) and panel b is from (Démoulin 2006).

4.4 Observational signatures of magnetic reconnection

4.4.1 Prominence/Filament

Prominences/filaments are long-lived coronal structures that are two orders of magnitude cooler and denser than the ambient plasma (Mackay et al. 2008). When these are viewed at the solar limb they are referred to as "prominences" (Figure 4.7). When viewed against the solar disk, the structures are referred to as "filaments". Noticeably, these structures are found to be located above polarity inversion lines (PILs) of the photospheric magnetic field (Mackay et al. 2008; Parenti 2014).

It is then imperative to find how such dense low temperature plasmas form

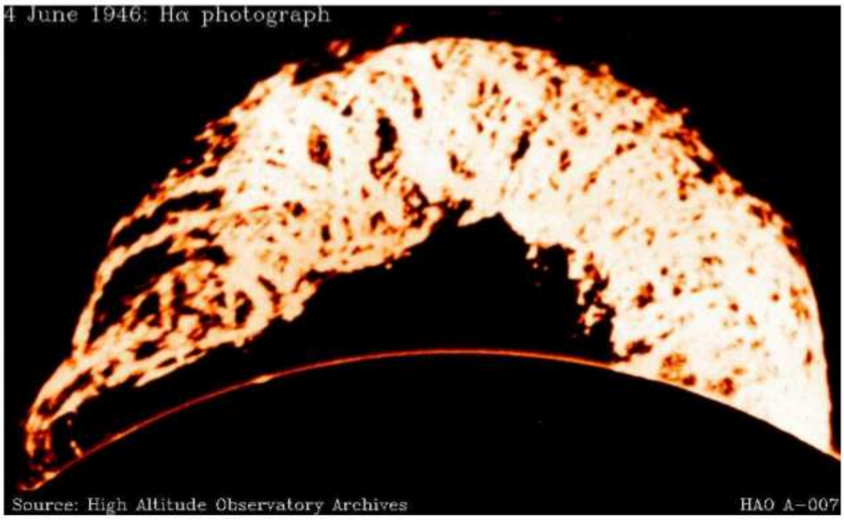

Figure 4.7: A famous gigantic prominence observed in H_α on 4 June 1946 from the High Altitude Observatory (HAO). Image source: http: //cass-www.ucsd.edu/archive/public/tutorial/Sun.html.

and sustain for a long time in the hot surrounding medium. The magnetic topology of a prominence is believed to be identical to twisted magnetic flux-rope which, in its skeletal form, is nested co-axial cylindrical magnetic flux surfaces made of helical field lines (Low 2001). In a more refined description, the helical field lines constituting the rope are dipped at the bottom to provide a support for the prominence mass (Priest et al. 1989; van Ballegooijen and Martens 1989; Gibson and Fan 2006; van Ballegooijen and Cranmer 2010). Notably, there are two ways to create flux-ropes in the solar corona: (1) flux-ropes emerge from below the photosphere, having been already formed in the solar interior (Fan and Gibson 2003, 2004; Fan 2010, 2011), or (2) magnetic reconnection at the PIL of a sheared magnetic arcade (van Ballegooijen and Martens 1989; Choe and Lee 1996; Amari et al. 1999; DeVore and Antiochos 2000; Amari et al. 2003; Aulanier et al. 2010; Xia et al. 2014). Both the ways find observational support. For instance, observations indicating the emergence of pre-twisted magnetic fields through the photosphere (Leka et al. 1996; Rust and Kumar 1996) agree with the first way. While the observational studies (Mackay et al. 2008; Cheng et al. 2011; Kumar et al. 2015b) favor the second way and hence underline the importance of magnetic reconnection.

4.4.2 Solar Flares

A solar flare is a sudden and explosive eruptive phenomena observed in the solar atmosphere, releasing an energy from 10^{28} to 10^{32}ergs on time scales varying from seconds to several minutes. Flares manifest their signatures in a wide range of electromagnetic spectrum, from radio to γ-rays, and involve substantial mass motion and particle acceleration; see review (Fletcher et al. 2011). The observations of solar flares in soft X-ray (SXR) wavelengths established two morphologically distinct classes of flares: confined and eruptive events (Pallavicini et al. 1977). Generally, the confined flares show impulsive and short duration brightening in a single magnetic loop which remains almost unchanged in shape and position throughout the event (left panel, Figure 4.8). In contrast, the eruptive flares are the long duration events (right panel, Figure 4.8) with larger spatial extension (Milligan et al. 2006; Fletcher et al. 2011). They are accompanied by a system of loops.

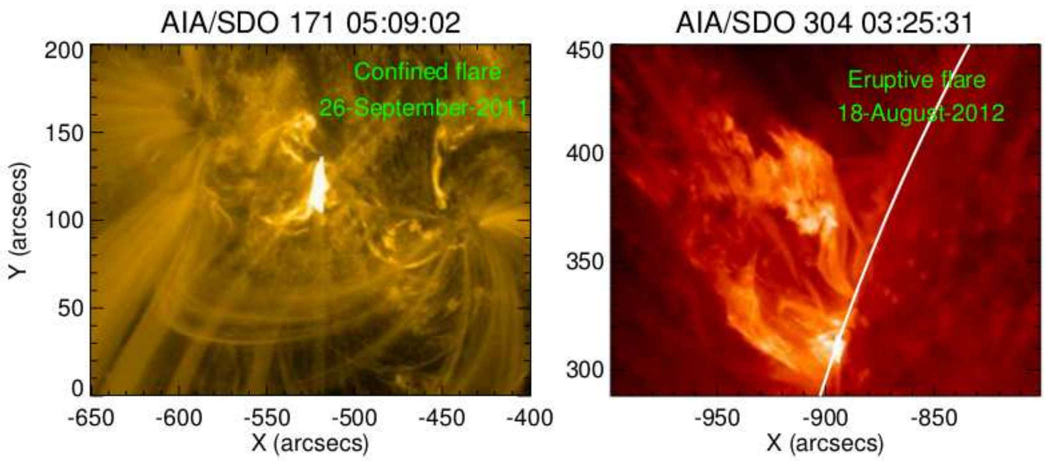

Figure 4.8: Left panel illustrates AIA 171Å image of a confined flare observed in active region NOAA 11302 on 26 September 2011. Right panel depicts AIA 304Å image of an eruptive flare observed in active region NOAA 11548 on 18 August 2012. Notable is brightenings in the coronal loop which are taken as a proxy of reconnections.

Towards identifying possible signatures of reconnections during a flare, notable are the observations of subtle changes in the configuration of EUV loops and localized episodic brightings in the early stage of a flare onset which are standardly taken as the signatures of repetitive reconnections (Joshi et al. 2011;

Kushwaha et al. 2015). It is believed that the repetitive reconnections provide a triggering mechanism for the following large-scale eruption (Chifor et al. 2007; Joshi et al. 2011; Kushwaha et al. 2015) which is characterized by rapid and intense emissions in hard X-rays (HXR), non-thermal microwave (MW) and in some cases also in γ-rays and white-light, providing the evidence of strong acceleration of charge particles (Joshi et al. 2011; Kushwaha et al. 2014, 2015). These radiation are further supplemented by strong enhancement of emissions of $H\alpha$, UV, and EUV. During this eruption, most of the energy stored in the magnetic field is released. Generally, magnetic reconnection is suggested to be responsible for such a sudden and intense energy release (Shibata and Magara 2011). The suggestion finds support from HXR emission which is traditionally viewed in terms of the bremsstrahlung process in which the X-ray production takes place when high-energy electrons accelerated in the coronal reconnection region (Masuda et al. 1994), come along magnetic loops and get decelerated while penetrating the denser transition region and chromosphere (Brown 1971; Syrovatskii and Shmeleva 1972).

To explain the occurrence of flares, several phenomenological models based on magnetic reconnection have been proposed (Carmichael 1964; Sturrock 1966; Hirayama 1974; Kopp and Pneuman 1976). These models assume more or less a similar configuration of magnetic field and its dynamic process, so they are commonly known as CSHKP model (or standard flare model) which explains various observational aspects of the eruptive flares. After the discovery of X-ray plasmoid (a blob of plasma) ejections from confined flares by Yohkoh satellite (Shibata et al. 1995; Ohyama et al. 1997; Ohyama and Shibata 1998), Shibata (Shibata 1996, 1997) proposed a unified model of solar flare by extending the CSHKP model, which explains onset of magnetic reconnection in eruptive as well as confined flares. In this model, the plasmoid ejection plays a key role in triggering reconnection (Figure 4.9). The rising plasmoid stretches the overlying MFLs. Underneath the plasmoid, the stretched MFLs are pushed towards each-other by inflow generated in response to the pressure depletion. The MFLs being oppositely directed generate magnetic reconnections. In this scenario, the reconnection rate (i.e., inflow speed) depends on how fast the plasmoid ejects.

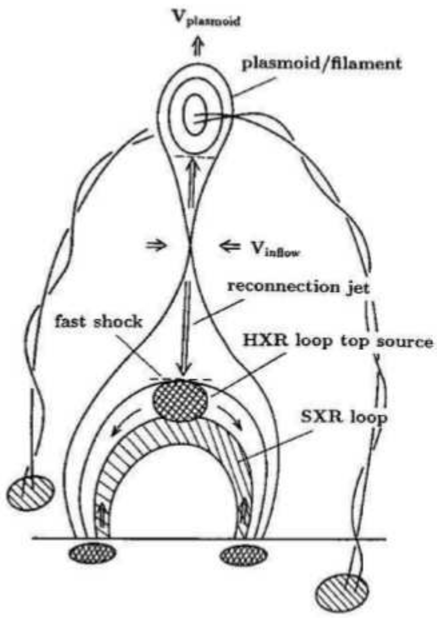

Figure 4.9: A schematic representation of unified flare model proposed by Shibata (Shibata 1996).

4.4.3 Coronal Mass Ejection

Coronal Mass Ejections usually refer to eruptions of plasma and embedded coronal magnetic field from the corona into interplanetary space. The total mass ejected in CMEs ranges from 10^{15}g to 10^{16}g and total energy from 10^{27}ergs to 10^{33}ergs (Vourlidas et al. 2002; Gopalswamy et al. 2004). CMEs are often observed with a coronagraph in white light. In white light observations, CMEs are seen due to Thomson scattering of photospheric light from the free electrons of coronal and heliospheric plasma (Vourlidas and Howard 2006; Howard and Tappin 2009). In general, CMEs have a three-part structure in white light: an outer bright frontal loop (i.e., a leading edge), a dark cavity and a bright core embedded in the cavity (Illing and Hundhausen 1985); cf. Figure 4.10. The leading edge may appear as a sharply defined single loop or highly structured loop system (Illing and Hundhausen 1985; Vourlidas and Howard 2006). The cavity is a region of lower plasma density but probably higher magnetic field strength

(Low 1996; Vourlidas and Howard 2006). The core can often be identified as prominence material (Low 1996; Schmieder et al. 2002).

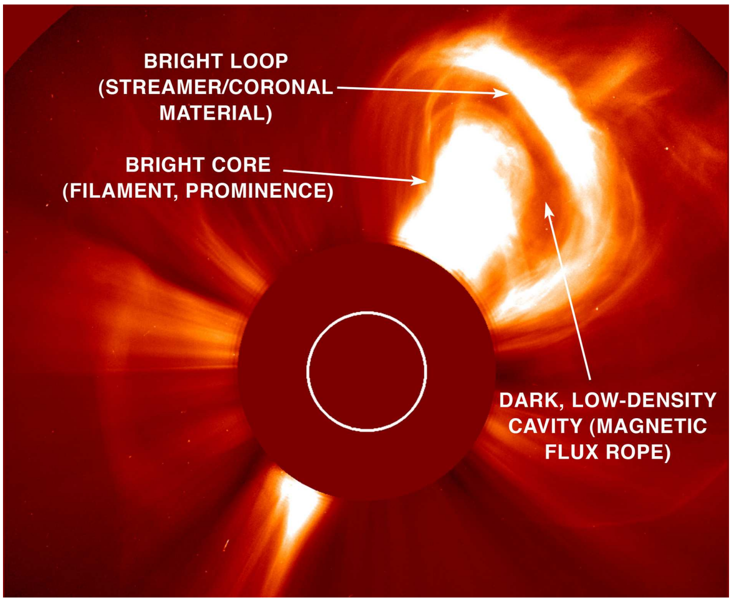

Figure 4.10: A classical three part CME viewed by LASCO on board SOHO in December 2002, showing a bright frontal loop surrounding a dark cavity with a bright core. Figure is taken from (Müller et al. 2013).

Magnetic reconnection is believed to play a significant role in initiating CMEs. To appreciate the role, here we present a general scenario of CME initiation (Low 1996; Chen 2011). It is widely accepted that most of the CMEs can be considered as erupting flux-rope systems, generating the classical three-part structure. Notably a flux-rope is kept in equilibrium by the overlying envelope magnetic arcades which are line-tied to the photosphere. In response to MRs or the loss of equilibrium, the flux-rope starts to rise (Chen 2011). With the rise, the parts of magnetic field lines of the overlying arcades located below the rope come to close proximity and, being anti-parallel, form a CS situated beneath the rope. The MR across the CS then cuts the overlying arcades, which removes the constraint for the rope and facilitates a rapid eruption of the rope. Moreover, the upward outflow generated from the reconnection region pushes the rope in the vertical direction, helping in the rapid eruption. The erupting flux-rope stretches-up the overlying closed magnetic field lines, forming a new density-enhanced pattern, i.e. the CME frontal edge. Due to its enhanced magnetic pressure, the flux-rope is generally related to the CME cavity. While the prominence material situated in the dip part of the flux-rope can explain the brighter core of the CME (Low 1996).

4.5 Summary

In this chapter, we have discussed the possible signatures of current sheets formation and magnetic reconnection in the solar corona. We choose the corona as a prototype example for our study because of the wealth of observational data available. The X-ray observations of the sun provide the evidence that the corona is highly structured medium. Under million degrees Kelvin temperature, the coronal magnetofluid remains frozen with the magnetic field because of the flux-freezing. Therefore, magnetic field lines are responsible for structuring the corona.

The coronal field lines remain rooted in the photosphere. The convective fluid motions quasi-statically shuffle the footpoints of the field lines resulting in an increased magnetic energy and complexity of field lines. According to magnetostatic theorem, a multitude of current sheets form through out the coronal volume. The CSs get dissipated via MRs which convert the magnetic energy into heat. Such development of CS and resultant MRs may provide an attractive mechanism to heat the corona to its million degrees Kelvin temperature.

Multi-wavelength observations of a solar flares suggest the magnetic reconnection to be a prime mechanism responsible for their occurrence. Further, we note that, the magnetic reconnections also play an important role in the prominence/filament formation by originating a flux-rope with helical field lines which is a promising magnetic structure to sustain the cooler plasma in the hotter corona. Moreover, magnetic reconnection plays a crucial role in the initiation of coronal mass ejections. All these observations favor the existence of MHD relaxation in the corona.

Chapter 5

Numerical Models

5.1 Introduction

Towards realizing a numerical model to mimic MHD relaxation successfully, we note the relaxation to be a two-step process. The first step includes the spontaneous generation of current sheets in accordance with the magnetostatic theorem. While the second step involves the decay of these CSs via magnetic reconnections. This two-step process is expected to repeat in time until the magnetofluid relaxes to a minimum energy state. Notably, the development of CSs requires the flux-freezing condition to be valid while, magnetic reconnection demands the presence of a finite magnetic diffusivity which breaks the flux-freezing. A successful numerical investigation of the relaxation then requires an intermittent diffusivity that appears only when and where the CSs have developed. Therefore, for our calculations, we utilize the well established numerical model EULAG-MHD (Smolarkiewicz and Charbonneau 2013) which is an extension of the hydrodynamic model EULAG predominantly used in atmospheric and climate research (Prusa et al. 2008). The EULAG-MHD is based on the spatio-temporally (at least) second-order accurate non-oscillatory forward-in-time (NFT) advection scheme multidimensional positive definite advection transport algorithm, MPDATA, (Smolarkiewicz and Margolin 1998; Smolarkiewicz 2006). The accuracy of MPDATA ensures the satisfaction of the flux-freezing with a high fidelity, an essential requirement for a numerical demonstration of

CSs. In addition, a feature unique to MPDATA and important in our calculations is its proven effectiveness in generating an intermittent and adaptive residual dissipation, whenever the concerned advective field is under-resolved (Margolin et al. 2006). The formation of CS in absence of magnetic diffusion provides an unbound sharpening of the corresponding field gradient and inevitably generates under-resolved scales. The MPDATA then produces the residual dissipation to regularize these scales through onset of simulated magnetic reconnections.

Furthermore, we realize that the magnetic flux surfaces are the potential sites for CS formation (chapter 3). Therefore, describing MHD in terms of magnetic flux surfaces instead of the vector magnetic field is physically attractive as it provides a direct visualization of the dynamics responsible for the origin of CSs—the first step of the relaxation. For the purpose, we utilize the advection of flux surfaces in the form of Euler-potentials (EPs) (Stern 1970). The corresponding advection equations (written in section 5.4) are integrated by numerical model EULAG-EP which is the EP based MHD version of EULAG.

The chapter first discusses the essential features of the advection scheme MPDATA and then presents the details of numerical models EULAG-MHD and EULAG-EP.

5.2 Advection solver MPDATA

MPDATA is a finite-difference algorithm invented by P. K. Smolarkiewicz in early 1980's (Smolarkiewicz 1983, 1984; Smolarkiewicz and Clark 1986). The algorithm is at least second-order accurate, positive definite, conservative, and computationally efficient. The second-order accuracy in MPDATA is achieved by utilizing the first-order accurate donor cell (also known as upstream or upwind) scheme in an iterative manner. The first iteration is a simple donor cell differencing. With a donor cell solution obtained from first iteration, MPDATA increases the accuracy of the calculation by estimating and compensating (second-order) truncation error in the second iteration. Similarly, additional iterations can be performed to approximately compensate the residual error produced from previous iteration which further enhance the accuracy.

Since its invention, MPDATA is extended to curvilinear coordinates, full monotonicity preservation, third-order accuracy and variable sign fields; for details cf. reviews (Smolarkiewicz and Margolin 1998; Smolarkiewicz 2006). Here we discuss basic concepts underlying the design of MPDATA schemes in Cartesian coordinates.

5.2.1 Derivation of MPDATA

To fix ideas, we consider a simple one-dimensional advection equation,

$$\frac{\partial \varphi}{\partial t} + \frac{\partial (k\varphi)}{\partial x} = 0, \tag{5.2.1}$$

for a scalar variable φ. The velocity k may also be a function of space and time. The donor cell discretization of the advection equation is given by,

$$\varphi_i^{n+1} = \varphi_i^n - \frac{\delta t}{\delta x}(k_{i+\frac{1}{2}}\varphi_r^n - k_{i-\frac{1}{2}}\varphi_l^n), \tag{5.2.2}$$

where φ_r^n and φ_l^n are chosen depending on the sign of $k_{i+\frac{1}{2}}$ and $k_{i-\frac{1}{2}}$:

$$\varphi_r^n = \begin{cases} \varphi_i^n, & k_{i+\frac{1}{2}} > 0, \\ \varphi_{i+1}^n, & k_{i+\frac{1}{2}} < 0, \end{cases} \tag{5.2.3}$$

and

$$\varphi_l^n = \begin{cases} \varphi_{i-1}^n, & k_{i-\frac{1}{2}} > 0, \\ \varphi_i^n, & k_{i-\frac{1}{2}} < 0, \end{cases} \tag{5.2.4}$$

with the integer and half-integer indices correspond to cell centers and cell walls. In equation (5.2.2), φ_i^{n+1} on the LHS is the solution sought at the grid point (t^{n+1}, x_i) with $\delta t = t^{n+1} - t^n$ and $\delta x = x_{i+1} - x_i$ representing temporal and spatial increments respectively. The above case distinctions can be avoided by writing the equation (5.2.2) in the following form,

$$\varphi_i^{n+1} = \varphi_i^n - \frac{\delta t}{2\delta x}[k_{i+\frac{1}{2}}(\varphi_i^n + \varphi_{i+1}^n) - k_{i-\frac{1}{2}}(\varphi_{i-1}^n + \varphi_i^n) \\ + \mid k_{i+\frac{1}{2}} \mid (\varphi_i^n - \varphi_{i+1}^n) - \mid k_{i-\frac{1}{2}} \mid (\varphi_{i-1}^n - \varphi_i^n)]. \tag{5.2.5}$$

Notably, if the sign of k determines the flow direction, this scheme always chooses the values of φ (for a given time) which lies in the upstream direction (Griebel et al. 1998). The donor cell approximation in flux form is expressed as,

$$\varphi_i^{n+1} = \varphi_i^n - [F(\varphi_i^n, \varphi_{i+1}^n, U_{i+\frac{1}{2}}) - F(\varphi_{i-1}^n, \varphi_i^n, U_{i-\frac{1}{2}})], \tag{5.2.6}$$

where the flux function F is

$$F(\varphi_L, \varphi_R, U) \equiv [U]^+ \varphi_L + [U]^- \varphi_R, \tag{5.2.7}$$

with $U \equiv \dfrac{a\delta t}{\delta x}$ represents the dimensionless local Courant number while, $[U]^+ \equiv 0.5(U + \mid U \mid)$ and $[U]^- \equiv 0.5(U - \mid U \mid)$ denoting the nonnegative and non-positive parts of the Courant number (Smolarkiewicz and Margolin 1998; Smolarkiewicz 2006).

The donor cell scheme is conditionally stable and the corresponding stability condition, for every time step, has a form

$$\max\left(\frac{\mid k_{i+\frac{1}{2}} \mid \delta t}{\delta x}\right) \leq 1 \quad \forall i. \tag{5.2.8}$$

Moreover, under the condition (5.2.8), the scheme is also positive definite, implying: if $\varphi_i^0 \geq 0 \quad \forall i$ then $\varphi_i^n \geq 0 \quad \forall i$ and n. These two properties as well as low computational cost and low phase error make the scheme (5.2.6) attractive for the numerical evaluation of the advection equation. However, the scheme being first-order accurate (both in space and time) produces large implicit numerical diffusion.

Towards quantifying the diffusion in (5.2.6), for simplicity we assume the k to be constant and φ to be nonnegative. A straightforward truncation analysis, expanding all dependent variables in a second-order Taylor series about the time level n and spatial point i, reveals that the scheme more accurately approximates the advection-diffusion equation

$$\frac{\partial \varphi}{\partial t} + \frac{\partial (k\varphi)}{\partial x} = \frac{\partial}{\partial x}\left(K\frac{\partial \varphi}{\partial x}\right), \tag{5.2.9}$$

where the diffusion coefficient

$$K = \frac{\delta x^2}{2\delta t}(\mid U \mid - U^2). \tag{5.2.10}$$

In other words, the scheme estimates the solution of the advection equation with a second-order truncation error. To enhance the accuracy, it is necessary to construct a numerical estimate of the error and subtract it from (5.2.6). The basic strategy, fundamental to all MPDATA schemes, is then to once again utilize a donor cell approximation to calculate the error term in order to preserve the properties of donor cell scheme. To do so, the error term, the RHS term of (5.2.9), is rewritten as

$$e^1 \equiv \frac{\partial}{\partial x}\left(K\frac{\partial \varphi}{\partial x}\right) = \frac{\partial (k^1\varphi)}{\partial x}, \tag{5.2.11}$$

where e^1 symbolizes error term and $k^1 \equiv \dfrac{K}{\varphi}\dfrac{\partial \varphi}{\partial x}$ is termed as pseudo velocity. The superscript (1) is used to mark the first iteration for subtracting the error. To compensate the error, we again use the donor cell scheme but this time with the pseudo velocity k^1 and the φ^{n+1} already available from (5.2.6) in lieu of the physical velocity k and the φ^n. A first-order accurate estimate of the pseudo velocity is

$$k^1_{i+\frac{1}{2}} \equiv \frac{2K}{\delta x}\frac{\varphi^{(1)}_{i+1} - \varphi^{(1)}_i}{\varphi^{(1)}_{i+1} + \varphi^{(1)}_i} \tag{5.2.12}$$

where $\varphi^{(1)}$ represents the first-order accurate φ^{n+1} estimated from (5.2.6). The modified Courant number is $V^1_{i+\frac{1}{2}} \equiv \dfrac{k^1_{i+\frac{1}{2}}\delta t}{\delta x}$. In the second iteration, we subtract a donor cell estimate of the error to improve the accuracy. The equation of the second iteration is

$$\varphi_i^2 = \varphi_i^1 - [F(\varphi_i^1, \varphi_{i+1}^1, V_{i+\frac{1}{2}}^1) - F(\varphi_{i-1}^1, \varphi_i^1, V_{i-\frac{1}{2}}^1)], \tag{5.2.13}$$

which estimates φ^{n+1} which is the second-order accurate while preserving the sign of φ. It is an easy matter to show that, like the donor cell scheme, MPDATA is consistent and conditionally stable (Smolarkiewicz 1983; Smolarkiewicz and Margolin 1998; Smolarkiewicz 2006). But, in contrast to the donor scheme, MPDATA does not contain strong numerical implicit diffusion because of the improved accuracy.

The extension of MPDATA to multiple dimension is straightforward. To demonstrate, we consider a simple two-dimensional advection equation,

$$\frac{\partial \varphi}{\partial t} + \frac{\partial (k\varphi)}{\partial x} + \frac{\partial (l\varphi)}{\partial y} = 0, \tag{5.2.14}$$

where k and l are velocities in x and y directions. The corresponding donor cell approximation is then

$$\begin{aligned} \varphi_{i,j}^{n+1} = \varphi_{i,j}^n &- [F(\varphi_{i,j}^n, \varphi_{i+1,j}^n, U_{i+\frac{1}{2},j}) - F(\varphi_{i-1,j}^n, \varphi_{i,j}^n, U_{i-\frac{1}{2},j})] \\ &- [F(\varphi_{i,j}^n, \varphi_{i,j+1}^n, V_{i,j+\frac{1}{2}}) - F(\varphi_{i,j-1}^n, \varphi_{i,j}^n, V_{i,j-\frac{1}{2}})], \end{aligned} \tag{5.2.15}$$

where the flux function is similar to (5.2.7) and, $U \equiv \dfrac{k\delta t}{\delta x}$ and $V \equiv \dfrac{l\delta t}{\delta y}$ are Courant numbers. Further, the Taylor's series expansion of (5.2.15) about the cell point (i, j) and the time level n with constant velocities yields the following advection-diffusion equation,

$$\frac{\partial \varphi}{\partial t} + \frac{\partial (k\varphi)}{\partial x} + \frac{\partial (l\varphi)}{\partial y} = K\frac{\partial^2 \varphi}{\partial x^2} + L\frac{\partial^2 \varphi}{\partial y^2} - \frac{UV\delta x\delta y}{\delta t}\frac{\partial^2 \varphi}{\partial x \partial y}, \tag{5.2.16}$$

with $K \equiv \dfrac{\delta x^2}{2\delta t}(\mid U \mid -U^2)$ and $L \equiv \dfrac{\delta y^2}{2\delta t}(\mid V \mid -V^2)$. To estimate the truncation error using the donor cell scheme, we rewrite the error terms, the RHS terms of (5.2.16), in the following form

$$K\frac{\partial^2\varphi}{\partial x^2}+L\frac{\partial^2\varphi}{\partial y^2}-\frac{UV\delta x\delta y}{\delta t}\frac{\partial^2\varphi}{\partial x\partial y}=\frac{\partial}{\partial x}(k^1\varphi)+\frac{\partial}{\partial x}(l^1\varphi) \tag{5.2.17}$$

where

$$k^1\equiv\frac{K}{\varphi}\frac{\partial\varphi}{\partial x}-\frac{UV\delta x\delta y}{2\delta t}\frac{1}{\varphi}\frac{\partial\varphi}{\partial y}\quad\text{and}\quad l^1\equiv\frac{L}{\varphi}\frac{\partial\varphi}{\partial y}-\frac{UV\delta x\delta y}{2\delta t}\frac{1}{\varphi}\frac{\partial\varphi}{\partial x} \tag{5.2.18}$$

are pseudo velocities in x and y directions. Utilizing these velocities and updated value of φ^{n+1} from (5.2.15), the donor cell scheme is used to estimate the error. In the second iteration, the error is subtracted to enhance the accuracy.

5.2.2 Extension to generalized transport equation

The general transport equation is

$$\frac{\partial\varphi}{\partial t}+\nabla\cdot(\mathbf{k}\varphi)=R, \tag{5.2.19}$$

where R combines all forcing and source terms. In general, both R and velocity $\mathbf{k}$ depend on variable φ. The forward-in-time discretization of (5.2.19) is assumed as,

$$\frac{\varphi^{n+1}-\varphi^n}{\delta t}+\nabla\cdot(\mathbf{k}^{n+\frac{1}{2}}\varphi^n)=R^{n+\frac{1}{2}}. \tag{5.2.20}$$

Expansion of (5.2.20) into the second-order Taylor series about the time level n shows that the scheme (5.2.20) approximates to the equation

$$\frac{\partial\varphi}{\partial t}+\nabla\cdot(\mathbf{k}\varphi)=R-\nabla\cdot\Big[0.5\delta t\mathbf{k}(\mathbf{k}\cdot\nabla\varphi)+0.5\delta t\mathbf{k}\varphi(\nabla\cdot\mathbf{k})\Big]+\nabla\cdot(0.5\delta t\mathbf{k}R)+\mathcal{O}(\delta t^2). \tag{5.2.21}$$

In RHS of (5.2.21), all $\mathcal{O}(\delta t)$ truncation errors originated by uncentered time differencing in (5.2.20) are already expressed by spatial derivatives. Specification of the time levels of both the advective velocity and the forcing term as $n+1/2$ in (5.2.20) eliminates $\mathcal{O}(\delta t)$ truncation errors which are proportional to their temporal derivatives (Smolarkiewicz and Clark 1986). From (5.2.21), it is clear that the formulation of second-order accurate forward-in-time scheme for (5.2.19) requires the compensation of $\mathcal{O}(\delta t)$ truncation errors to at least the second-order accuracy.

For such a formulation, we note $\mathcal{O}(\delta t)$ error terms in (5.2.21) have two distinct components. The first component is merely due to advection and does not involve the forcing R. In contrast, the second component depends on the forcing R. Towards compensating the first component, notable is the reduction of (5.2.19) to homogeneous transport equation for $R = 0$. Then, MPDATA scheme retains the form of the basic scheme (subsection 5.2.1) where the first donor cell iteration utilizes the advective velocity $\mathbf{k}^{n+\frac{1}{2}}$ and φ^n, and subsequent iterations use pseudo velocities and φ calculated from the preceding iteration; for details cf. (Smolarkiewicz 1991; Smolarkiewicz and Margolin 1993, 1998; Smolarkiewicz 2006). Compensation of the second component requires subtracting of a first-order accurate approximation of the error from the RHS of (5.2.20). A simple, efficient, and second-order accurate MPDATA for (5.2.19) can then be symbolically written as,

$$\varphi_i^{n+1} = \mathcal{A}_i(\varphi^n + 0.5\delta t R^n, \mathbf{k}^{n+\frac{1}{2}}) + 0.5\delta t R_i^{n+1}, \tag{5.2.22}$$

where $\mathcal{A}$ denotes the basic MPDATA advection scheme (Smolarkiewicz 1991; Smolarkiewicz and Margolin 1993). In this equation, we assume $R^{n+\frac{1}{2}} = 0.5(R^n + R^{n+1})$ with R^{n+1} representing $\mathcal{O}(\delta t^2)$ accurate approximation of R at time level $(n+1)$. Noticeably, first donor cell iteration in the MPDATA scheme uses the auxiliary variable $\varphi^n + 0.5\delta t R^n$ in lieu of the physical variable φ^n with a physical advective velocity $\mathbf{k}^{n+\frac{1}{2}}$. The advection of the auxiliary field is important for preserving the global accuracy and stability of the forward in time approximations (Smolarkiewicz 1991; Smolarkiewicz and Margolin 1993, 1997).

The advective velocity at intermediate $n + \frac{1}{2}$ time level may be approximated by linear interpolation or extrapolation

$$\mathbf{k}^{n+\frac{1}{2}} = \frac{1}{2}(\mathbf{k}^{n+1} + \mathbf{k}^{n}), \tag{5.2.23}$$

$$\mathbf{k}^{n+\frac{1}{2}} = \frac{1}{2}(3\mathbf{k}^{n} - \mathbf{k}^{n-1}), \tag{5.2.24}$$

either of which is sufficient to maintain second-order accuracy in (5.2.22). For the subtleties involved in a particular choice of $\mathbf{k}^{n+\frac{1}{2}}$, readers are refereed to (Smolarkiewicz and Clark 1986).

5.2.3 Nonoscillatory MPDATA

The basic MPDATA scheme discussed above preserves sign* but not monotonicity of the advected variables (Smolarkiewicz 1983, 1984; Smolarkiewicz and Clark 1986) and, in general, the solutions are not free of spurious oscillations particularly in presence of steep gradients (Smolarkiewicz and Grabowski 1990; Smolarkiewicz 1991). However, MPDATA is made fully monotone (Smolarkiewicz 1991) by adapting the flux-corrected-transport (FCT) methodology (Boris and Book 1973; Book et al. 1975; Boris and Book 1976). Actually, MPDATA is well suited for this kind of approach for a number of reasons. First, the initial MPDATA iteration is the donor cell scheme—a low-order monotone scheme which is commonly used as the reference in the FCT design. Second, assuring monotonicity of subsequent iterations provides a higher-order accurate reference solution for the next iteration with the effect of improving the overall accuracy of the resulting FCT scheme. Third, since all MPDATA iterations have similar low phase errors characteristic of the donor cell scheme (Smolarkiewicz and Clark 1986), the FCT procedure mixes solutions with consistent phase errors. This benefits significantly the overall accuracy of the resulting FCT scheme (Smolarkiewicz and Grabowski 1990).

*For historical reasons, we refer to this property as positive-definiteness in the previous subsections.

5.3 EULAG-MHD

The numerical model EULAG is an established model for simulating fluid flows across a wide range of scales and physical scenarios (Prusa et al. 2008). The name EULAG alludes to the capability to solve the fluid equations in either an Eulerian (Smolarkiewicz and Margolin 1993) or a Lagrangian (Smolarkiewicz and Pudykiewicz 1992) mode. The numerics of EULAG are unique, owing to a combination of MPDATA advection schemes, robust elliptic solver, and generalized coordinate formulation enabling grid adaptivity. The EULAG-MHD is a spin-off of the numerical model EULAG (Smolarkiewicz and Charbonneau 2013). Here, we describe the numerical apparatus of EULAG-MHD utilized for our calculations.

5.3.1 Governing equations of EULAG-MHD

MHD equations for an incompressible magnetofluid with infinite electrical conductivity are cast in the following form

$$\frac{d\mathbf{v}}{dt} = -\nabla\pi + \frac{1}{4\pi\rho_0}\mathbf{B}\cdot\nabla\mathbf{B} + F_\nu, \tag{5.3.1}$$

$$\frac{d\mathbf{B}}{dt} = \mathbf{B}\cdot\nabla\mathbf{v} - \mathbf{B}\nabla\cdot\mathbf{v}, \tag{5.3.2}$$

$$\nabla\cdot\mathbf{v} = 0, \tag{5.3.3}$$

$$\nabla\cdot\mathbf{B} = 0, \tag{5.3.4}$$

in a non-rotating Cartesian coordinate. The Lagrangian derivative is related the Eulerian derivative in the usual manner

$$\frac{d}{dt} \equiv \frac{\partial}{\partial t} + (\mathbf{v}\cdot\nabla). \tag{5.3.5}$$

On the RHS of the momentum transport equation (5.3.1), π is a density normalized pressure in which thermodynamic pressure is subsumed to magnetic pressure. F_ν symbolizes the viscous drag force. All other symbols have their usual meaning.

On a general note, EULAG's governing equations are formulated and solved in transformed time-dependent generalized curvilinear coordinates

$$(\bar{t}, \bar{\mathbf{x}}) \equiv (t, F(t, \mathbf{x})). \tag{5.3.6}$$

The physical domain (t, x), where the physical problem is posed, is assumed to be any stationary orthogonal coordinate system (i.e., Cartesian, spherical and cylindrical). Moreover, the transformed horizontal coordinates $(\bar{x}, \bar{y})$ are assumed to be independent of the vertical coordinate z (Prusa and Smolarkiewicz 2003). The calculations carried out in this thesis implement the physical domain to be Cartesian and, therefore both the computational domain and the physical domain are identical, i.e., $(\bar{t}, \bar{x}) \equiv (t, x)$. Here, we present the details of the EULAG-MHD for Cartesian domain. The generalized coordinate formulation of EULAG-MHD utilizes the rigorous tensorial exposition of MHD equations; cf. (Smolarkiewicz and Charbonneau 2013).

5.3.2 Numerics

Utilizing equations (5.3.3) and (5.3.4), the momentum transport equation (5.3.1) and the induction equation (5.3.2) can be rewritten as,

$$\frac{\partial \mathbf{\Psi}}{\partial t} + \nabla \cdot (\mathbf{v}\mathbf{\Psi}) = \mathbf{R} \tag{5.3.7}$$

where

$$\mathbf{\Psi} = \{\mathbf{v}, \mathbf{B}\}^T \tag{5.3.8}$$

represents the vector of dependent variables and

$$\mathbf{R} = \{\mathbf{R_v}, \mathbf{R_B}\}^T \tag{5.3.9}$$

denotes the RHS forcing terms in (5.3.1) and (5.3.2). Notably, in (5.3.7), the Lorentz force term of the momentum transport equation and the convective term of the induction equation are cast in the conservative forms via relations,

$$\mathbf{B} \cdot \nabla \mathbf{B} = \nabla \cdot \mathbf{BB}, \qquad \mathbf{B} \cdot \nabla \mathbf{v} = \nabla \cdot \mathbf{Bv}. \tag{5.3.10}$$

In addition, an ad hoc term $-\nabla\pi^\star$ is added to RHS of the induction equation, in the spirit of the pressure π in the momentum transport equation, to ensure $\nabla \cdot \mathbf{B} = 0$ in numerical integrations.

The equation (5.3.7) is integrated using nonoscillatory forward-in-time algorithm MPDATA. Following section (5.2.2), an EULAG template algorithm for integration of the (5.3.7) can be compactly written as,

$$\mathbf{\Psi}_i^{n+1} = \mathcal{A}_i(\mathbf{\Psi}^n + 0.5\delta t \mathbf{R}^n, \mathbf{v}^{n+\frac{1}{2}}) + 0.5\delta t \mathbf{R}_i^{n+1} \equiv \hat{\mathbf{\Psi}}_i + 0.5\delta t \mathbf{R}_i^{n+1}, \tag{5.3.11}$$

where $\mathbf{\Psi}_i^{n+1}$ is the solution sought at the grid point (t^{n+1}, x_i).

For an inviscid dynamics (F_ν=0), the model template algorithm (5.3.11) is implicit for all dependent variables in (5.3.1) and (5.3.2) because all forcing terms are assumed to be unknown at time level $n+1$. To retain the proven structure of (5.3.11) for the MHD system, EULAG-MHD template can be viewed as

$$\mathbf{\Psi}_i^{n+1,q} = \hat{\mathbf{\Psi}}_i + \frac{\delta t}{2}\mathbf{L\Psi} \,|_i^{n+1,q} + \frac{\delta t}{2}\mathbf{N}(\mathbf{\Psi}) \,|_i^{n+1,q-1} - \frac{\delta t}{2}\nabla\mathbf{\Theta} \,|_i^{n+1,q}, \tag{5.3.12}$$

where the RHS forcing $\mathbf{R}$ is decomposed into linear term $\mathbf{L\Psi}$ with $\mathbf{L}$ denoting a linear operator, non linear-term $\mathbf{N}(\mathbf{\Psi})$, and potential term $-\nabla\Theta$ with $\Theta \equiv (\pi, \pi, \pi, \pi^\star, \pi^\star, \pi^\star)$. In (5.3.12), $q = 1, ..., m$ numbers fixed point iterations. The algorithm (5.3.12) is still implicit with respect to the forcing terms $\mathbf{L\Psi}$ and $-\nabla\Theta$. Using straight-forward algebraic manipulations, the representation (5.3.12) can be cast into a closed form

$$\mathbf{\Psi}_i^{n+1,q} = [\mathbf{I} - 0.5\delta t \mathbf{L}]^{-1} \left(\hat{\hat{\mathbf{\Psi}}} - 0.5\delta t \nabla \mathbf{\Theta}^{n+1,q}\right)_i, \tag{5.3.13}$$

where the explicit element is modified to

$$\hat{\hat{\mathbf{\Psi}}} \equiv \hat{\mathbf{\Psi}} + 0.5\delta t \mathbf{N}(\mathbf{\Psi})\,|^{n+1,q-1}\,. \tag{5.3.14}$$

The viscous forcing within this algorithm frame work is incorporated by integrating explicitly to the first-order accuracy in time and then adding to the the auxiliary argument of MPDATA operator $\mathcal{A}$. Now the argument modifies as $\tilde{\mathbf{\Psi}} \equiv \mathbf{\Psi}^n + 0.5\delta t(\mathbf{R}^n + 2\tilde{\mathbf{R}})$ where $\tilde{\mathbf{R}}$ symbolizing the first-order time accurate viscous forcing. All the dependent variables being spatially co-located in (5.3.13), the time updated $\mathbf{\Psi}$ is obtained by solving two the discrete elliptic equations for π and π^* generated by the solenoidality constraints (5.3.3) and (5.3.4) discretized consistently with the divergence operator implied by $\mathcal{A}$; see (Prusa et al. 2008). Under appropriate boundary conditions, these elliptic equations are solved iteratively using a preconditioned generalized conjugate residual (GCR) algorithm (Eisenstat et al. 1983; Eisenstat 1983; Smolarkiewicz et al. 1997). Because the GCR is an iterative scheme, to distinguish the iterations appearing in (5.3.12) and in the GCR solver, the iteration in (5.3.12) is refereed as "outer", while the iteration corresponds to GCR is termed as "inner". The convergence of the outer iteration is generally controlled by the time step of the model and monitored by the convergence of the inner iteration in the GCR solvers (Smolarkiewicz and Szmelter 2009, 2011). With the completion of the outer iteration loop, the solution updates and, the total implicit forcing $\mathbf{RI} = \mathbf{L\Psi} - \nabla\Theta$ in (5.3.12) is returned as $\mathbf{RI}_i^n = \dfrac{2}{\delta t}(\mathbf{\Psi}_i^n - \hat{\hat{\mathbf{\Psi}}}_i)$. While, the total explicit forcing $\mathbf{RE} = \mathbf{N}(\mathbf{\Psi}) + \tilde{\mathbf{R}}$ is calculated according to its definition using the updated solution, so $\mathbf{RE}_i^n = \mathbf{RE}_i(\mathbf{\Psi}^n)$. The total forcing $\mathbf{R} = \mathbf{RI} + \mathbf{RE}$ is then stored for the use in the subsequent time step in the auxiliary argument of MPDATA operator in (5.3.11).

In the following, we briefly discuss the actual implementation of iterative formulation of (5.3.11). The iterations progress stepwise such that the most current update of a dependent variable is used in the ongoing step, wherever possible. Each outer iteration has two distinct blocks. The first block involves the integration of the momentum transport equation where the magnetic field enters the Lorentz force and is taken as supplementary. Being at the half of a single outer iteration, it is denoted by the index $q-1/2$. This block ends with the final update of the velocity via the solution of the elliptic equation for π. Hence, this block actually mirrors standard EULAG solution of hydrodynamic equations (Prusa et al. 2008), leading to the nomenclature "hydrodynamic block". The second block, referred as "magnetic block", uses the current updates of the velocities to integrate the induction equation. It ends with the final update of the magnetic field via the solution of the elliptic equation for $\pi^\star$ to clean the divergence of magnetic field. In the following we summarize sequence of steps fulfilled at each outer iteration for integrating the MHD equations (5.3.1)-(5.3.4). For brevity, the superscripts n are dropped everywhere as by now there should be no ambiguity. Moreover, at $q=1$ the initial guess for $\mathbf{v}$ and $\mathbf{B}$ is assumed as $\mathbf{v}^0 = 2\mathbf{v}^{n+1} - \mathbf{v}^n$ and $\mathbf{B}^0 = 2\mathbf{B}^{n+1} - \mathbf{B}^n$, respectively.

The first step of the hydrodynamic block starts with the estimation of the magnetic field $\mathbf{B}^{q-1/2}$ at time t^{n+1} by inverting the induction equation,

$$\mathbf{B}_i^{q-1/2} = \hat{\mathbf{B}}_i + 0.5\delta t\Big[\mathbf{B}^{q-1/2}\cdot\nabla\mathbf{v}^{q-1} - \mathbf{B}^{q-1/2}tr\{\nabla\mathbf{v}^{q-1}\}\Big]_i. \tag{5.3.15}$$

The subsequent step uses this latest magnetic field to obtain velocity following the standard EULAG procedure,

$$\mathbf{v}_i^q = \hat{\mathbf{v}}_i + \frac{0.5\delta t}{\rho_0\mu_0}(\nabla\cdot\mathbf{BB})_i^{q-1/2} - 0.5\delta t(\nabla\pi)_i^q. \tag{5.3.16}$$

Plugging this velocity in the discrete form of the equation (5.3.3) produces the elliptic equation for the pressure π, the solution of which provides the updated solenoidal velocity $\mathbf{v}$.

The first step of the magnetic block begins with estimation of magnetic field $\mathbf{B}^{q-1/4}$ at t^{n+1} using the update velocity, and the latest magnetic field is evaluated implicitly in analogy to (5.3.15):

$$\mathbf{B}_i^{q-1/4} = \hat{\mathbf{B}}_i + 0.5\delta t\Big[\mathbf{B}^{q-1/4}\cdot\nabla\mathbf{v}^q - \mathbf{B}^{q-1/4}tr\{\nabla\mathbf{v}^q\}\Big]_i. \tag{5.3.17}$$

where the superscript $q-1/4$ symbolized as such for being a quarter of iteration away from the accomplishment. The subsequent step follows in the spirit of the momentum transport equation, using the conservative form of the forcing terms in the induction equation:

$$\mathbf{B}_i^q = \hat{\mathbf{B}}_i + 0.5\delta t(\nabla\cdot\mathbf{B}^{q-1/4}\mathbf{v}^q)_i - 0.5\delta t(\nabla\pi^\star)_i^q. \tag{5.3.18}$$

Implementing the magnetic field in the discrete form of the solenoidality condition (5.3.4) produces the elliptic equation for auxiliary pressure term $\pi^\star$, the solution of which provides the updated solenoidal magnetic field $\mathbf{B}$.

5.4 EULAG-EP

Given that the description of the evolution in terms of magnetic flux surfaces provides a better conceptual understanding of CSs formations, we utilize the advection of flux surfaces in place of vector magnetic field. Notably, the flux surface description is achieved by the Euler Potential representation of of magnetic field (Stern 1967, 1970, 1976),

$$\mathbf{B} = W(\psi,\phi)\nabla\psi\times\nabla\phi, \tag{5.4.1}$$

where ψ and ϕ are two scalar functions of position, known as Euler Potentials, and W represents the amplitude which is an explicit function of ψ and ϕ (Bhattacharyya et al. 2010). The $\nabla\cdot\mathbf{B} = 0$ condition is evident from the above expression. Importantly, with conditions $\mathbf{B}\cdot\nabla\psi = \mathbf{B}\cdot\nabla\phi = 0$ being satisfied, level sets of ψ and ϕ are global MFSs, the intersections of which generate magnetic field lines. Since the field aligned current $\mathbf{J}\cdot\mathbf{B} = 0$, the field lines of $\mathbf{B}$ are untwisted.

The advection equations for ψ and ϕ are realized by noting that a particular level set of the above two EPs can also be identified to fluid surfaces. Once identified, under the flux-freezing, the level sets evolve as fluid surfaces defined by the material elements lying on it (chapter 2) and thus satisfy the advection equations

$$\frac{d\psi}{dt} = 0, \tag{5.4.2}$$
$$\frac{d\phi}{dt} = 0, \tag{5.4.3}$$

implying

$$\frac{\partial\psi}{\partial t} + \mathbf{v} \cdot \nabla\psi = 0, \tag{5.4.4}$$
$$\frac{\partial\phi}{\partial t} + \mathbf{v} \cdot \nabla\phi = 0. \tag{5.4.5}$$

Noteworthy, an identification of level sets of EPs as fluid surfaces is non-unique but once identified at some initial time, the above advection equations maintain this identity throughout their evolution under the condition of flux-freezing. For details, the reader are referred to (Bhattacharyya et al. 2010). Moreover, we note that the above simple advection equations can also be obtained by integrating the induction equation (5.3.2) with respect to the spatial coordinates (Bhattacharyya et al. 2010).

The above flux-surface representation comes with a caveat that the twisted magnetic field, in general, can not be represented by a globally extended pair of flux surfaces ψ and ϕ. The global flux-surface representation of the twisted magnetic field $\mathbf{B}$ is then achieved by linearly decomposing $\mathbf{B}$ into the untwisted component fields (Low 2006). Therefore, the twisted field $\mathbf{B}$ may be written as,

$$\mathbf{B} = \sum_{i=1}^{n} \mathbf{B}_i \equiv \sum_{i=1}^{n} W_i(\psi_i, \phi_i)\nabla\psi_i \times \nabla\phi_i, \tag{5.4.6}$$

where the each component field $\mathbf{B}_i$ is solenoidal, untwisted and expressible by a pair of globally defined Euler potentials ψ_i, ϕ_i. These Euler potentials identify families of fluid surfaces at some initial time as level surfaces. Once so identified, these fluid surfaces remain the same level surfaces as they evolve, so that the decomposition (5.4.6) is valid till the violation of the flux-freezing. Therefore, under the flux-freezing, the time evolution of the EPs ψ_i, ϕ_i is governed by advection equations

$$\frac{\partial \psi_i}{\partial t} + \mathbf{v} \cdot \nabla \psi_i = 0, \tag{5.4.7}$$

$$\frac{\partial \phi_i}{\partial t} + \mathbf{v} \cdot \nabla \phi_i = 0, \tag{5.4.8}$$

for $i = 1, n$. The number of untwisted component fields is not unique. However, generally at least three such component fields are required to represent an arbitrary twisted magnetic field; cf. recent review (Low 2015).

Towards solving the advection equation of flux surfaces, notable is the requirement of preservation of the flux-freezing to an accuracy such that the identity of a fluid surface as a magnetic flux is maintained to a reasonable approximation during the magnetofluid evolution. The computational requirement is then a minimization of numerically generated dissipation and dispersion errors. If present, these errors destroy the connectivity of the flux surfaces and are thus ambiguous to their evolution in a magnetofluid under flux-freezing. For the purpose, we adapt a numerical framework congruent with the EULAG-MHD which is based on the advection scheme MPDATA. The advection scheme ensures the higher-order accuracy away from steep gradients in the advected field variables. The new numerical scheme (named as EULAG-EP) solves the advection equations for flux surfaces (5.4.7)-(5.4.8) to describe the magnetic field evolution, along with momentum equation (5.3.1) to determine the evolution of velocity field. As discussed in section 5.3, these equations can be cast into the form (5.3.7) but, for this case, variable Ψ corresponds to the EPs ψ_i, ϕ_i and three components of velocity field $\mathbf{v}$. Moreover, the transport of ψ_i and ϕ_i takes the elementary homogeneous form with forcing $R \equiv 0$ which simplifies the problem. As MPDATA being fully second-order-accurate in space and time, solving (5.3.7) for the EPs prior to momenta readily provides the $\mathcal{O}(\delta t^3)$ estimates of $\mathbf{B}$, via (5.4.6), and of Lorentz force at t^{n+1}. This considerably simplifies the solution procedure compared to the EULAG-MHD, and leads to a fully second-order solution for the governing system. By casting the induction equation in terms of the Euler potentials, the only unknown at t^{n+1} on the RHS of (5.3.7) is the pressure π^{n+1}, which is obtained by solving the discrete elliptic equation generated through the incompressibility (5.3.3) using the GCR solvers. The viscous forcing term is included in the similar manner as in EULAG-MHD (see section 5.3.1).

EULAG-MHD and EULAG-EP are fully parallelized with MPI (Message Passing Interface) supporting NetCDF for writing output data and NCAR graphics for visualization. The models are presently running on the High Performance Computing Cluster: Vikram-100, operational at Physical Research Laboratory, which is a hundred teraflops machines with 97 computing nodes and offers 2,328 CPU cores, 1,15,200 GPU Cores, 25 terabytes (TB) of RAM and 300 TB of high performance parallel filesystem (https://www.prl.res.in/hpc). For visualization, we also complement the NCAR Graphics with the VAPOR (Visualization and Analysis for Ocean, Atmosphere, and Solar Researchers) which can easily handle data up-to terabytes (Clyne and Rast 2005).

5.5 Implicit large eddy simulation

As discussed above, EULAG-MHD and EULAG-EP both are based on MPDATA advection scheme. Notably, the higher-order truncation terms of MPDATA provide an implicit turbulence model (Domaradzki et al. 2003; Margolin et al. 2006) and hence, allow to conduct large eddy simulations (LESs) without using an explicit subgrid model (Smolarkiewicz and Prusa 2002; Domaradzki et al. 2003; Domaradzki and Radhakrishnan 2005; Rider 2006; Prusa et al. 2008). In contrast to the standard LESs which filter out the under-resolved scales by applying explicit subgrid-scale models, MPDATA filter-outs the under-resolved scales by utilizing the residual dissipation—intermittent and adaptive to generation of under-resolved scales—produced via numerics which mimics the action of explicit subgrid scale turbulence models. In literature, such calculations relying on the properties of nonoscillatory numerics are referred as implicit large eddy simulations (ILESs). A comprehensive review of ILES with numerous examples are provided in the volume edited by Grinstein et al. (Grinstein et al. 2007), including applications to local and global solar/stellar convection.

In a simulation of MHD relaxation, with fixed grid resolution, development of CSs generates under-resolved scales as a consequence of unbounded increase in the magnetic field gradient. MPDATA then removes these under-resolved scales by producing locally effective residual dissipation, sufficient to sustain monotonic nature of the solution. Being intermittent and adaptive, the residual dissipation, as mentioned above, facilitate the model to perform ILESs. Such ILESs performed with the model have already been successfully utilized to simulate regular solar cycles (Ghizaru et al. 2010), with the rotational torsional oscillations subsequently characterized and analyzed in (Beaudoin et al. 2013). The simulations conducted with EULAG-MHD continue relying on the effectiveness of ILES in regularizing the onset of magnetic reconnections, concurrent and collocated with developing CSs (Kumar et al. 2013, 2015a; Kumar and Bhattacharyya 2016). While in simulations performed with EULAG-EP, the dissipation breaks the flux-freezing and results in reconnection of field lines across the developed CSs; effectively providing a termination point for the simulations since the identity of flux surfaces to fluid surfaces are preserved only in presence of the flux-freezing (Kumar et al. 2014, 2015c).

5.6 Summary

This chapter describes the numerical models EULAG-MHD and EULAG-EP used to explore the MHD relaxation. The numerical models are based on (at least) second-order accurate (both in space and time) non-oscillatory forward in-time advection scheme MPDATA. MPDATA basically utilizes the donor-cell scheme in iterative manner to improve the accuracy of the solution while preserving the properties of the donor cell scheme. We discuss the derivation of

MPDATA along with its features which are relevant to our calculations. Then, we review the numerics of the numerical model EULAG-MHD. The model employs the established frame-work of EULAG with an additional magnetic block to solve the induction equation. To describe evolution in terms of the flux surfaces, we use EULAG-EP which is an EP-based adaption of EULAG-MHD for solving advections equations for flux surfaces. Notably, the proven property of MPDATA to produce locally adaptive residual dissipations in response to generation of under-resolved scales, facilitates the numerical models to perform implicit large eddy simulations.

Chapter 6

Initial Value Problems: Current Sheet Formations

6.1 Introduction

If a magnetic flux surface is identified with a fluid surface defined by the material elements to which the field lines are tied, the flux-freezing assures a maintenance of the identity throughout an evolution. Under the flux-freezing, pushing of fluid parcels then results in contortions of flux surfaces. With favorable contortions, a physical scenario is possible where two portions of a given MFS or two entirely different MFSs come arbitrarily close to each other by squeezing out the interstitial fluid. Under this circumstance, the gradient in magnetic field may increase depending on the relative orientation of MFLs lying on the approaching flux surfaces and thereby current sheets may develop. In the ideal case of $\lambda = 0$, it is then expected that the favorable contortions bring more and more non-parallel MFLs in close proximity and, consequently increase local magnetic pressure which in turn, opposes further contortions. Eventually, the magnetofluid is expected to settle down in a steady state where magnetic field gets discontinuous and CSs are generated. Relevantly, this scenario is congruent with the magnetostatic theorem.

Importantly, a successful numerical demonstration of CS formation requires the computations to be commensurate with the requirements of magnetostatic theorem. Equivalently, an evolving magnetofluid must satisfy the two prerequisite conditions: invariance of magnetic topology as a consequence of flux freezing, and local force-balance obtained in a terminal state of the evolution. The invariance of magnetic topology is a condition which is to be imposed by a proper choice of numerical model whereas the condition of local force balance can be realized by allowing the magnetofluid to relax only through viscous dissipation, under a strict satisfaction of flux-freezing. To elaborate the viscous relaxation, we consider an infinitely conducting, incompressible, and viscous magnetofluid which is described by following MHD equations. Written in a dimensionless form, the equations are

$$\frac{\partial \mathbf{v}}{\partial t} + (\mathbf{v}\cdot\nabla)\,\mathbf{v} = -\nabla p + (\nabla\times\mathbf{B})\times\mathbf{B} + \frac{\tau_a}{\tau_\nu}\nabla^2\mathbf{v}, \tag{6.1.1}$$

$$\nabla\cdot\mathbf{v} = 0, \tag{6.1.2}$$

$$\frac{\partial \mathbf{B}}{\partial t} = \nabla\times(\mathbf{v}\times\mathbf{B}), \tag{6.1.3}$$

$$\nabla\cdot\mathbf{B} = 0, \tag{6.1.4}$$

in usual notations. The variables are normalized according to

$$\mathbf{B} \longrightarrow \frac{\mathbf{B}}{B_0}, \tag{6.1.5}$$

$$\mathbf{v} \longrightarrow \frac{\mathbf{v}}{v_a}, \tag{6.1.6}$$

$$L \longrightarrow \frac{L}{L_0}, \tag{6.1.7}$$

$$t \longrightarrow \frac{t}{\tau_a}, \tag{6.1.8}$$

$$p \longrightarrow \frac{p}{\rho_0 {v_a}^2}. \tag{6.1.9}$$

Here, the constants B_0 and L_0 are generally arbitrary, but can be fixed by the magnetic field strength and size of the system. Furthermore, v_a is the Alfvén speed and ρ_0 is the constant mass density. The constants τ_a and τ_ν have dimensions of time, and represent Alfvén transit time ($\tau_a = L_0/v_a$) and viscous diffusion time scale ($\tau_\nu = L_0^2/\nu$) respectively, with ν being the kinematic viscosity. Importantly, a dimensionless representation of the MHD equations clarifies any evolution to be independent of the involved physical scales but dependent only on the magnitude of the dimensionless number τ_a/τ_ν. In presence of a physical magnetic diffusivity, in addition to τ_a/τ_ν the evolution also depends on the Lundquist number. We utilize this concept throughout our calculations to fix τ_a/τ_ν to its desired value by selecting a parameter set (in cgs units) which optimizes the corresponding simulation. The MHD equations are formally closed by making pressure p to satisfy the elliptic partial differential equation

$$\nabla^2 \left(p + \frac{v^2}{2}\right) = \nabla \cdot \left[(\nabla \times \mathbf{B}) \times \mathbf{B} - (\nabla \times \mathbf{v}) \times \mathbf{v}\right] \tag{6.1.10}$$

generated by imposing incompressibility (6.1.2) on momentum trasnport equation (6.1.1); cf. (Bhattacharyya et al. 2010) and the references therein. From an initial nonequilibrium state, the magnetofluid would relax towards a terminal state by converting magnetic energy W_M to kinetic energy W_K through equations

$$\frac{dW_K}{dt} = \int [(\nabla \times \mathbf{B}) \times \mathbf{B}] \cdot \mathbf{v}\ d^3x - \frac{\tau_a}{\tau_\nu} \int |\nabla \times \mathbf{v}|^2\ d^3x, \tag{6.1.11}$$

$$\frac{dW_M}{dt} = - \int [(\nabla \times \mathbf{B}) \times \mathbf{B}] \cdot \mathbf{v}\ d^3x, \tag{6.1.12}$$

$$\frac{dW_T}{dt} = -\frac{\tau_a}{\tau_\nu} \int |\nabla \times \mathbf{v}|^2\ d^3x, \tag{6.1.13}$$

satisfying conditions that the net magnetic and velocity fluxes through the boundaries of the computational domain are individually zero. Since the Lorentz force is conservative, the kinetic energy is dissipated via viscous drag. In absence of magnetic diffusivity, the condition of flux-freezing holds and the terminal state is expected to be in magnetostatic equilibrium (3.2.1), identical in magnetic topology to the initial state. In simulations, however, only a quasi-steady state is achieved, maintained by a partial balance of Lorentz force, pressure gradient and viscous drag. The magnetostatic theorem then predicts development of CSs in the terminal state if the initial magnetic field is topologically complex which we ensure by constructing relevant initial value problems (IVPs). Notably, the viscous relaxation ensures a local force-balance in a magnetofluid evolving with invariant magnetic topology.

Although introduced here as a mathematical requirement to demonstrate CS formation, a viscous relaxation is also physically realizable depending on the ratio of fluid Reynolds number (R_F) to magnetic Reynolds number (R_M). For instance, in solar corona $R_F \approx 100$ in comparison to $R_M \approx 10^{11}$ (Aschwanden 2005) opening up the possibility of a dominant viscous drag at scales larger than the scales where magnetic diffusion is effective. Other examples where the ratio of viscous to resistive dissipation is of the order of unity or more, can be found in a variety of circumstances related to stellar and galactic plasmas (Parker 1994).

The possibility of CS formation through a viscous relaxation have already been demonstrated in two recent numerical experiments (Bhattacharyya et al. 2010; Kumar et al. 2015a), referred hereafter as NE1 and NE2 respectively. Although conceptually the same, the two experiments utilize two different numerical approaches. In NE1, the initial magnetic field is represented in terms of two intersecting families of global MFSs each of which is a level surface defined by a constant Euler potential. The advantage of NE1 is then in its advection of MFSs instead of magnetic field, leading to simpler equations along with elimination of post-processing errors in determining magnetic topology. An apt trade-off for this advantage is the choice of an untwisted magnetic field to construct the relevant initial value problems, as only for such fields global MFSs exist (chapter 5). However, the magnetic field in astrophysical plasmas are believed to be twisted (Kumar and Bhattacharyya 2011; Wiegelmann and Sakurai 2012). Consequently, the NE2 demonstrates CS formation with an initial twisted magnetic field in relevance to general magnetic morphology of the solar corona. For the purpose, NE2 is based on the advection of magnetic field rather than the flux surfaces. The feature common to both NE1 and NE2 is the finding that the CSs develop near the magnetic field reversal layers, or the magnetic nulls, which are the natural sites for magnetic field to become discontinuous.

Against the above backdrop, the motivation of the present chapter is twofold.

First is to understand the physical process, in terms of magnetic flux surface evolution, which spontaneously develops current sheets in a magnetofluid with interlaced and hence, topologically complex field lines. Second is to assess the importance of the intensity of field line complexity in the spontaneous development of current sheets. To achieve these objectives, we perform two separate sets of numerical experiment with suitable IVPs. For both the sets, the flux surfaces are advected using the numerical model EULAG-EP (chapter 5) in an idealized scenario of incompressible magnetofluid with infinite electrical conductivity and constant viscosity.

With spontaneous development of CSs being a fundamental property of magnetohydrodynamics, a particular choice of boundary condition is not expected to alter the outcome. The simulations presented in this chapter utilize a periodic boundary and in light of the above understanding deviate from the solar corona only by the difference in numerical values of τ_a/τ_ν and Lundquist number S. In our computations, the effective S^{-1} is negligibly small apart from the sites of current sheets. The residual dissipation generated by MPDATA being intermittent in time and space, a quantification of it is meaningful only in the spectral space where, in analogy to the eddy-viscosity of explicit subgrid-scale models for turbulent flows, it only acts on the shortest modes admissible on the grid (Domaradzki et al. 2003); in particular, in the vicinity of steep gradients in simulated fields. Furthermore, for parameter values relevant to solar corona (Aschwanden 2005), the ratio of Alfvén transit time to the viscous time scale $\tau_a/\tau_v \approx 10^{-4}$, which is around one order of magnitude smaller than that adopted in the computations presented in this chapter. Realizing that the flux surface representation looses its validity with onset of reconnection, the numerical value of τ_a/τ_ν is selected so as to slowdown the dynamics for a better visualization, and hence understanding, of CS formation. This, however, only affects the time scale over which the magnetofluid evolves. Being incompressible, flow in our computations is volume preserving—an assumption also used in other works (Dahlburg et al. 1991; Aulanier et al. 2005). While compressibility is important for the thermodynamics of coronal plasma (Ruderman and Roberts 2002), our focus is only on elucidating the role of MFSs in spontaneous formation of CSs.

The rest of the chapter is organized as follows. In section II, we construct the first set initial value problem with interlaced MFLs. The results attribute the development of spontaneous CSs to contortions of magnetic flux surfaces. Section III describes initial value problems and results corresponding to second set of numerical experiment where we access the role of the intensity of field line interlacing in spontaneous formation current sheets. Section IV summarizes the results of both the numerical experiments and highlights the key findings.

6.2 Numerical experiment I

6.2.1 Initial value problem

To develop a relevant initial value problem, we consider the magnetic field $\mathbf{B} = \{B_x, B_y, B_z\}$ where

$$
\begin{aligned}
B_x = {} & \sqrt{3}\sin\left(\frac{2\pi}{L}x\right)\cos\left(\frac{2\pi}{L}y\right)\sin\left(\frac{2\pi}{s_0 L}z\right) \\
& + \cos\left(\frac{2\pi}{L}x\right)\sin\left(\frac{2\pi}{L}y\right)\cos\left(\frac{2\pi}{s_0 L}z\right), && (6.2.1)\\
B_y = {} & -\sqrt{3}\cos\left(\frac{2\pi}{L}x\right)\sin\left(\frac{2\pi}{L}y\right)\sin\left(\frac{2\pi}{s_0 L}z\right) \\
& + \sin\left(\frac{2\pi}{L}x\right)\cos\left(\frac{2\pi}{L}y\right)\cos\left(\frac{2\pi}{s_0 L}z\right), && (6.2.2)\\
B_z = {} & 2s_0\sin\left(\frac{2\pi}{L}x\right)\sin\left(\frac{2\pi}{L}y\right)\sin\left(\frac{2\pi}{s_0 L}z\right), && (6.2.3)
\end{aligned}
$$

defined in a triply periodic Cartesian domain of horizontal (x and y) extent L and vertical (z) extent $s_0 L$. The factor s_0 is a dimensionless constant and L represents the characteristic length scale of the system. The above choice is based on the understanding that for $s_0 = 1$, $\mathbf{B}$ reduces to a linear force-free field (lfff) $\mathbf{B}_{lfff}$ satisfying

$$\nabla \times \mathbf{B}_{lfff} = \alpha_0 \mathbf{B}_{lfff} \quad , \tag{6.2.4}$$

with $\alpha_0 = (2\pi\sqrt{3})/L$. The parameter α_0 is the magnetic circulation per unit flux and hence measures the twist in magnetic field lines; cf. chapter 3. To recap, the Lorentz force exerted by $\mathbf{B}_{lfff}$ is zero and the equilibrium is maintained by a balance between the magnetic tension and the magnetic pressure (Choudhuri 1998). Interestingly, the lfff being the special solution of a force-free equilibrium, is frequently used to model the solar coronal magnetic field; cf. chapter 4. The corresponding magnetic topology is complex enough in terms of twisted field lines along with the usual abundance of two-dimensional magnetic nulls complemented with sparsely located three-dimensional magnetic nulls (Kumar et al. 2013). Based on the above understanding, the field $\mathbf{B}$ can be perceived to be obtainable from $\mathbf{B}_{lfff}$ with a scaling factor $s_0 \neq 1$. The Lorentz force exerted by $\mathbf{B}$ is non zero and has the functional form

$$
\begin{aligned}
(\mathbf{J}\times\mathbf{B})_x = 4\left(1-s_0^2\right)\cos\left(\frac{2\pi}{L}x\right)\sin\left(\frac{2\pi}{L}x\right)& \\
\times\sin^2\left(\frac{2\pi}{L}y\right)\sin^2\left(\frac{2\pi}{s_0L}z\right)&, \qquad (6.2.5)\\
(\mathbf{J}\times\mathbf{B})_y = 4\left(1-s_0^2\right)\sin^2\left(\frac{2\pi}{L}x\right)\sin\left(\frac{2\pi}{L}y\right)& \\
\times\cos\left(\frac{2\pi}{L}y\right)\sin^2\left(\frac{2\pi}{s_0L}z\right)&, \qquad (6.2.6)\\
(\mathbf{J}\times\mathbf{B})_z = 2\left(s_0-\frac{1}{s_0}\right)\sin^2\left(\frac{2\pi}{L}x\right)\cos^2\left(\frac{2\pi}{L}y\right)& \\
\times\sin\left(\frac{2\pi}{s_0L}z\right)\cos\left(\frac{2\pi}{s_0L}z\right)& \\
+2\left(s_0-\frac{1}{s_0}\right)\cos^2\left(\frac{2\pi}{L}x\right)\sin^2\left(\frac{2\pi}{L}y\right)& \\
\times\sin\left(\frac{2\pi}{s_0L}z\right)\cos\left(\frac{2\pi}{s_0L}z\right)&. \qquad (6.2.7)
\end{aligned}
$$

Hereafter, for all computations performed in this section we set $L = 2\pi$. The modified magnetic field is then represented by $\mathbf{B} = \{B_x, B_y, B_z\}$ where

$$B_x = \sqrt{3}\sin x \cos y \sin\left(\frac{z}{s_0}\right) + \cos x \sin y \cos\left(\frac{z}{s_0}\right), \tag{6.2.8}$$

$$B_y = -\sqrt{3}\cos x \sin y \sin\left(\frac{z}{s_0}\right) + \sin x \cos y \cos\left(\frac{z}{s_0}\right), \tag{6.2.9}$$

$$B_z = 2s_0 \sin x \sin y \sin\left(\frac{z}{s_0}\right), \tag{6.2.10}$$

defined in the domain of volume $s_0(2\pi)^3$. We use this modified field $\mathbf{B}$ as the initial magnetic field for the presented simulations. Figure 6.1 illustrates that the maximum amplitude of Lorentz force (solid line) along with magnetic helicity (dashed line) and magnetic energy (dotted line) integrated over the domain volume, increase with s_0. For a comparison with the linear force-free field, the plotted magnetic energy and the helicity are normalized to their corresponding values for $s_0 = 1$.

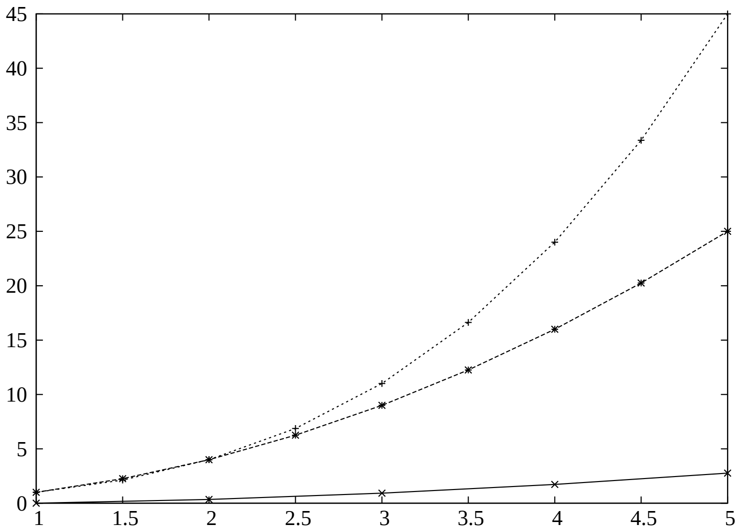

Figure 6.1: Variation of magnetic energy (dotted line), magnetic helicity (dashed line) and $\mid \mathbf{J} \times \mathbf{B} \mid_{max}$ (solid line) with an increase in s_0. The abscissa is s_0 whereas the ordinate represents the magnetic energy, magnetic helicity and $\mid \mathbf{J} \times \mathbf{B} \mid_{max}$. The magnetic energy and the magnetic helicity are normalized to their corresponding values for $s_0 = 1$ (lfff). The plots show an increase in magnetic energy, magnetic helicity and Lorentz force with an increase in s_0.

To further quantify this increase we note that a straightforward calculation yields the domain integrated magnetic energy and the magnetic helicity (K_M) in the following form

$$W_M = 2\pi^2\left(2 + s_0^2\right)\int_0^{2\pi s_0} dz, \tag{6.2.11}$$

$$K_M = 2\sqrt{3}\pi^2 s_0 \int_0^{2\pi s_0} dz, \tag{6.2.12}$$

where the factor s_0 outside the integral sign is contributed by the amplitude of B_z. The limits of the definite integrals indicate further contributions of s_0 to the values of W_M and K_M through the size of the vertical extension. We must point out here that the above calculation of magnetic helicity uses its classical expression

$$K_M = \int \mathbf{A}\cdot\mathbf{B}dV, \tag{6.2.13}$$

with $\mathbf{A}$ as the vector potential and the integral being over the domain volume. This expression of K_M for a periodic domain, as in our case, is valid only with a constant gauge. A more general gauge independent representation of magnetic helicity along with the involved physics can be found in references (Berger 1997; Bhattacharyya and Janaki 2004; Low 2011). In continuation, it is also to be emphasized that the simulations presented here preserve the initial magnetic topology, once fixed by the EPs, by numerical means discussed in chapter 5. Thus, an explicit analysis of magnetic helicity in our simulations is inconsequential, and we do not pursue in this direction further.

For a selection of s_0 appropriate to our simulations, we recall from Figure 6.1 that the initial Lorentz force increases with s_0. The selection criteria is then based on the generation of an initial Lorentz force such that the evolving CSs can be well resolved in time and space with a minimal computational expanse. Based on an auxiliary numerical study, we select $s_0 = 2$ and $s_0 = 3$ for the simulations discussed. Figure 6.2 (a) illustrates the distribution of 2D and 3D magnetic nulls in the computational domain for $s_0 = 3$. In Figure 6.2 (b) we have illustrated the same for $s_0 = 1$ to demonstrate the similar spatial distribution of magnetic nulls

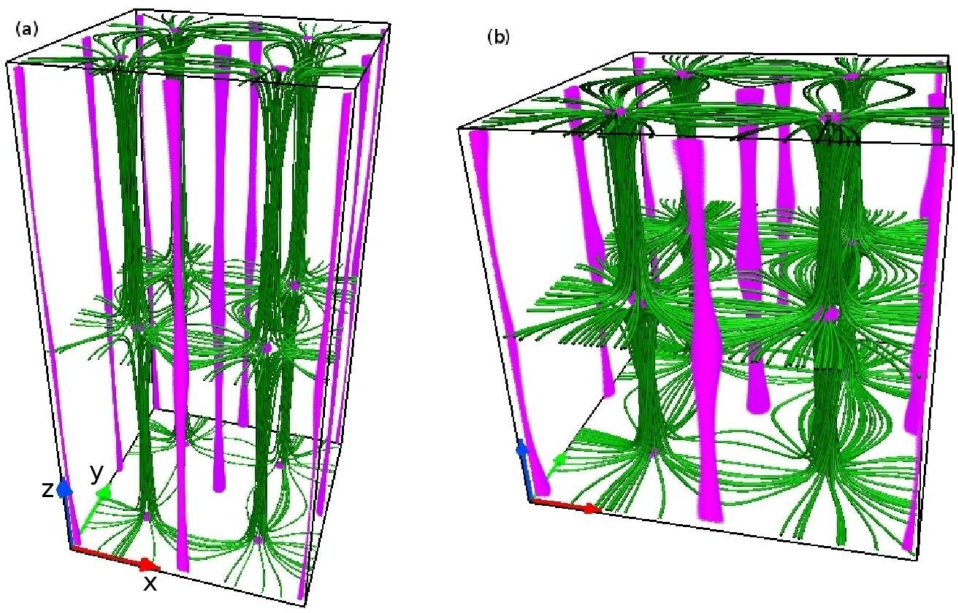

Figure 6.2: The panel a illustrates magnetic nulls of the initial field $\mathbf{B}$ for $s_0 = 3$. Panel b shows the same for the corresponding linear force-free field characterized by $s_0 = 1$. The figure depicts the similarity in spatial distribution of magnetic nulls between the lfff and the initial field $\mathbf{B}$.

for the corresponding lfff. In this and subsequent figures, the arrows in colors red, green, and blue depict the directions x, y, and z respectively. Noticeably, the illustration of magnetic nulls employs the condition $\mathbf{B} \equiv \{B_x,\ B_y,\ B_z\} = 0$ in a Gaussian construct (Kumar et al. 2013)

$$\chi(x,y,z) = exp\left[-\sum_{i=x,y,z}\frac{(B_i(x,y,z)-H_0)^2}{d_0}\right]. \tag{6.2.14}$$

where $\sqrt{d_0}$ determines width of the Gaussian and H_0 represents a particular isovalue of B_x, B_y and B_z. By choosing $H_0 \approx 0$ and a small d_0, the function $\chi(x,y,z) \neq 0$ only if $B_i \approx H_0$ for each i. The three dimensional nulls are the points where the three isosurfaces $B_x = H_0, B_y = H_0, B_z = H_0$ intersect. It should be noted that at the immediate vicinity of a 3D null all the three components of magnetic field is nonzero. Similarly, a two dimensional null in a 3D coordinate space can be described as a line of intersection between H_0 isosurfaces of two nonzero magnetic field components while the third component is trivially zero at this line. Using the above technique, in Figure 6.2 we have depicted nulls of $\mathbf{B}$ by selecting parameters $H_0 = 0.01$ and $d_0 = 0.05$. The accuracy of the depiction can easily be verified from the analytical expression of **B** in equations (6.2.8)-(6.2.10). Figure 6.2 documents the presence of 3D in the form of point and 2D nulls in the form of lines.

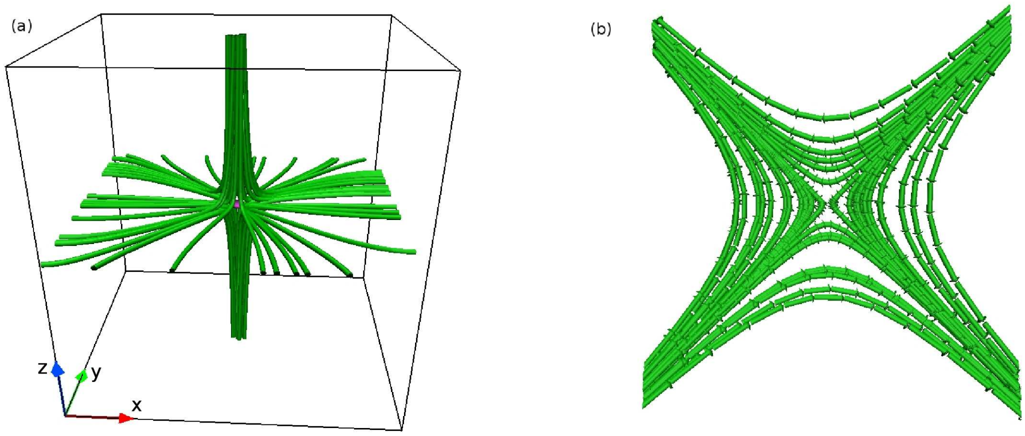

Figure 6.3: The panel a shows a typical 3D null of the **B** with corresponding spine axes and fan. The field topology near the 2D null of the **B** located at $x = \pi$; $y = \pi$; $z = 3\pi$ is depicted in the panel b. Clearly, the 2D null has the X-type geometry.

In Figure 6.3(a), we have drawn the magnetic field lines in the neighborhood of a 3D null along with its spine axes and overlapping fan structures. Further insight about the 2D nulls can be obtained by expanding the field components in a Taylor series in the immediate neighborhood of $x = \pi$, $y = \pi$; for a constant z. Retaining only the first order terms, equations (6.2.8)-(6.2.10) reduce to

$$B_x = \sqrt{3}\,(x-\pi)\sin\left(\frac{z_0}{s_0}\right) + (y-\pi)\cos\left(\frac{z_0}{s_0}\right), \tag{6.2.15}$$

$$B_y = (x-\pi)\cos\left(\frac{z_0}{s_0}\right) - \sqrt{3}\,(y-\pi)\sin\left(\frac{z_0}{s_0}\right), \tag{6.2.16}$$

$$B_z = 0. \tag{6.2.17}$$

It is straightforward to verify that the components B_x and B_y given by equations (6.2.15) and (6.2.16) have point antisymmetry about co-ordinates $(x, y) = (\pi, \pi)$ along the z-line, confirming every point on the line to be an X-type neutral point. Figure 6.3 (b) shows the field line geometry in the vicinity of one such

X-type neutral point situated at $z = 3\pi$. Similarly, in Figure 6.2, other lines located at $(x, y) = (0, 0), (0, \pi), (\pi, 0), (0, 2\pi), (2\pi, 0), (\pi, 2\pi), (2\pi, \pi)$ and $(2\pi, 2\pi)$ also represent the X-type neutral lines.

To put our work in general relevance to the contemporary studies of CS formation utilizing stretched magnetic field (Janse and Low 2009; Parker 2012; Pontin and Huang 2012); we note that the functional form of $\mathbf{B}$ complemented with a vertical extension of $2\pi s_0$ alters the wave number of a Fourier mode in the z-direction by an amount $1/s_0$. For $s_0 > 1$ then, the corresponding wavelength gets elongated by an amount s_0 in comparison to the same for the lfff characterized by $s_0 = 1$. Hence for a choice of $s_0 > 1$, the computational setup presented here inherently couples deepening of the vertical extension to a deviation of $\mathbf{B}$ from its corresponding linear force-free configuration.

To obtain an EP representation of $\mathbf{B}$ utilizing equation (5.4.6), we note that an individual component field $\mathbf{B}_i$ has to be untwisted in order to have two intersecting families of global MFSs on which the field lines of $\mathbf{B}_i$ lie. Utilizing this criteria, a valid EP representation of $\mathbf{B}$ can be written with $\mathbf{B} = \sum_{i=1}^{3} \mathbf{B}_i$, where

$$\mathbf{B}_1 = \sqrt{3} \sin x \cos y \sin\left(\frac{z}{s_0}\right) \hat{e}_x - \sqrt{3} \cos x \sin y \sin\left(\frac{z}{s_0}\right) \hat{e}_y \ , \tag{6.2.18}$$

$$\mathbf{B}_2 = \cos x \sin y \cos\left(\frac{z}{s_0}\right) \hat{e}_x + s_0 \sin x \sin y \sin\left(\frac{z}{s_0}\right) \hat{e}_z \ , \tag{6.2.19}$$

$$\mathbf{B}_3 = \sin x \cos y \cos\left(\frac{z}{s_0}\right) \hat{e}_y + s_0 \sin x \sin y \sin\left(\frac{z}{s_0}\right) \hat{e}_z \ . \tag{6.2.20}$$

The component fields $\mathbf{B}_1$, $\mathbf{B}_2$ and $\mathbf{B}_3$ are solenoidal and untwisted, the latter can be verified by noting that $(\nabla \times \mathbf{B}_i) \cdot \mathbf{B}_i = 0$.
An EP representation for each component field is then given by

$$\mathbf{B}_i = \nabla \psi_i(x, y, z) \times \nabla \phi_i(x, y, z) \ , \tag{6.2.21}$$

where $i = 1, 2, 3$ and the amplitudes $W_1 = W_2 = W_3 = 1$ (cf. chapter 5). Under the condition of flux freezing, the EPs ψ_i, ϕ_i evolve according to the simple advection equations (5.4.7)-(5.4.8) for $i = 1, 2, 3$. A suitable EP representation

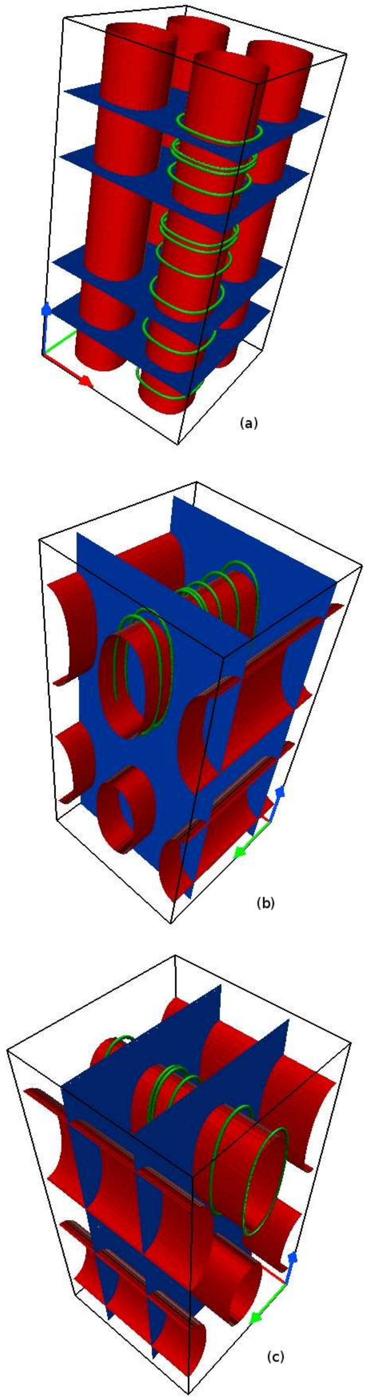

Figure 6.4: Panel a depicts the Euler surfaces $\psi_1 = 1.3, -1.3$ (in red); and $\phi_1 = 0.25, -0.25$ (in blue) overlaid with magnetic field lines (in green). Panel b plots the Euler surfaces $\psi_2 = 0.85, -0.85$ (in red); and $\phi_2 = 0.25$ (in blue) with corresponding magnetic field lines (in green). The Euler surfaces $\psi_3 = 0.85, -0.85$ (in red); and $\phi_3 = 0.25$ (in blue) overlaid with field lines (in green) are shown in panel c.

of the initial magnetic field $\mathbf{B}$ is then constructed as

$$\mathbf{B}_1 = \nabla\left(s_0\sqrt{3}\sin x\sin y\right)\times\nabla\left(-\cos\left(\frac{z}{s_0}\right)\right)\ , \tag{6.2.22}$$

$$\mathbf{B}_2 = \nabla\left(s_0\cos x\sin\left(\frac{z}{s_0}\right)\right)\times\nabla\cos y\ , \tag{6.2.23}$$

$$\mathbf{B}_3 = \nabla\left(s_0\cos y\sin\left(\frac{z}{s_0}\right)\right)\times\nabla\left(-\cos x\right)\ . \tag{6.2.24}$$

Figures 6.4(a), 6.4(b) and 6.4(c) illustrate the level sets of the above EPs in pairs—(ψ_1, ϕ_1), (ψ_2, ϕ_2) and (ψ_3, ϕ_3) respectively, with ψ-constant surfaces in color red and ϕ-constant surfaces in color blue, overlaid with field lines (in color green) which are closed curves since the component fields are untwisted. The plots are for $s_0 = 3$. It is straightforward to confirm the existence of a field-reversal layer in $\mathbf{B}_1$ at $z = 3\pi$. Further from Figure 6.4(a), the axes of ψ_1 constant Euler surfaces are lines along the z-direction located at $(x, y) = (\pi/2, \pi/2)$, $(x, y) = (3\pi/2, \pi/2)$, $(x, y) = (\pi/2, 3\pi/2)$ and $(x, y) = (3\pi/2, 3\pi/2)$ respectively. These axes represent O-type neutral lines at which $\mid \mathbf{B}_1 \mid = 0$. Likewise, the other two component fields $\mathbf{B}_2$ and $\mathbf{B}_3$ have field-reversal layers at planes $y = \pi$ and $x = \pi$ respectively. The O-type neutral lines for $\mathbf{B}_2$ are along the y-axis and are located at $(x, z) = (\pi, 3\pi/2)$ and $(x, z) = (\pi, 9\pi/2)$. Whereas, $\mathbf{B}_3$ has O-type neutral lines oriented along the x-direction and is located at $(y, z) = (\pi, 3\pi/2)$ and $(y, z) = (\pi, 9\pi/2)$.

6.2.2 Results

The simulations are carried out with zero initial velocity, on the $128\times128\times256$ grid in x, y, and z. Also we provide computational results for two different viscosities $\nu_1 = 0.0075$ and $\nu_2 = 0.0085$, for each s_0. Rest of the selected parameter sets are $[\rho_0 = 1,\ L_0 = 4\pi,\ \ B_0 = 1]$ for $s_0 = 2$, and $[\rho_0 = 1,\ L_0 = 6\pi,\ \ B_0 = 1.5]$ for $s_0 = 3$; where B_0 and L_0 are the amplitude of the initial $\mathbf{B}$ and vertical length of the domain respectively. The parameter sets amount to $\tau_a \approx 45s$, $\tau_{\nu_1} \approx 2.1\times10^4 s$, $\tau_{\nu_2} \approx 1.8\times10^4 s$ for $s_0 = 2$; and $\tau_a \approx 45s$, $\tau_{\nu_1} \approx 4.7\times10^4 s$,

$\tau_{\nu_2} \approx 4.1 \times 10^4 s$ for $s_0 = 3$. For comparison, $\tau_a \approx 10s$ and $\tau_\nu \approx 10^5 s$ for the solar corona (Aschwanden 2005).

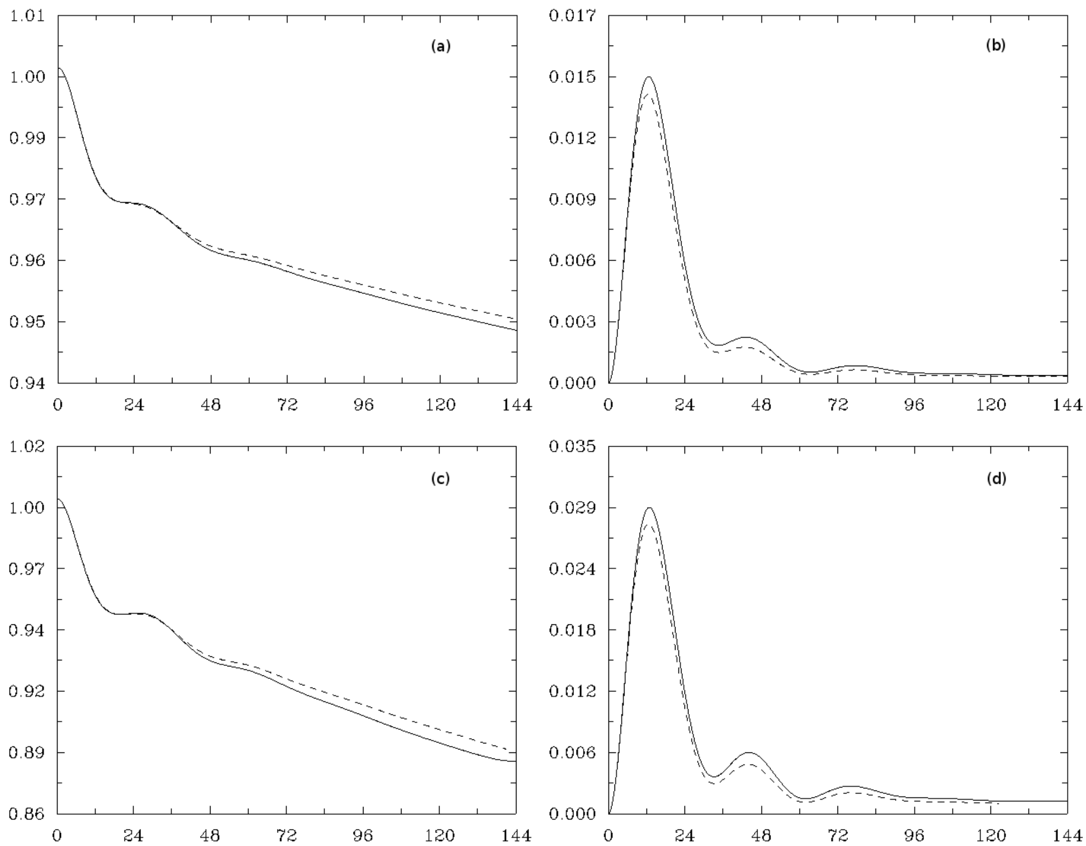

Figure 6.5: Time evolution of normalized magnetic and kinetic energies for $s_0 = 2$ (panels a and b) and $s_0 = 3$ (panels c and d). The abscissas represent time and the ordinates are the energies. Each plot is for two different viscosities ν_1 (solid line) and ν_2 (dashed line). The energies are normalized to the initial total energy. The plots highlight the initial peaks and the quasi-steady phase in kinetic energy. A delayed formation of kinetic energy peak for higher viscosity is in agreement with the general understanding.

To obtain an overall understanding of the simulated viscous relaxation, in Figure 6.5 we have plotted the magnetic and kinetic energies normalized to the initial total energy (kinetic + magnetic). The solid and dashed lines in the figures represent evolution with ν_1 and ν_2 respectively. The kinetic energy curves show a sharp rise as the initial Lorentz force pushes the magnetofluid and drives flow at the expanse of magnetic energy. This increase in fluid velocity is arrested by viscosity resulting in the peaks of kinetic energy appearing near $t = 12s$. Subsequently, the magnetofluid relaxes to a quasi-steady phase marked from

$t = 64s$ to $t = 144s$ as the magnetic field is depleted of its free energy. This quasi-steady phase is characterized by an almost constant kinetic energy while the change in magnetic energy is restricted to $\approx 20\%$ of its total variation. The higher amplitude of the peak kinetic energy for $s_0 = 3$ compared to that of $s_0 = 2$, for both ν_1 and ν_2, is in agreement with the understanding that the initial Lorentz force increases with s_0 (Figure 6.1).

The formation of CSs are indicative from Figures 6.6(a) and 6.6(b) which depict a tendency of rise in volume averaged and maximum total current densities denoted as $<\mid \mathbf{J} \mid>$ and $\mid \mathbf{J} \mid_{max}$ respectively. To explain the observed non-monotonic rise of $<\mid \mathbf{J} \mid>$ and $\mid \mathbf{J} \mid_{max}$, in Figures 6.6(c), 6.6(d) and 6.6(e) we display evolution of the component current densities $<\mid \mathbf{J}_1 \mid>$, $<\mid \mathbf{J}_2 \mid>$ and $<\mid \mathbf{J}_3 \mid>$ where

$$\mathbf{J}_i = \nabla \times \mathbf{B}_i \tag{6.2.25}$$

and,

$$\mathbf{J} = \sum_{i=1}^{3} \mathbf{J}_i \ . \tag{6.2.26}$$

for viscosities ν_1 (solid line) and ν_2 (dashed line). Noteworthy is the monotonic increase of all component current densities with time, which attributes the lack of monotonicity in evolution of $<\mid \mathbf{J} \mid>$ and $\mid \mathbf{J} \mid_{max}$ to the possibility of component current densities becoming anti-parallel to each other.

Figures 6.7(a) to 6.7(c) depict the relevant cross terms $\mathbf{J}_i \cdot \mathbf{J}_j$ becoming negative in accordance with the above understanding. The plots confirm that till $t = 24s$ the averages $< \mathbf{J}_1 \cdot \mathbf{J}_2 >$, $< \mathbf{J}_1 \cdot \mathbf{J}_3 >$ are almost zero while $< \mathbf{J}_2 \cdot \mathbf{J}_3 >$ is positive and increases with time. Whereas after $t = 24s$, $< \mathbf{J}_1 \cdot \mathbf{J}_2 >$ and $< \mathbf{J}_1 \cdot \mathbf{J}_3 >$ become negative and start decreasing. These negative contributions to the magnitude of total volume current density arrest the monotonic rise resulting in formation of the corresponding peaks in $<\mid \mathbf{J} \mid>$ and $\mid \mathbf{J} \mid_{max}$ at $t = 32s$ and $t = 96s$. Subsequently, from $t = 120s$ onwards the negative contributions from $< \mathbf{J}_1 \cdot \mathbf{J}_2 >$ and $< \mathbf{J}_1 \cdot \mathbf{J}_3 >$ are superseded by other monotonically increasing positive terms—

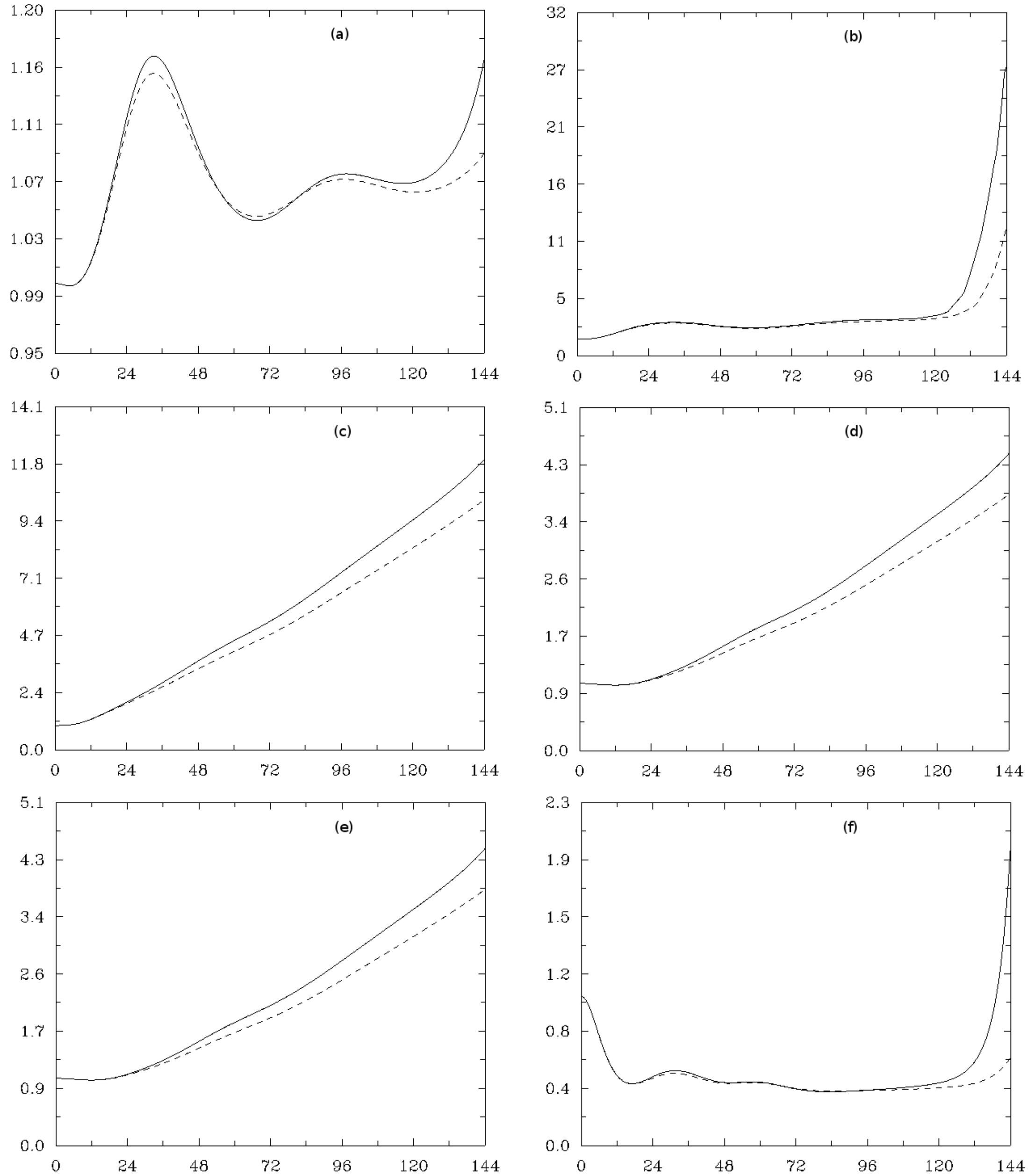

Figure 6.6: History of a: $<|\ \mathbf{J}\ |>$, b: $|\ \mathbf{J}_{max}\ |$, c: $<|\ \mathbf{J}_1\ |>$, d: $<|\ \mathbf{J}_2\ |>$, e: $<|\ \mathbf{J}_3\ |>$ and f: grid averaged Lorentz force, for $s_0 = 3$ with viscosities ν_1 (solid lines) and ν_2 (dashed lines); normalized with respect to their initial values. The abscissa of each panel shows time while the ordinate represents corresponding plotted quantity. The panels a and b show a lack of monotonicity in evolution of the average and maximum total current density whereas panels c to e depict the component currents increases monotonically.

$< \mathbf{J}_2 \cdot \mathbf{J}_3 >$, $< |\ \mathbf{J}_1\ |>$, $<|\ \mathbf{J}_2\ |>$, and $<|\ \mathbf{J}_3\ |>$; resulting in an increase of the maximum and average of total volume current density. The monotonic increase of all the component current densities are in general conformity to formation of

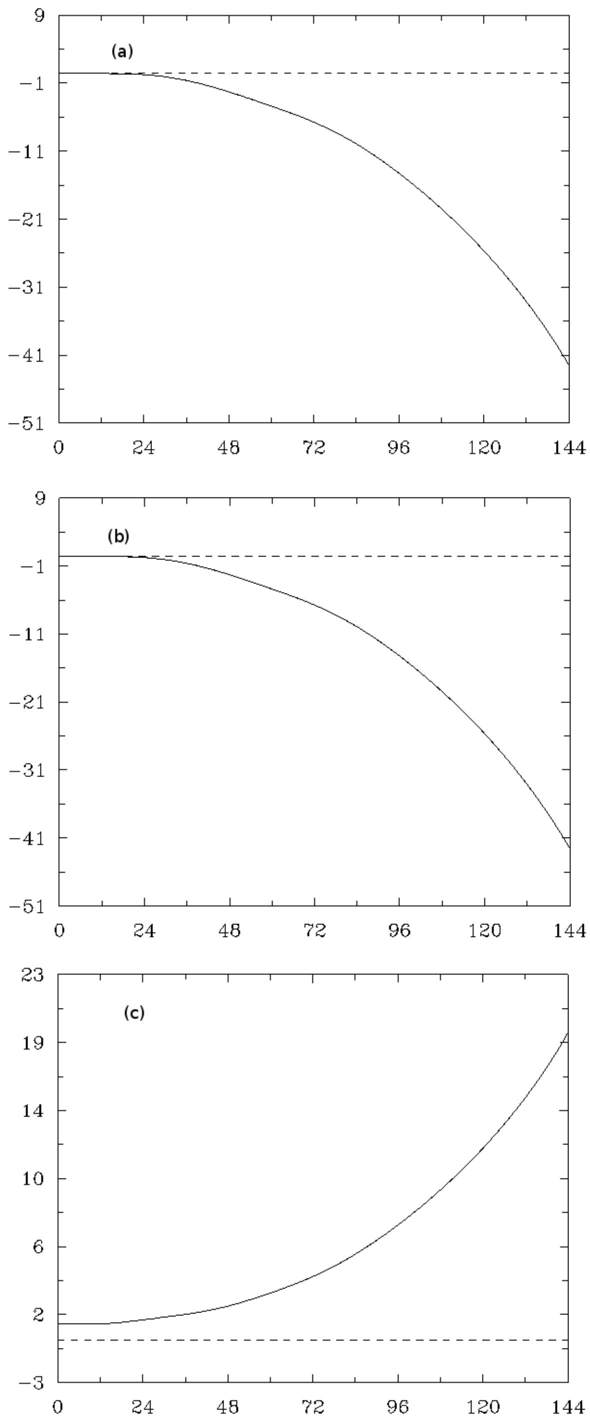

Figure 6.7: Time profiles of the normalized a: $< \mathbf{J}_1 \cdot \mathbf{J}_2 >$, b: $< \mathbf{J}_1 \cdot \mathbf{J}_3 >$ and c: $< \mathbf{J}_2 \cdot \mathbf{J}_3 >$ for $s_0 = 3$ and viscosity ν_1; plotted with solid lines. The abscissa represents time whereas the ordinate depicts corresponding plotted quantity. For comparison, zero lines are plotted with dash. The normalization is done with respect to initial value of $< \mathbf{J}_2 \cdot \mathbf{J}_3 >$. The plots exhibit the flipping in direction of component current densities after $t = 24s$.

CSs in component fields.

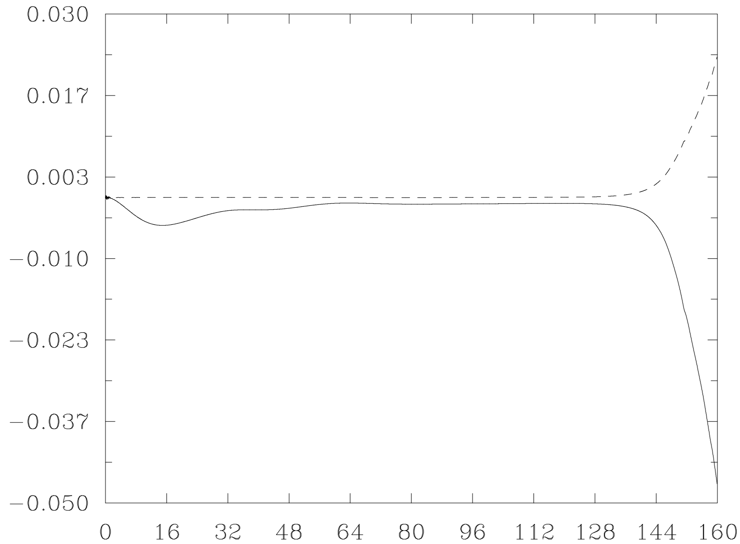

Figure 6.8: The history of energy budget for kinetic (solid) and magnetic (dashed) energies for $s_0 = 3$ and viscosity ν_1, normalized to the initial total energy. The abscissa is time while the ordinate is the energy budget. The plot shows an almost accurate balance in magnetic energy and an acceptable deviation in kinetic energy balance. Both the energy balances are lost at $t = 144s$ onwards and provides a termination point for the simulations.

To verify computational accuracy, in Figure 6.8 we have plotted the energy budgets for normalized kinetic (solid line) and magnetic (dashed line) energies by calculating the numerical deviations in computed energy balance equations from their analytically correct expressions given by equations (6.1.11)-(6.1.12) for $\nu = \nu_1$. The plots show the maintenance of this numerical accuracy to be almost precise with a small deviation in kinetic energy balance at $t = 12s$ from its analytically correct value of zero. Noteworthy is the almost accurate maintenance of magnetic energy balance which excludes any possibility of artificially induced magnetic reconnection. From $t = 144s$ onwards the deviations in both magnetic and kinetic energy balance become high and are of the same order. This large deviation in magnetic energy balance points to possible magnetic reconnections mediated via the residual dissipation generated in response to the under-resolved scales. As a consequence, the magnetic topology changes and the EP representation loses its validity since the post-reconnection field lines lie on a different set of EP surfaces. An appreciable numerical deviation in energy budget (for both magnetic and kinetic) after $t = 144s$ (Figure 6.8) then provides a natural termination point for the set of simulations presented here.

To complete the overall understanding, in Figure 6.6(f) we have plotted the normalized Lorentz force for ν_1 and ν_2. The plot shows an initial decrease followed by a quasi-steady phase till $t = 120s$. Subsequently the Lorentz force increases rapidly while being concurrent with the sharp rise in the maximum volume current density.

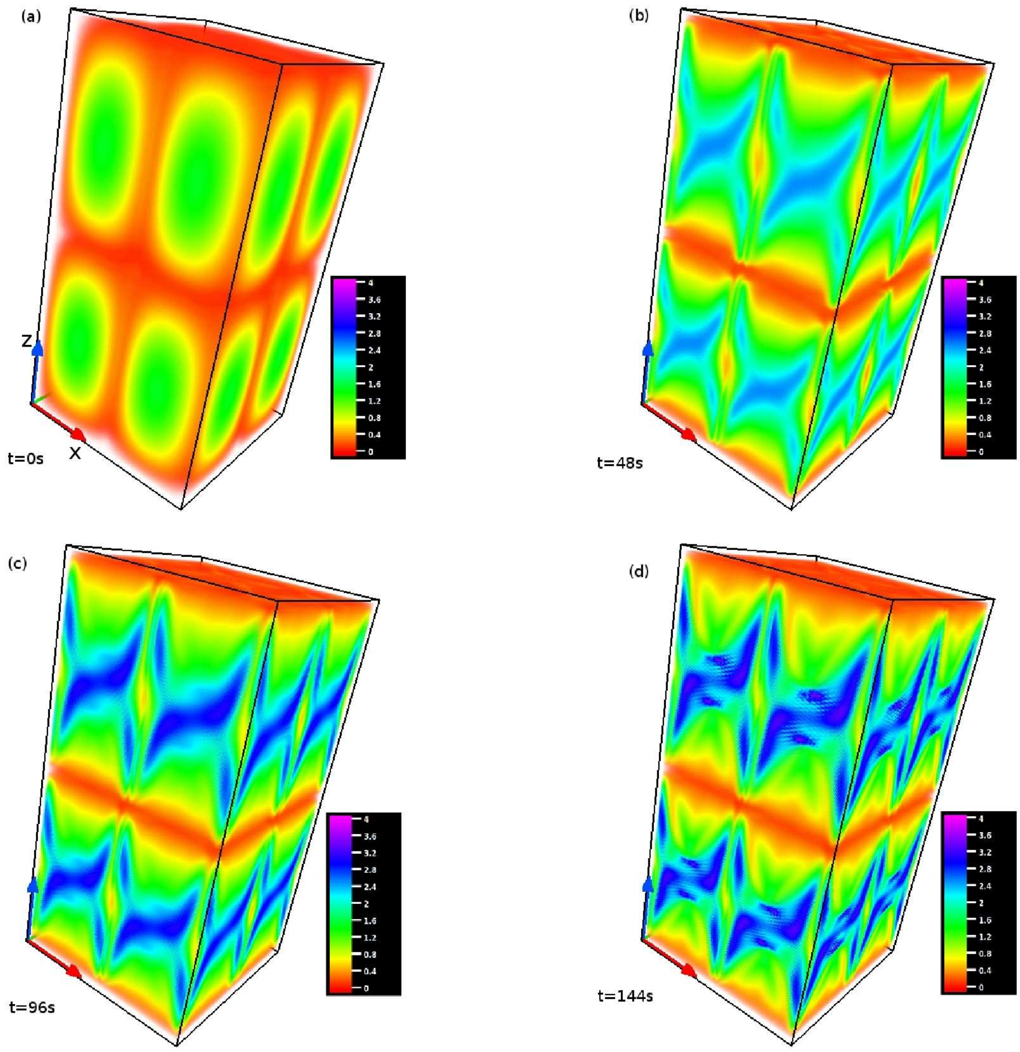

Figure 6.9: Time sequence of direct volume rending of total current density $\mid \mathbf{J} \mid$ for $s_0 = 3$ with viscosity ν_2. The color bar shows the values of $\mid \mathbf{J} \mid$. The figure highlights the appearances of higher values of total current density becoming localized and two-dimensional in structure, from an initially three-dimensional non-localized form.

From the above discussions then the following general picture emerges. The initial Lorentz force pushes the magnetofluid and generates flow by converting magnetic energy into kinetic energy. The monotonic increase in component current densities are supportive to the possibility of CS formation till a threshold in gradient of $\mathbf{B}$ is achieved. In numerical computations presented here, the threshold gradient of developing CSs are provided by the fixed grid resolutions below which the CSs decay through the magnetic reconnection. The plots also show that for a magnetofluid with higher viscosity the CS formation is delayed in time which is in accordance with the general expectation.

Towards a confirmation of CS formation, in Figure 6.9 we display the Direct Volume Rendering (DVR) of $\mid \mathbf{J} \mid$ for computation with viscosity ν_2. The DVR confirms that with a progress in time, the $\mid \mathbf{J} \mid$ becomes more two-dimensional in appearance from its initial three-dimensional structure. Further insight is obtained from the time sequence of magnetic nulls depicted in Figure 6.10 overlaid with a selected isosurface of $\mid \mathbf{J} \mid_{max}$ having an isovalue which is 30% of its maximum value. Hereafter, we refer this isosurface as $J-30$. The appearance of this surface near $t = 96s$ followed by its spatial extension with time while being concurrent with the increase in $\mid \mathbf{J} \mid_{max}$, is a tell-telling sign of CS formation. An important property of this $J-30$ surface is in its appearance at spatial locations away from the magnetic nulls. The above finding is further validated by considering other isovalues of $\mid \mathbf{J} \mid_{max}$ but not presented here to minimize the number of figures. This is a key finding of this work since the appearance of CSs away from the magnetic null has already been apprehended by the optical analogy.

To arrive at a detail understanding of the above finding, in the following we inspect the evolution of EPs along with their corresponding component current densities. For the purpose, in Figures 6.11, 6.13, and 6.14 we have displayed the time sequence of EP surfaces: $\phi_1 = 0.25, -0.25$; $\psi_2 = 0.85, -0.85$; and $\phi_2 = -0.40$ overlaid with selected isosurfaces of $\mid \mathbf{J}_1 \mid$ and $\mid \mathbf{J}_2 \mid$ using the nomenclature $J_1 - 60$ and $J_2 - 60$ respectively. Since $\mathbf{J}_1$, $\mathbf{J}_2$ and $\mathbf{J}_3$ are components of $\mathbf{J}$, so the appearance of $J_1 - 60$ and $J_2 - 60$ surfaces (along with $J_3 - 60$ surface) contribute to the development of the $J - 30$ surface. Considering these contributions along with those from the cross terms in $\mid \mathbf{J} \mid$, we have chosen the optimal isovalues for

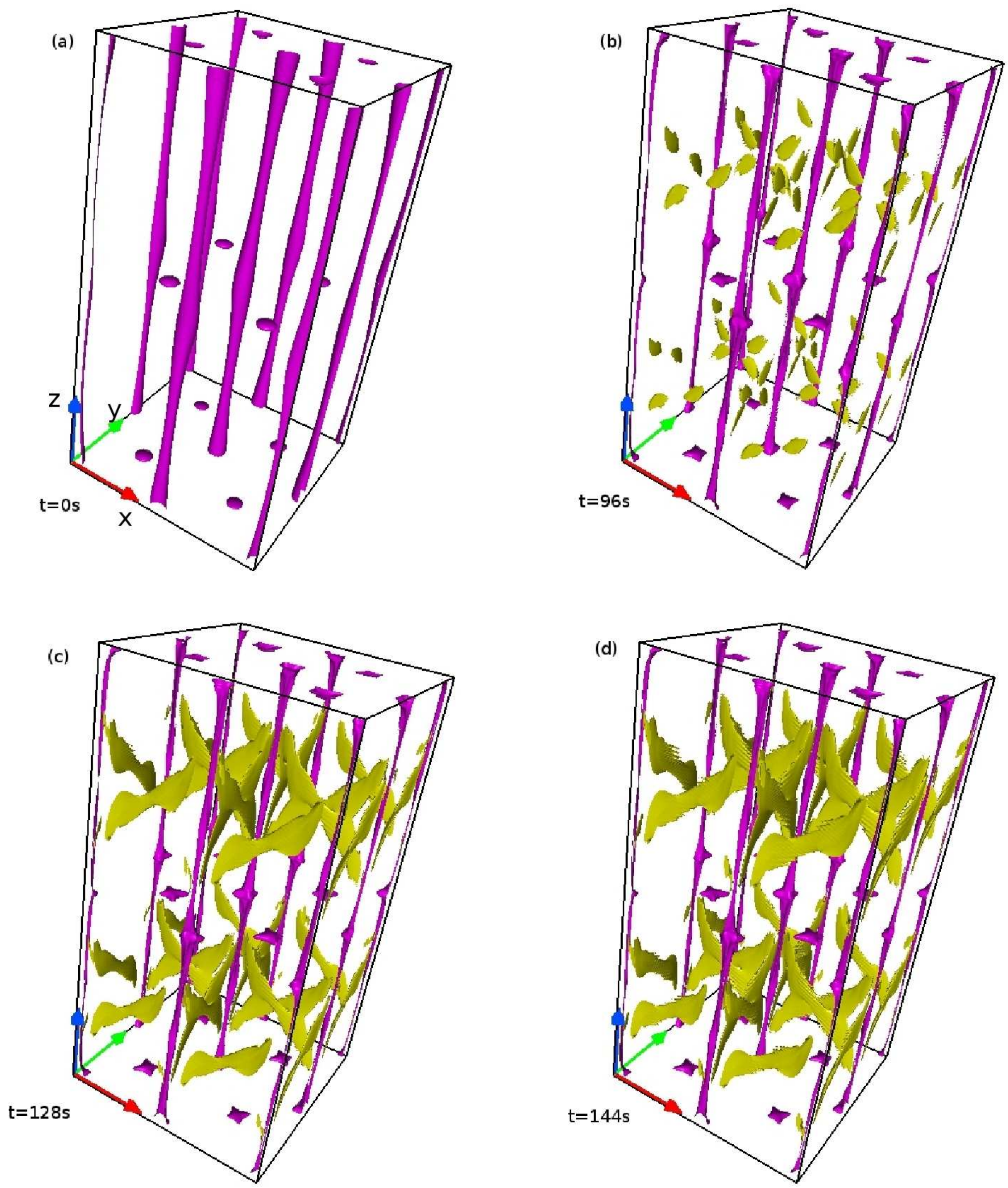

Figure 6.10: Time evolution of magnetic nulls (in pink), overlaid with isosurface (in yellow) of total current density having a magnitude of 30% of its maximum value (J-30). The figure illustrates the spatial locations in computational domain where the CSs are forming. Noteworthy is the development of CS away from the magnetic nulls where they are generally expected. Also the topology of the initial magnetic field in terms of spatial distribution of magnetic nulls is preserved throughout the time sequence.

the component current densities to be of 60% of $\mid \mathbf{J} \mid_{max}$. Figure 6.11 clarifies the important finding that the appearance of $J_1 - 60$ surface around $t = 96s$ is due to

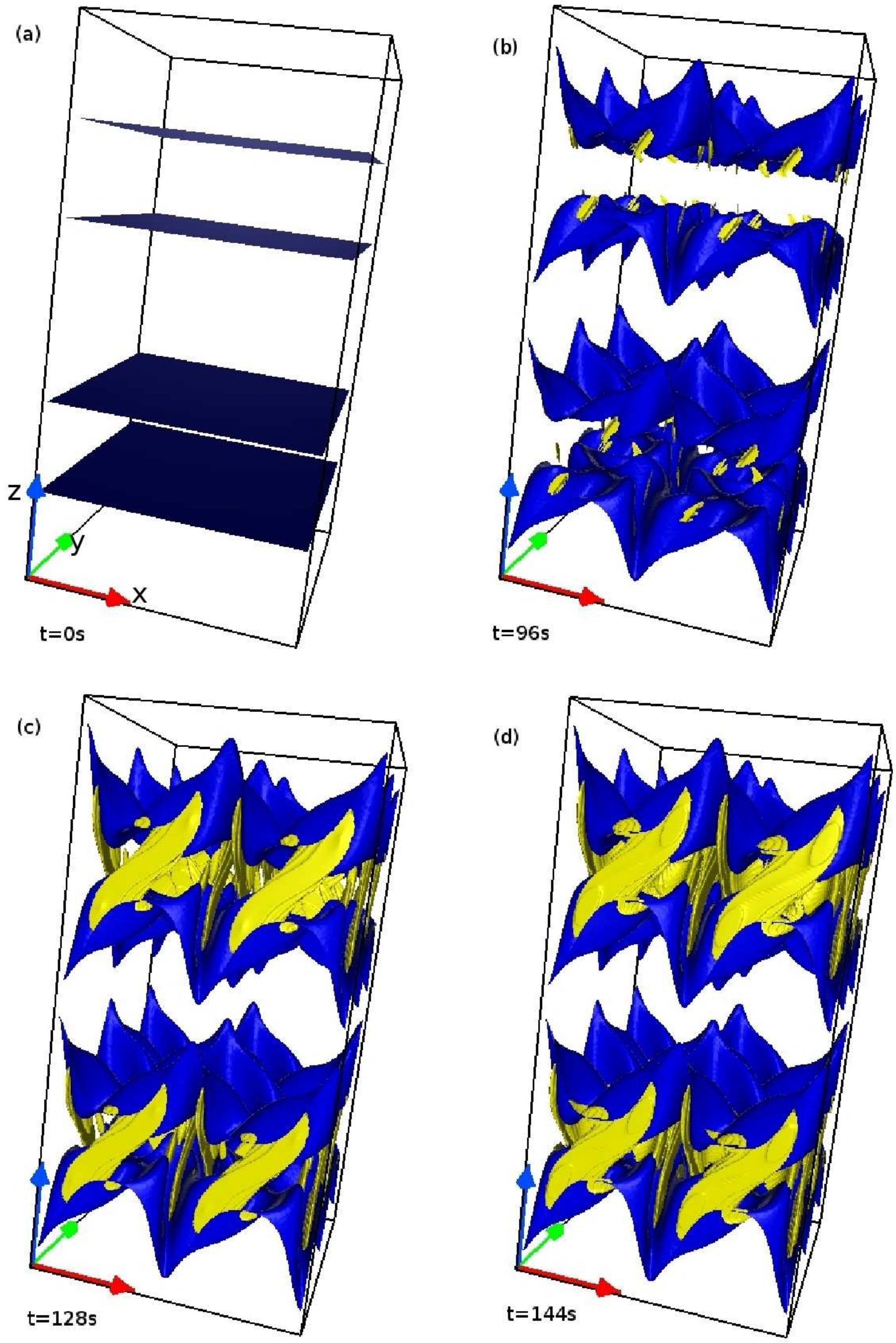

Figure 6.11: Evolution of Euler surfaces $\phi_1 = 0.25, -0.25$ (in blue), overlaid with $J_1 - 60$ surface (in yellow). The appearance of $J_1 - 60$ surface are co-located to a contortion of ϕ_1 favorable to bring two oppositely directed field lines towards each other.

contortion of the ϕ_1 Euler surface. In addition, the $J_1 - 60$ surface is concurrent in time sequence with the development of the $J - 30$ surface. Further, the two sets of surfaces are co-located in the computational domain and have similar structures.

This structural similarity along with concurrent and co-located appearance of $J - 30$ and $J_1 - 60$ surfaces ascertain that most of the contribution in $J - 30$ is from $J_1 - 60$. This is in conformity with the observation that the rate of increase of $\mid \mathbf{J}_1 \mid$ is substantially higher than the the same for the other two component current densities. We also note that the contortions of the ϕ_1 Euler surface are spread over the whole MFS and not localized near the intersections with the corresponding O-type neutral line. The cumulative effect of this spread in contortion along with the major contribution of $\mid \mathbf{J} \mid$ coming from $\mid \mathbf{J}_1 \mid$ then culminates into generating CSs in total volume current density that are away from the magnetic nulls.

Further, in Figure 6.12 we present plots of the ϕ_1 Euler surface overlaid with the isosurfaces of $\mid \mathbf{B}_1 \mid$. The panels a and b correspond to instants $t = 48s$ and $t = 128s$ respectively. The isovalue for the $\mid \mathbf{B}_1 \mid$ isosurfaces is chosen to be of 90% of its maximum value at a given instant. As the ϕ_1 Euler surface contorts, oppositely directed field lines come closer resulting in a local increase of the density of field lines and hence the $\mid \mathbf{B}_1 \mid$. In fact, the isovalue for the plotted $\mid \mathbf{B}_1 \mid$ isosurface at $t = 128s$ is almost 3.5 times larger than the same at $t = 48s$. A comparison between the two panels clearly shows a reduction in intersections of the $\mid \mathbf{B}_1 \mid$ isosurfaces with the ϕ_1 Euler surface as it gets more contorted. This reduction in intersections of the two isosurfaces with a concurrent increase of local $\mid \mathbf{B}_1 \mid$ then supports the general understanding that the ϕ_1 Euler surface is more contorted at $t = 128s$ to avoid the zone characterized by an intense $\mid \mathbf{B}_1 \mid$—a concept essential to the optical analogy.

The other two component current densities, namely the $\mid \mathbf{J}_2 \mid$ and $\mid \mathbf{J}_3 \mid$, also owe their increase to favorable contortions of the corresponding flux surfaces. Because of such contortions, two sets of $J_2 - 60$ surfaces lying approximately on x-constant and y-constant planes develop as shown in Figures 6.13 and 6.14. The current surface akin to the x-constant plane is developed by squeezing out the interstitial fluid across the O-type neutral line as displayed in Figure 6.13. While the second current surface identifiable by its approximate orientation similar to a y-constant plane develops from the contortions of the ϕ_2 Euler surfaces (Figure

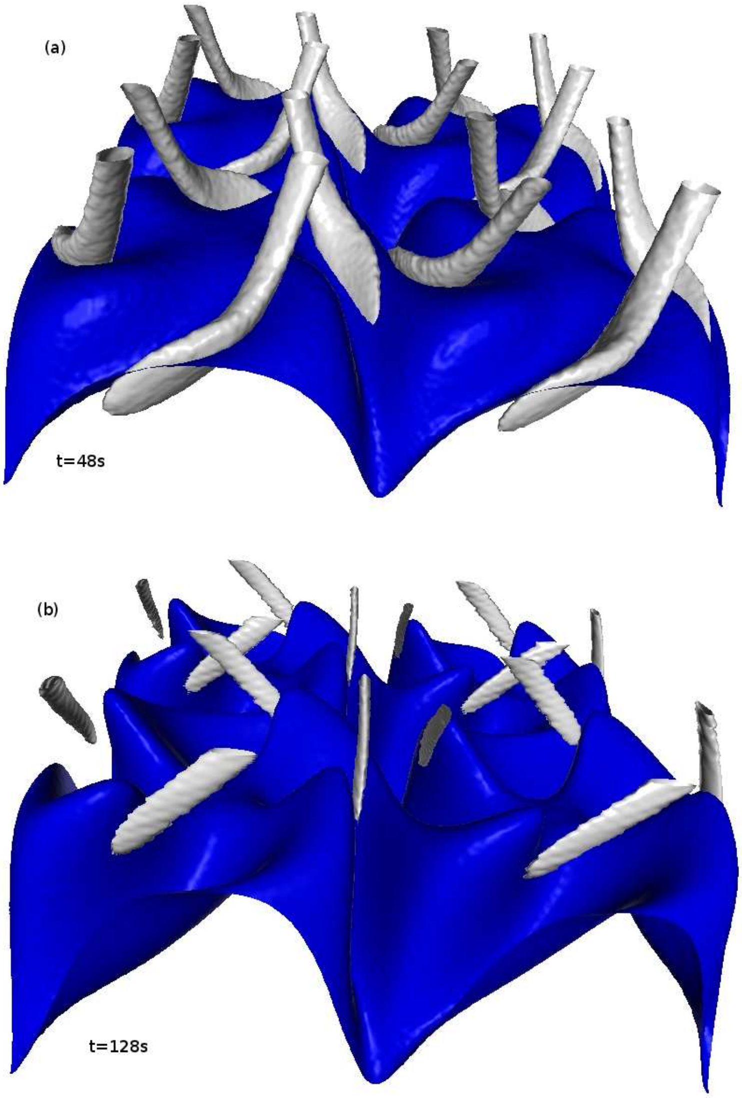

Figure 6.12: The Euler surface ϕ_1 (in Blue) at two time instants overlaid with isosurfaces of $\mid \mathbf{B}_1 \mid$ (in Grey). The reduction in intersections between the two isosurfaces along with a concurrent rise in $\mid \mathbf{B}_1 \mid$ is in general agreement with the understanding that magnetic field lines exclude a local region with intense magnetic field.

6.14) across the field reversal layer at $y = \pi$. The time delay between the appearance of these two sets is due to a combined effect of less contortions in the ϕ_2 Euler surface along with less magnitude of the corresponding component magnetic field and hence, the related current density near the field reversal layer. Similar arguments hold true for an emergence of $J_3{-}60$ surface, the time sequence of which can be visualized through rotating Figure 6.13 by $\pi/2$ along the vertical.

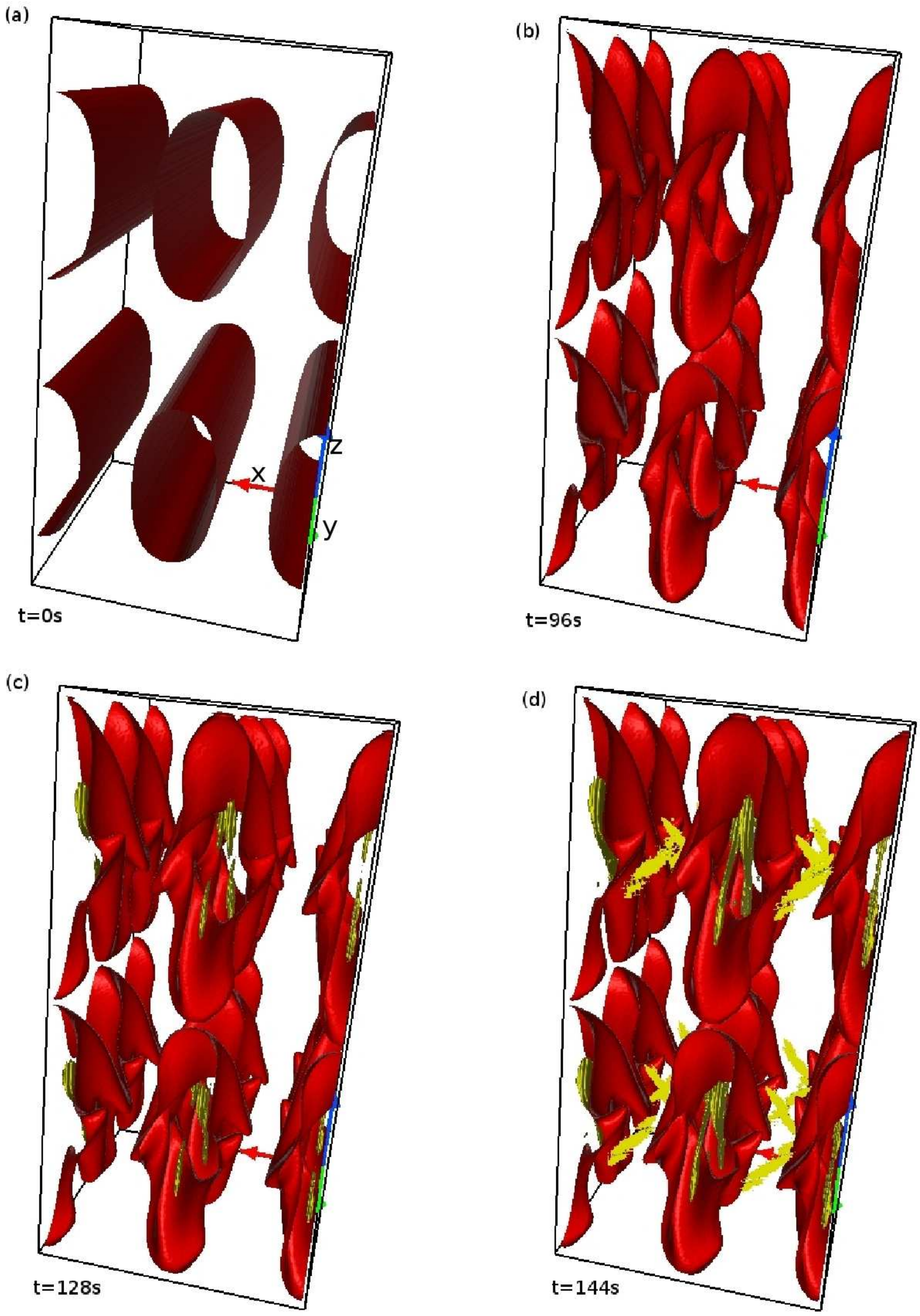

Figure 6.13: Evolution of Euler surfaces $\psi_2 = 0.85, -0.85$ (in red), overlaid with $J_2 - 60$ (in yellow). Noteworthy are the appearances of the $J_2 - 60$ surfaces along the axis of the Euler surfaces as the Euler surfaces get squeezed across the O-type null. The squeezing enables the two oppositely directed parts of the same field lines (lying on the Euler surface) to come close and develops current sheet.

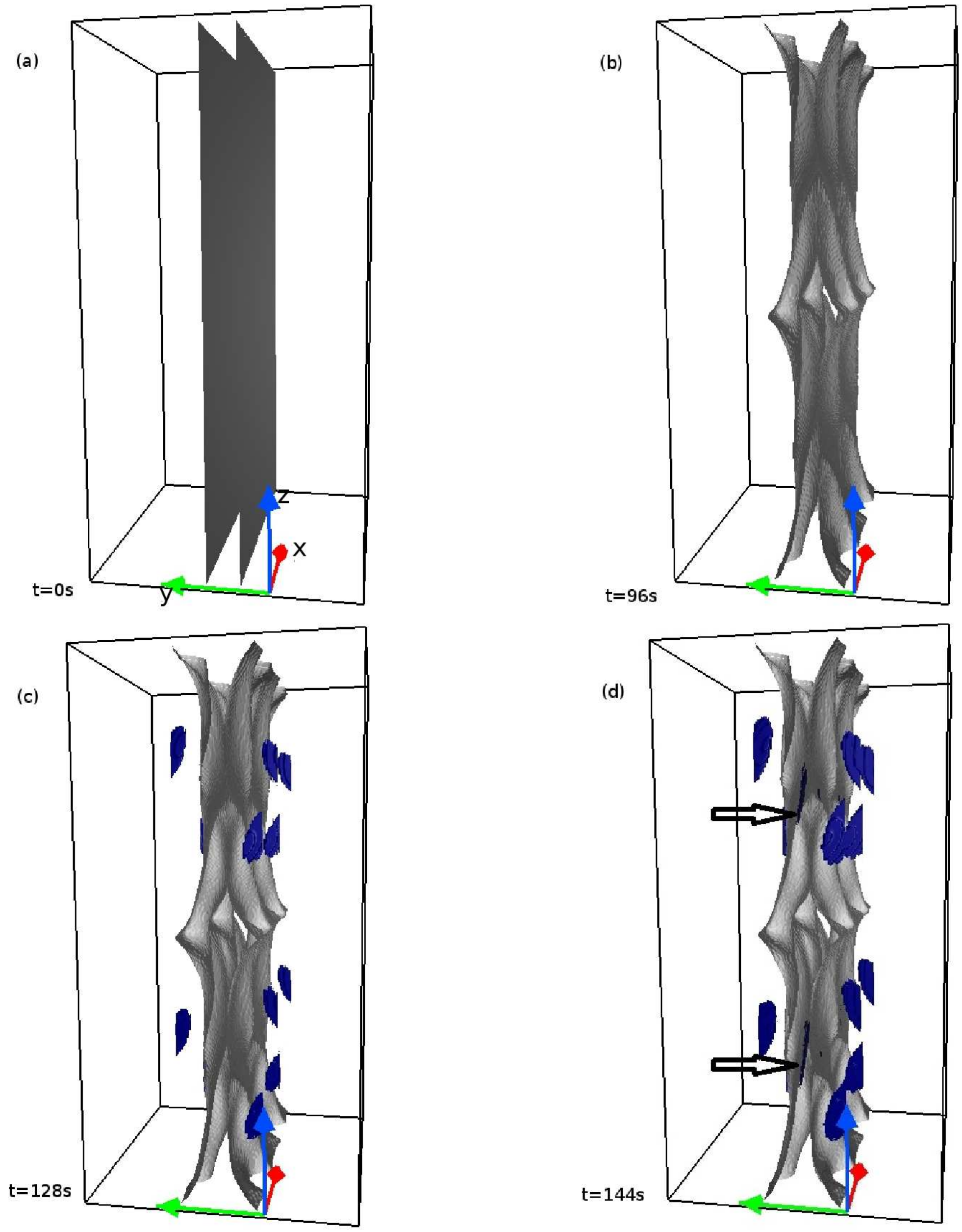

Figure 6.14: Time sequence of Euler surfaces $\phi_2 = -0.40$ (in grey), overlaid with $J_2 - 60$ (in blue). The two Euler surfaces depicted in the figure reside on two opposite sides of the field reversal layer. Formation of CSs (marked by arrows) through contortions of ϕ_2 is evident from the figure. A different color scheme in this particular figure is used for a better depiction of CS formation.

6.3 Numerical experiment II

6.3.1 Initial value problem

For this case, the initial value problem is constructed by realizing that a magnetic field with non-interlaced field lines can be written in terms of a global pair of flux surfaces ψ_1 and ϕ_1 (Bhattacharyya et al. 2010; Low 2015). Then, from chapter 5 the magnetic field is given as,

$$\mathbf{B}_1 = W_1(\psi_1, \phi_1)\nabla\psi_1 \times \nabla\phi_1, \tag{6.3.1}$$

where ψ_1 and ϕ_1 represent EPs and W_1 is the amplitude. The field is devoid of aligned current, i.e. $\mathbf{J}_1 \cdot \mathbf{B}_1 = 0$, documenting the corresponding field lines to be non-interlaced simple closed curves. It is noteworthy that $\mathbf{B}_1$, in general, has a nonzero $\mathbf{J}_1$ and hence although untwisted, is not a potential field. Interlaced field lines are generated by superposing $\mathbf{B}_1$ with another $\mathbf{B}_2$, represented by a separate pair of EPs $\{\psi_2, \phi_2\}$ and having an amplitude W_2. The superposed field $\mathbf{B}$ is given by

$$\begin{aligned} \mathbf{B} &= \mathbf{B}_1 + \epsilon_0 \mathbf{B}_2, && (6.3.2) \\ &= (\nabla\psi_1 \times \nabla\phi_1) + \epsilon_0 (\nabla\psi_2 \times \nabla\phi_2), && (6.3.3) \end{aligned}$$

where the amplitudes $W_1 = W_2 = 1$ and the constant ϵ_0 is related to the intensity of interlacing. Notably, a representation of any magnetic field by superposition of two untwisted or non-interlaced component fields is not general enough, and at least three such component fields are required to represent an arbitrary magnetic field; cf. recent review (Low 2015). Our specific choice (6.3.2) of two component fields for the purpose of superposition is based only on having a single parameter ϵ_0 to alter the intensity of interlacing. Based on our previous work (Kumar et al. 2014) presented in the section 6.2, we select the following EPs

$$\psi_1(x, y, z) = a_0 \cos x \sin z, \tag{6.3.4}$$

$$\phi_1(x, y, z) = a_0 \cos y, \tag{6.3.5}$$

and

$$\psi_2(x, y, z) = a_0 \sin x \sin y, \tag{6.3.6}$$

$$\phi_2(x, y, z) = -a_0 \cos z, \tag{6.3.7}$$

with an amplitude a_0 and defined in an uniform triply periodic Cartesian domain of period 2π. Figures 6.15(a) and 6.15(b) illustrate the level sets of the above EPs in pairs, (ψ_1, ϕ_1) and (ψ_2, ϕ_2) respectively for $a_0 = 1$, with ψ-constant surfaces in color grey and ϕ-constant surfaces in color red. The closed lines generated by intersection of the two surfaces are MFLs which are untwisted, as can easily be verified from their appearances. To further facilitate visualization, we overlay Figure 6.15 with $y = \pi$ plane depicted in color green. Notably, under the flux-freezing, the time evolution of these EPs is obtained by the equations (5.4.7)-(5.4.8) for $i = 1, 2$.

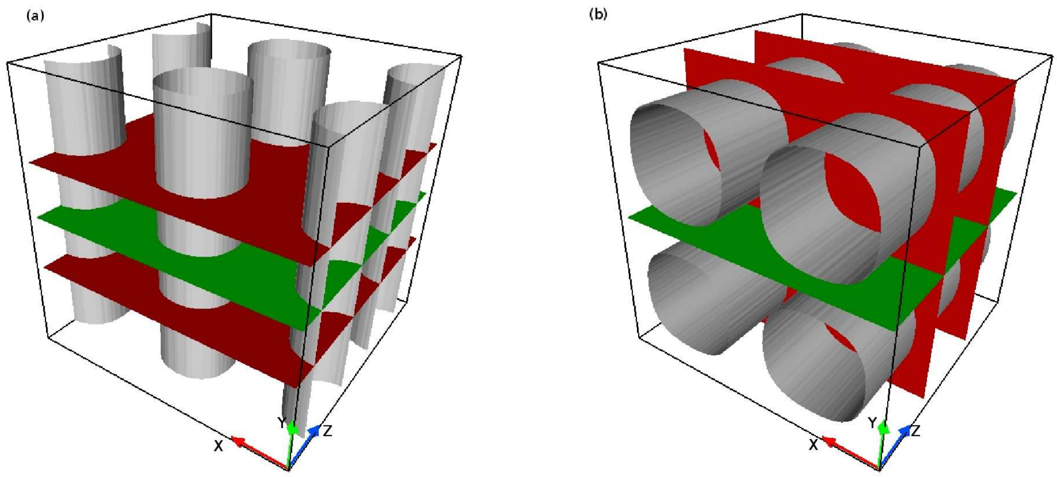

Figure 6.15: Panel a depicts initial Euler surfaces $\psi_1 = \pm 0.5$ in grey and $\phi_1 = -0.35$ in red. Panel b depicts initial Euler surfaces $\psi_2 = \pm 0.1$ in grey and $\phi_2 = 0.15$ in red. The surface in green marks the $y = \pi$ plane.

From (6.3.3), the initial component fields $\mathbf{B}_1 = \{B_{1x}, B_{1y}, B_{1z}\}$ and $\mathbf{B}_2 = \{B_{2x}, B_{2y}, B_{2z}\}$ are

$$B_{1x} = {a_0}^2 \cos x \sin y \cos z, \tag{6.3.8}$$

$$B_{1y} = 0, \tag{6.3.9}$$

$$B_{1z} = {a_0}^2 \sin x \sin y \sin z, \tag{6.3.10}$$

and

$$B_{2x} = {a_0}^2 \sin x \cos y \sin z, \tag{6.3.11}$$

$$B_{2y} = -{a_0}^2 \cos x \sin y \sin z, \tag{6.3.12}$$

$$B_{2z} = 0. \tag{6.3.13}$$

The superposed field $\mathbf{B} = \{B_x, B_y, B_z\}$ is

$$B_x = {a_0}^2 \left(\cos x \sin y \cos z + \epsilon_0 \sin x \cos y \sin z\right), \tag{6.3.14}$$

$$B_y = -{a_0}^2 \left(\epsilon_0 \cos x \sin y \sin z\right), \tag{6.3.15}$$

$$B_z = {a_0}^2 \left(\sin x \sin y \sin z\right). \tag{6.3.16}$$

The Lorentz force exerted by $\mathbf{B}$ is

$$L_x = {a_0}^4 \left[\left(\epsilon_0^2 - 1\right) \sin 2x \sin^2 y \sin^2 z - \left(\frac{\epsilon_0}{4}\right) \cos 2x \sin 2y \sin 2z \right], \tag{6.3.17}$$

$$L_y = {a_0}^4 \left[\left(\epsilon_0^2 - \frac{1}{2}\right) \sin^2 x \sin 2y \sin^2 z - \left(\frac{\epsilon_0}{4}\right) \sin 2x \cos 2y \sin 2z - \left(\frac{1}{2}\right) \cos^2 x \sin 2y \cos^2 z \right], \tag{6.3.18}$$

$$L_z = -{a_0}^4 \left[\left(\frac{\epsilon_0^2}{2} - 1\right) \cos^2 x \sin^2 y \sin 2z + \left(\frac{\epsilon_0}{4}\right) \sin 2x \sin 2y \cos 2z + \left(\frac{\epsilon_0^2}{2}\right) \sin^2 x \cos^2 y \sin 2z \right]. \tag{6.3.19}$$

Noting the initial Lorentz force to be a function of ϵ_0, the amplitude a_0 is adjusted to perform computations with initial fields having different ϵ_0 but identical magnitude of average Lorentz force.

The field-aligned current density and the global magnetic helicity for $\mathbf{B}$ are

$$(\nabla \times \mathbf{B}) \cdot \mathbf{B} = {a_0}^4 \epsilon_0 (\sin^2 x \cos^2 y \sin^2 z + \cos^2 x \sin^2 y \cos^2 z + 2 \sin^2 y \sin^2 z), \tag{6.3.20}$$

$$K_M = 2{a_0}^4 \epsilon_0 \pi^3, \tag{6.3.21}$$

which reveal that they are directly proportional to ϵ_0. The global magnetic helicity is calculated here using the classical expression given by the equation (6.2.13). The global magnetic helicity is a measure of interlinkages between MFLs and hence, is explicitly related to interlacing of field lines. The direct proportionality to ϵ_0 in equations (6.3.20) and (6.3.21) is affirmative of an increase in interlacing, and hence making MFLs of $\mathbf{B}$ more topologically complex. The above inference can further be validated from Figure 6.16 which visually clarifies an increase of interlacing in MFLs with ascending values of ϵ_0.

To facilitate presentation, in the following we discuss the topology of $\mathbf{B}$ in relation to ϵ_0. In Figure 6.17, we plot MFLs of $\mathbf{B}$ for four separate values: $\epsilon_0 = \{0.1, 0.3, 0.5, 0.7\}$ in the vicinity of $y = \pi$ plane. Features evident in this figure are helical MFLs for $\epsilon_0 = 0.1$, and the deviation of MFLs from this helical structure with an increase of ϵ_0 culminating into MFLs depicted in panels b, c and d. To explain these features we revert to equations (6.3.14)-(6.3.16) and note that for $\epsilon_0 = 0$, the field lines of $\mathbf{B}$ are closed disjoint curves tangential to y-constant planes (since the component B_y is zero). For any other ϵ_0, the component field $\mathbf{B}_2$ provides a nonzero B_y resulting in lifting up MFLs of $\mathbf{B}$ out of the y constant planes. In addition, a nonzero ϵ_0 contributes to the component B_x. The net result is then a deformation of MFLs in directions both perpendicular and parallel to y-constant planes. For a small value of ϵ_0 this deformation is also small, resulting in helical field lines with projections on y-constant planes similar in geometry to the closed curves of $\epsilon_0 = 0$. Larger values of ϵ_0 deform field lines more, leading to

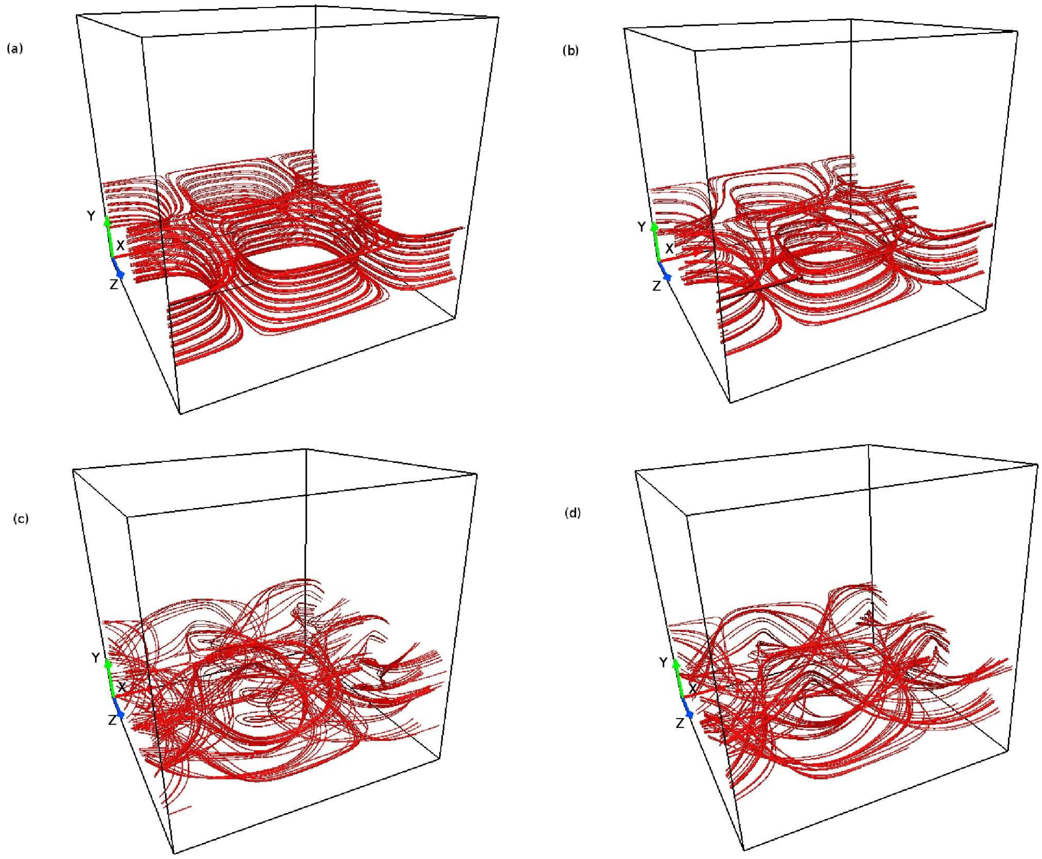

Figure 6.16: The panels a, b, c and d illustrate magnetic field lines of the initial field $\mathbf{B}$ for $\epsilon_0 = 0.1, 0.3, 0.5$ and 0.7 respectively. Notably, the field lines are becoming more interlaced as ϵ_0 increases.

MFLs depicted in panels b, c and d. A first order Taylor expansion of equations (6.3.14)-(6.3.16) near the $y = \pi$ plane for constant x and z yields

$$B_x = -{a_0}^2\epsilon_0 \sin x_0 \sin z_0 - {a_0}^2 (y - \pi) \cos x_0 \cos z_0, \tag{6.3.22}$$

$$B_y = {a_0}^2\epsilon_0 (y - \pi) \cos x_0 \sin z_0, \tag{6.3.23}$$

$$B_z = -{a_0}^2 (y - \pi) \sin x_0 \sin z_0, \tag{6.3.24}$$

evincing B_y and B_z to flip sign across the $y = \pi$ plane. However for $\epsilon_0 \neq 0$, B_x flips sign at $y = \pi - y_1$ where y_1 satisfies the condition

$$y_1 > \frac{\epsilon_0 \sin x_0 \sin z_0}{\cos x_0 \cos z_0}. \tag{6.3.25}$$

A pair of oppositely directed MFLs across $y = \pi$ plane are shifted by y_1, which in turn increases with ϵ_0 (Fig. 6.17), rendering an initial $\mathbf{B}$ with larger ϵ_0 less favorable to develop CSs.

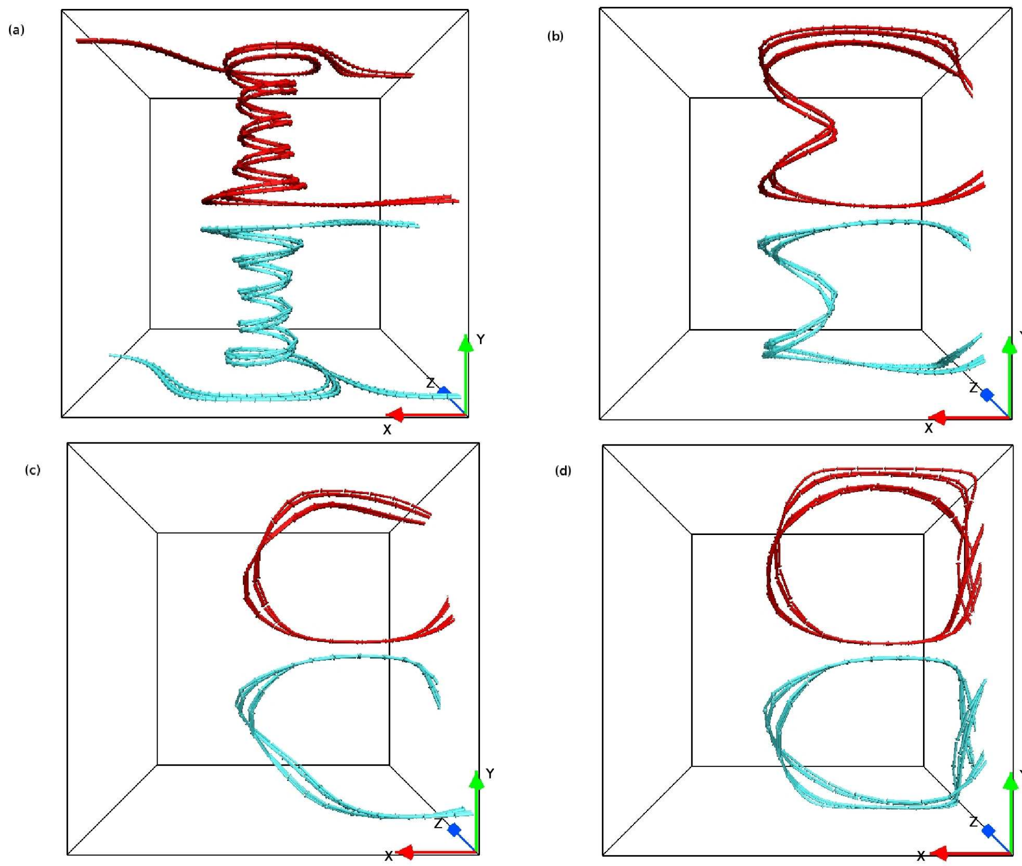

Figure 6.17: Panels a, b, c and d show field lines of $\mathbf{B}$ for $\epsilon_0 = 0.1, 0.3, 0.5$ and 0.7 respectively. These field lines are plotted in close proximity of the $y = \pi$ plane and with $z \in \{0, \pi\}$. The figure indicates the field lines to be helical for $\epsilon_0 = 0.1$, while for larger ϵ_0, the field lines deviate from this helical structure. Importantly, the distance between two anti-parallel field lines located across the $y = \pi$ plane increases with ϵ_0.

Further insight into topology of the initial field is gained by constructing its skeleton in terms of magnetic nulls, since these are the sites where development of CSs are expected. To illustrate the nulls, we employ the same technique utilized in the experiment I (cf. subsection 6.2.1). Using this technique, in Figure 6.18 we have depicted nulls of $\mathbf{B}$ for $\epsilon_0 = 0.5$ by selecting parameters $H_0 = 0.01$ and $d_0 = 0.05$. The Figure 6.18 straightaway confirms only the presence of 2D nulls in the form of lines and a complete absence of 3D nulls. Similar results are obtained for the $\epsilon_0 = 0.1, 0.3$, and 0.7 values, shown in Figures 6.24(a), 6.26(a), and 6.31(a), respectively.

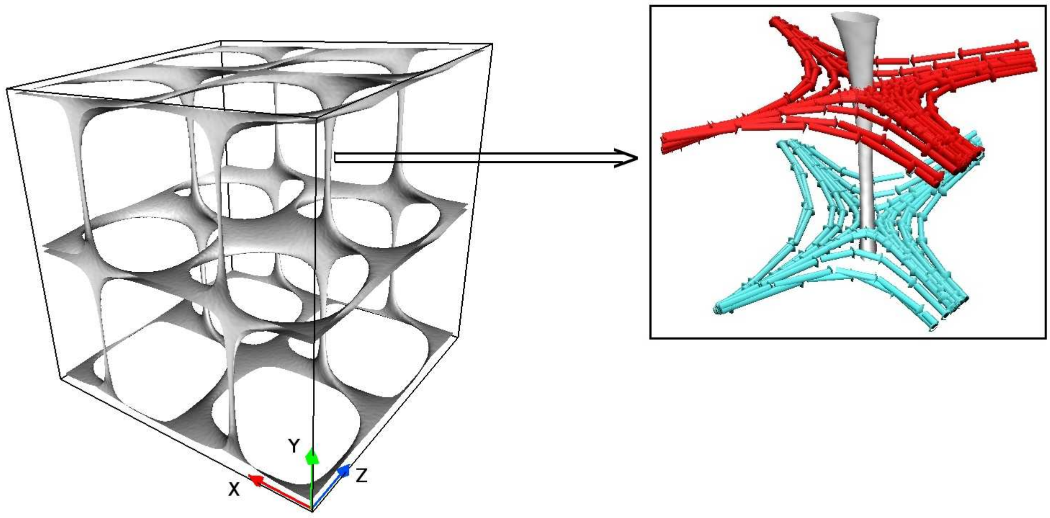

Figure 6.18: The figure demonstrates the magnetic nulls by isosurfaces of $\chi(x, y, z)$, defined in (6.2.14), with parameter $H_0 = 0.01$ and $d_0 = 0.05$, for $\epsilon_0 = 0.5$. The presence of 2D nulls and complete absence of 3D nulls is evident from the figure. The field topologies near the neutral line located at $x = \pi/2$, $z = \pi$ is depicted in inset; which correspond to X-type nulls.

To further identify the 2D nulls, we expand components of $\mathbf{B}$ in a Taylor series in the immediate vicinity of $x = \pi/2, z = \pi$ for a constant y to get

$$B_x = {a_0}^2 \left(x - \frac{\pi}{2}\right) \sin y_0 - {a_0}^2 \left(z - \pi\right) \epsilon_0 \cos y_0, \tag{6.3.26}$$

$$B_y = 0, \tag{6.3.27}$$

$$B_z = -{a_0}^2 \left(z - \pi\right) \sin y_0. \tag{6.3.28}$$

Notably, the non-zero components B_x and B_z have point antisymmetry about co-ordinates $x = \pi/2, z = \pi$ along the y-line rendering every point on it to be an X-type neutral point. The MFLs near two such neutral points are shown in the inset (Fig. 6.18). Similarly the z-line (extending in z-direction) is also X-type neutral line. Moreover, the Taylor series expansion of components field in the immediate neighborhood of $y = \pi, z = \pi$ for a constant x yields,

$$B_x = {a_0}^2\,(y-\pi)\cos x_0 - {a_0}^2\,(z-\pi)\,\epsilon_0 \sin x_0, \tag{6.3.29}$$

$$B_y = 0, \tag{6.3.30}$$

$$B_z = 0, \tag{6.3.31}$$

thus confirming the line along the x-axis with co-ordinates $y = z = \pi$ to be a neutral line.

6.3.2 Results

The results are presented for numerical computations carried out with zero initial velocity and ϵ_0 in the range of $\{0.1, 0.7\}$, in steps of 0.1. The computational grid has uniform resolution of 128^3 and corresponds to a physical volume of $(2\pi)^3$ with vertical extension $L_0 = 2\pi$. The coefficient of viscosity and the mass density are set to $\nu = 0.008$ and $\rho_0 = 1$ respectively. Then, $\tau_\nu \approx 5 \times 10^3 s$ for each ϵ_0 value. Moreover, $\{\tau_a \approx 27s,\ 26s,\ 24s,\ 23s\}$ for $\{\epsilon_0 = 0.1,\ 0.3,\ 0.5,\ 0.7\}$ with corresponding $\{B_0 = 0.82,\ 0.85,\ 0.90,\ 0.96\}$.

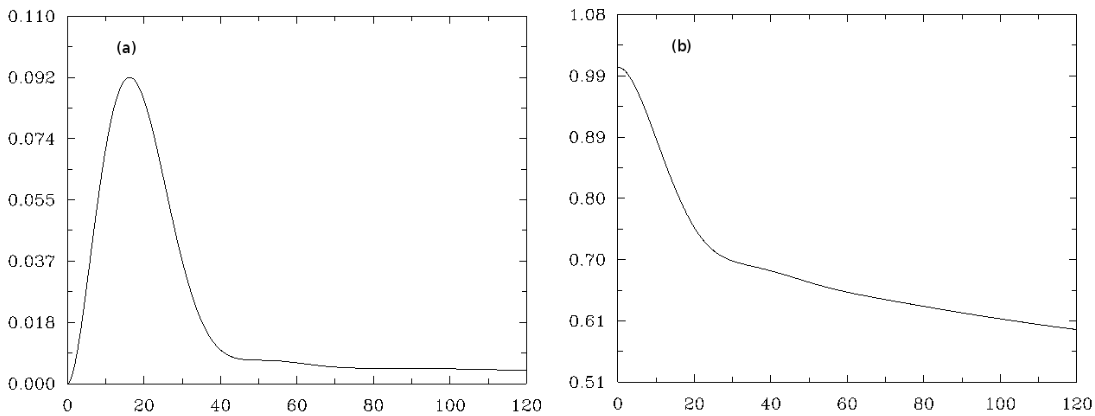

Figure 6.19: Time evolution of normalized kinetic and magnetic energies for $\epsilon_0 = 0.1$ (panels a and b). The normalization is done with the initial total energy. The abscissas are times whereas the ordinates are the energies. The plots highlight the initial peak in kinetic energy and the quasi-steady phase of the evolution.

When released from an initial non-equilibrium state, the dynamics develops because of an imbalance between the Lorentz force and the pressure gradient with zero initial value. The resulting increase in velocity gets arrested by viscous drag and the magnetofluid relaxes towards a quasi-steady state while preserving its magnetic topology. For a general understanding of this viscous relaxation, Figure 6.19 plots the histories of kinetic and magnetic energies for $\epsilon_0 = 0.1$, normalized to the initial total (magnetic +kinetic) energy. The development of the peak in kinetic energy centered at $t = 20s$ is due to the viscous arrest. The quasi-steady phase of the evolution is in the temporal range $t \in \{60s, 120s\}$ and is characterized by an almost constant kinetic energy, while the change in magnetic energy is restricted to 13% of its total variation. For other values of ϵ_0, the magnetic and kinetic energy curves show the same qualitative behavior but with different timing and amplitudes.

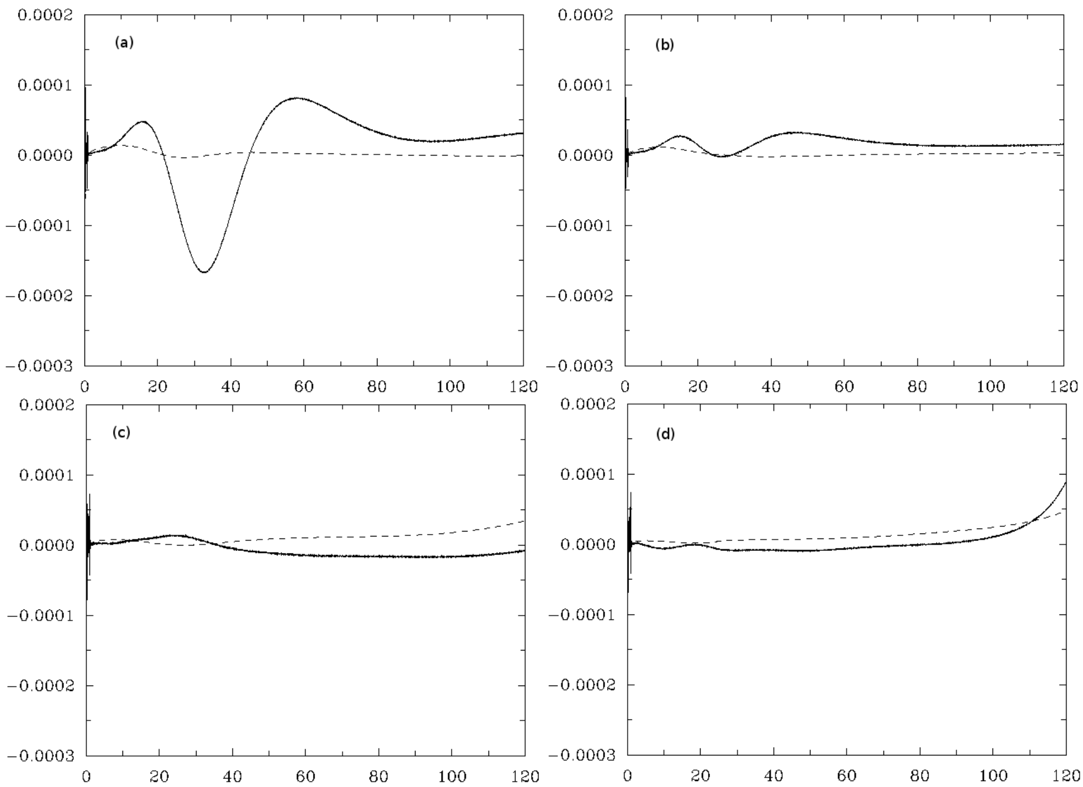

Figure 6.20: Panels a, b, c, and d illustrate deviations of normalized kinetic (dashed) and magnetic (solid) energy rates from their analytical values during computations with $\epsilon_0 = 0.1, 0.3, 0.5$, and 0.7 respectively. The normalization is with respect to the initial total energy. The abscissas represent times while the ordinates show the energy rates. The plots document an almost accurate maintenance of the energy rates.

The accuracy of computations is assessed in Figure 6.20 displaying numerical deviations of normalized kinetic (dashed line) and magnetic (solid line) energy rates from their analytical values in (6.1.11) and (6.1.12). The displayed deviations are for different ϵ_0 values: $\epsilon_0 = 0.1, 0.3, 0.5$, and 0.7, which we have selected as the representative cases. The plots confirm the numerical accuracy to be maintained with acceptable precision; the maximal deviation being 0.0002 (panel *d*). This accurate maintenance of energy rates denies any possibility of numerical MRs and hence, confirms the preservation of magnetic topology throughout the computations.

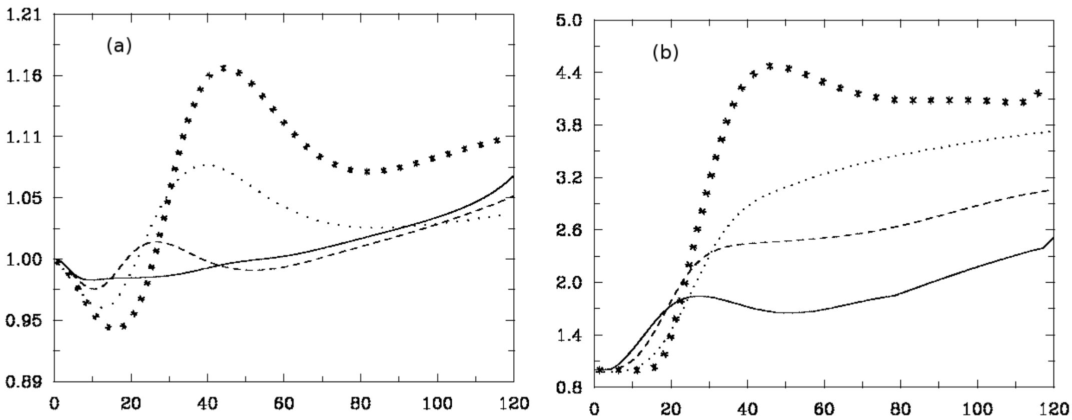

Figure 6.21: Panels *a* and *b* show time evolution of normalized $<\mid \mathbf{J} \mid>$ and $J_{\rm max}$ respectively for $\epsilon_0 = 0.1$ (starred line), 0.3 (dotted line), 0.5 (dashed line), and 0.7 (solid line). The abscissas are times and the ordinates are the current densities. The overall increase in current densities with time suggests development of CSs.

The overall tendency to form CSs can be established from panels *a* and *b* of Figure 6.21, plotting the evolution of average total current density $<\mid \mathbf{J} \mid>$ and maximal value of $\mid \mathbf{J} \mid$ respectively. We denote the latter by $J_{\rm max}$ and the current densities in the plots are normalized to their initial values. Notable is their tendency to increase, albeit without monotonicity, from the respective initial values. Because for every ϵ_0 the average component current density $<\mid \mathbf{J}_2 \mid>=<\mid \nabla \times \mathbf{B}_2 \mid>$ shows a monotonous increase, and the scalar product $< \mathbf{J}_1 \cdot \mathbf{J}_2 >$ (where $\mathbf{J}_1 = \nabla \times \mathbf{B}_1$) remains negative (cf. panels *a* and *b* of Fig. 6.22) throughout evolution, this lack of monotonicity in $<\mid \mathbf{J} \mid>$ is exclusively due to contribution from the $<\mid \mathbf{J}_1 \mid>$ (panel *c*, Fig. 6.22). Similar analysis yields contributions from the corresponding maximum $\mid \mathbf{J}_1 \mid$ to be responsible for the lack of monotonicity in $J_{\rm max}$.

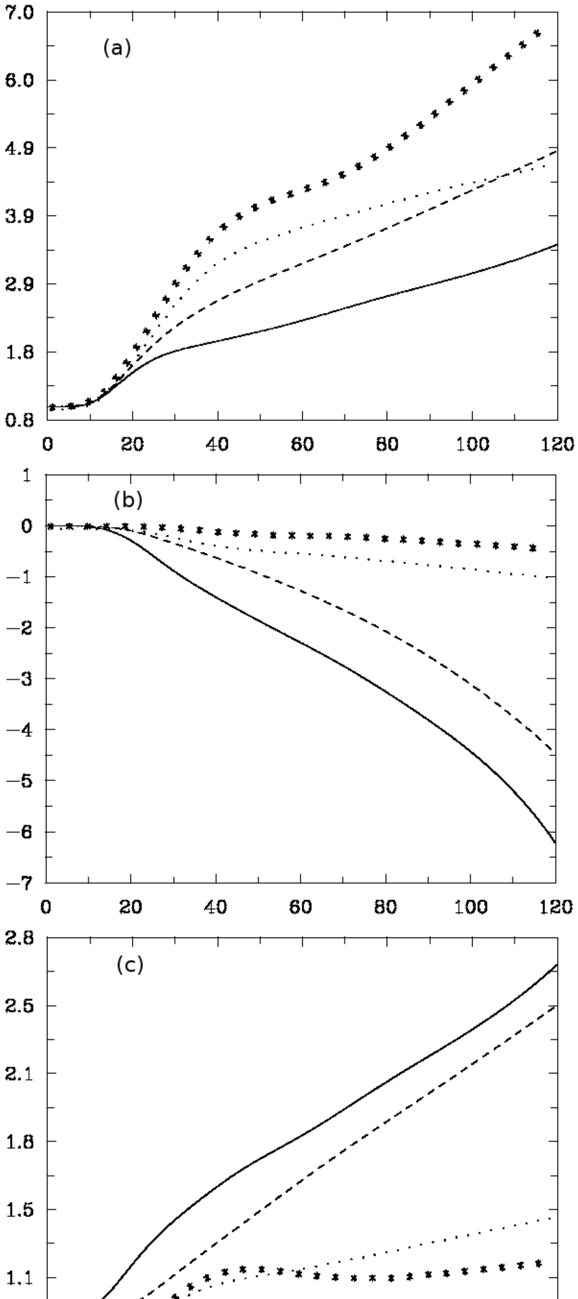

Figure 6.22: Panels a, b, and c illustrate time evolution of $<|\mathbf{J}_2|>$, $<\mathbf{J}_1 \cdot \mathbf{J}_2>$, and $<|\mathbf{J}_1|>$ respectively for $\epsilon_0 = 0.1$ (starred line), 0.3 (dotted line), 0.5 (dashed line), and 0.7 (solid line). The abscissas show times whereas the ordinates are the current densities. The current densities are normalized to their initial values.

Additional computations are performed for different uniform grid resolutions varying from 96^3 to 160^3 in steps of 16^3, with $\epsilon_0 = 0.1$ and $\epsilon_0 = 0.5$ as the representative cases. The resulting plots (Fig. 6.23) document scaling of $J_{\max}$

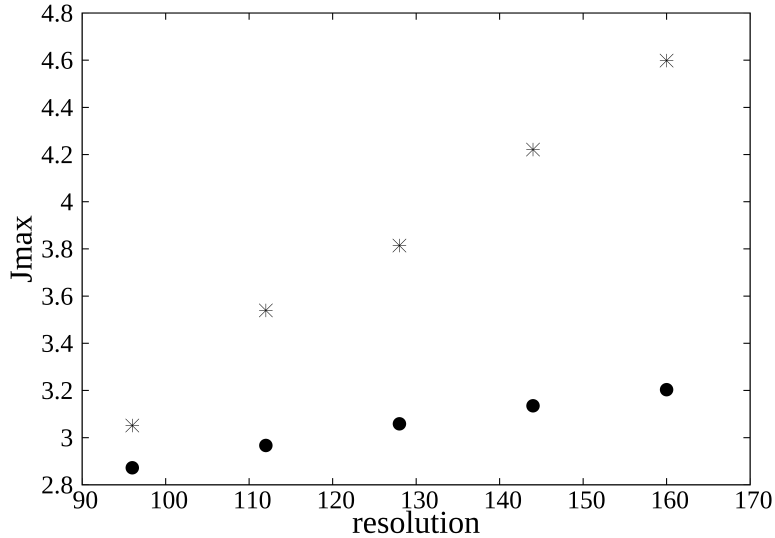

Figure 6.23: The plot of $J_{\max}$ against grid resolution for $\epsilon_0 = 0.1$ (stars) and $\epsilon_0 = 0.5$ (dots). The monotonous increase of $J_{\max}$ with resolution confirms the development of CSs for both the ϵ_0 values. Also, the plot documents a stronger scaling with resolution for the case $\epsilon_0 = 0.1$.

with resolution, which points in favor of CS formations (Mellor et al. 2005). Moreover, the scaling is stronger for $\epsilon_0 = 0.1$, where the $y = \pi$ plane is favorable for CS formation. In contrast, for $\epsilon_0 = 0.5$, with no apparent favorable location for CS formation, the scaling is weaker. Such comparative scaling is a signature of scenarios where CSs develop at three-dimensional magnetic nulls against CSs developing away from the nulls (Craig and Effenberger 2014; Craig and Pontin 2014; Wilmot-Smith 2015).

To identify and locate onset of CSs, in the following we further analyze the four cases separately. The analyzes are for the computations with 128^3 grid resolution where we follow appearances and geometries of the isosurface of $\mid \mathbf{J} \mid$, referred hereafter as $J-50$, with an isovalue which is 50% of maximum $\mid \mathbf{J} \mid$ for each ϵ_0. Also to facilitate the general understanding, we overlay these isosurfaces with magnetic nulls.

6.3.2.1 Case (I) $\epsilon_0 = 0.1$

The evolution of the corresponding $J - 50$ surfaces overlaid with magnetic nulls is illustrated in Figure 6.24. Based on their shape, these surfaces can be

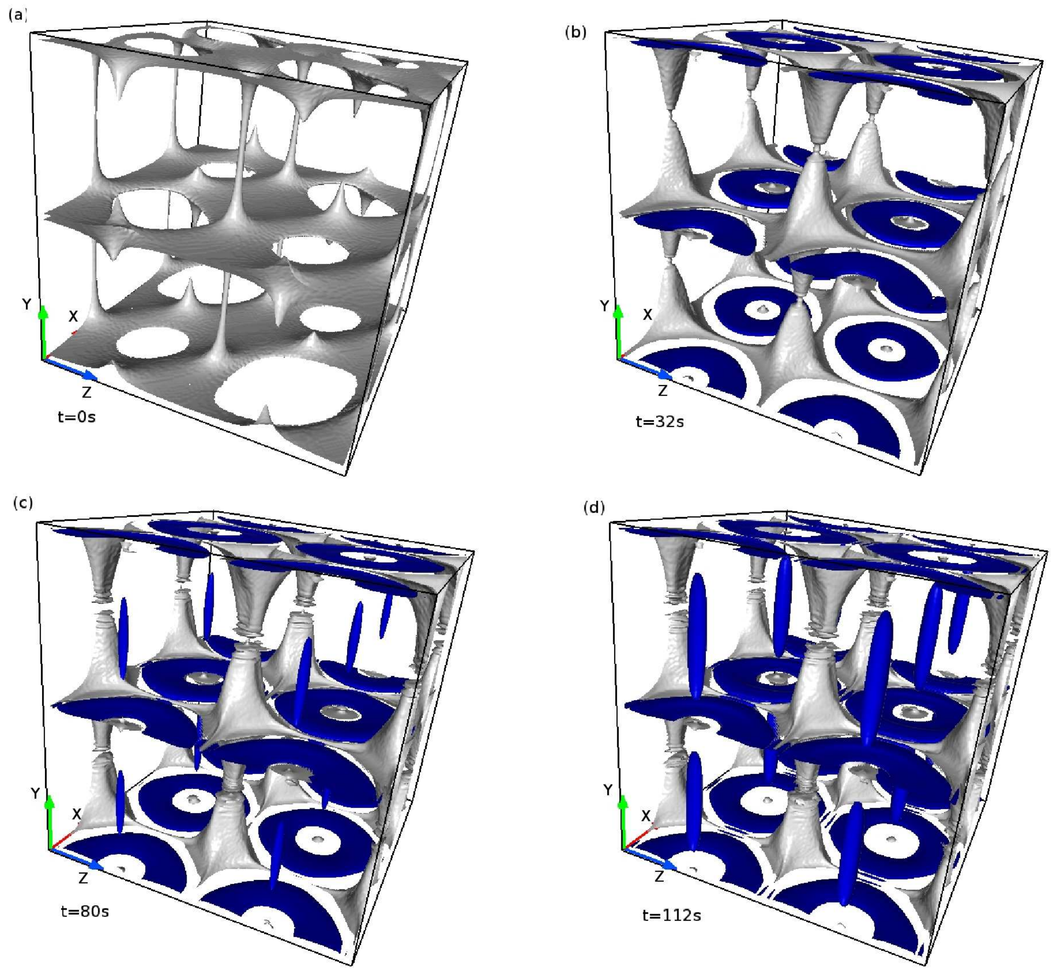

Figure 6.24: Evolution of the isosurface $J-50$ (in blue), having an isovalue which is 50% of the maximum $\mid \mathbf{J} \mid$ for $\epsilon_0 = 0.1$. The figure is further overlaid with magnetic nulls (in grey). Noteworthy is the development of CSs at $y=\pi$ plane where they are generally expected because of the presence of favorable field line topology. The figure also shows the generation of closed elongated $J-50$ surfaces.

classified into two geometrically distinct categories: the open surfaces appearing at the $y=\pi$ plane and the elongated closed surfaces distributed sparsely in the volume. Evident from the magnetic field line evolution depicted in Figure 6.25, the open surfaces are the CSs developed by two antiparallel complimentary field lines approaching towards the $y=\pi$ plane. Additionally, the figure identifies generation of the closed $J-50$ surfaces to an increase in the local number density of parallel field lines, resulting in an increase in $\mid \mathbf{B} \mid$ and hence $\mid \mathbf{J} \mid$. A sharpening of field gradient playing no role in the generation, therefore, the

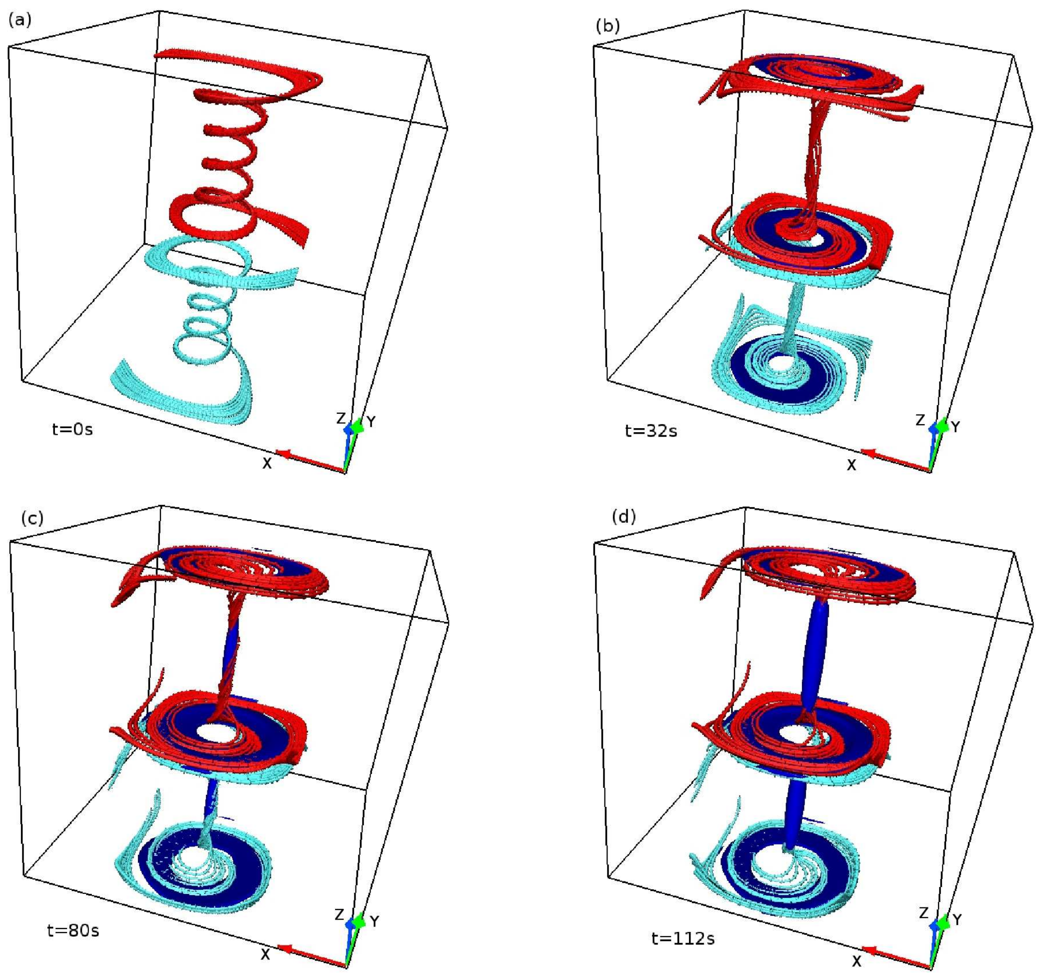

Figure 6.25: History of two complementary sets of oppositely directed MFLs of the **B** along with $J-50$ surfaces (in blue) for $\epsilon_0 = 0.1$. The plots confirm development of CSs at the $y = \pi$ plane as two oppositely directed field lines approach each other. The figure also relates the closed $J-50$ surfaces to an increase in parallel field lines density, implying their onset does not indicate CS formation.

closed surfaces do not qualify as current sheets.

6.3.2.2 Case (II) $\epsilon_0 = 0.3$

To complement results of Case I, here we analyze $J-50$ surfaces for computation with $\epsilon_0 = 0.3$. In Figure 6.26, we illustrate the history of $J-50$ surfaces overlaid with magnetic nulls. It is evident from the figure that most of the $J-50$ surfaces are elongated closed structures similar to the case of $\epsilon_0 = 0.1$. In addition, development of localized current layers at the $y = \pi$ plane is noted.

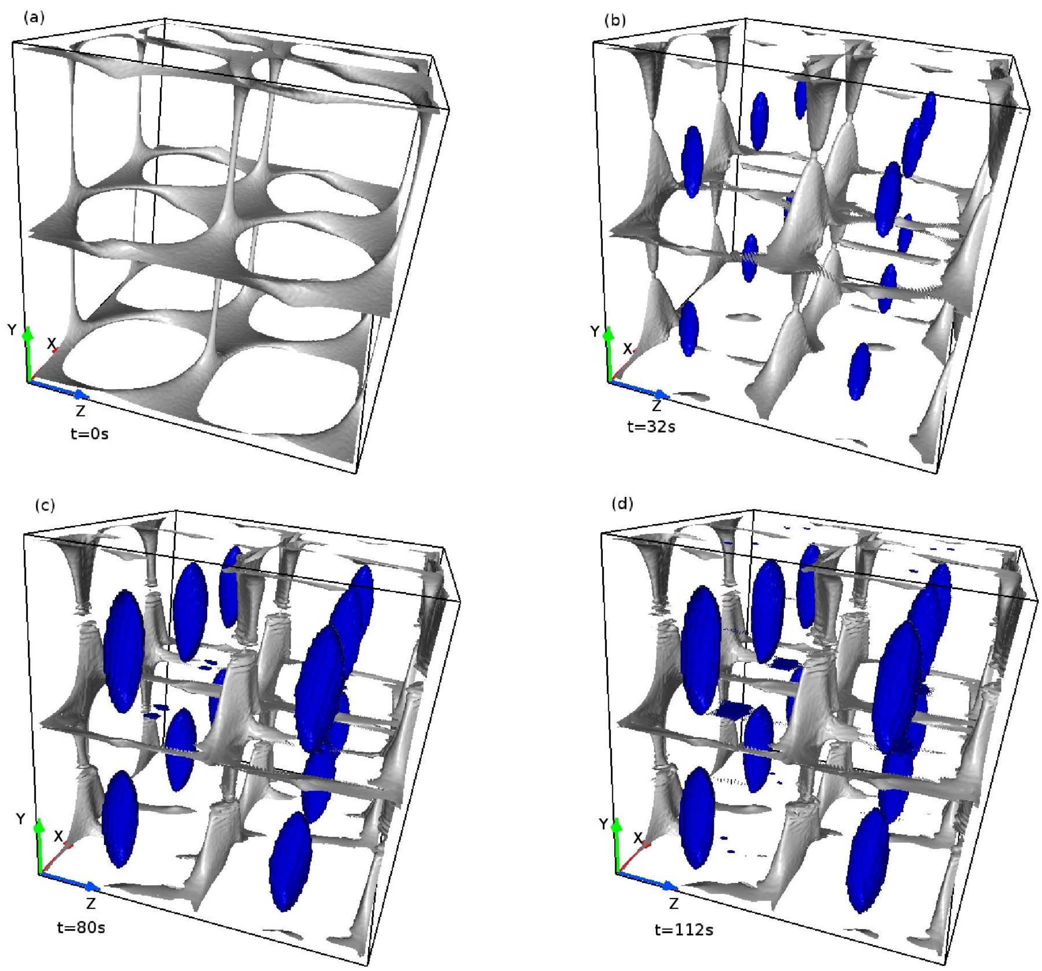

Figure 6.26: Time sequence of the isosurface $J-50$ (in blue) overlaid with magnetic nulls (in grey), for $\epsilon_0 = 0.3$. The figure illustrates the generation of two types of current structures. Based on previous case $\epsilon_0 = 0.1$, it is possible to infer that open surfaces at $y=\pi$ plane represent current sheets. While the closed elongated current structures are due to local enhancement of the magnitude of magnetic field and hence they are not current sheets.

Like the previous case, here also an enhancement in density of parallel MFLs is responsible for a local increase in magnitude of $\mathbf{J}$, leading to the formation of these closed current surfaces. More importantly, Figure 6.26 indicates a delay in the generation of CSs in comparison to the earlier case. This is expected since the initial topology of field lines for larger ϵ_0 is less favorable and hence, two oppositely directed MFLs require additional push to onset the $J-50$ surfaces. Also, the spatial extension of these CSs is lesser compared to the case I.

6.3.2.3 Case (III) $\epsilon_0 = 0.5$

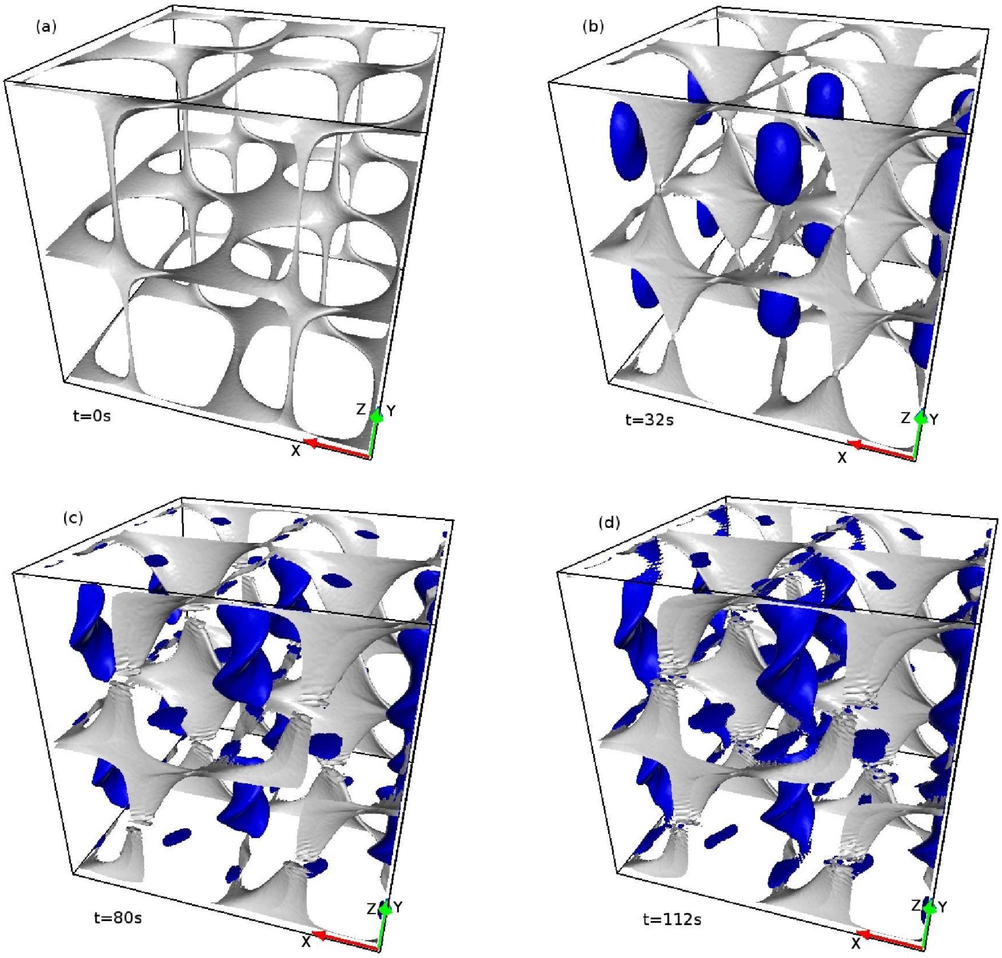

Figure 6.27: Evolution of the surface $J - 50$ (in blue) overlaid with magnetic nulls (in grey), for $\epsilon_0 = 0.5$. Noteworthy is the development of CSs away from the nulls.

With $\epsilon_0 = 0.5$, the initial favorable topology around $y = \pi$ plane is almost destroyed and the MFLs are interlaced everywhere (panel c, Fig. 6.16). The appearances of $J-50$ surface (overlaid with magnetic nulls) is depicted in Figure 6.27. The $J - 50$ surfaces start to appear around $t = 32s$ and in their initial phase of evolution are closed surfaces, suggesting a localized increase in $\mid \mathbf{B} \mid$. With time, these closed surfaces become increasingly open; generating CSs in the form of helices extended along the y direction and patches located at the $y = \pi$ plane. Importantly these CSs are located away from the magnetic nulls.

To understand this development of CSs away from the magnetic nulls, the

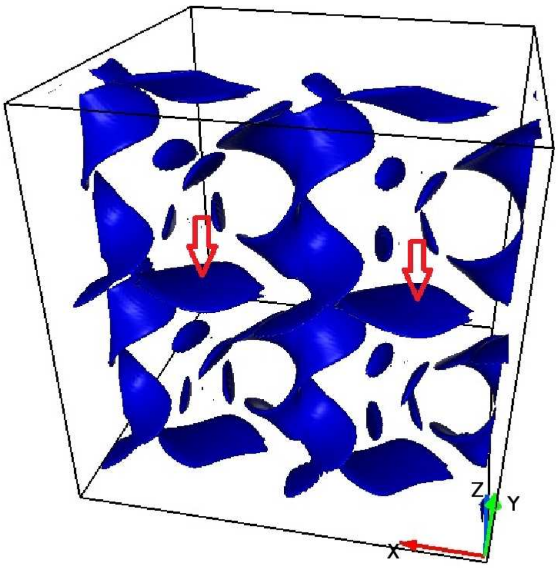

Figure 6.28: Appearance of $J_1 - 40$ surfaces at $t = 112s$ for $\epsilon_0 = 0.5$, plotted in the half computational domain with $z \in \{0, \pi\}$. The $J_1 - 40$ surfaces are comprised of helices extended along the y axis and patches (marked by downward arrows) located at the $y = \pi$ plane.

time evolution of appropriate Euler surfaces and selected isosurfaces of $\mid \mathbf{J}_1 \mid$ and $\mid \mathbf{J}_2 \mid$ is explored in the following. Considering the negative contribution from $\mathbf{J}_1 \cdot \mathbf{J}_2$, we set the optimal isovalues to 40% of the maximum of $\mid \mathbf{J}_1 \mid$ or $\mid \mathbf{J}_2 \mid$, depending on the component current density under consideration. These isosurfaces are nomneclatured as $J_1 - 40$ and $J_2 - 40$ surfaces respectively. The Figure 6.28 illustrates a snapshot of $J_1 - 40$ surfaces at the instant $t = 112s$, displayed in the half computational domain $z \in \{0, \pi\}$. Notably, the $J_1 - 40$ surfaces are also in the forms of helices and patches (marked by downward arrows), structurally similar and co-located to the $J - 50$ surfaces. This structural similarity and co-located appearance ascertains the $J_1 - 40$ surfaces to be major contributors towards the development of $J - 50$ surfaces. The helical $J_1 - 40$ surfaces originate from favorable contortions of $\psi_1 -$constant Euler surfaces, evident from the Figure 6.29. However, the patches are due to contortions of $\phi_1 -$ constant Euler surfaces near the $y = \pi$ plane (cf. Figure 6.30). Identical contortions of $\psi_2 -$constant and $\phi_2 -$constant Euler surfaces generate the corresponding $J_2 - 40$ surfaces.

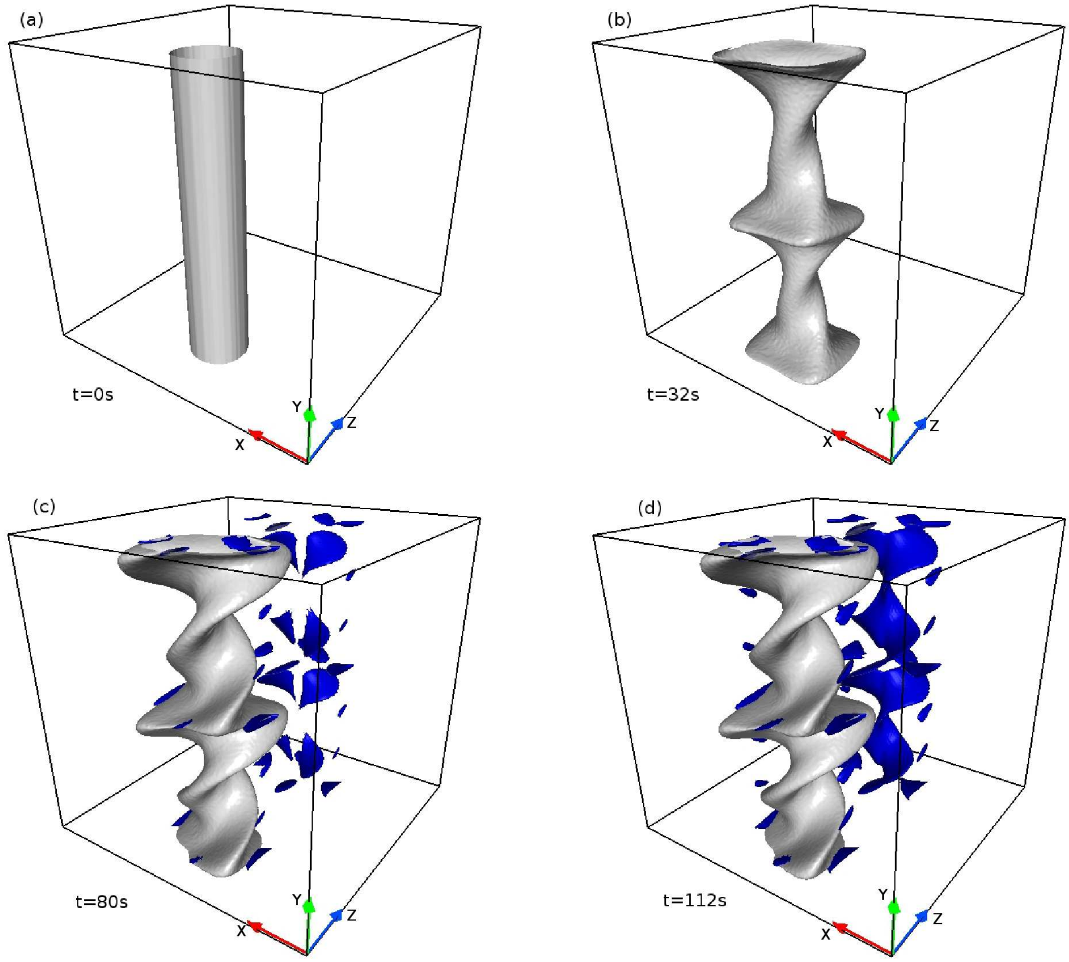

Figure 6.29: Evolution of Euler surface $\psi_1 = -0.65$ (in grey) overlaid with the $J_1 - 40$ surface (in blue), for $\epsilon_0 = 0.5$. For better visualization, the evolution is shown in the subdomain $x \in \{\frac{2\pi}{3}, \frac{4\pi}{3}\}$. Noteworthy, the $J_1 - 40$ surface is co-located with the contortion of $\psi_1 = -0.65$ surface, inferring the causality between them.

6.3.2.4 Case (IV) $\epsilon_0 = 0.7$

In this case, the initial MFLs are interlaced more strongly (panel d, Fig. 6.16). To complement the findings in Case (III), in Figure 6.31 we depict appearances of $J - 50$ surface. Evidently, these surfaces are initially closed and hence are due to local enhancements in $\mid \mathbf{B} \mid$. Later in their evolution, these surfaces become open and morphed into CSs. In comparison to the previous case, these CSs are distributed more extensively in the computational domain and hence, signify that more intensely interlaced field lines produce CSs with lesser preference for locations; a finding which is in conformity with the magnetostatic theorem.

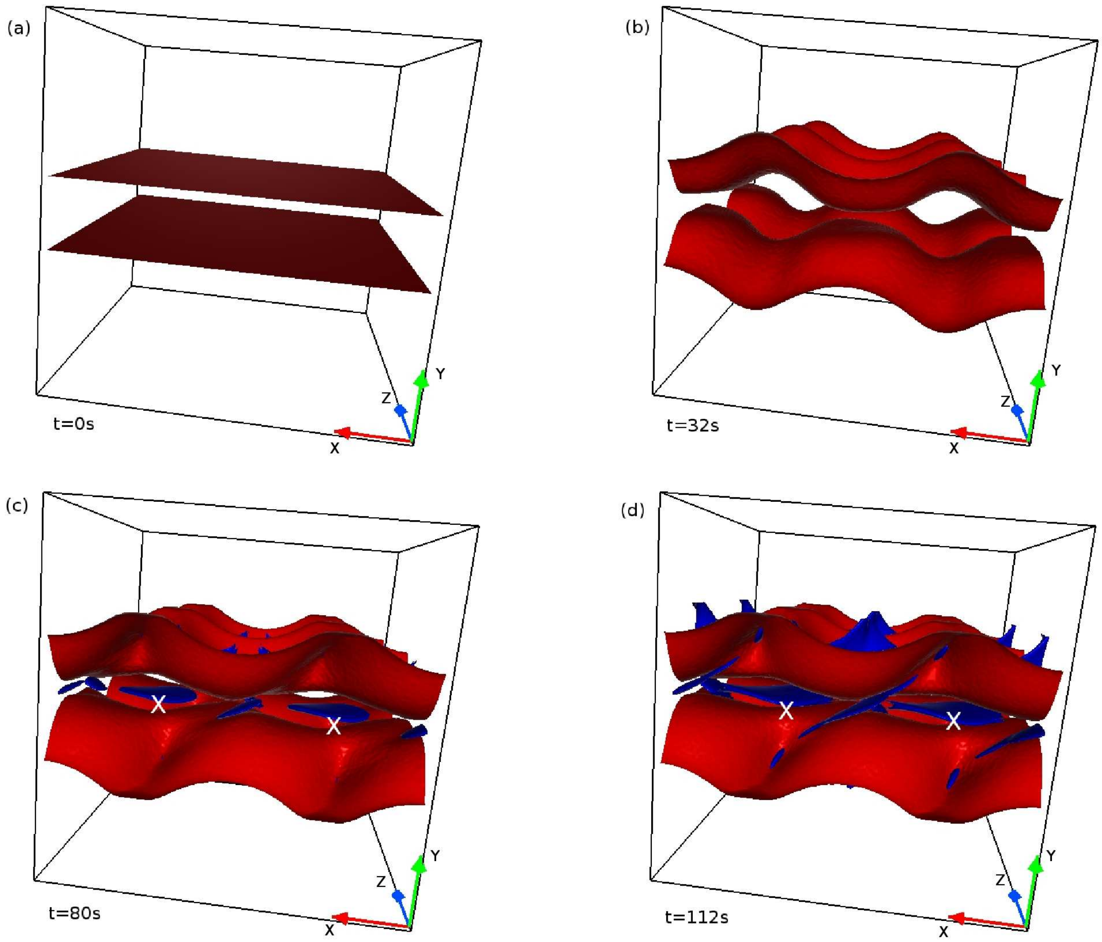

Figure 6.30: Time profile of Euler surfaces $\phi_1 = -0.60$ (in red) overlaid with the surface $J_1 - 40$ (in blue) for $\epsilon_0 = 0.5$, plotted in a selected portion of the computational domain. The two Euler surfaces depicted in the figure reside on two opposite sides of the $y = \pi$ plane. The figure identifies the development of current patches (marked by X) to favorable contortions of ϕ_1.

Figure 6.32 shows the $J - 50$ surfaces at $t = 112s$, plotted in the half computational domain. Like the previous case, these $J - 50$ surfaces can also be classified into helices and patches (marked by the upward arrows). To explain their origin, in Figure 6.33 we illustrate the corresponding $J_1 - 40$ surface at the instant $t = 112s$. The figure confirms, the helical $J - 50$ surfaces owe their origin to a development of $J_1 - 40$ surfaces. Further, Figure 6.34 relates the onset of these $J_1 - 40$ surfaces to contortions of $\psi_1 -$ constant Euler surfaces. The development of the patches is attributed to $J_2 - 40$ surfaces, as suggested by Figure 6.35 that depicts evolution of a single $J_2 - 40$ surface located at the immediate vicinity of a patch. The figure is overlaid with evolution of $\phi_2 -$ constant Euler

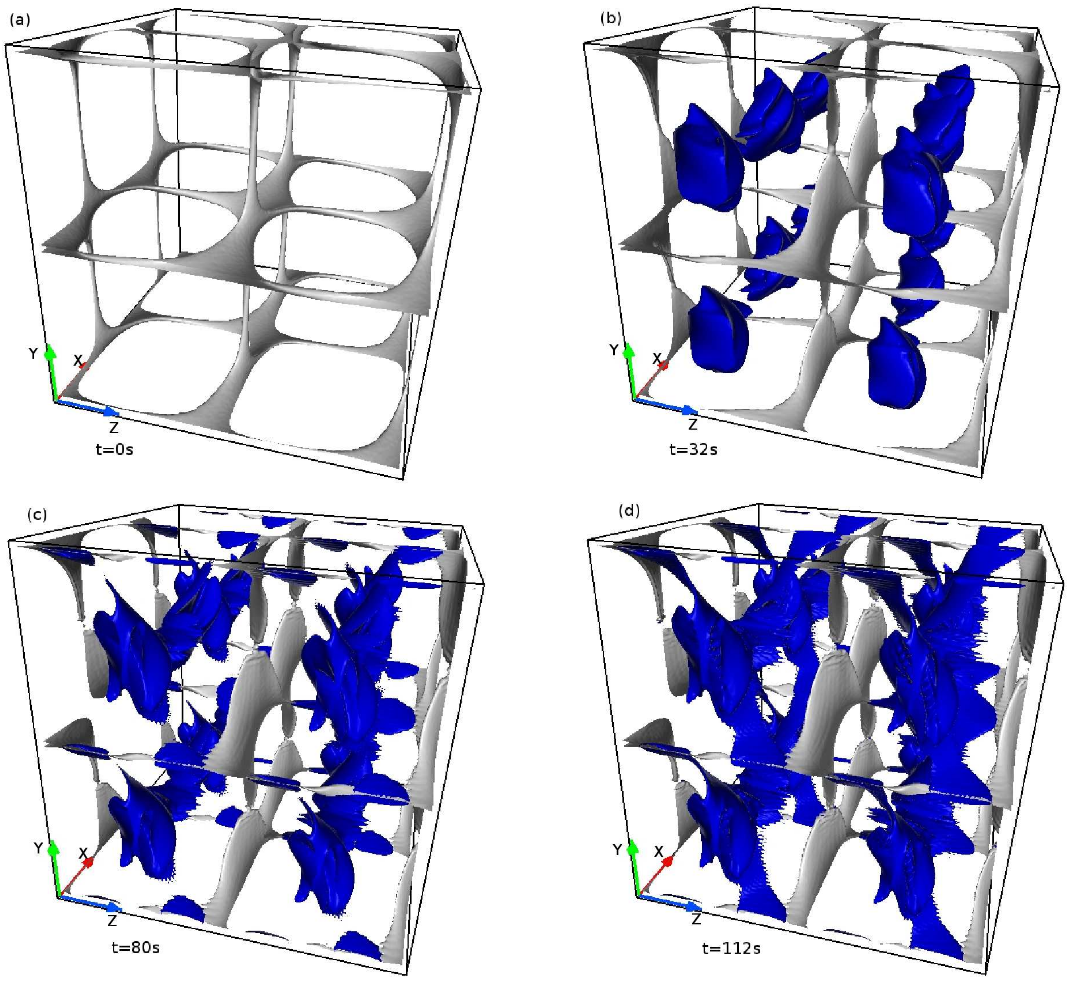

Figure 6.31: Development of the surface $J-50$ (in blue) overlaid with magnetic nulls (in grey), for $\epsilon_0 = 0.7$. The figure substantiates onset of CSs which are away from magnetic nulls and the $y = \pi$ plane. Furthermore, these CSs are distributed through out the computation volume.

surfaces co-located to the $J_2 - 40$ surface. From the figure, it is clear that the onset of $J_2 - 40$ surfaces are due to contortions of the ϕ_2-constant Euler surface.

In view of the above discussion, the comparative scaling documented in Figure 6.23, can now be put into its proper perspective. The intensity of CSs developing at favorable locations (cases I and II) have stronger scaling with resolution than the intensity of CSs that develop in absence of favorable locations (cases III and IV). In a recent work, Craig and Effenberger (Craig and Effenberger 2014) found similar comparative scaling in the scenario of CS formation at 3D nulls against CS formation at quasi-separatrix layers. The QSLs are regions where the magnetic connectivity between a pair of boundaries changes drastically (cf.

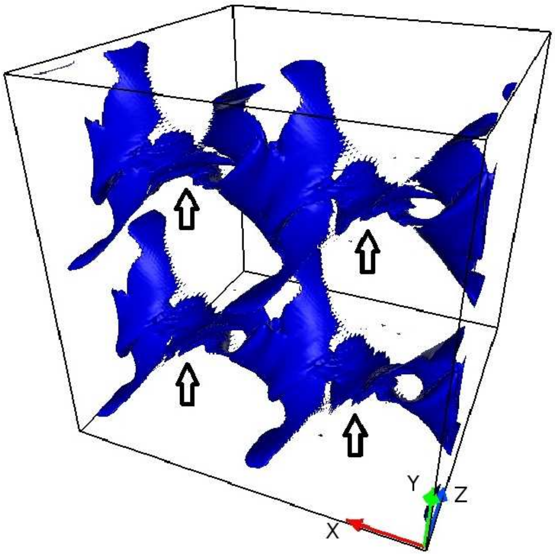

Figure 6.32: A snapshot of the $J - 50$ surfaces at $t = 112s$, for $\epsilon_0 = 0.7$. The surfaces are plotted in the half computational domain with $z \in \{0, \pi\}$. From the figure, evident are the helical CSs extending along the y axis and the current patches (marked by upward arrows) tangential to y-constant planes.

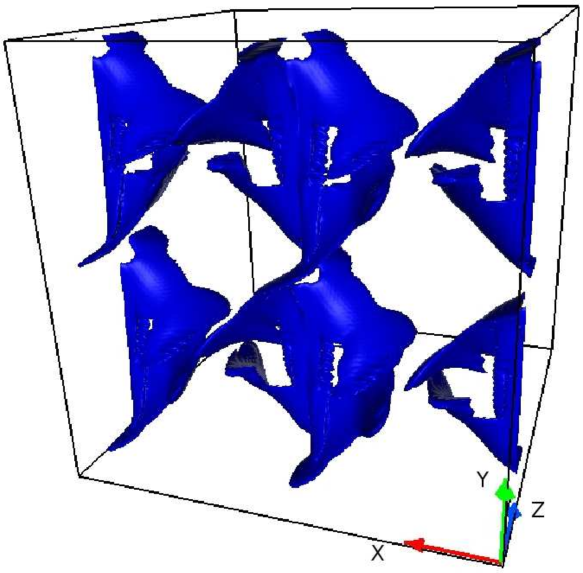

Figure 6.33: Appearances of $J_1 - 40$ surface at $t = 112s$ for $\epsilon_0 = 0.7$, depicted in the half computational domain with $z \in \{0, \pi\}$. The $J_1 - 40$ surfaces are elongated along the y axis.

chapter 4). Along with separators (Galsgaard and Nordlund 1997; Stevenson et al. 2015), QSLs are known to be the sites, away from nulls, where CSs can develop (Craig and Effenberger 2014; Aulanier et al. 2005). It is then imperative

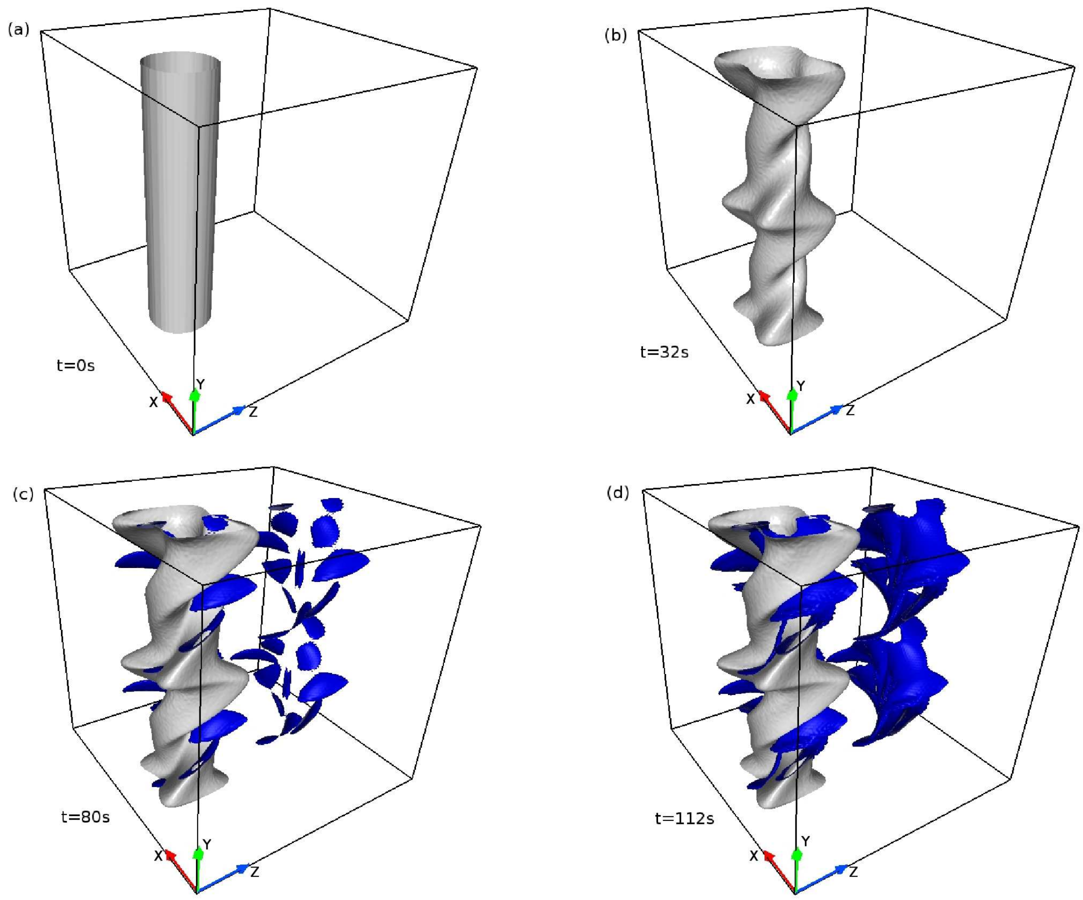

Figure 6.34: Evolution of Euler surfaces $\psi_1 = -0.60$ (in grey) overplotted with the surface $J_1 - 40$ (in blue) for $\epsilon_0 = 0.7$, shown in the computational domain with $x \in \{\frac{2\pi}{3}, \frac{4\pi}{3}\}$. The figure indicates contortions of ψ_1-constant Euler surfaces to be responsible for onset of the helical $J_1 - 40$ surfaces.

to seek QSLs in $\mathbf{B}$ and their relation to CS formation.

In Figure 6.36, we plot MFLs at the immediate vicinity of a helical CS for $\epsilon_0 = 0.5$. The plots are for instants $t = 0s$ and $t = 112s$. The figure documents the connectivity of two sets of MFLs (in colors red and cyan) connecting plane C with planes D and E. The different connectivities of the two sets are evident from the figure. With CS (marked in color blue) being co-located with the layer where the connectivity changes, existence of QSL structures containing the CS is suggested. A comparison between the two instants further reports MFLs to get more helical with development of the CS, indicating causality between the favorable contortions and the dynamics of QSLs.

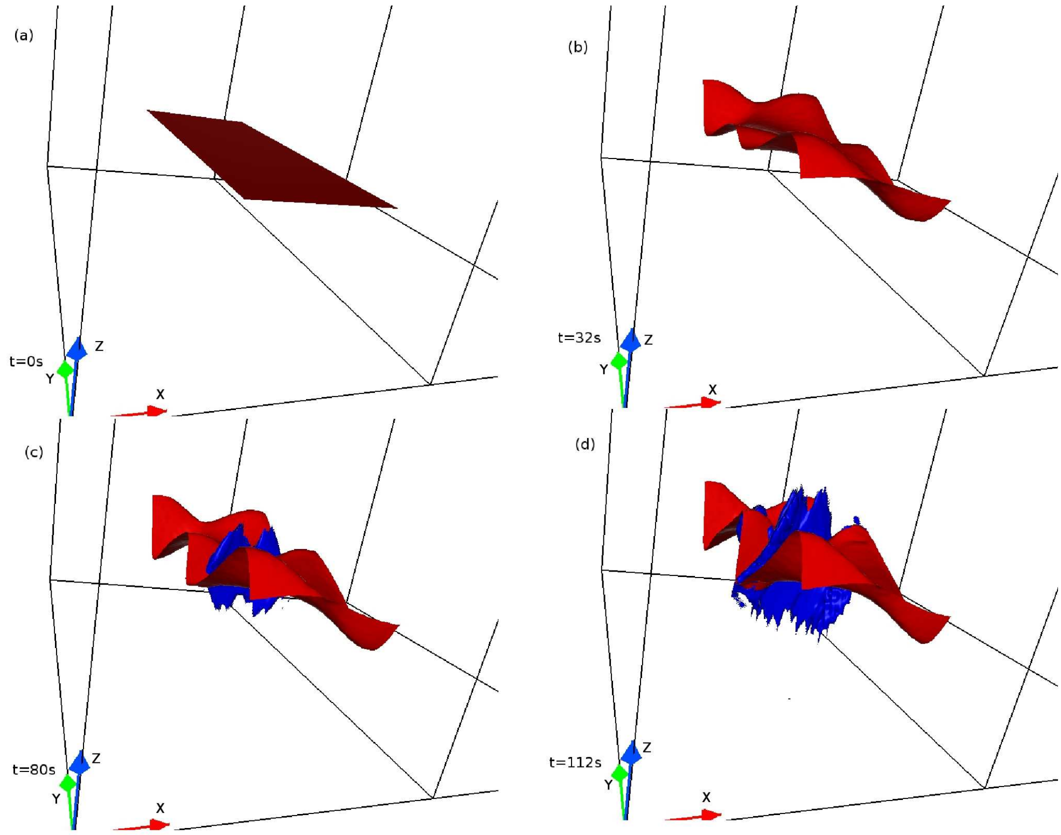

Figure 6.35: Evolution of Euler surfaces $\phi_2 = 0.05$ (in red) overlaid with the surface $J_2 - 40$ (in blue) for $\epsilon_0 = 0.7$. The figure indicates, contortions of the ϕ_2-constant surfaces are responsible for developing the patches of $J_2 - 40$ tangential to y-constant planes.

6.4 Summary

In this chapter we present two separate sets of numerical experiment, aiming to explore the spontaneous development of current sheet and to assess the role of intensity of field lines interlacing in the development. For the purpose, we formulate relevant initial value problems. For simplicity, the computational domain is of Cartesian geometry with periodic boundaries. From the magnetostatic theorem such CS formation is unavoidable in an equilibrium magnetofluid with interlaced magnetic field lines. To be in conformity with the analytical requirements for generation of CSs, we utilize the viscous relaxation of an incompressible, infinitely electrical conducting magnetofluid. The relaxation provides a terminal quasi-steady state which is identical in magnetic topology to the initial non-equilibrium state. The uniqueness of presented computations is

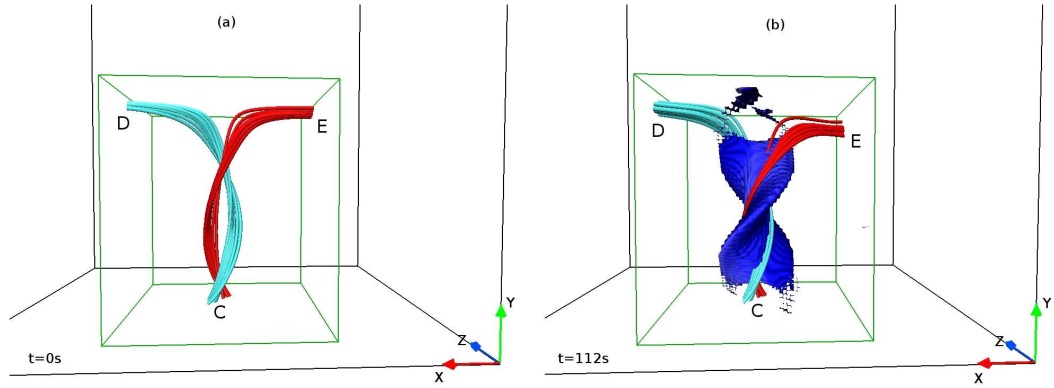

Figure 6.36: Two sets of MFLs (colored red and cyan) $\mathbf{B}$ overlaid with the $J-50$ surfaces (in blue) at $t = 0s$ and $t = 112s$, for $\epsilon_0 = 0.5$. The bifurcation of the MFLs, with the red set connecting the planes C and E and the cyan set connecting the planes C and D, documents a change in field line connectivity. The appearances of CS (in blue) co-located to the layers across which the MFLs bifurcate, suggest the presence of QSL structures in $\mathbf{B}$. Additionally, the MFLs at $t = 112s$ (with the CS fully develop) are more helical compared to the MFLs at $t = 0s$ (in absence of CS); indicating a causal connection between the favorable contortions and the dynamics of QSLs.

in its advection of magnetic flux surfaces for the initial twisted magnetic fields. In both the sets, the flux surfaces are advected by using the numerical model EULAG-EP. The accuracy of corresponding advection scheme MPDATA ensures the preservation of the initial magnetic topology during the computations.

For the first experiment, initial field is constructed from a linear force-free field. This construction is based on the understanding that the magnetic topology of the lfff is complex enough in terms of interlaced magnetic field lines and the presence of 2D and 3D nulls. In this work, we present both indirect and direct evidences of CS formation. The plots of the total average current density and the total maximum current density show tendency to increase with time but also lack monotonicity. We attribute this lack of monotonicity to the flipping of directions in component current densities relative to each other. Realizing the vector nature of $\mathbf{J}$, the observed monotonic increase in every component current density is indicative of CSs formation. It is also found that the process of CSs formation is sensitive to viscosity. For the same initial Lorentz force, the CSs are forming earlier in time for less viscous magnetofluid as is evident from all the current density plots. This is in agreement with the physical expectation.

A key finding of the experiment I is in its demonstration of CS formation away from the magnetic nulls. The corresponding dynamics is explored by analyzing the evolution of MFSs. The analysis confirms that the MFSs contort in such a way that portions of the same flux surface having oppositely directed field lines come close to each other and thereby increase the gradient of magnetic field. This increased gradient of magnetic field is then responsible for the observed CS formation away from the magnetic nulls. Notably, these computations provide two important insights for a complete interpretation of CS formation in an evolving magnetofluid. First, any parameter related only to the magnitude of volume current density (for example, $\mid \mathbf{J} \mid_{max}$ and $<\mid \mathbf{J} \mid>$) is not enough to determine CS formation. In context to our simulations, it is the component current densities that show a monotonic rise whereas the $\mid \mathbf{J} \mid_{max}$ and $<\mid \mathbf{J} \mid>$ develop intermediate peaks. This is expected since a CS formation or the equivalent sharpening of magnetic field gradient is a quality of the vector $\mathbf{J}$ or $\mathbf{B}$ but not its magnitude alone. Second, the CSs may also develop away from the magnetic nulls as apprehended in the optical analogy proposed by Parker. Recognizing the importance of MFSs in the optical analogy, computations utilizing a flux surface representation of magnetic field can be more effective in determining the definitive process through which such CSs develop. In our case, we find this process to be the contortions of magnetic flux surfaces in a way favorable to CS formation. Additionally, these contortions are found to be in general agreement with Parker's conclusion that streaming magnetic field lines exclude a region where the amplitude of the magnetic field is intense.

After successfully demonstrating the development of current sheets, next we aim to study the properties of current sheets. For the purpose, in the experiment II we derive the suitable initial magnetic field by superposing two untwisted fields, where each field is represented by a pair of global magnetic flux surfaces. The magnetic field lines of the superposed field are interlaced and the intensity of interlacing increases with the relative amplitude ϵ_0 of the component fields. The particular initial field used here, enables us to divide the magnetic topology into two broad categories: one with favorable MFL geometry having complementary field lines directed anti-parallel to each other across the $y = \pi$ plane; and the other with interlaced field lines without any such favorable geometry. In this experiment also, the overall tendency to form CSs is confirmed by the history of component average current densities for different ϵ_0. To identify the locations of CSs in the computation domain and obtain a detail understanding, utilizing experience gained from the experiment I, we analyze the evolution of isosurfaces of total current density having sufficiently high value. For smaller ϵ_0 (i.e. for ϵ_0=0.1 and 0.3), the analyzes establish generation of CSs at the $y = \pi$ plane which is location favorable to CS development. With an increase of ϵ_0, this favorable topology of field lines gets destroyed. For larger ϵ_0 (i.e. for ϵ_0=0.5 and 0.7), additional CSs appear which are located away from the $y = \pi$ plane and the magnetic nulls. Further analysis identifies the origin of these CSs to favorable contortions of co-located magnetic flux surfaces. Noteworthy are the insights gained on the relation between the intensity of interlacing and the onset of CSs. We have demonstrated that a magnetic field with less interlacing develop CSs at locations where such development is topologically favorable. Also these CSs are localized at the immediate neighborhood of the favorable location. In contrast, for more interlaced field lines the CSs develop away from magnetic nulls or any such topologically favorable sites. Further, the CSs being distributed throughout the volume with spatial extensions that increase with intensity of interlacing, their development supports the magnetostatic theorem to its full generality. The onset of CSs are further found to be near possible QSLs and related to their dynamics.

Altogether, the computations reported here substantiate and extend the magnetostatic theorem by relating the intensity of MFL interlacing to the spatial distribution of CSs and identifying MFS contortions as the rationale behind the onset of CSs away from the favorable locations. The contortions are related to possible QSL structures which, provides a basis to extend the EP based computations to the solar corona. Combined with the scenario of secondary CS development which, in general, increases the topological complexity; the findings of the presented works point towards the ubiquity of CSs in a high R_M magnetofluid. To relate this ubiquity to observation, it is crucial to include field line topologies similar to the coronal loops along with magnetic reconnections, and this warrants a separate study which we present in the next chapter.

Chapter 7

Initial Value Problems: Magnetic Reconnections

7.1 Introduction

The simulations presented in the previous chapter, being congruent with the magnetostatic theorem, demonstrate the spontaneous development of current sheets. These simulations attribute the appearance of CSs to favorable contortions of magnetic flux surfaces, generic to dynamics of high R_M (equivalently S) magnetofluids. In presence of an otherwise negligible magnetic diffusivity, as in astrophysical magnetofluids, the CS is dissipated by magnetic reconnection. Once the CS is decayed, the magnetic field lines are once again tangential to other fluid surfaces and their contortions may lead to second generation of CSs and reconnections. These two complementary processes, the development of CSs and the following relaxation through MRs is then expected to be continued until the magnetic energy achieves an allowable lower bound. In the Taylor's theory of relaxation, this lower bound of the magnetic energy is determined by an approximate preservation of magnetic helicity. Hence, a single reconnection can initiate consecutive secondary MRs, intermittent in space and time, which may shape up the dynamics of high R_M magnetofluids. In a recent computational study (Kumar et al. 2015a) a scenario was explored, where repeated reconnections were identified as a cause for generating various magnetic structures, some duplicating magnetic antics of the Sun.

Towards realizing the above scenario in solar corona, we note that hard X-ray coronal sources are standardly accepted as signatures of magnetic reconnection in solar flares (Krucker et al. 2008). High resolution measurements show multiple peaks of non-thermal nature in flare's time profile, which suggest the corresponding energy releases and hence, the underlying reconnections, to be episodic (Joshi et al. 2011). Recent observations at multiple channels (hard X-ray and extreme ultraviolet) reveal intense localized brightenings to occur below an ascending flux-rope (Cheng et al. 2011; Kushwaha et al. 2015) which indicate a causal connection between MRs (occurring beneath the rope) and the ascend (Cho et al. 2009; Cheng et al. 2011).

In the above perspective, the objective of this chapter is to first numerically establish the scenario of repeated reconnections by demonstrating the development of secondary current sheets and, then to clarify whether repeated reconnections can provide a standalone autonomous mechanism to govern the dynamics of an observable magnetic structure. For the purpose, in this chapter, we perform two different sets of numerical experiment. The first set aims to demostrate the process of secondary CSs formation while, the second set targets to scrutinize the importance of repeated reconnections in engendering the observable magnetic structures in the solar corona. To ensure the spontaneous generation of reconnections, we simulate the viscous relaxation (cf. chapter 6) of an incompressible magnetofluid with infinite electrical conductivity for both the sets. The simulations are performed by using the numerical model EULAG-MHD which advects the vector magnetic field in lieu of magnetic flux surfaces. Notably, as thickness of the developing CSs falls below the selected grid resolution, scales become under-resolved. The non-oscillatory advection scheme MPDATA then filters out these under-resolved scales by generating an intermittent and adaptive residual dissipation which facilitates the model to perform ILESs. The computations reported are in the spirit of ILESs where simulated magnetic reconnections, being intermittent in space and time, mimic physical reconnections in high R_M magnetofluids.

For the first set of experiment, as a suitable initial magnetic field, we reconsider the magnetic field **B** described in the subsection 6.2.1 of the previous chapter, since it successfully manifests the generation of CSs. In the section 6.2, **B** was represented in terms of MFSs to directly visualize physical process responsible for spontaneous development of CSs. This approach provides important insights about the definitive process which leads to origin of such CSs. But the MFS representation being only valid until CS formation, the dissipation of these CSs and possibility of secondary CSs formation could not be explored. In the present work, the advection of vector magnetic field enables us to examine the decay of first generation CSs (via MRs) and the subsequent dynamics. The simulations performed evince the formation of secondary CSs near two-dimensional and three-dimensional magnetic nulls as well as in absence of the nulls after the decay of first generation of CSs which develop away from the nulls (section 6.2).

Whereas for the second set of experiment, we consider the initial magnetic field with loop-like topology similar to the observed solar coronal loops. The computations illustrate the complete evolution of a flux-rope in terms of its creation from initial bipolar field lines and continuous ascend, mediated via the common process of repeated reconnections. This contrasts with the contemporary simulations of flux-ropes that judiciously precondition rope evolution—either by specifying preexisting twisted magnetic structures that emerge from below the photosphere (Fan and Gibson 2003; Fan 2001, 2010, 2011), or by forcing magnetic reconnections inside a sheared arcade with select (shearing and/or converging) initial flows (van Ballegooijen and Martens 1989; Choe and Lee 1996; Amari et al. 1999, 2003; Aulanier et al. 2010; Xia et al. 2014). While the present work also explores MRs inside sheared arcades, the computations being in agreement with the magnetostatic theorem generate spontaneous reconnections which provide an autonomous mechanism to govern dynamics of any high R_M magnetofluid. The novelty of this work is in its approach to establish creation and activation of a physically realizable flux-rope as a consequence of the autonomous mechanism. Introspectively, such a rope has the flavor of a self-organized state (Kusano et al. 1994).

In computations presented in this chapter, selections of the parameter set are based on the requirement to obtain fast and efficient dynamics which develops secondary CSs and subsequent reconnetions at minimal computational expense. The rest of the chapter is organized as follows. Section II discusses the results of simulations done for the first set of numerical experiment which utilizes initial value problem given in the subsection 6.2.1. Section III is dedicated to initial value problem and results for the second set of numerical experiment having initial field lines geometry identical to the coronal loop. In section IV, we summarize results of both the sets and highlight important findings.

7.2 Numerical experiment I

7.2.1 Results

The computations are performed on the $128 \times 128 \times 256$ grid resolving the domain $[0, 2\pi]\times[0, 2\pi]\times[0, 6\pi]$, respectively, in x, y and z. The selected parameter set is $[\nu = 0.0045,\ \rho_0 = 1,\ B_0 = 6,\ L_0 = 6\pi]$. The set leads to $\tau_a \approx 11s$ and $\tau_\nu \approx 7.8 \times 10^4 s$.

To develop an overall understanding of the simulated viscous relaxation, in Figure 7.1, we plot the time profile of normalized kinetic energy. As the initial Lorentz force pushes the magnetofluid from rest, kinetic energy rises at the expense of magnetic energy and this rise gets arrested by viscosity, resulting in the peak of kinetic energy appearing at $t = 4s$. Also to be noted is the existence of four more distinct peaks centered at $t = 12s$, $t = 20s$, $t = 100s$, and $t = 140s$ in the kinetic energy curve.

To identify and locate onset of CSs, in Figure 7.2 we display isosurfaces of $\mid \mathbf{J} \mid$ with an isovalue which is 40% of maximum current density $\mid \mathbf{J} \mid_{\max}$ at instance $t = 8s$. The appearances of isosurfaces (overlaid with magnetic nulls) show the development of CSs away from the nulls and distributed throughout the volume, confirming results presented in the previous chapter. The consequent MRs generate flow which is dissipated by viscous drag, explaining the peak in kinetic energy at $t = 12s$. Figure 7.3 shows evolution of MFLs in the

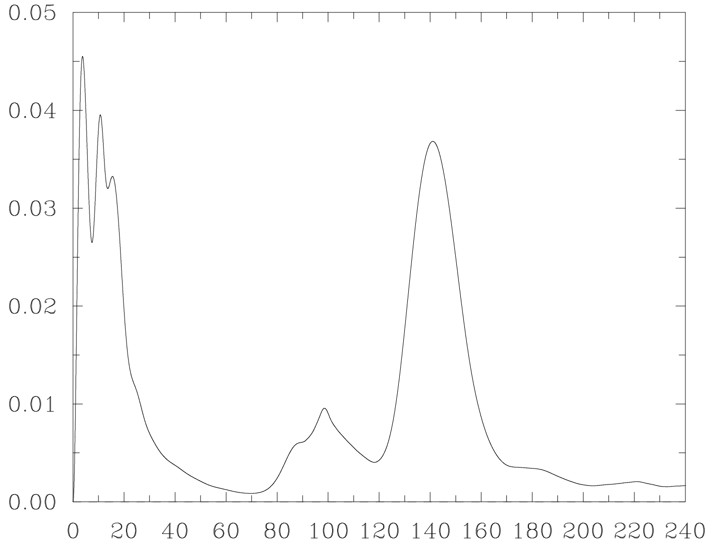

Figure 7.1: The evolution of kinetic energy, normalized to initial total (kinetic+magnetic) energy. The abscissa represents time and the ordinate is the energy. The five distinct peaks at $t = 4s$, $t = 12s$, $t = 20s$, $t = 100s$, and $t = 140s$ are evident.

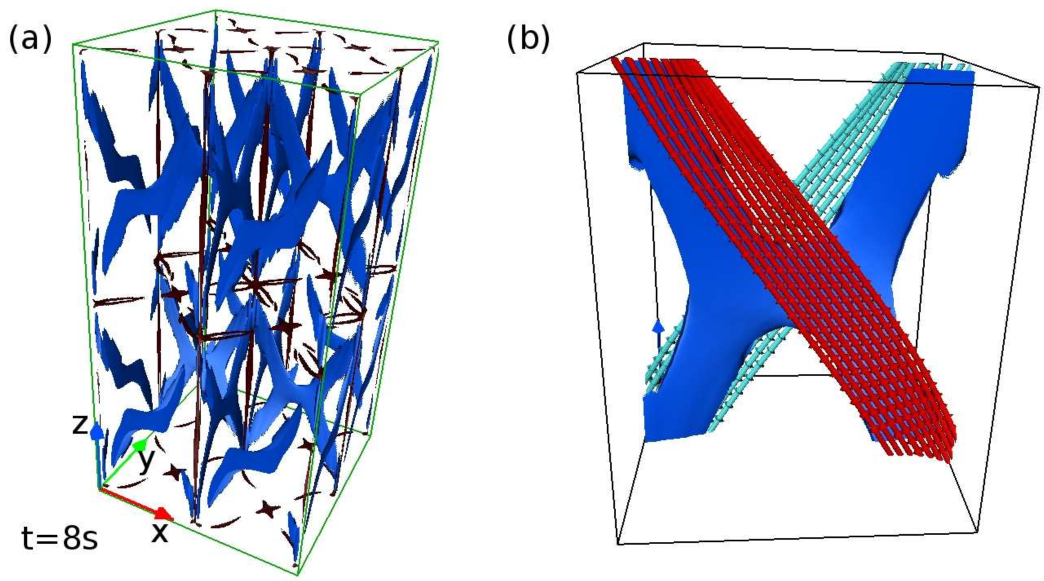

Figure 7.2: Panel a shows isosurfaces of $\mid \mathbf{J} \mid$ (in blue) having a magnitude of 40% of the $\mid \mathbf{J} \mid_{\max}$ at $t = 8s$. The panel is overplotted with magnetic nulls (in color maroon), highlighting formation of CSs away from nulls and distributed throughout the computational volume. Panel b shows MFLs in the locality of such a CS. Noticeably, the MFLs across the CS are misaligned by an angle around 90°.

neighborhoods of X-type nulls located at $(x, y, z) = (\pi, \pi, 2.64\pi)$, $(\pi, \pi, 3\pi)$, and $(\pi, \pi, 3.36\pi)$. Noticeably, the MFLs in $z = 3\pi$ plane become concave towards the point $(x, y, z) = (\pi, \pi, 3\pi)$, generating a void depleted of MFLs (marked by R in panel b). Consequently, parts of two complementary anti-parallel MFLs from the opposite sides of the $z = 3\pi$ plane, are dragged (along z) into this void and develop a CS. The scenario is in general agreement with Parker's optical analogy. The decay of this CS and the corresponding viscous arrest, lead to the kinetic energy peak at $t = 20s$. Also the X-type nulls reappear after the decay.

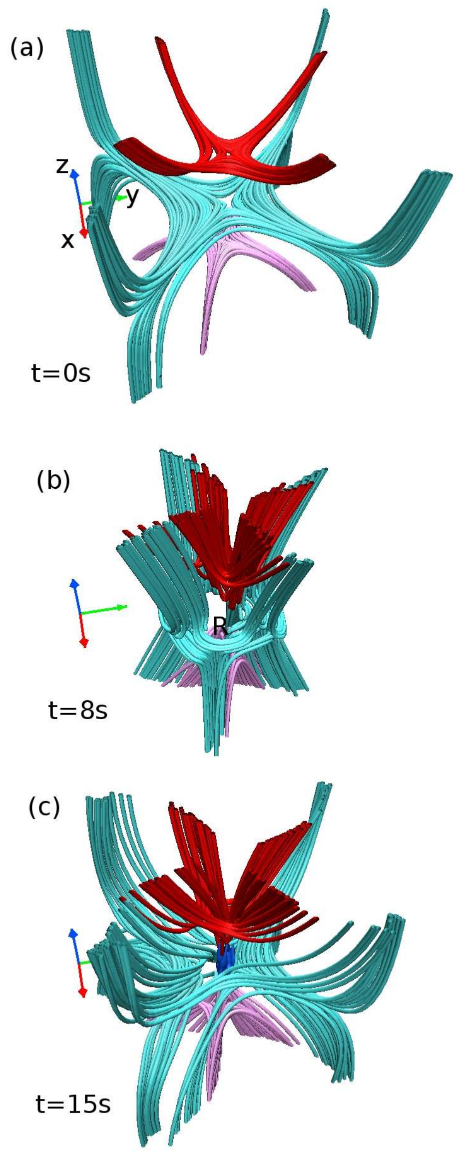

Figure 7.3: Evolution of MFLs in neighborhoods of X-type nulls situated at $(x, y, z) = (\pi, \pi, 2.64\pi)$, $(\pi, \pi, 3\pi)$, and $(\pi, \pi, 3.36\pi)$, depicted in colors magenta, cyan and red respectively. The plots are overlaid with $|\ \mathbf{J}\ |$ isosurface (in blue) at 40% of its maximum in the neighborhoods. Important are the emergence of MFLs depleted zone in $z = 3\pi$ plane (symbolized by R in panel b) and consequent CS formation (panel c).

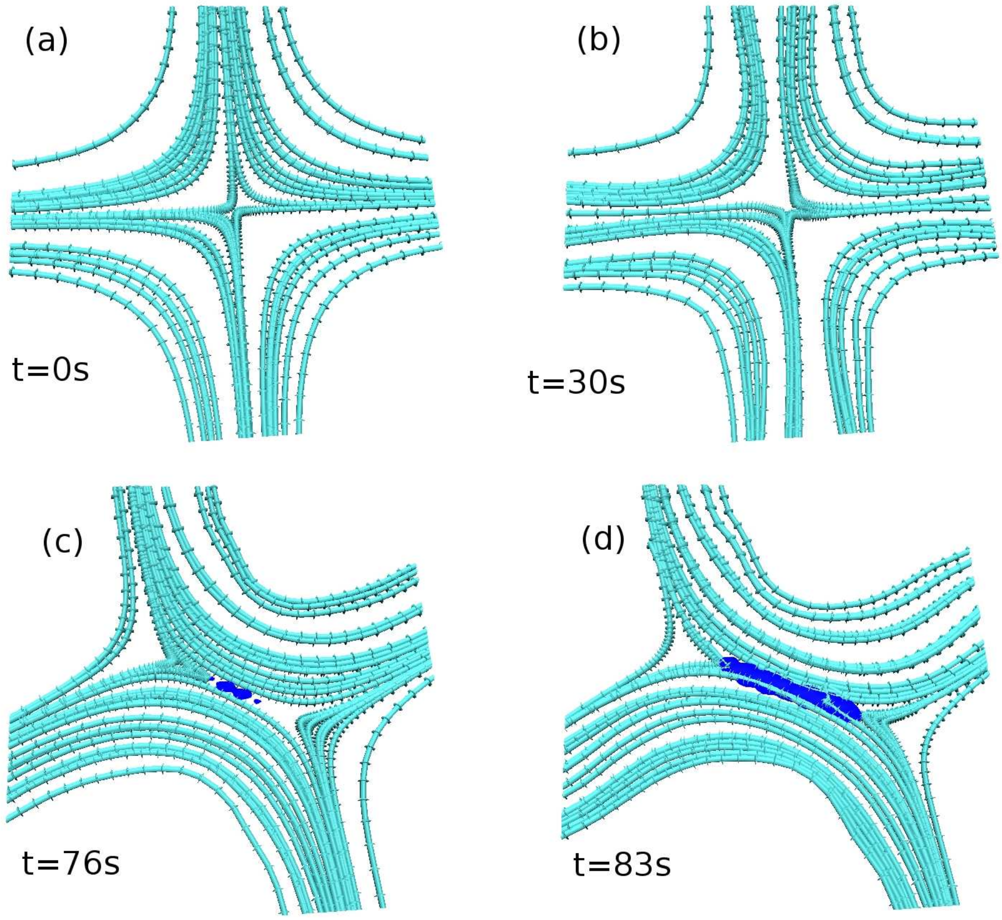

Figure 7.4: History of MFLs in the vicinity of an X-type null situated at $(x, y, z) = (\pi, \pi, 3\pi/2)$, overplotted with isosurface of $\mid \mathbf{J} \mid$ at 40% of $\mid \mathbf{J} \mid_{\max}$ in the vicinity. Noteworthy is the generation of an extended CS along with two Y-type nulls.

To explore the subsequent dynamics, in Figure 7.4 we illustrate the evolution in the neighborhood of an X-type null which is situated at $(x, y, z) = (\pi, \pi, 3\pi/2)$. Notably, the X-type null gets squashed and generates an extended CS along with two Y-type nulls at $t = 83s$. Figure 7.5 shows time profile of MFLs in the vicinity of a 3D null. Important is the loss of fan and spine structures central to a 3D null. The collapse brings non-parallel MFLs in close proximity resulting in CSs at $t = 90s$. The collective decay of CSs, near X-type and 3D nulls, engender the kinetic energy peak at $t = 100s$. With all 2D and 3D nulls destroyed, the subsequent relaxation ranging from $t \in \{120s, 240s\}$ develops next generation of distributed CSs (Figure 7.6), having geometry similar to the ones which appear at $t = 8s$ (Fig. 7.2) but with different spatial distribution. Such

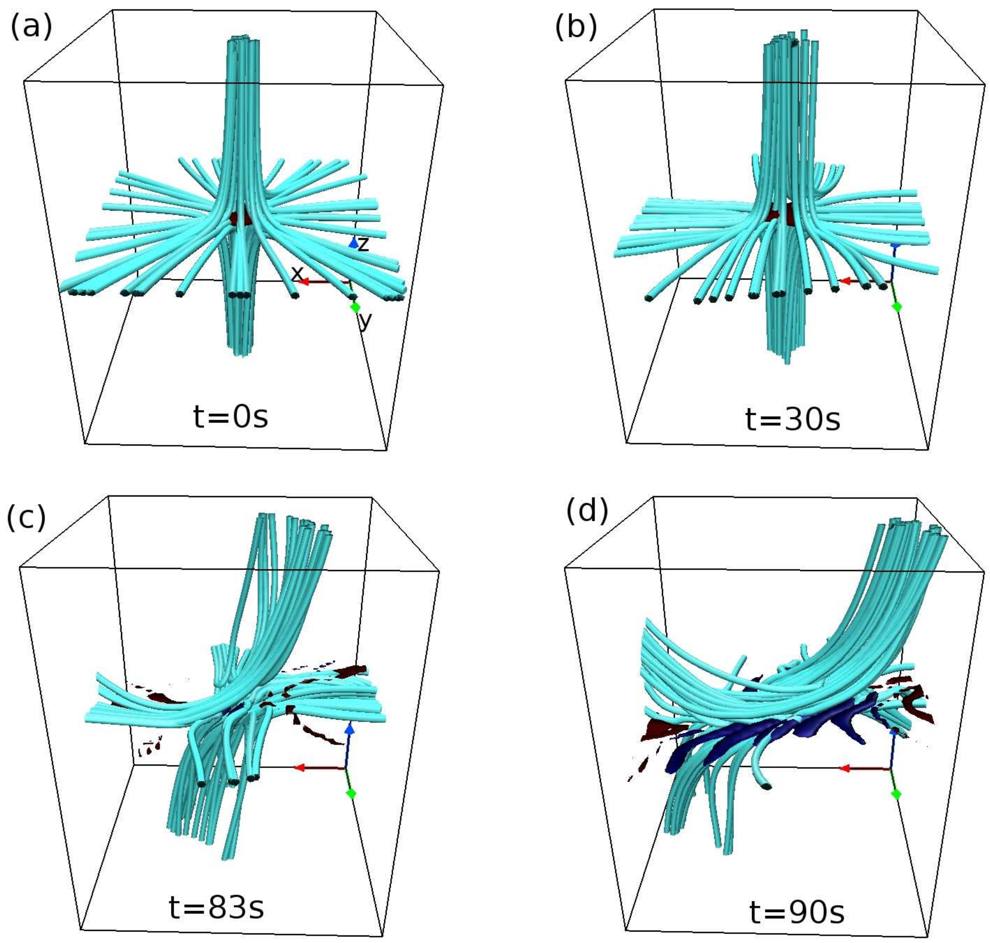

Figure 7.5: Time sequence of MFLs in the immediate neighborhood of a representative 3D magnetic null situated at $(x, y, z) = (\pi/2, \pi/2, 3\pi)$ in their important phases of evolution. The plots are further overlaid with current density isosurfaces (in blue) at 40% of its maximum value in the neighborhood. Noticeable is the development of CSs by the collapse of fan and spine structures of the 3D null.

spontaneous development of CSs in absence of any topologically favorable sites further supports the magnetostatic theorem. The decay of these distributed CSs explain the last peak in kinetic energy at $t = 140s$.

Based on the above analysis, the CSs can broadly be classified into three categories. The first one corresponds to the distributed CSs that develop away from the nulls or in absence of the nulls (Fig. 7.2). The second consists of the CSs originating around 2D nulls (Fig. 7.3 and Fig. 7.4). The CSs created by the collapse of 3D nulls fall into the third category (Fig. 7.5). To explore the features associated with these three types of CSs, we carry-out additional

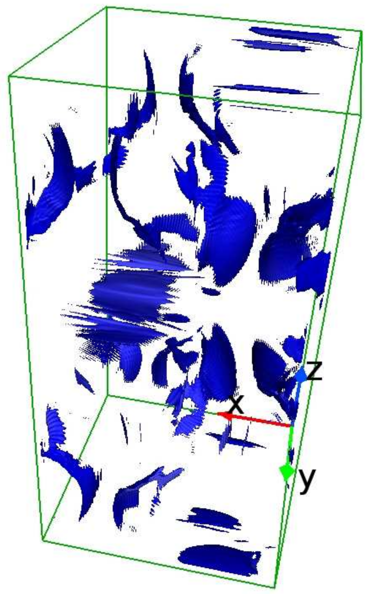

Figure 7.6: Figure depicts isosurfaces of $|\mathbf{J}|$ (in blue) having a magnitude of 40% of the $|\mathbf{J}|_{\max}$ at $t = 130s$, documenting the development of the next generation of distributed CSs in absence of any magnetic null.

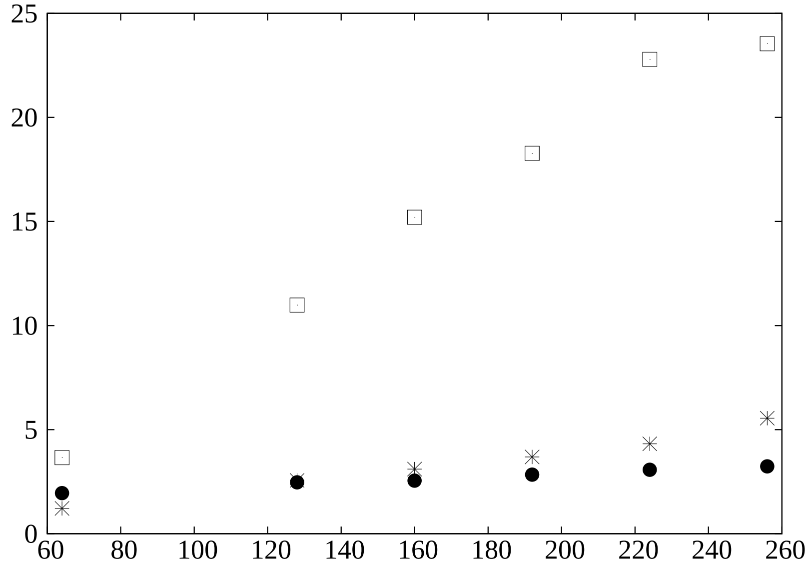

Figure 7.7: Scaling of $|\mathbf{J}|_{\max}$ with resolution, for the CSs near 2D nulls at $t = 83s$ (squares), 3D nulls at $t = 90s$ (stars), and away from these nulls at $t = 8s$ (dots). The abscissa is grid resolution along z whereas the ordinate is $|\mathbf{J}|_{\max}$. The plot illustrates a strongest scaling for the CSs near 2D nulls.

computations on different sized grids — $32 \times 32 \times 64$, $64 \times 64 \times 128$, $80 \times 80 \times 160$, $96 \times 96 \times 192$, and $112 \times 112 \times 224$. Figure 7.7 documents scaling of peak current density $|\mathbf{J}|_{\max}$ with resolution, for the CSs depicted in Figures 7.2, 7.4 and 7.5

as the representative cases. The figure confirms that the CSs near 2D nulls have strongest scaling compared to the CSs near 3D nulls or the distributed ones. In addition, the figure also reveals the $|\mathbf{J}|_{max}$ to be larger for the CSs around 2D nulls than the other types of CSs. This difference in $|\mathbf{J}|_{max}$ can be attributed to the angle by which the MFLs are misaligned across a CS. For instance, the MFLs are misaligned by the angle 180° for a CS around 2D null (panel d, Fig. 7.4). While the angle is much less than 180° for a CS which generates away from the nulls (panel b, Fig. 7.2).

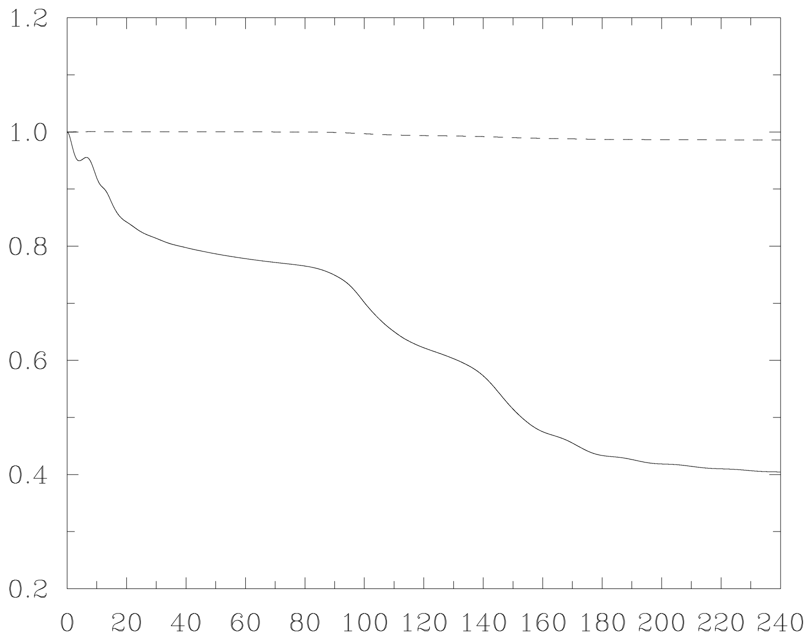

Figure 7.8: History of, magnetic energy (solid line) and magnetic helicity (dashed line) normalized to their initial values. The abscissa is time while the ordinate represents the energy and helicity. The observed small variation in magnetic helicity ($\approx 2\%$) compare to the large variation in magnetic energy ($\approx 60\%$) points towards an approximate preservation of magnetic helicity during reconnections.

To make direct contact with general understanding of MHD relaxation, in Figure 7.8 we show the evolution of magnetic energy and global magnetic helicity normalized with their initial values. We employ the Coulomb gauge to calculate vector potential for the magnetic helicity calculation. The figure shows a reduction in magnetic energy which is $\approx 60\%$ from its initial value. In comparison, magnetic helicity is decreased only $\approx 2\%$ from its initial value, documenting the approximate preservation of magnetic helicity which matches with the general understanding.

7.3 Numerical experiment 2

7.3.1 Initial value problem

To construct an initial magnetic field with field-line topology similar to coronal loops, we choose $\mathbf{B}(\mathbf{r}, t = 0)$ with the corresponding components

$$B_x = k_z \sin(k_x x) \exp\left(-\frac{k_z z}{s_0}\right), \tag{7.3.1}$$

$$B_y = \sqrt{{k_x}^2 - {k_z}^2} \sin(k_x x) \exp\left(-\frac{k_z z}{s_0}\right), \tag{7.3.2}$$

$$B_z = s_0 k_x \cos(k_x x) \exp\left(-\frac{k_z z}{s_0}\right), \tag{7.3.3}$$

defined in the positive half-space ($z \geq 0$) of a Cartesian domain, assumed periodic in x. The field is two-dimensional as it only depends on x and z but not on y and hence, satisfy translational symmetry along y. The merit of this choice is that for $s_0 = 1$ $\mathbf{B}$ is reduced to a gauge-invariant form of the linear force-free field

$$\nabla \times \mathbf{B_{lf}} = \alpha_0 \mathbf{B_{lf}} \tag{7.3.4}$$

with the (constant) magnetic circulation per unit flux $\alpha_0 = \sqrt{{k_x}^2 - {k_z}^2}$, and the associated Lorentz force $(\nabla \times \mathbf{B}) \times \mathbf{B} := \mathbf{J} \times \mathbf{B} \equiv 0$. In the conducted simulation, the translational symmetry is crucial for an identification of detached magnetic structure with flux-rope. It helps to establish the reconnected field lines that generate a magnetic flux surface, while providing fundamental understanding necessary to explore activation of a three dimensional rope. With the initial $\mathbf{B}$ having congruent analytical form as $\mathbf{B}_{\mathrm{lf}}$ (Appendix A), the field lines are expected to resemble coronal loops. The shear angle between x-axis and the projection of an initial field line on the $z = 0$ plane,

$$\phi = \tan^{-1}\left(\frac{\sqrt{{k_x}^2 - {k_z}^2}}{k_z}\right), \tag{7.3.5}$$

is independent of s_0. If $k_x = k_z$, $\phi = 0$, and the field lines are tangential to y-constant planes. Generally, the Lorentz force exerted by the field defined in (7.3.1)-(7.3.3) is

$$(\mathbf{J}\times\mathbf{B})_x = \left[-k_x({k_x}^2 - {k_z}^2) + k_x s_0\left(s_0{k_x}^2 - \frac{{k_z}^2}{s_0}\right)\right] \sin^2(k_x x)\exp\left(-\frac{2k_z z}{s_0}\right), \tag{7.3.6}$$

$$(\mathbf{J}\times\mathbf{B})_y = 0, \tag{7.3.7}$$

$$(\mathbf{J}\times\mathbf{B})_z = \left[\frac{k_z}{s_0}({k_x}^2 - {k_z}^2) - k_z\left(s_0{k_x}^2 - \frac{{k_z}^2}{s_0}\right)\right] \frac{\sin(2k_x x)}{2}\exp\left(-\frac{2k_z z}{s_0}\right). \tag{7.3.8}$$

For all $s_0 \neq 1$, $\mathbf{J}\times\mathbf{B} \neq 0$, so the Lorentz force contributes to the viscous relaxation. To assure sheared field lines, we set $k_x = 1$ and $k_z = 0.9$ in the initial field (7.3.1)-(7.3.3). Furthermore, we set $s_0 = 6$, to optimize between computation cost and efficient development of dynamics leading to formation of CSs and their subsequent reconnections. This selection relied on the monotonous dependence of the maximal initial Lorentz force on s_0, Figure 7.9, and some auxiliary simulations (not reported here).

To aid further understanding, the following presents a detailed analysis of the initial magnetic field. For relevant depictions, hereafter, we set $x \in \{0, \pi\}$, because similar structures and dynamics are repeated in $x \in \{\pi, 2\pi\}$ due to the assumed periodicity. The MFLs for $s_0 = 6$ are shown in Figure 7.10 (a). The arrows in colors red, green, and blue denote the axes x, y, and z respectively. The plotted MFLs are sheared loops with a straight polarity inversion line located at $(x, z) = (\pi/2, 0)$. To highlight the shear, Figure 7.10 (b) illustrates projection of the field lines on $z = 0$ plane which are inclined to the x-axis at an angle $\phi \equiv \tan^{-1}(0.48) = 25.6°$. We keep ϕ fixed to this value for our simulations. Notably,

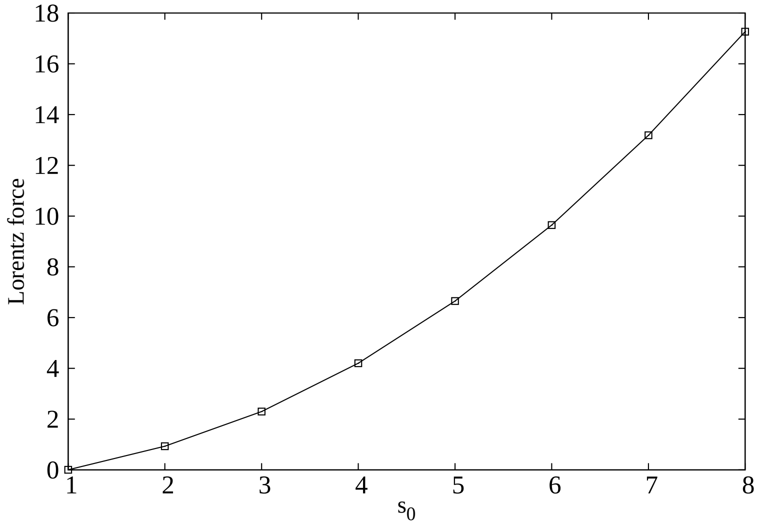

Figure 7.9: Variation of $\mid \mathbf{J} \times \mathbf{B} \mid_{\max}$ with an increase in s_0. The plot shows a monotonous increase in Lorentz force with an increase in s_0.

the MFLs maintain translational symmetry along y since $\mathbf{B}$ is independent of y. For comparison, in panels a and b of Figure 7.11, we plot MFLs of the corresponding $\mathbf{B}_{\mathrm{lf}}$ (for $s_0 = 1$) and their projections on the $z = 0$ plane.

Coronal arcades—associated with flux rope formation—are generally believed to evolve from an initial quasi-equilibrium state, devoid of any major electric current density. An appropriate physical mechanism is then required to generate dynamics from the quasi-equilibrium. Such onset of dynamics can be achieved by a specialized photospheric flow used in (DeVore and Antiochos 2000), where fully compressive MHD simulations demonstrate generation of ropes through reconnections. The present computations, however, start from an initial non-equilibrium state with appreciable electric current density to make them harmonious with general framework of the viscous relaxation. For instance, the initial electric current density is roughly 15 times larger for the $\mathbf{B}$ in comparison to the $\mathbf{B}_{\mathrm{lf}}$ (cf. Figures 7.10 and 7.11).

7.3.2 Results

The simulations are performed on four differently sized grids—$128\times128\times256$, $64 \times 64 \times 128$, $40 \times 40 \times 80$ and $32 \times 32 \times 64$—resolving the computational domain $0, 2\pi \times 0, 2\pi \times 0, 8\pi$ (respectively in x, y, and z), all starting from a

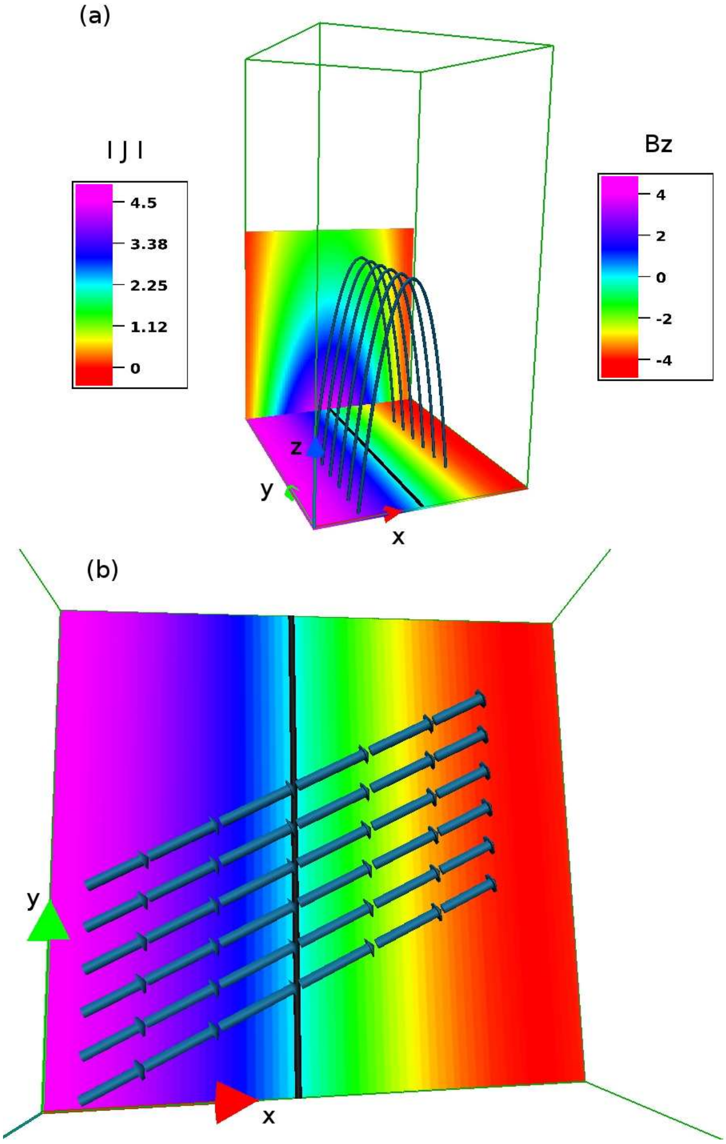

Figure 7.10: The panel a and b illustrate magnetic field lines of the initial field $\mathbf{B}$ for $s_0 = 6$ and their projections of the $z = 0$ plane respectively. The projected field lines are inclined to the x-axis with an angle ϕ, manifesting the sheared nature of MFLs. Both panels are overlaid with contours of the z-component of $\mathbf{B}$ (plotted on $z = 0$ plane) along with straight PIL (in color black), indicating polarities of footpoints. Additionally, in panel a, contours of magnitude of current density ($|\ \mathbf{J}\ |$) are plotted on a y-constant plane to depict the current density inside the sheared arcades.

motionless state and initial field (7.3.1)-(7.3.3). The boundary conditions along x are periodic, and open in z. The y direction is analytically ignorable, because the governing equations (6.1.1)-(6.1.4) and the initial conditions assure all dependent variables invariant in y. However, for efficacy of the results postprocessing and

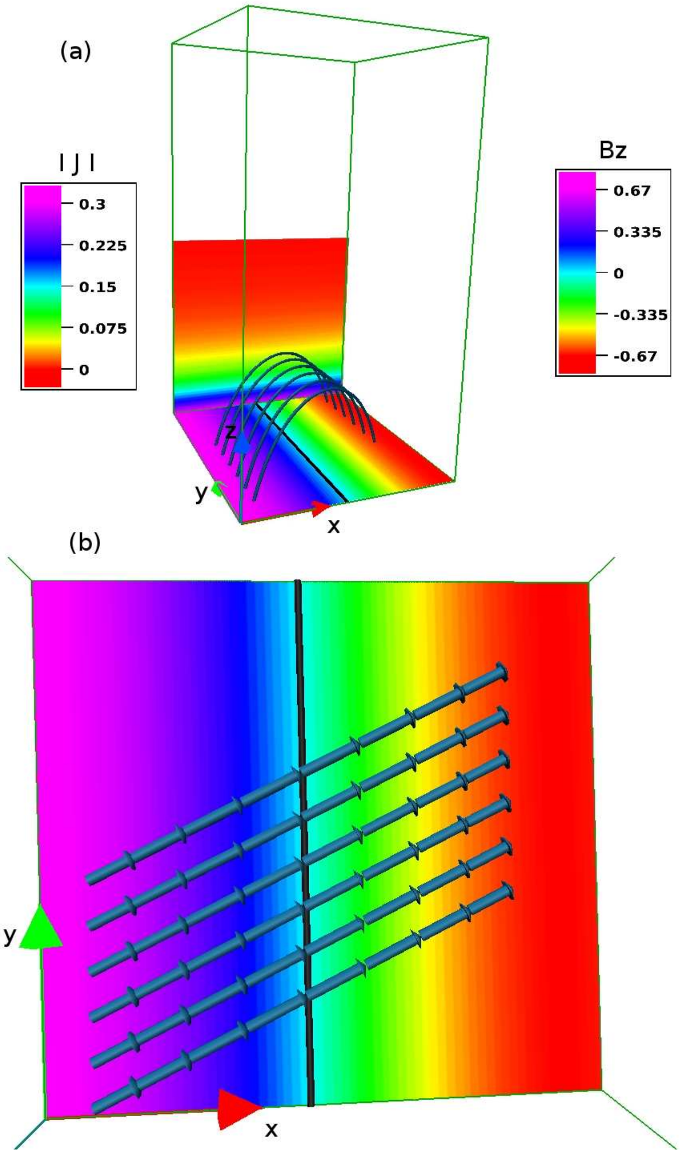

Figure 7.11: As in Fig. 7.10 but for field lines of $\mathbf{B}_{\mathrm{lf}}$ and their projections on the $z = 0$ plane. The figure demonstrates the morphology and shear of the initial field $\mathbf{B}$ to be identical to the corresponding $\mathbf{B}_{\mathrm{lf}}$ characterized by $s_0 = 1$.

their analysis with the VAPOR visualization package (Clyne and Rast 2005) we allow field variables to have all the three components while circumventing discrete differentiations in y. This makes field variables to have a translational symmetry along y, the maintenance of which can easily be verified from relevant plots presented in the paper. Moreover, for the case $32 \times 32 \times 64$ we have performed a fully 3D simulation, with no ignorable coordinate, and found results to be in exact agreement with the corresponding 2.5D run. Moreover, we select the parameter set: $\nu = 0.0005$, $\rho_0 = 1$, $B_0 = 4$, $L_0 = 8\pi$ to have $\tau_a \approx 20s$ and $\tau_\nu = 1.2 \times 10^6 s$. Notably, τ_a is almost equal to coronal value while τ_ν is one order greater than the corona. This one order difference only decreases the time interval between two reconnections without an effect on change in field line topology. The results for computation with resolutions $128 \times 128 \times 256$ are presented below.

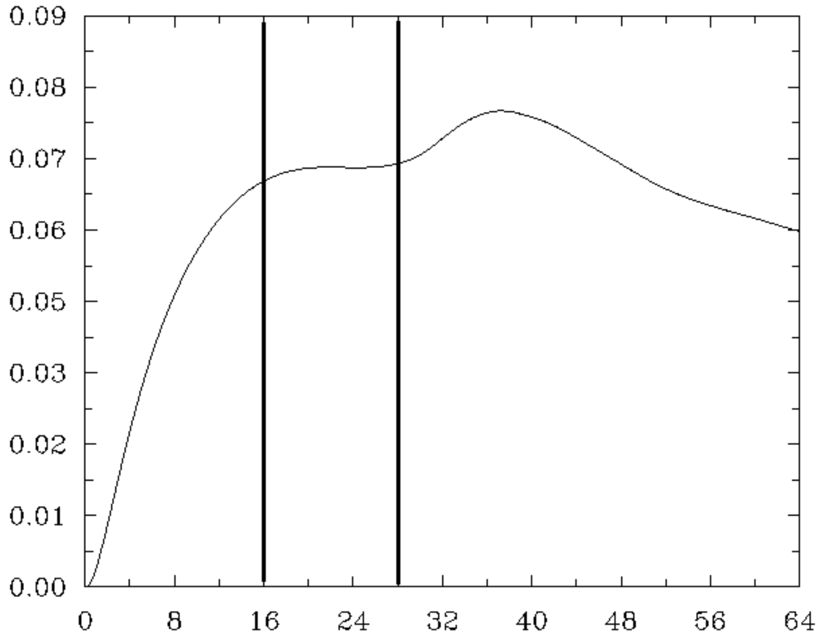

Figure 7.12: The evolution of kinetic energy, normalized to initial total (kinetic+magnetic) energy. The abscissa corresponds to time and the ordinate to the energy. Noteworthy are the three distinct phases of the evolution, marked by vertical lines in the plot.

To obtain overall understanding of the evolution, in Figure 7.12, we plot the time profile of normalized kinetic energy. The time profile shows four distinct phases which can approximately be divided into three overlapping intervals ranging from $t \in \{0s, 16s\}$, $t \in \{16s, 28s\}$, and $t > 28s$; separated by the vertical lines in the figure. The first phase corresponds to a rise in kinetic energy as the initial Lorentz force pushes the magnetofluid from rest. This rise is then arrested by viscous drag and the fluid settles down to a quasi-steady state which is characterized by an almost constant kinetic energy, representing the onset of the second phase. Also to be noted are the further rise and the following decay of kinetic energy which correspond to the third phase.

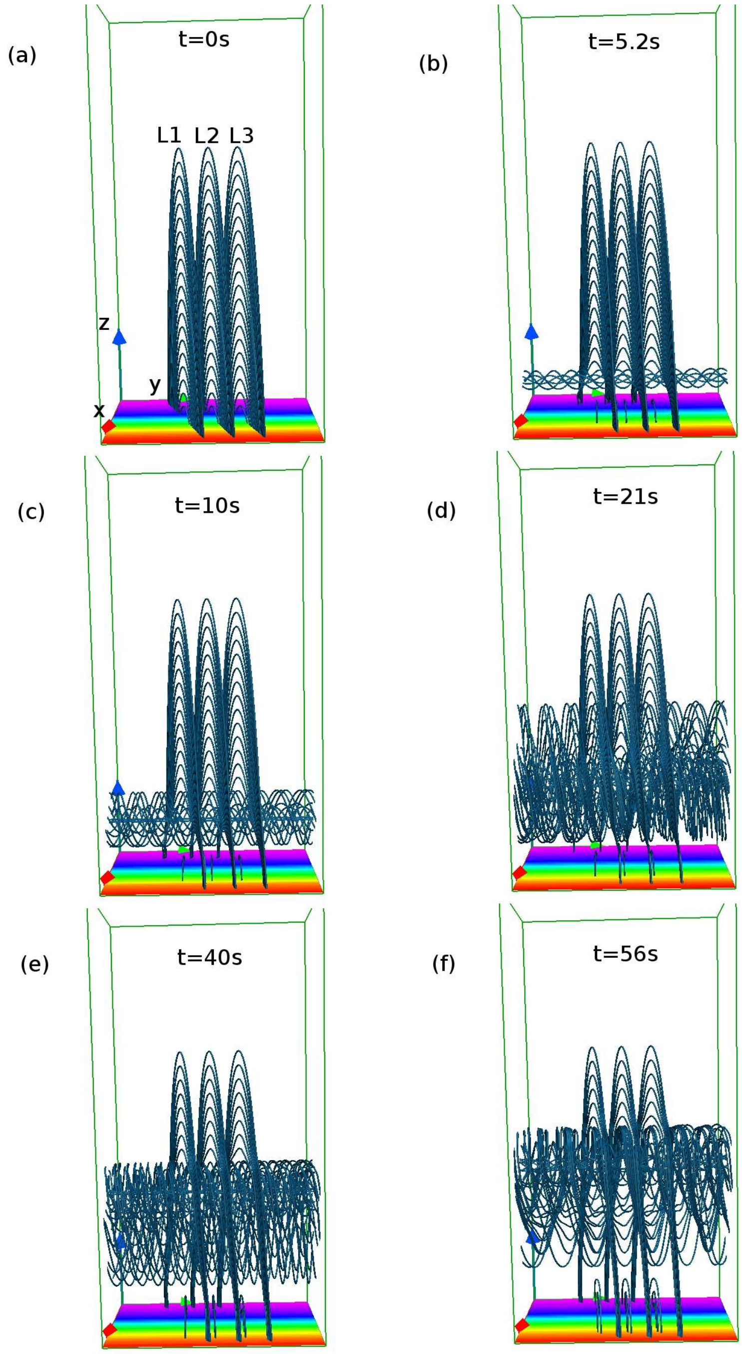

Figure 7.13: Time sequences of magnetic field lines in their important phases of evolution. Three different sets of magnetic loops are sketched, denoted by L_1, L_2 and L_3 in panel a of the figure. Important is formation of detached magnetic structure resembling a magnetic flux-rope. Also evident is the ascend of this structure while being situated over the PIL.

Figure 7.13 illustrates three sets of magnetic loops L1, L2, and L3, the evolution of which leads to a topologically distinct structure with field lines detached

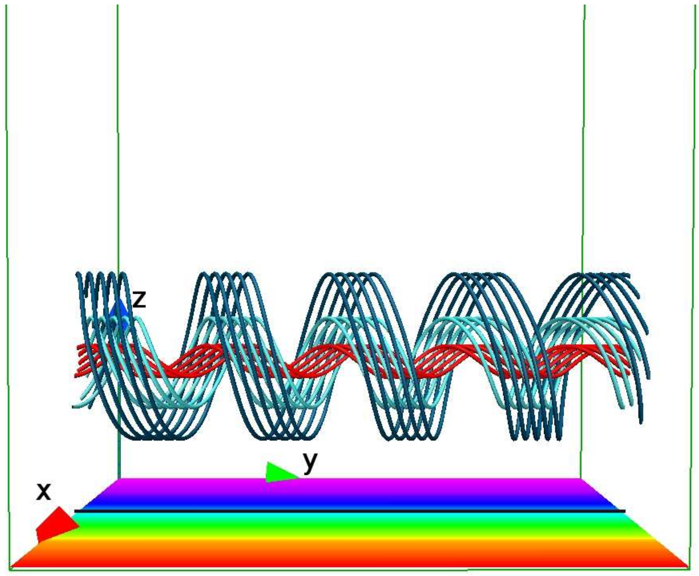

Figure 7.14: Snapshot of field lines at $t = 10s$, plotted in the neighborhood of the detached structure. The figure verifies the detached magnetic structure to be comprised of a stack of co-axial cylindrical magnetic flux surfaces which are made of helical field lines.

from the $z = 0$ surface. This detached structure resembles a magnetic flux-rope propagating along the y. For substantiation, in Figure 7.14 we plot the field lines in vicinity of the detached structure. The plot establishes the detached structure to be a flux-rope, made by helical field lines that are tangential to nested co-axial cylindrical surfaces. Away from the axis, the helices are more tightly wound. Importantly, the Figure documents a sustained ascend of the flux-rope along the vertical while being always situated above the PIL. The latter is a general requirement for magnetic structures to represent solar prominences or filaments.

Towards an explanation for generation of the rope, notable is the implosion of MFLs with a simultaneous increase in their footpoint (the point at which MFLs intersect the $z = 0$ plane) separation as displayed in panel b of Figure 7.15. During the implosion, reconnection of footpoints is prohibited because only parallel MFLs are bundled together. With magnitude of the Lorentz force diminishing exponentially along the vertical, the implosion is non-uniform, being more effective at lower heights. The non-uniform implosion generates a void depleted of MFLs, leading to a local decrease in magnetic pressure on a y constant

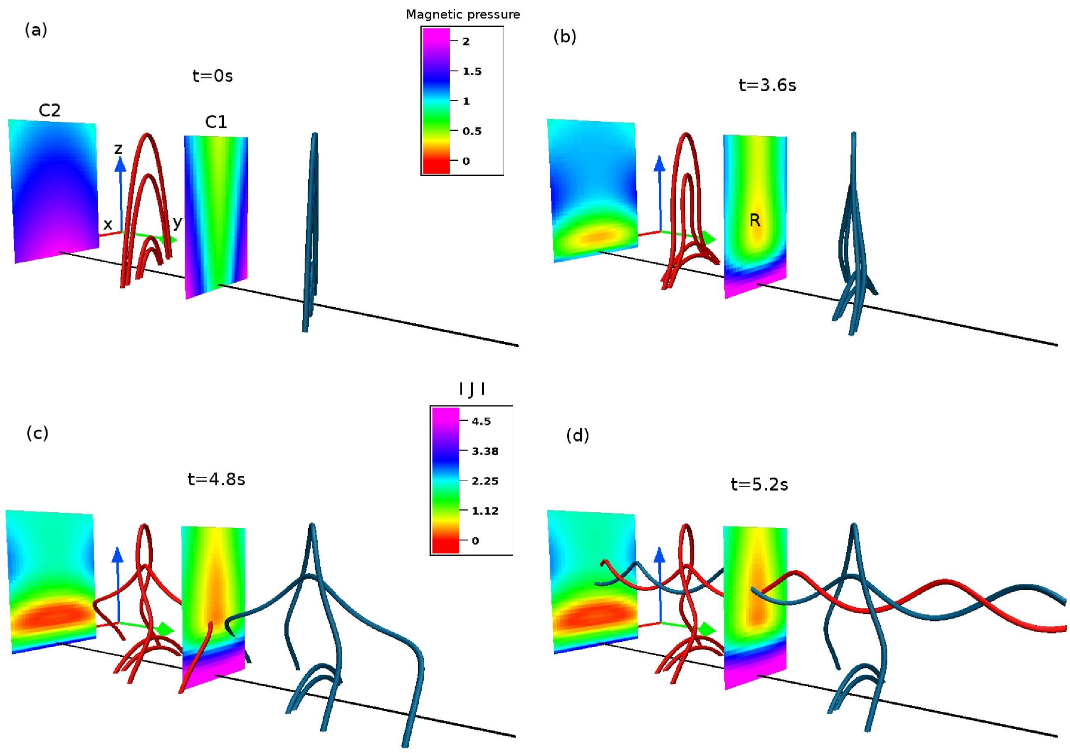

Figure 7.15: Evolution of magnetic field lines concurrent with the first phase. The figure is overlaid with contours of magnetic pressure (marked by C1 in panel a) and magnitude of current density (marked by C2 in panel a) drawn on different y-constant planes. The PIL is the solid black line. Panel b documents the implosion of MFLs situated at lower height along with an increase in their footpoint separation which results in depletion of magnetic pressure (marked by R) in the y-constant plane. Parts of MFLs are dragged into this pressure depleted region R from both sides of PIL, which sharpens up the gradient in $\mathbf{B}$ (panel c). Subsequent reconnection leads to the generation of detached helical field lines (panel d). The current contours confirm the absence of an extended CS.

plane; cf. panel b of Figure 7.15. Consequently, parts of two complementary anti-parallel field lines, located on opposite sides of the PIL, are stretched along x and enter into this void (panel c). As a result, the gradient of $\mathbf{B}$ along x sharpens up, as confirmed by the Figure 7.16 that documents scaling of current density with resolution in the vicinity of the void. Consequently, magnetic reconnection takes place as the scales become under-resolved (panel d of Fig. 7.15). Such reconnections, repeated in time, are responsible for the origin of the rope. Crucial is the non-zero shear, or equivalently $B_y \neq 0$, which makes the reconnected field lines helical. In absence of shear, MFLs would have been closed disjoint curves

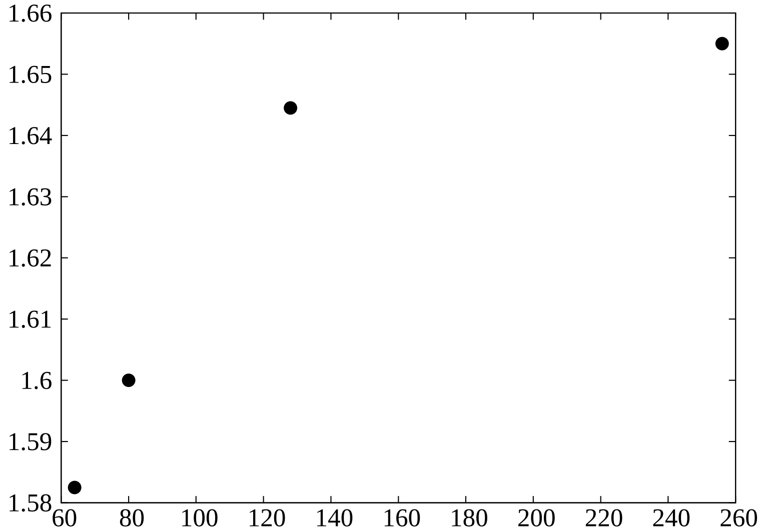

Figure 7.16: The plot of current density (in vicinity of R as marked in panel b of Fig. 7.15) against grid resolution. The abscissa is grid resolution along z whereas the ordinate is current density. The monotonous increase of current density with resolution asserts the increase of gradient in magnetic field.

tangential to y-constant planes—thus corresponding to a flux tube, but not a rope.

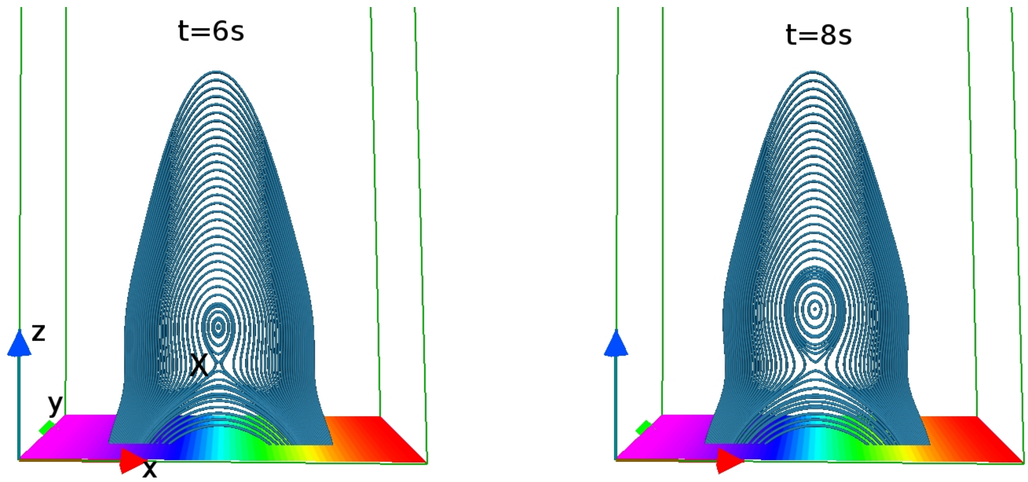

Figure 7.17: Time sequence of field lines at instances $t = 6s$ and $t = 8s$, projected on a y-constant plane. Panel a documents the presence of a magnetic island, reminiscent of the rope, along with an X-type null (marked by the symbol X) below the island. The panel b shows the number of field lines constituting the island increases while the center rises along the vertical.

The projection of the rope on a y-constant plane corresponds to a magnetic island. In Figure 7.17 we plot evolution of the island at $t = 6s$ and $t = 8s$. Important is the appearance of an X-type magnetic null located below the island;

illustrated in Figure 7.17 (a) by the symbol X. The MRs at the X-type neutral point increase number of MFLs constituting the island (panel b of Fig. 7.17). Also, the outflow generated by these repeated MRs at the X-point lifts the island center along the vertical. Notably, the above MRs are occurring while preserving the X-type null and no extended CS is developed, as documented by contours of current density in the Figure 7.15. The development of an extended CS by squashing an X-type null requires a favorable force missing in this period of evolution.

In Figure 7.18, we illustrate MFLs projected on a y-constant plane (panels a and b) and contours of current density (panels c and d) at instances $t = 16s$ and $t = 21s$, which correspond to the second phase of the evolution. From the figure, as reconnections at the X-type null continue, the magnetic pressure, below and above the two quadrants of the X-type null (denoted by $X1$ and $X2$ in panel a of the figure), increases. The increased magnetic pressure results in squashing of the X-type null and leads to formation of two Y-type nulls along with an extended CS (panels b and d). Importantly, the development of this extended CS is concurrent with the quasi-steady phase of the evolution $t \in \{16s, 28s\}$, as demanded by the magnetostatic theorem. The decay of this CS is responsible for the post quasi-steady rise in kinetic energy, marking onset of the third phase.

The corresponding dynamics of MFLs in the third phase is documented in Figure 7.19 for time instances $t = 30s$, $t = 40s$, $t = 50s$, and $t = 55s$. Noticeably, the reconnection at the extended CS reduces the pressure beneath the flux-rope because of a localized decrease in magnetic field strength. The neighboring field lines are stretched into this pressure depleted region, from all sides, rendering the rope to be dipped at the bottom portion. This dip corresponds to the observed dipped portion of a prominence, where the mass of the prominence is believed to be situated (van Ballegooijen and Cranmer 2010). Along with the stretched field lines located below the pressure depleted region, the dipped portion of the rope generates a new X-type null—denoted by X3 in the figure. Along with the rope, this new X-type null also moves upward. Further evolved, the MFLs constituting the flux-rope reconnect and the rope loses its well defined structure.

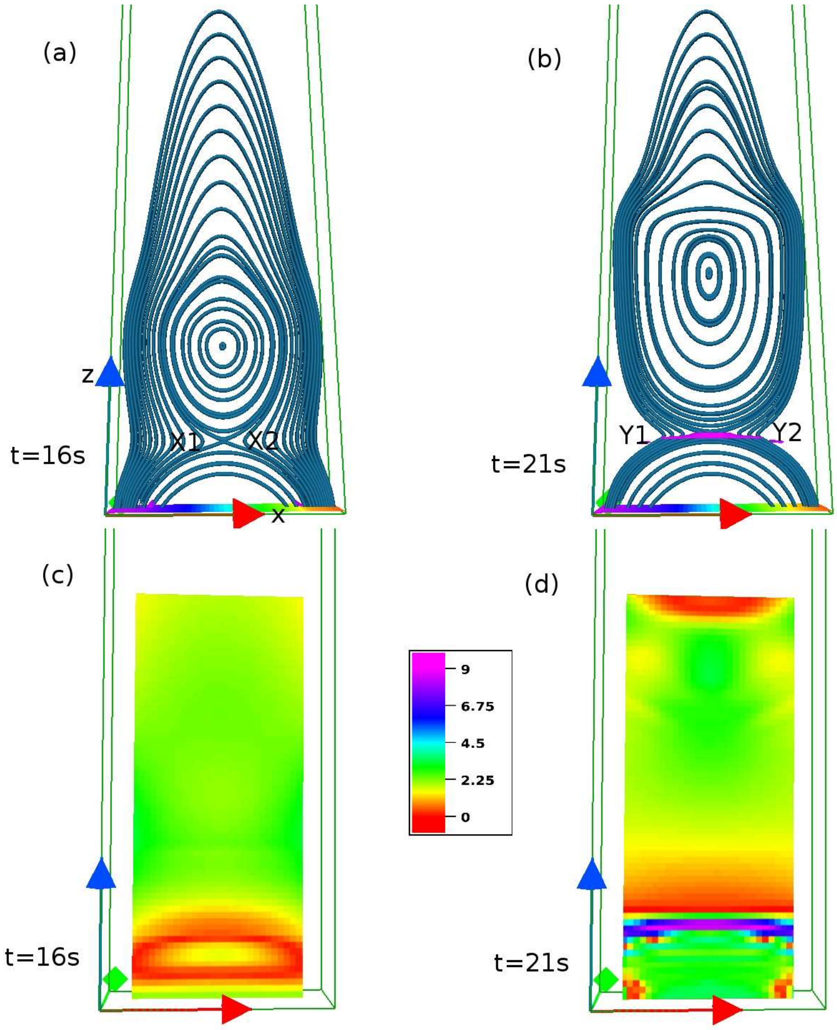

Figure 7.18: Evolution of field lines (projected on a y-constant plane) coincides with quasi-steady state of the relaxation (panels a and b). In addition, the contours of magnitude of current density the y-constant plane are plotted in panels c and d. The color bar represents the magnitude of current density. Noteworthy are the pressing of two quadrants (shown by symbols X1 and X2 in panel a) and generation of two Y-type nulls (denoted by symbols Y1 and Y2 in panel b) along with an extended CS (depicted in color pink in panel b). The development of extended CS is also attested by the current contours in panel d.

Noteworthy is importance of the translational symmetry in identifying the detached magnetic structure with a flux-rope—which is first and foremost a magnetic flux surface by its mathematical definition. Towards recognizing the importance, projection of a helical field line constituting the detached structure (Figure 7.14) on a y-constant surface is a closed curve. Because of the symmetry, a translation of this closed curve along y generates a surface on which the helical

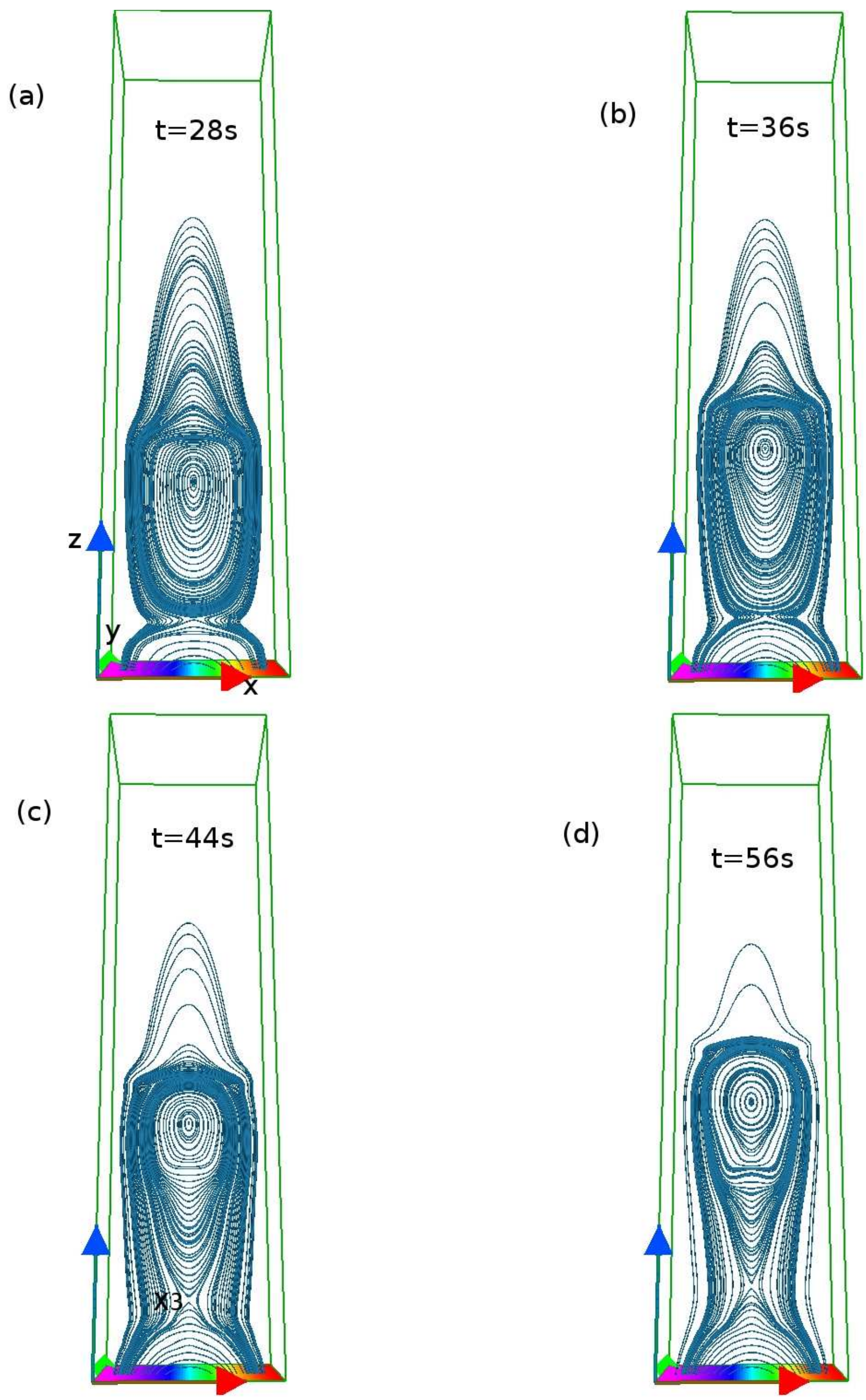

Figure 7.19: The figure plots field lines during the third phase of evolution. The field lines are projected on a y-constant plane. Important is the onset of a new X-type null (illustrated by $X3$) while the bottom portion of the rope develops a dip (panel c). Also, the newly formed X-point moves upward along with the rope (panel d).

field lines are also tangential; confirming the detached structure to be a magnetic flux surface. In absence of the symmetry, the identification is not straightforward as field lines are always postprocessed and the processing error contributes to the topology of the obtained MFLs. Conventionally, however, the magnetostatic theorem applies to three-dimensional fields, which favors the actual evolution of solar magnetized plasma. To consolidate the simulation results further, in the following we present two auxiliary computations where the symmetry is removed. The three-dimensional simulations are performed on a grid of size $128 \times 128 \times 256$, resolving the same computational domain as in the symmetric case. The boundary conditions along x and y are periodic, and open in z. For consistency, all other parameters are kept identical to the symmetric case.

7.3.2.1 Auxiliary simulation I

For the first simulation, the initial magnetic field $\mathbf{B}^\star$ (Appendix B) is constructed by superposing a three-dimensional solenoidal field on the $\mathbf{B}$ expressed in equations (7.3.1)-(7.3.3). Notable is the structural similarity of the two superposed fields that individually reduce to a linear force free field for $s_0 = 1$. The evolution for this 3D simulation is shown in Figures 7.20 and 7.21. Figure 7.20 displays the time series for two sets of field lines, where panel a corresponds to the initial field $\mathbf{B}^\star$. The PIL is curved, thus attesting to the absence of translational symmetry along the y. The figure is overlaid with contours of magnetic pressure drawn on a y-constant plane. Similar to evolution depicted in Figure 7.15, repeated reconnections generate a detached magnetic structure which, based on the 2.5D computation, can be identified to a flux-rope. The Figure 7.21 illustrates the evolution with more densely plotted field lines where panel a corresponds to the initial field $\mathbf{B}^\star$. The field lines constituting the rope are marked in red, and with an ascend maintained by underlying reconnections document an evolution with overall similarity to its 2.5D counterpart.

Figure 7.22 shows the field lines at instances $t = 10.4s$ and $t = 36s$ overlaid with contours of $\mid \mathbf{B}^\star \mid$ in y-constant plane and isosurfaces of corresponding current density $\mathbf{J}^\star$ with isovalues 15% and 20% of maximum $\mid \mathbf{J}^{\star\star} \mid$. Based on

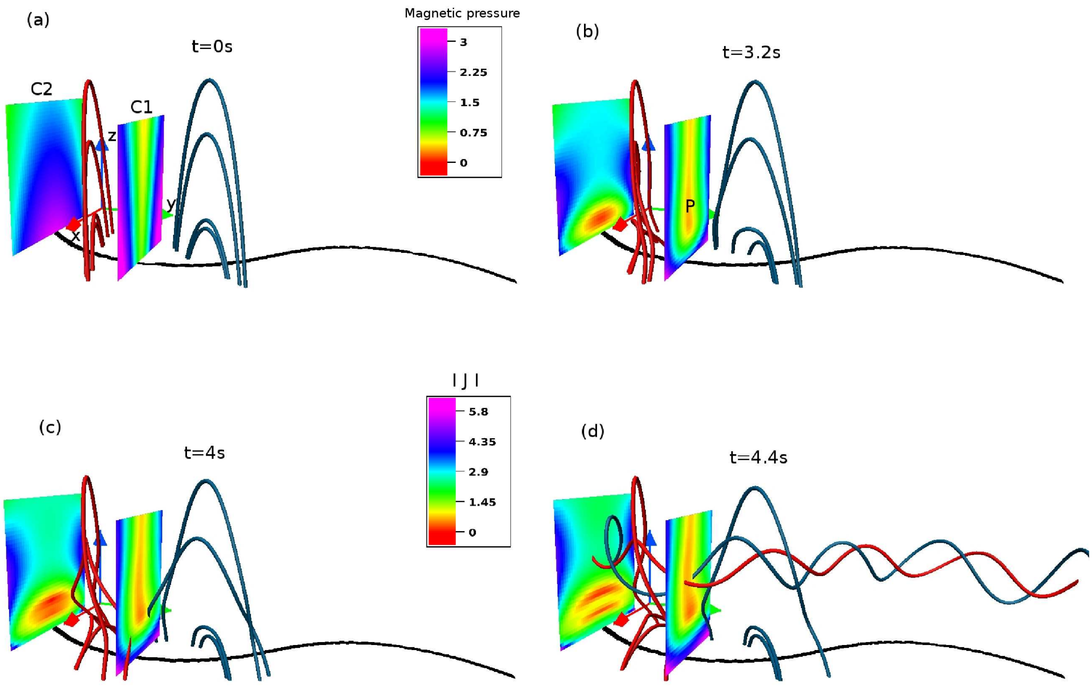

Figure 7.20: Time sequences of two sets of field lines for the three-dimensional simulation with initial field $\mathbf{B}^{\star}$. The panel a shows the field lines of the initial field. Important to note is the curved PIL (the solid black line). The figure is further overlaid with contours of magnetic pressure (denoted by C1 in panel a) and current density (denoted by C2 in panel a) plotted on different y-constant planes. Panels b, c and d document the development of magnetic pressure depleted region (marked by P) in the y-constant plane and subsequent reconnection which leads to the generation of a flux-rope. Also, the flux-rope is situated above the PIL.

their appearances, the isosurfaces can be classified into two distinct categories: the surfaces appearing at the z-constant plane below the rope (marked by C1 in panel b) and the elongated surfaces located at horizontal sides of the rope (marked by C2 in panel b). The figure identifies generation of the elongated surfaces to an increase in the local number density of parallel field lines, resulting in an increase in $\mid \mathbf{B}^{\star} \mid$ and hence $\mid \mathbf{J}^{\star} \mid$ without any sharpening of field gradient. Hence, these surfaces do not represent current sheets (Kumar et al. 2015c). In contrast, the surfaces lying in z-constant plane originate without a co-located enhancement in $\mid \mathbf{B}^{\star} \mid$, suggesting the development of these surfaces by a local increase in the field gradient. Thus, the appearances of these surfaces indicate the

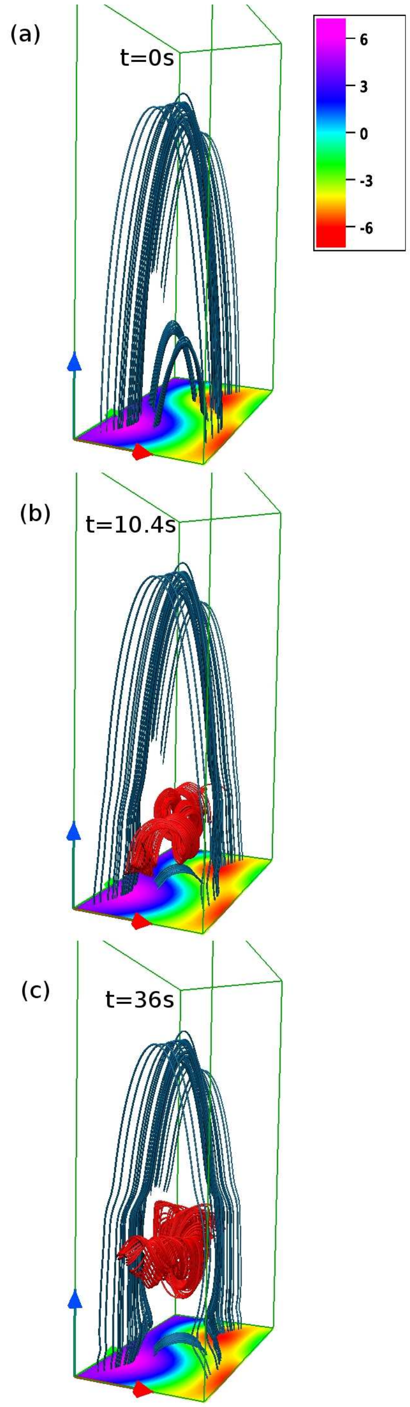

Figure 7.21: Time sequences of evolution with more densely plotted field lines of the $\mathbf{B}^{\star}$. The figure is overlaid with contours of the z-component of $\mathbf{B}^{\star}$ to show polarities of footpoints and the color bar represents the values of the z-component. The lines in red marks the flux-rope. The overall evolution is similar to the 2.5D case. Noticeable is the ascend of the rope.

formation of current sheets below the rope (Kumar et al. 2015c). Importantly, the current sheet has a non-uniform intensity distribution along the rope, where

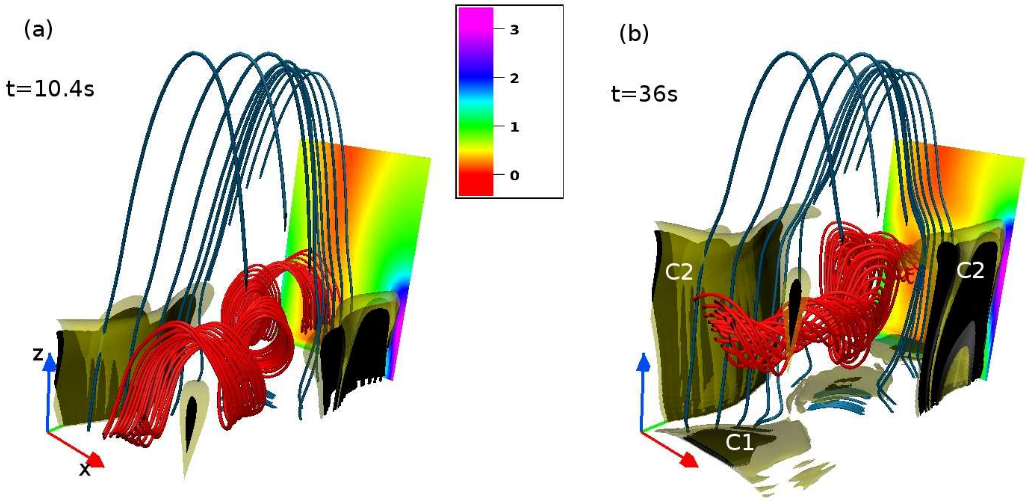

Figure 7.22: Field lines for the three-dimensional simulation with initial field $\mathbf{B}^{\star}$ at instances $t = 10.4s$ and $t = 36s$. The flux rope is marked in color red. The figure is further oveplotted with isosurfaces of current density with isovalues 15% (in color yellow) and 20% (in color black) of its maximum and contours of $\mid \mathbf{B}^{\star} \mid$ on a y-constant plane. The color bar corresponds to the values of $\mid \mathbf{B}^{\star} \mid$. Notable is the development of current sheet below the rope (marked by C1 in panel b). The elongated surfaces (marked by C2 in panel b) being co-located with enhanced $\mid \mathbf{B}^{\star} \mid$ region in y-constant plane imply that their onset does not indicate CS formation.

patches of intense currents are marked in black while low currents are marked in yellow; which agrees with the general expectation.

7.3.2.2 Auxiliary simulation II

For the second simulation, the initial field $\mathbf{B}^{\star\star}$ (Appendix C) is derived by superposing the $\mathbf{B}^{\star}$ with another solenoidal field $\mathbf{B}'_p$ where the $\mathbf{B}'_p$ reduces to potential field for $s_0 = 1$. The corresponding evolution is shown in Figures 7.23 and 7.24. Figure 7.23 illustrates the time sequences of two sets of field lines. Panel a of the figure shows the initial field lines of $\mathbf{B}^{\star\star}$ having a curved PIL. The figure confirms the formation of flux-rope via repeated reconnections similar to the auxiliary simulation I. Further, in Figure 7.24 we illustrate the evolution of magnetic field lines overplotted with contours of $\mid \mathbf{B}^{\star\star} \mid$ in y-constant plane and isosurfaces of corresponding current density $\mathbf{J}^{\star\star}$ with isovalues 15% and 20% of maximum $\mid \mathbf{J}^{\star\star} \mid$. The figure demonstrates the ascend of the rope (marked in red) by repetitive reconnections similar to auxiliary simulation I (Fig. 7.21). Moreover, identical to the auxiliary simulation I (Fig. 7.22), the figure identifies the emergence of two types of current isosurfaces: first one appears at z-constant plane situated beneath the rope and second one originates as the elongated surfaces located at horizontal sides of the rope. In this case also, the surfaces at z-constant plane corresponds to the CSs while, the elongated surfaces, formed due to the enhancement in $\mid \mathbf{B}^{\star\star} \mid$, do not represent CSs. Moreover, the intensity distribution of the CS is found to be non-uniform along the rope which further validates the general expectation.

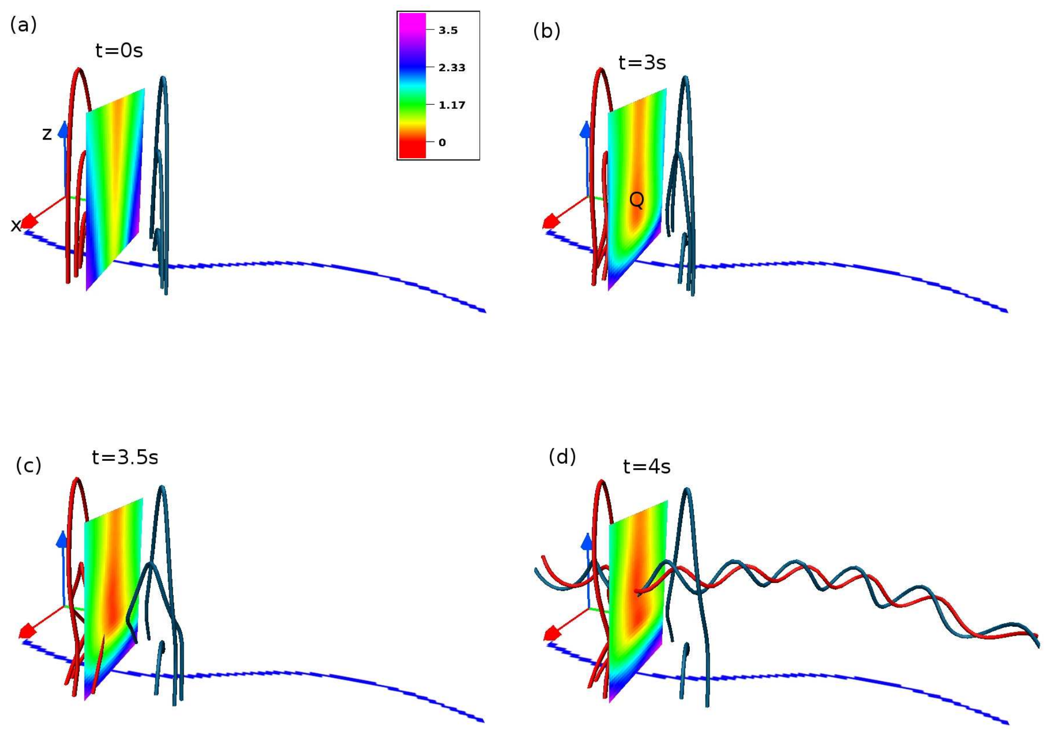

Figure 7.23: Evolution of two sets of field lines for the three-dimensional simulation with initial field $\mathbf{B}^{\star\star}$. The figure is overplotted with contours of magnetic pressure on a y-constant plane and corresponding values are represented by the color bar. The panel a depicts the field lines of $\mathbf{B}^{\star\star}$ with the curved PIL (in color blue). Notable is the development of magnetic pressure depleted region (marked by Q in panel b) in the y-constant plane. Consequently, oppositely directed field lines come close and get reconnected which produce a flux-rope located above the PIL.

With the ascending flux ropes having underlying reconnections in agreement

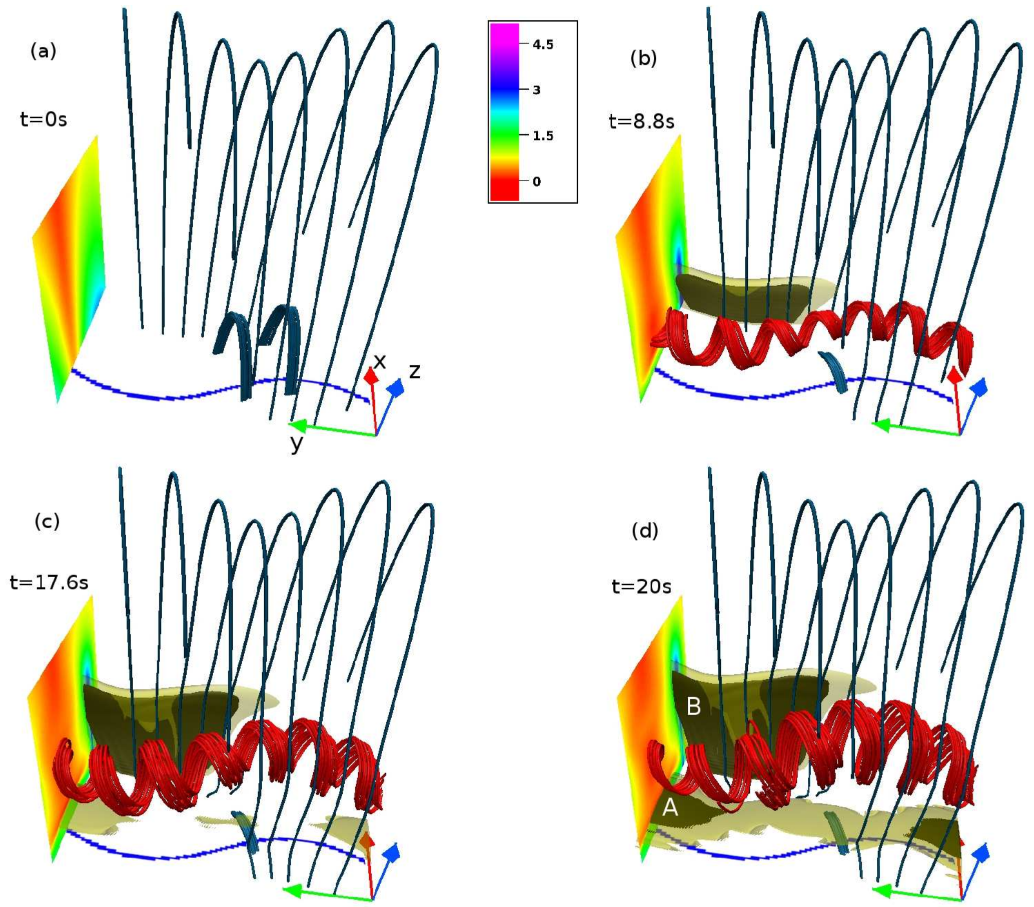

Figure 7.24: Evolution of field lines for the three-dimensional simulation with initial field $\mathbf{B}^{\star\star}$, illustrated in panel a (the curved PIL is shown by the solid blue line). Isosurfaces of current density with isovalues 15% (in color yellow) and 20% (in color black) of its maximum and contours of $\mid \mathbf{B}^{\star\star} \mid$ on a y-constant plane are also plotted in the figure. The color bar shows the values of $\mid \mathbf{B}^{\star\star} \mid$. for The helical red field lines identify the flux-rope which rises in the vertical direction. Important is the formation of CS beneath the rope (marked by A in panel d). The elongated current surfaces (marked by B in panel d) are co-spatial with increased $\mid \mathbf{B}^{\star\star} \mid$ region in y-constant plane. This confirms that onsets of the elongated surfaces do not show CS formation.

with the standard flare model (Shibata and Magara 2011), the reported simulations identify spontaneous repeated MRs as the initial driver for the rope formation and triggering its ascend. Further, the simulations underline that MRs play an active role in the feedback mechanism between flux-rope dynamics and reconnections, central to the standard flare model. This is in harmony with contemporary observations (Temmer et al. 2008, 2010; Cho et al. 2009; Cheng et al. 2011).

7.4 Summary

In this chapter, the computations are performed to establish the scenario of repetitive reconnections by demonstrating secondary current sheets formations and to explore the role of these reconnections in generation of the observed structures. For the purpose, two sets of numerical experiment are conducted. For both the sets, the simulations start from a select motionless state. Importantly, the computations being commensurate with the requirements of the magnetostatic theorem, the reconnections are spontaneous and inherent to the evolving fluid. The computational commensuration with the theorem is achieved by viscous relaxation of an incompressible high R_M magnetofluid maintaining the condition of flux-freezing. During the relaxation, sharpening of magnetic field gradient is unbounded, ultimately leading to MRs at locations of CSs where separation of non-parallel field lines approaches grid resolution. The MR process per se is underresolved, but effectively regularized by locally adaptive dissipation of MPDATA, in the spirit of ILES subgrid-scale turbulence models. In effect, the post-reconnection condition of flux-freezing is restored, and field lines tied to the reconnection outflow push other sets of MFLs, leading to secondary CSs and MRs. The whole process is replicated in time to realize repetitive reconnections.

For the first set of numerical experiment, the initial field is same as used in the first numerical experiment of previous chapter. This choice is based on the understanding that the field is proven to spontaneously develop the CSs. The simulated viscous relaxation shows the decay of distributed CSs (discussed in previous chapter) via MRs. The subsequent dynamics reveals the formation of secondary CSs near the 2D (X-type) and 3D nulls as well as in absence of these nulls at different times. The CS at X-type null formed by squashing of the X-type to two Y-type nulls. More importantly, the simulations demonstrate a complete collapse of fan and spine structures of the 3D nulls which enables pressing of non-parallel MFLs to generate CSs. After the destruction of both the 2D and 3D nulls, one more generation of CSs spontaneously develops which are once again distributed through-out the computational volume. Notably, compared to CSs near the 3D nulls or which are volume-distributed, the maximum current density near the 2D nulls is found to be largest for a given resolution and show strongest scaling with numerical resolution. With the smallest resolvable scale being fixed for a given computation, scaling seems to be related to the amount of anti-parallel field lines which are pushed together to generate a CS and hence depends on magnetic topology around the current sheet. The strongest scaling physically signifies the reconnections near the 2D nulls to be faster (Craig and Litvinenko 2005) and energetically more explosive than the ones near the volume-distributed CSs. This indicates that the solar eruptive events involve reconnections occurring near 2D nulls while the nano-flares are produced by reconnections generated by distributed CSs. This indication finds support from the standard flare model which takes into account the reconnection across the extended CS near 2D null to explain the eruption during solar flares.

After successful demonstration of secondary CSs formations and repetitive reconnections, we perform the second set of computations with magnetic field congruent to a gauge-invariant form of linear force-free field having loop-like field lines with translational symmetry in y. The simulated relaxation process comprises three distinct phases. In the first phase, a combination of incompressibility and the initial Lorentz force deforms initial field lines such that the field gradient sharpens in a direction implied by the initial condition (herein x). Further push eventuates in reconnection and development of an X-type neutral point along with a detached flux-rope. Repeated reconnections around the X-type null generate more detached field lines which contribute to the rope. Moreover, being frozen to the outflow, the rope ascends vertically. Because the reconnections are localized below the evolving rope, the scenario is in general agreement with observations. As the magnetofluid relaxes to a quasi-steady state, the process enters the second phase of the relaxation with the X-type null being squashed to generate two Y-type nulls along with an extended CS beneath the rope. In the third phase the extended CS decay, resulting in an increase in the kinetic energy of mass flow. Because of the corresponding decrease in magnetic intensity near the decaying CS, MFLs from all side of the CS are stretched into the field depleted region. The rope becomes dipped at the bottom and a new X-type null is generated which ascends with the rope. Continued further in time, the flux-rope reconnects internally and loses its structure. Fully three-dimensional simulations are also performed to verify the robustness of repeated spontaneous MRs in creation and ascend of a rope accordant to a more realistic evolution. Importantly, the three-dimensional simulations document the intensity of CSs developed over respective PILs to be non-uniform—a feature expected in realistic ropes developed via reconnections.

Overall, the computations extend Parker's magnetostatic theorem to the scenario of evolving magnetic fields which can undergo magnetic reconnection. Notably, the theorem in absence of magnetic diffusivity leads to CSs, having true mathematical singularities in magnetic field which are end states of any evolution. But in presence of small but non-zero magnetic diffusivity, as in astrophysical plasmas, the theorem opens up the possibility of spontaneous generation of secondary CSs and subsequent MRs that may contribute to the dynamics of the plasma. The computations confirm the contribution to be meaningful as it can generate observed magnetic structures and govern their dynamics which, in this case, is the complete evolution of a flux-rope in terms of its generation and ascend in a magnetic topology relevant to the solar corona. Additionally, in context of the standard flare model, the simulations imply a direct involvement of magnetic reconnection in the activation of flux-ropes.

Chapter 8

Summary and Future Works

8.1 Summary of the thesis

In the thesis we have numerically studied the subject of MHD relaxation in the astrophysical context. MHD relaxation in these large magnetic Reynolds number (R_M) magnetofluids proceeds through ceaseless magnetic reconnections. Notably, the current sheet development is a prerequisite for reconnection to take place in an otherwise non-diffusive high R_M magnetofluid. Thus, a complete understanding of MHD relaxation requires investigation of dynamics of current sheet formation and magnetic reconnection. The analytical theories for the MHD relaxation utilize variational calculus to obtain the relaxed state, and hence, do not capture the dynamics leading to the relaxation. Because of the inherent non-linearity and coupled nature of the MHD equations, an analytical study of the relaxation dynamics is formidable and calls for numerical simulations.

Based on the above background, the thesis aims to explore the governing dynamics of MHD relaxation in large R_M magnetofluids by studying spontaneous generation of current sheets and their subsequent decay through magnetic reconnections. For the purpose, suitable initial value problems are formulated and MHD equations are solved numerically. Special attention is given to magnetic topologies relevant to the solar corona because of its large magnetic Reynolds number along with the availability of relevant observations.

Notably, the Parker's magnetostatic theorem advocates the autonomous generation of current sheets in magnetofluid with infinite electrical conductivity and complex magnetic topology relaxing towards an equilibrium state. The spontaneity arises from simultaneous satisfaction of the flux-freezing and local force-balance. Under the flux-freezing, if initially a fluid surface is identified as a magnetic flux surface, then any subsequent arbitrary evolution always maintains the identity. During evolution, a flux surface is then expected to contort with deformation of the corresponding fluid surface. When favorable, such contortions can generate current sheets by bringing two oppositely directed field lines to close proximity. Realizing that a large R_M magnetofluid has a small but non-zero magnetic diffusivity, the current sheets will further decay through magnetic reconnections. Importantly, these magnetic reconnections have a connotation of spontaneity since development of the involved current sheets is inherent to the magnetofluid evolution. In post reconnection dynamics, the flux-freezing is once again restored and the magnetofluid is expected to develop second generation of current sheets and further magnetic reconnections. Therefore, a scenario is possible where the repeated reconnections provide an autonomous mechanism to create coherent magnetic structures in astrophysical plasmas and govern their dynamics.

In backdrop of the above scenario, the objective of the thesis is broadly divided into two parts. In the first part, we understand the physics behind spontaneous onset of current sheets and relate their locations to the complexity of magnetic topology. The second part focuses on exploration of the subsequent evolution which includes the decay of first generation current sheets through magnetic reconnections, formation of secondary current sheets and assessment of repeated reconnections in further shaping up the dynamics of an astrophysical magnetofluid. To achieve these objectives, we solve MHD equations utilizing numerical models EULAG-MHD and EULAG-EP. Further, to keep the computations harmonious with the magnetostatic theorem, we simulate viscous relaxation for an incompressible, viscous magnetofluid with infinite electrical conductivity.

To obtain the first part of the objective, we follow evolution of magnetic flux surfaces instead of the vector magnetic field to gain a better insight of the processes leading to creation of current sheets. For the advection of flux-surfaces, we employ the numerical model EULAG-EP. The numerical precision in preservation of the initial magnetic topology is ensured by the accuracy of the MPDATA—the advection scheme used in the model. In the following, we briefly summarize the results of these computations presented in the thesis.

For numerical demonstration of the autonomous development of current sheets, the computations are performed with the initial magnetic fields constructed from a twisted linear force free field having complex magnetic topology with the presence of 2D and 3D nulls. The linear force free field is a special solution of force free equilibrium, realizable in the solar corona. The existence of 2D and 3D nulls in the corona is also well established. A key finding is the demonstration that current sheets can develop at locations which are away from magnetic nulls. Analysis reveals that favorable contortions of flux surfaces are responsible for generating the above-mentioned current sheets by bringing non-parallel field lines close to each other. The accompanied increase in magnetic field gradient ultimately develops the current sheets. The contortions being distributed all over the computational volume and not being localized near the magnetic nulls, lead to the generation of distributed current sheets which are located away from the nulls. Importantly, the contortions are found to be in general agreement with the optical analogy. The simulations yield additional important insights. First, the results clearly illustrate that any parameter related to only the magnitude of volume current density is not a standalone definitive marker to conclude the development of current sheets. Second, although the magnetic nulls are topologically attractive locations for current sheet formation, but current sheets can also develop away from these nulls as pointed out in the magnetostatic theorem.

Next, we assess the importance of complex magnetic topology (determined by the interlacing of field lines) in spontaneous development of current sheets. A relevant initial value problem is formulated by superposing two untwisted components fields—each being represented by a pair of global flux surfaces. The relative magnitude of the superposed fields determines the strength of interlacing. Computations are performed by varying this amplitude to achieve the aim. An important finding is that the spatial distribution of spontaneously generated current sheets are directly related to the complexity of the field lines. More interlaced field lines are found to generate additional volume distributed current sheets. However, magnetic field with less interlaced field lines generate current sheets which are localized near the topologically attractive locations like magnetic nulls and field reversal layers.

After successfully exploring the dynamics behind spontaneous formation of current sheets, we moved towards completion of the second general objective. For the purpose, we advect vector magnetic field in lieu of magnetic flux surfaces as the flux surface description loses its validity if the magnetofluid undergoes reconnection. To initiate magnetic reconnection, we depend on the proven implicit large eddy simulation mode of EULAG-MHD which regularizes the under-resolved scales (developed via generation of current sheets) through onset of magnetic reconnection; cotemporal and cospatial with the developing current sheets. The salient features are summarized in the following.

For examining the development of secondary current sheets during MHD relaxation, we utilize initial field which is derived from a linear force free field, as it is proven to develop distributed current sheets. The simulations demonstrate generation of secondary current sheets near 2D and 3D nulls after the decay of the first generation of the volume distributed current sheets. Moreover, the subsequent dynamics illustrates the development of the next generation current sheets in absence of any nulls. Noticeably, the simulations illustrate a complete collapse of the 3D null before any development of current sheets. The evolution proceeds further by squeezing in more non-parallel field lines in a volume of magnetofluid and thereby creating current sheets. Further, the peak current densities for current sheets pertaining to different magnetic topologies are found to scale differently with numerical resolution. The current sheets which originate near the 2D nulls have the largest strength and exhibit the strongest scaling in comparison to other current sheets which develop either near 3D nulls or away from the nulls. Such comparative scaling indicates that the reconnection will be faster and energetically more explosive across current sheets near

2D nulls than the current sheets which are volume distributed—a scenario congruent with the energetics of eruptive events and possible nano-flares, occurring at the solar corona. Importantly, the simulations also confirm that magnetic helicity remains approximately constant in comparison to magnetic energy during the relaxation—a feature central to most of the analytical models for MHD relaxation.

To explore the role of repeated reconnections in determining dynamics of observed magnetic structures, we perform computations where the magnetic field lines resembles bipolar magnetic loops in the solar corona. The computations recognize repeated magnetic reconnections as an autonomous mechanism for the complete evolution of a flux-rope starting from its generation to its ascend. The corresponding manifestations of magnetic topology—in likes of reconnections occurring at a height, reconnections being localized below the rope and development of dips at the bottom part of the rope—are in general harmony with observations. Thus, the simulations agree with the scenario where the repeated reconnetions play an important role in shaping-up the dynamics of high R_M magnetofluids and can generate magnetic structures which are physically realizable. In our simulations, the repeated magnetic reconnections govern the complete evolution of a flux-rope in a field line geometry relevant to the solar corona.

In essence, the thesis explores the interplay between small scales (current sheets, where magnetic diffusion is operative) and large scales (where the flux-freezing is applicable) during MHD relaxation of astrophysical plasmas. The computations presented in the thesis identify a novel physics of small scales formation via favorable contortions of magnetic flux surfaces under the flux-freezing. These contortions being distributed in the volume, develop small scales without any preference to particular sites—supporting the magnetostatic theorem and hence the Parker's nano-flare model for coronal heating. The results further show that, with the dissipation of first generation of small scales via reconnections, the large scales once again prevail in the system which leads to second generations of small scales and further reconnections. The computations recognize that these reconnections can be responsible for generation of observed magnetic structures in the astrophysical plasmas. Therefore, the thesis proposes the MHD relaxation, sustained by this ubiquitous coupling of the small scales and the large scales, may provide a standalone mechanism which governs the dynamics of astrophysical plasmas. Moreover, during the relaxation, the magnetic energy is dissipated in a rate faster than the magnetic helicity, suggesting the relaxation to be Taylor-type where reconnections occur spontaneously in accordance with the magnetostatic theorem.

8.2 Future works

8.2.1 Continuation of the present work

Overall, the thesis recognizes flux surface based computations to be more insightful for understanding onset of current sheets. These computations will be continued to magnetic geometries resembling coronal loops to directly match results with observations. For the purpose, the existing EULAG-EP model will be modified to incorporate open boundary conditions. Also the present computations use Cartesian coordinates. The use of spherical coordinates is more desirable to simulate the global corona, and will be incorporated in future studies. Furthermore the present focus is on magnetic topology of the coronal plasma and neglects its thermodynamic properties like temperature and mass density. Further assumption is incompressibility, resulting into preservation of fluid volumes enclosed by flux surfaces and allowing an instantaneous rearrangement of thermodynamic pressure. In future research, these assumptions will be relaxed to perform computations which more accurately simulate the coronal dynamics.

8.2.2 Development of Hall-MHD based numerical model

The simulations presented in the thesis are in the spirit of implicit large eddy simulations where simulated magnetic reconnections, being intermittent in space and time, mimic physical reconnections which occur in high R_M magnetofluids. In this thesis, our primary aim was to understand the role of these reconnections in development of observable magnetic structures in a relaxing astrophysical magnetofluid. The model dependent residual dissipation of a implicit large eddy simulation serves our purpose since such a dissipation is adaptive and intermittent by definition. However, such simulations in absence of a physical magnetic diffusivity, provide a qualitative description of reconnections with no direct estimation of the reconnection rate. Therefore, inclusion of an apt physical diffusivity is required for the quantification of magnetic reconnections.

To identify a proper magnetic diffusivity, an important observation is the rapid and sudden growth of solar flares from a relatively quiescent background. The corresponding reconnection is not only fast but also impulsive, with an abrupt increase in time derivative of the reconnection rate. Moreover, with $S \approx 10^{13}$, the rough estimation of width of the current sheet provide the thickness of a current sheet to be below the ion inertial length in the solar corona. The ions then decouple from the electrons and the magnetic field lines are frozen into the electron fluid instead of the bulk plasma (Bhattacharjee 2004). At this scales the single fluid MHD is not valid and the collisionless terms that are otherwise neglected in generalized Ohm's law are expected to be important (Bhattacharjee 2004; Morales et al. 2006). Therefore, Ohm's law modifies as (neglecting electron inertia and electrical resistivity),

$$\mathbf{E} + \frac{1}{c}\mathbf{v} \times \mathbf{B} = \frac{1}{ne}\mathbf{J} \times \mathbf{B}, \tag{8.2.1}$$

where n is electron or ion density, e is electron charge, $\mathbf{v}$ is plasma flow velocity and $\mathbf{J}$ is current density. The minimal approximation of such a plasma is then provided by equations of the Hall-MHD where hall term $\frac{1}{ne}\mathbf{J} \times \mathbf{B}$ in Ohm's law imitates a physical diffusivity (Bhattacharjee 2004; Morales et al. 2006). To study the influence of this Hall term in decaying current sheets, we propose to develop a Hall-MHD based numerical model within the general framework of the EULAG.

Appendices

Appendix A

To solve a linear force-free equation, the magnetic field is identified as a Chandrasekhar-Kendall (Chandrasekhar and Kendall 1957) eigenfunction which, in Cartesian coordinate can be written as

$$\mathbf{Y} = \nabla \times \psi \hat{e_y} + \frac{1}{\alpha_0} \nabla \times (\nabla \times \psi \hat{e_y}) \quad , \tag{A.0.1}$$

where $\psi = \psi(x, y, z)$ is a scalar function and α_0 is constant. Substitution of $\mathbf{Y}$ in the linear force-free equation gives,

$$\nabla \times (\nabla \times \nabla \times \psi \hat{e_y} - {\alpha_0}^2 \psi \hat{e_y}) = 0 \quad , \tag{A.0.2}$$

implying,

$$(\nabla \times \nabla \times \psi \hat{e_y} - {\alpha_0}^2 \psi \hat{e_y}) = \nabla \lambda \quad , \tag{A.0.3}$$

where the scalar function $\lambda = \lambda(x, y, z)$ represents an arbitrary gauge. Using the identity

$$\nabla \times \nabla \times \psi \hat{e_y} = -\nabla^2 \psi \hat{e_y} + \nabla(\nabla \cdot \psi \hat{e_y}) \quad , \tag{A.0.4}$$

results in the inhomogeneous vector Helmholtz equation for the magnetic field

$$(\nabla^2 \psi + {\alpha_0}^2 \psi) \hat{e_y} = \nabla(\nabla \cdot \psi \hat{e_y} - \lambda) \quad . \tag{A.0.5}$$

Standardly, a three dimensional analytical solution of the linear force-free equation is obtained by only solving the homogeneous equation which corresponds to the selection of

$$\lambda = \nabla \cdot \psi \hat{e_y} \ , \tag{A.0.6}$$

for the gauge. If $\partial/\partial y \equiv 0$, the solution for the linear force-free equation is gauge independent, and the scalar function ψ satisfies Helmholtz equation

$$\nabla^2 \psi + \alpha_0^2 \psi = 0 \quad . \tag{A.0.7}$$

Consequently, for a geometry relevant to solar corona, the field components are

$$B_{\mathrm{lf}\,x} = k_z \sin(k_x x) \exp\left(-k_z z\right) , \tag{A.0.8}$$

$$B_{\mathrm{lf}\,y} = \sqrt{{k_x}^2 - {k_z}^2} \sin(k_x x) \exp\left(-k_z z\right) , \tag{A.0.9}$$

$$B_{\mathrm{lf}\,z} = k_x \cos(k_x x) \exp\left(-k_z z\right) , \tag{A.0.10}$$

with $\alpha_0 = \sqrt{{k_x}^2 - {k_z}^2}$.

Appendix B

A three dimensional linear force-free field $\mathbf{B}'_{lf}$, with the choice of gauge, has components

$$B'_{lf\,x} = \alpha_0 l_y \sin(l_x x)\cos(l_y y)\exp(-l_z z) - l_x l_z \cos(l_x x)\sin(l_y y)\exp(-l_z z)\,, \tag{B.0.1}$$

$$B'_{lf\,y} = -\alpha_0 l_x \cos(l_x x)\sin(l_y y)\exp(-l_z z) - l_y l_z \sin(l_x x)\cos(l_y y)\exp(-l_z z)\,, \tag{B.0.2}$$

$$B'_{lf\,z} = ({l_x}^2 + {l_y}^2)\sin(l_x x)\sin(l_y y)\exp(-l_z z)\,, \tag{B.0.3}$$

with $\alpha_0 = \sqrt{{l_x}^2 + {l_y}^2 - {l_z}^2}$. The three dimensional simulation is performed with an initial field

$$\mathbf{B}^\star = \mathbf{B} + a_0\mathbf{B}' \tag{B.0.4}$$

where $a_0 = .5$, $\mathbf{B}$ is given by (7.3.1)-(7.3.3) and, $\mathbf{B}'$ (constructed from $\mathbf{B}'_{lf}$) has the components

$$B'_x = \sin(x)\cos(y)\exp\left(-\frac{z}{s_0}\right) - \cos(x)\sin(y)\exp\left(-\frac{z}{s_0}\right), \tag{B.0.5}$$

$$B'_y = -\cos(x)\sin(y)\exp\left(-\frac{z}{s_0}\right) - \sin(x)\cos(y)\exp\left(-\frac{z}{s_0}\right), \tag{B.0.6}$$

$$B'_z = 2s_0\sin(x)\sin(y)\exp\left(-\frac{z}{s_0}\right). \tag{B.0.7}$$

The Lorentz force exerted by the $\mathbf{B}^\star$ is

$$
\begin{aligned}
(\mathbf{J}^\star\times\mathbf{B}^\star)_x &= s_0\left(\frac{1}{2s_0}-s_0\right)\sin x\cos x\sin^2 y\exp\left(-\frac{2z}{s_0}\right)-\frac{1}{2}\sin^2 x\sin^2 y\exp\left(-\frac{2z}{s_0}\right)\\
&+\left(s_0\left({k_x}^2-\frac{{k_z}^2}{s_0}\right)\sin y+\frac{\sqrt{{k_x}^2-{k_z}^2}}{2}(\cos y-\sin y)\right)\sin x\sin(k_x x)\exp\left(-\frac{(1+k_z)z}{s_0}\right)\\
&+\left(s_0k_x\left(\frac{1}{2s_0}-s_0\right)\cos x-\frac{k_x}{2}\sin x\right)\cos(k_x x)\sin y\exp\left(-\frac{(1+k_z)z}{s_0}\right)\\
&+\left(\frac{s_0k_x}{2}\left(s_0{k_x}^2-\frac{{k_z}^2}{s_0}\right)-\frac{k_x({k_x}^2-{k_z}^2)}{2}\right)\sin(2k_x x)\exp\left(-\frac{2k_z z}{s_0}\right)\\
&+\frac{1}{4}\sin x(\sin y-\cos y)\left(\cos x\sin y-\sin x\cos y\right)\exp\left(-\frac{2z}{s_0}\right)\\
&+\frac{k_x\sqrt{{k_x}^2-{k_z}^2}}{2}\cos(k_x x)\left(\cos x\sin y-\sin x\cos y\right)\exp\left(-\frac{(1+k_z)z}{s_0}\right),
\end{aligned}
\tag{B.0.8}
$$

$$
\begin{aligned}
(\mathbf{J}^\star\times\mathbf{B}^\star)_y &= s_0\left(\frac{1}{2}-s_0\right)\sin^2 x\sin y\cos y\exp\left(-\frac{2z}{s_0}\right)+\sin x\cos x\sin^2 y\exp\left(-\frac{2z}{s_0}\right)\\
&+\frac{1}{4}\sin x(\sin y-\cos y)\left(\sin x\sin y-\cos x\sin y\right)\exp\left(-\frac{2z}{s_0}\right)\\
&+\frac{k_x\sqrt{{k_x}^2-{k_z}^2}}{2}\cos(k_x x)\left(\sin x\sin y-\cos x\sin y\right)\exp\left(-\frac{(1+k_z)z}{s_0}\right)\\
&+\left(\frac{k_z}{2}(\sin y-\cos y)-k_z\sqrt{{k_x}^2-{k_z}^2}\right)\sin x\sin(k_x x)\exp\left(-\frac{(1+k_z)z}{s_0}\right)\\
&+\left(k_z\left(\frac{1}{2}-s_0\right)\sin x\cos y+k_x\cos x\sin y\right)\cos(k_x x)\exp\left(-\frac{(1+k_z)z}{s_0}\right),
\end{aligned}
\tag{B.0.9}
$$

$$
\begin{aligned}
(\mathbf{J}^\star\times\mathbf{B}^\star)_z &= \left(\frac{\sin x}{4s_0}-\left(\frac{1}{2s_0}-s_0\right)\frac{\cos x}{2}\right)\sin y\left(\sin x\sin y-\cos x\sin y\right)\exp\left(-\frac{2z}{s_0}\right)\\
&+\left(\frac{1}{2}\left(\frac{1}{2}-s_0\right)\sin x\cos y+\frac{1}{2s_0}\cos x\sin y\right)\left(\cos x\sin y-\sin x\cos y\right)\exp\left(-\frac{2z}{s_0}\right)\\
&+\frac{k_z\sqrt{{k_x}^2-{k_z}^2}}{2s_0}\sin(k_x x)\left(\cos x\sin y-\sin x\cos y\right)\exp\left(-\frac{(1+k_z)z}{s_0}\right)\\
&-\left(\sqrt{{k_x}^2-{k_z}^2}\left(\frac{1}{2}-s_0\right)\sin x\cos y+\frac{\sqrt{{k_x}^2-{k_z}^2}}{s_0}\cos x\sin y\right)\sin(k_x x)\exp\left(-\frac{(1+k_z)z}{s_0}\right)\\
&+\left(\frac{k_z({k_x}^2-{k_z}^2)}{s_0}+k_z\left(\frac{{k_z}^2}{s_0}-s_0{k_x}^2\right)\right)\sin^2(k_x x)\exp\left(-\frac{2k_z z}{s_0}\right)\\
&+\frac{1}{2}\left(\frac{{k_z}^2}{s_0}-s_0{k_x}^2\right)\sin(k_x x)\left(\sin x\sin y-\cos x\sin y\right)\exp\left(-\frac{(1+k_z)z}{s_0}\right)\\
&+\left(\frac{k_z}{2s_0}\sin x-k_z\left(\frac{1}{2s_0}-s_0\right)\cos x\right)\sin(k_x x)\sin y\exp\left(-\frac{(1+k_z)z}{s_0}\right).
\end{aligned}
\tag{B.0.10}
$$

Appendix C

The force-free field $\mathbf{B}_{\mathrm{lf}}$ (Appendix A) reduces to a two-dimensional potential field $\mathbf{B}_p$ with $k_x = k_z = k$. Then, the components of the $\mathbf{B}_p$ are

$$B_{p_x} = k\sin(kx)\exp\left(-kz\right), \tag{C.0.1}$$

$$B_{p_y} = 0, \tag{C.0.2}$$

$$B_{p_z} = k\cos(kx)\exp\left(-kz\right), \tag{C.0.3}$$

with $\alpha_0 = 0$. The additional three dimensional simulation is conducted with the initial field

$$\mathbf{B}^{\star\star} = \mathbf{B}^{\star} + \mathbf{B}_p' \tag{C.0.4}$$

where $\mathbf{B}^{\star}$ is given by (B.0.4) (Appendix B) and $\mathbf{B}_p'$ (derived from the $\mathbf{B}_p$) has the components

$$B_{p_x}' = \sin(x)\exp\left(-\frac{z}{s_0}\right), \tag{C.0.5}$$

$$B_{p_y}' = 0, \tag{C.0.6}$$

$$B_{p_z}' = s_0\cos(x)\exp\left(-\frac{z}{s_0}\right). \tag{C.0.7}$$

The functional form of the Lorentz force applied by $\mathbf{B}^{\star\star}$ is

$$
\begin{aligned}
(\mathbf{J}^{\star\star} \times \mathbf{B}^{\star\star})_x = (\mathbf{J}^{\star} \times \mathbf{B}^{\star})_x &+ \left(s_0 \left(s_0 - \frac{1}{s_0} \right) \sin^2 x \sin y - \sin 2x \right) \exp\left(-\frac{2z}{s_0} \right) \\
&+ \left(s_0 \left(s_0 - \frac{1}{s_0} \right) \sin x \cos x + s_0 \left(\frac{1}{2s_0} - s_0 \right) \cos^2 x \sin y \right) \exp\left(-\frac{2z}{s_0} \right) \\
&+ s_0 \left(s_0 {k_x}^2 - \frac{{k_z}^2}{s_0} \right) \cos x \sin(k_x x) \exp\left(-\frac{(1+k_z)z}{s_0} \right) \\
&+ s_0 k_x \left(s_0 - \frac{1}{s_0} \right) \sin x \cos(k_y y) \exp\left(-\frac{(1+k_z)z}{s_0} \right),
\end{aligned}
\tag{C.0.8}
$$

$$
\begin{aligned}
(\mathbf{J}^{\star\star} \times \mathbf{B}^{\star\star})_y = (\mathbf{J}^{\star} \times \mathbf{B}^{\star})_y &+ \left(\frac{\sin^2 x}{2} (\sin y - \cos y) + \cos^2 x \sin y \right) \exp\left(-\frac{2z}{s_0} \right) \\
&- s_0 \left(s_0 - \frac{1}{2} \right) \sin x \cos x \cos y \exp\left(-\frac{2z}{s_0} \right) \\
&+ k_x \sqrt{{k_x}^2 - {k_z}^2} \left(\sin x \cos(k_x x) - \cos x \sin(k_x x) \right) \exp\left(-\frac{(1+k_z)z}{s_0} \right),
\end{aligned}
\tag{C.0.9}
$$

$$
\begin{aligned}
(\mathbf{J}^{\star\star} \times \mathbf{B}^{\star\star})_z = (\mathbf{J}^{\star} \times \mathbf{B}^{\star})_z &- \left(\left(\frac{1}{2s_0} - s_0 \right) \frac{\sin 2x}{2} \sin y + \frac{\sin^2 x}{2s_0} \sin y \right) \exp\left(-\frac{2z}{s_0} \right) \\
&- \left(s_0 - \frac{1}{2} \right) \sin x \left(\frac{1}{2} (\sin x \sin y - \cos x \sin y) + \sin x \right) \exp\left(-\frac{2z}{s_0} \right) \\
&+ \left(k_z \left(s_0 - \frac{1}{s_0} \right) - \left(s_0 {k_x}^2 - \frac{{k_z}^2}{s_0} \right) \right) \sin x \sin(k_x x) \exp\left(-\frac{(1+k_z)z}{s_0} \right).
\end{aligned}
\tag{C.0.10}
$$

Bibliography

Alfvén, H.: 1942, *Nature* **150**, 405

Amari, T. and Aly, J. J.: 1990, *Astron. Astrophys.* **231**, 213

Amari, T. and Aly, J. J.: 1992, *Astron. Astrophys.* **265**, 791

Amari, T., Luciani, J. F., Aly, J. J., Mikic, Z., and Linker, J.: 2003, *Astrophys. J.* **585**, 1073

Amari, T., Luciani, J. F., Mikic, Z., and Linker, J.: 1999, *Astrophys. J.* **518**, L57

Aschwanden, M. J.: 2005, *Physics of the Solar Corona. An Introduction with Problems and Solutions (2nd edition)*, Springer

Aulanier, G., Pariat, E., and Démoulin, P.: 2005, *Astron. Astrophys.* **444**, 961

Aulanier, G., Török, T., Démoulin, P., and DeLuca, E. E.: 2010, *Astrophys. J.* **708**, 314

Beaudoin, P., Charbonneau, P., Racine, E., and Smolarkiewicz, P. K.: 2013, *Solar Phys.* **282**, 335

Bellan, P. M.: 2008, *Fundamentals of Plasma Physics*, Cambridge University Press

Berger, M. A.: 1997, *J. Geophys. Res.* **102**, 2637

Berger, M. A. and Field, G. B.: 1984, *Journal of Fluid Mechanics* **147**, 133

Bhattacharjee, A.: 2004, *Ann. Rev. Astron. Astrophys.* **42**, 365

Bhattacharyya, R. and Janaki, M. S.: 2004, *Physics of Plasmas* **11**, 5615

Bhattacharyya, R., Janaki, M. S., and Dasgupta, B.: 2000, *Physics of Plasmas* **7**, 4801

Bhattacharyya, R., Janaki, M. S., and Dasgupta, B.: 2003, *Plasma Physics and Controlled Fusion* **45**, 63

Bhattacharyya, R., Low, B. C., and Smolarkiewicz, P. K.: 2010, *Physics of Plasmas* **17(11)**, 112901

Book, D. L., Boris, J. P., and Hain, K.: 1975, *Journal of Computational Physics* **18**, 248

Boris, J. P. and Book, D. L.: 1973, *Journal of Computational Physics* **11**, 38

Boris, J. P. and Book, D. L.: 1976, *Journal of Computational Physics* **20**, 397

Born, M. and Wolf, E.: 1975, *Principles of optics. Electromagnetic theory of propagation, interference and diffraction of light*, Cambridge University Press

Brown, J. C.: 1971, *Solar Phys.* **18**, 489

Carcedo, L., Brown, D. S., Hood, A. W., Neukirch, T., and Wiegelmann, T.: 2003, *Solar Phys.* **218**, 29

Carmichael, H.: 1964, *NASA Special Publication* **50**, 451

Chandrasekhar, S. and Kendall, P. C.: 1957, *Astrophys. J.* **126**, 457

Chen, P. F.: 2011, *Living Reviews in Solar Physics* 8

Cheng, X., Zhang, J., Liu, Y., and Ding, M. D.: 2011, *Astrophys. J.* **732**, L25

Chifor, C., Tripathi, D., Mason, H. E., and Dennis, B. R.: 2007, *Astron. Astrophys.* **472**, 967

Chiuderi, C., Giachetti, R., and van Hoven, G.: 1977, *Solar Phys.* **54**, 107

Cho, K.-S., Lee, J., Bong, S.-C., Kim, Y.-H., Joshi, B., and Park, Y.-D.: 2009, *Astrophys. J.* **703**, 1

Choe, G. S. and Lee, L. C.: 1996, *Astrophys. J.* **472**, 372

Choudhuri, A. R.: 1998, *The Physics of Fluids and Plasmas: An Introduction for Astrophysicists*, Cambridge University Press

Choudhuri, A. R.: 2010, *Astrophysics for Physicists*, Cambridge University Press

Clyne, J. and Rast, M.: 2005, in R. F. Erbacher, J. C. Roberts, M. T. Gröhn, and K. Börner (eds.), *Visualization and Data Analysis 2005*, Vol. 5669, pp 284–294

Craig, I. J. D. and Effenberger, F.: 2014, *Astrophys. J.* **795**, 129

Craig, I. J. D. and Litvinenko, Y. E.: 2005, *Physics of Plasmas* **12(3)**, 032301

Craig, I. J. D. and Pontin, D. I.: 2014, *Astrophys. J.* **788**, 177

Daglis, I. A., Thorne, R. M., Baumjohann, W., and Orsini, S.: 1999, *Reviews of Geophysics* **37**, 407

Dahlburg, R. B., Antiochos, S. K., and Zang, T. A.: 1991, *Astrophys. J.* **383**, 420

Dasgupta, B., Janaki, M. S., Bhattacharyya, R., Dasgupta, P., Watanabe, T., and Sato, T.: 2002, *Phys. Rev. E* **65(4)**, 046405

del Toro Iniesta, J. C.: 2003, *Introduction to Spectropolarimetry*, Cambridge University Press

Démoulin, P.: 2006, *Advances in Space Research* **37**, 1269

Demoulin, P., Priest, E. R., and Anzer, U.: 1989, *Astron. Astrophys.* **221**, 326

DeVore, C. R. and Antiochos, S. K.: 2000, *Astrophys. J.* **539**, 954

Domaradzki, J. A. and Radhakrishnan, S.: 2005, *Fluid Dynamics Research* **36**, 385

Domaradzki, J. A., Xiao, Z., and Smolarkiewicz, P. K.: 2003, *Physics of Fluids* **15**, 3890

Drenkhahn, G. and Spruit, H. C.: 2002, *Astron. Astrophys.* **391**, 1141

Dungey, J. W.: 1961, *J. Geophys. Res.* **66**, 1043

Eisenstat, S. C.: 1983, *SIAM Journal on Numerical Analysis* **20**, 358

Eisenstat, S. C., Elman, H. C., and Martin, H. S.: 1983, *SIAM Journal on Numerical Analysis* **20**, 345357

Fan, Y.: 2001, *Astrophys. J.* **554**, L111

Fan, Y.: 2010, *Astrophys. J.* **719**, 728

Fan, Y.: 2011, *Astrophys. J.* **740**, 68

Fan, Y. and Gibson, S. E.: 2003, *Astrophys. J.* **589**, L105

Fan, Y. and Gibson, S. E.: 2004, *Astrophys. J.* **609**, 1123

Fletcher, L., Dennis, B. R., Hudson, H. S., Krucker, S., Phillips, K., Veronig, A., Battaglia, M., Bone, L., Caspi, A., Chen, Q., Gallagher, P., Grigis, P. T., Ji, H., Liu, W., Milligan, R. O., and Temmer, M.: 2011, *Space Sci. Rev.* **159**, 19

Foukal, P. V.: 1976, *Astrophys. J.* **210**, 575

Galsgaard, K. and Nordlund, Å.: 1997, *J. Geophys. Res.* **102**, 231

Gary, G. A.: 2001, *Solar Phys.* **203**, 71

Gershberg, R. E.: 1983, in P. B. Byrne and M. Rodono (eds.), *IAU Colloq. 71: Activity in Red-Dwarf Stars*, Vol. 102 of *Astrophysics and Space Science Library*, pp 487–495

Ghizaru, M., Charbonneau, P., and Smolarkiewicz, P. K.: 2010, *Astrophys. J.* **715**, L133

Giannios, D.: 2010, *Mon. Not. Roy. Astron. Soc.* **408**, L46

Gibson, S. E. and Fan, Y.: 2006, *Journal of Geophysical Research (Space Physics)* **111**, A12103

Goedbloed, J. P. and Hagebeuk, H. J. L.: 1972, *Physics of Fluids* **15**, 1090

Goldston, R. J. and Rutherford, P. H.: 1995, *Introduction to Plasma Physics*, Institute of Physics Publishing

Golub, L., Bookbinder, J., Deluca, E., Karovska, M., Warren, H., Schrijver, C. J., Shine, R., Tarbell, T., Title, A., Wolfson, J., Handy, B., and Kankelborg, C.: 1999, *Physics of Plasmas* **6**, 2205

Golub, L. and Pasachoff, J. M.: 1997, *The Solar Corona*, Cambridge University Press

Gopalswamy, N., Yashiro, S., Vourlidas, A., Lara, A., Stenborg, G., Kaiser, M. L., and Howard, R. A.: 2004, in *American Astronomical Society Meeting Abstracts #204*, Vol. 36 of *Bulletin of the American Astronomical Society*, p. 738

Griebel, M., Dornseifer, T., and Neunhoeffer, T.: 1998, *Numerical simulation in fluid dynamics: a practical introduction*, the Society for Industrial and Applied Mathematics

Grinstein, F. F., Margolin, L. G., and Rider, W. J. (eds.): 2007, *Implicit Large Eddy Simulation: Computing Turbulent Fluid Dynamics*, Combridge Univeristy Press

Hasegawa, A.: 1985, *Advances in Physics* **34**, 1

Heyvaerts, J. and Priest, E. R.: 1984, *Astron. Astrophys.* **137**, 63

Hirayama, T.: 1974, *Solar Phys.* **34**, 323

Howard, T. A. and Tappin, S. J.: 2009, *Space Sci. Rev.* **147**, 31

Illing, R. M. E. and Hundhausen, A. J.: 1985, *J. Geophys. Res.* **90**, 275

Janse, A. M. and Low, B. C.: 2009, *Astrophys. J.* **690**, 1089

Joshi, B., Veronig, A. M., Lee, J., Bong, S.-C., Tiwari, S. K., and Cho, K.-S.: 2011, *Astrophys. J.* **743**, 195

Klimchuk, J. A.: 2006, *Solar Phys.* **234**, 41

Kohl, J. L., Noci, G., Antonucci, E., Tondello, G., Huber, M. C. E., Gardner, L. D., Nicolosi, P., Strachan, L., Fineschi, S., Raymond, J. C., Romoli, M., Spadaro, D., Panasyuk, A., Siegmund, O. H. W., Benna, C., Ciaravella, A., Cranmer, S. R., Giordano, S., Karovska, M., Martin, R., Michels, J., Modigliani, A., Naletto, G., Pernechele, C., Poletto, G., and Smith, P. L.: 1997, *Solar Phys.* **175**, 613

Kopp, R. A. and Pneuman, G. W.: 1976, *Solar Phys.* **50**, 85

Krucker, S., Battaglia, M., Cargill, P. J., Fletcher, L., Hudson, H. S., MacKinnon, A. L., Masuda, S., Sui, L., Tomczak, M., Veronig, A. L., Vlahos, L., and White, S. M.: 2008, *Astron. Astrophys. Rev.* **16**, 155

Kumar, D. and Bhattacharyya, R.: 2011, *Physics of Plasmas* **18(8)**, 084506

Kumar, D., Bhattacharyya, R., and Smolarkiewicz, P. K.: 2013, *Physics of Plasmas* **20(11)**, 112903

Kumar, D., Bhattacharyya, R., and Smolarkiewicz, P. K.: 2015a, *Physics of Plasmas* **22(1)**, 012902

Kumar, P., Yurchyshyn, V., Wang, H., and Cho, K.-S.: 2015b, *Astrophys. J.* **809**, 83

Kumar, S. and Bhattacharyya, R.: 2016, *Physics of Plasmas* **23(4)**, 044501

Kumar, S., Bhattacharyya, R., Joshi, B., and Smolarkiewicz, P. K.: 2016, *Astrophys. J.* p. (in press)

Kumar, S., Bhattacharyya, R., and Smolarkiewicz, P. K.: 2014, *Physics of Plasmas* **21(5)**, 052904

Kumar, S., Bhattacharyya, R., and Smolarkiewicz, P. K.: 2015c, *Physics of Plasmas* **22(8)**, 082903

Kuperus, M., Ionson, J. A., and Spicer, D. S.: 1981, *Ann. Rev. Astron. Astrophys.* **19**, 7

Kusano, K., Maeshiro, T., Miike, H., Yokoyama, T., and Sakurai, T.: 2004, *J. Plasma Fusion Res. SERIES* **6**, 115

Kusano, K., Suzuki, Y., Kubo, H., Miyoshi, T., and Nishikawa, K.: 1994, *Astrophys. J.* **433**, 361

Kushwaha, U., Joshi, B., Cho, K.-S., Veronig, A., Tiwari, S. K., and Mathew, S. K.: 2014, *Astrophys. J.* **791**, 23

Kushwaha, U., Joshi, B., Veronig, A. M., and Moon, Y.-J.: 2015, *Astrophys. J.* **807**, 101

Lang, K. R.: 2006, *Sun, Earth and Sky*, Springer

Lau, Y.-T. and Finn, J. M.: 1990, *Astrophys. J.* **350**, 672

Leka, K. D., Canfield, R. C., McClymont, A. N., and van Driel-Gesztelyi, L.: 1996, *Astrophys. J.* **462**, 547

Lin, R. P., Krucker, S., Hurford, G. J., Smith, D. M., Hudson, H. S., Holman, G. D., Schwartz, R. A., Dennis, B. R., Share, G. H., Murphy, R. J., Emslie, A. G., Johns-Krull, C., and Vilmer, N.: 2003, *Astrophys. J.* **595**, L69

Longcope, D. W. and Parnell, C. E.: 2009, *Solar Phys.* **254**, 51

Low, B. C.: 1996, *Solar Phys.* **167**, 217

Low, B. C.: 2001, *J. Geophys. Res.* **106**, 25141

Low, B. C.: 2006, *Astrophys. J.* **649**, 1064

Low, B. C.: 2011, *Physics of Plasmas* **18(5)**, 052901

Low, B. C.: 2015, *Science China Physics, Mechanics, and Astronomy* **58(1)**, 5626

Mackay, D. H., Gaizauskas, V., and Yeates, A. R.: 2008, *Solar Phys.* **248**, 51

Margolin, L. G., Rider, W. J., and Grinstein, F. F.: 2006, *Journal of Turbulence* **7**, N15

Masuda, S., Kosugi, T., Hara, H., Tsuneta, S., and Ogawara, Y.: 1994, *Nature* **371**, 495

Mellor, C., Gerrard, C. L., Galsgaard, K., Hood, A. W., and Priest, E. R.: 2005, *Solar Phys.* **227**, 39

Milligan, R. O., Gallagher, P. T., Mathioudakis, M., and Keenan, F. P.: 2006, *Astrophys. J.* **642**, L169

Morales, L. F., Dasso, S., Gómez, D. O., and Mininni, P. D.: 2006, *Advances in Space Research* **37**, 1287

Mullan, D. J.: 1986, *NASA Special Publication* 492

Müller, D., Marsden, R. G., St. Cyr, O. C., and Gilbert, H. R.: 2013, *Solar Phys.* **285**, 25

Nandy, D., Hahn, M., Canfield, R. C., and Longcope, D. W.: 2003, *Astrophys. J.* **597**, L73

Nandy, D., Hahn, M., Canfield, R. C., and Longcope, D. W.: 2004, in A. V. Stepanov, E. E. Benevolenskaya, and A. G. Kosovichev (eds.), *Multi-Wavelength Investigations of Solar Activity*, Vol. 223 of *IAU Symposium*, pp 473–474

Ohyama, M. and Shibata, K.: 1998, *Astrophys. J.* **499**, 934

Ohyama, M., Shibata, K., Yokoyama, T., and Shimojo, M.: 1997, *Advances in Space Research* **19**, 1849

Ortolani, S. and Schnack, D. D.: 1993, *Magnetohydrodynamics of Plasma Relaxation*, World Scientific Publishing Co. Pte. Ltd.

Pallavicini, R., Serio, S., and Vaiana, G. S.: 1977, *Astrophys. J.* **216**, 108

Parenti, S.: 2014, *Living Reviews in Solar Physics* 11

Parker, E. N.: 1957, *J. Geophys. Res.* **62**, 509

Parker, E. N.: 1972, *Astrophys. J.* **174**, 499

Parker, E. N.: 1988, *Astrophys. J.* **330**, 474

Parker, E. N.: 1989a, *Geophysical and Astrophysical Fluid Dynamics* **45**, 159

Parker, E. N.: 1989b, *Geophysical and Astrophysical Fluid Dynamics* **45**, 169

Parker, E. N.: 1989c, *Geophysical and Astrophysical Fluid Dynamics* **46**, 105

Parker, E. N.: 1990, *Geophysical and Astrophysical Fluid Dynamics* **50**, 229

Parker, E. N.: 1994, *Spontaneous current sheets in magnetic fields : with applications to stellar x-rays. International Series in Astronomy and Astrophysics, Vol. 1. New York : Oxford University Press, 1994.* 1

Parker, E. N.: 2005, in D. E. Innes, A. Lagg, and S. A. Solanki (eds.), *Chromospheric and Coronal Magnetic Fields*, Vol. 596 of *ESA Special Publication*, p. 1.1

Parker, E. N.: 2012, *Plasma Physics and Controlled Fusion* **54(12)**, 124028

Pesnell, W.: 2010, in *38th COSPAR Scientific Assembly*, Vol. 38 of *COSPAR Meeting*, p. 2

Petschek, H. E.: 1964, *NASA Special Publication* **50**, 425

Poletto, G., Pallavicini, R., and Kopp, R. A.: 1988, *Astron. Astrophys.* **201**, 93

Pontin, D. I.: 2012, *Philosophical Transactions of the Royal Society of London Series A* **370**, 3169

Pontin, D. I. and Huang, Y.-M.: 2012, *Astrophys. J.* **756**, 7

Priest, E.: 2014, *Magnetohydrodynamics of the Sun*, Cambridge University Press

Priest, E. and Forbes, T.: 2006, *Magnetic Reconnection: MHD Theory and Applications*, Cambridge University Press

Priest, E. R. and Démoulin, P.: 1995, *J. Geophys. Res.* **100**, 23443

Priest, E. R. and Forbes, T. G.: 1986, *J. Geophys. Res.* **91**, 5579

Priest, E. R., Heyvaerts, J. F., and Title, A. M.: 2002, *Astrophys. J.* **576**, 533

Priest, E. R., Hood, A. W., and Anzer, U.: 1989, *Astrophys. J.* **344**, 1010

Priest, E. R. and Titov, V. S.: 1996, *Proceedings of the Royal Society of London Series A* **354**, 2951

Prusa, J. M. and Smolarkiewicz, P. K.: 2003, *Journal of Computational Physics* **190**, 601

Prusa, J. M., Smolarkiewicz, P. K., and Wyszogrodzki, A. A.: 2008, *Computers Fluids* **37**, 11931207

Pulkkinen, T.: 2007, *Living Reviews in Solar Physics* 4

Raeder, J.: 2006, *Annales Geophysicae* **24**, 381

Reynolds, R. J., Haffner, L. M., and Tufte, S. L.: 1999, *Astrophys. J.* **525**, L21

Rider, W. J.: 2006, *International Journal for Numerical Methods in Fluids* **50**, 1145

Romanova, M. M. and Lovelace, R. V. E.: 1992, *Astron. Astrophys.* **262**, 26

Ruderman, M. S. and Roberts, B.: 2002, *Astrophys. J.* **577**, 475

Rust, D. M. and Kumar, A.: 1996, *Astrophys. J.* **464**, L199

Sarff, J., Almagri, A., Anderson, J., Brower, D., Craig, D., Deng, B., den Hartog, D., Ding, W., Fiksel, G., Forest, C., Mirnov, V., Prager, S., and Svidzinski, V.: 2005, in K. T. Chyzy, K. Otmianowska-Mazur, M. Soida, and R.-J. Dettmar (eds.), *The Magnetized Plasma in Galaxy Evolution*, pp 48–55

Schmieder, B., van Driel-Gesztelyi, L., Aulanier, G., Démoulin, P., Thompson, B., De Forest, C., Wiik, J. E., Saint Cyr, C., and Vial, J. C.: 2002, *Advances in Space Research* **29**, 1451

Shibata, K.: 1996, *Advances in Space Research* 17

Shibata, K.: 1997, in A. Wilson (ed.), *Fifth SOHO Workshop: The Corona and Solar Wind Near Minimum Activity*, Vol. 404 of *ESA Special Publication*, p. 103

Shibata, K. and Magara, T.: 2011, *Living Reviews in Solar Physics* 8

Shibata, K., Masuda, S., Shimojo, M., Hara, H., Yokoyama, T., Tsuneta, S., Kosugi, T., and Ogawara, Y.: 1995, *Astrophys. J.* **451**, L83

Smolarkiewicz, P. and Szmelter, J.: 2011, *Acta Geophysica* **59**, 1109

Smolarkiewicz, P. K.: 1983, *Monthly Weather Review* **111**, 479

Smolarkiewicz, P. K.: 1984, *Journal of Computational Physics* **54**, 325

Smolarkiewicz, P. K.: 1991, *Monthly Weather Review* **119**, 2505

Smolarkiewicz, P. K.: 2006, *International Journal for Numerical Methods in Fluids* **50**, 1123

Smolarkiewicz, P. K. and Charbonneau, P.: 2013, *Journal of Computational Physics* **236**, 608

Smolarkiewicz, P. K. and Clark, T. L.: 1986, *Journal of Computational Physics* **67**, 396

Smolarkiewicz, P. K. and Grabowski, W. W.: 1990, *Journal of Computational Physics* **86**, 355

Smolarkiewicz, P. K., Grubišić, V., and Margolin, L. G.: 1997, *Monthly Weather Review* **125**, 647

Smolarkiewicz, P. K. and Margolin, L. G.: 1993, *Monthly Weather Review* **121**, 1847

Smolarkiewicz, P. K. and Margolin, L. G.: 1997, *Atmosphere Ocean* **35**, 127

Smolarkiewicz, P. K. and Margolin, L. G.: 1998, *Journal of Computational Physics* **140**, 459

Smolarkiewicz, P. K. and Prusa, J. M.: 2002, *International Journal for Numerical Methods in Fluids* **39**, 799

Smolarkiewicz, P. K. and Pudykiewicz, J. A.: 1992, *Journal of Atmospheric Sciences* **49**, 2082

Smolarkiewicz, P. K. and Szmelter, J.: 2009, *Journal of Computational Physics* **228**, 33

Spitzer, L.: 1962, *Physics of Fully Ionized Gases*

Stern, D.: 1967, *J. Geophys. Res.* **72**, 3995

Stern, D. P.: 1970, *American Journal of Physics* **38**, 494

Stern, D. P.: 1976, *Reviews of Geophysics and Space Physics* **14**, 199

Stevenson, J. E. H., Parnell, C. E., Priest, E. R., and Haynes, A. L.: 2015, *Astron. Astrophys.* **573**, A44

Sturrock, P. A.: 1966, *Nature* **211**, 695

Sweet, P. A.: 1958, in B. Lehnert (ed.), *Electromagnetic Phenomena in Cosmical Physics*, Vol. 6 of *IAU Symposium*, p. 499

Syrovatskii, S. I. and Shmeleva, O. P.: 1972, *Sov. Astronom.* **16**, 273

Taylor, J. B.: 1974, *Physical Review Letters* **33**, 1139

Taylor, J. B.: 1986, *Reviews of Modern Physics* **58**, 741

Taylor, J. B.: 2000, *Physics of Plasmas* **7**, 1623

Temmer, M., Veronig, A. M., Kontar, E. P., Krucker, S., and Vršnak, B.: 2010, *Astrophys. J.* **712**, 1410

Temmer, M., Veronig, A. M., Vršnak, B., Rybák, J., Gömöry, P., Stoiser, S., and Maričić, D.: 2008, *Astrophys. J.* **673**, L95

Tsuneta, S.: 1996, *Astrophys. J.* **456**, L63

van Ballegooijen, A. A. and Cranmer, S. R.: 2010, *Astrophys. J.* **711**, 164

van Ballegooijen, A. A. and Martens, P. C. H.: 1989, *Astrophys. J.* **343**, 971

Verbunt, F.: 1982, *Space Sci. Rev.* **32**, 379

Vourlidas, A., Buzasi, D., Howard, R. A., and Esfandiari, E.: 2002, in A. Wilson (ed.), *Solar Variability: From Core to Outer Frontiers*, Vol. 506 of *ESA Special Publication*, pp 91–94

Vourlidas, A. and Howard, R. A.: 2006, *Astrophys. J.* **642**, 1216

Wheatland, M. S.: 1999, *Astrophys. J.* **518**, 948

Wiegelmann, T. and Sakurai, T.: 2012, *Living Reviews in Solar Physics* 9

Wiegelmann, T. and Solanki, S. K.: 2004, *Solar Phys.* **225**, 227

Wilmot-Smith, A. L.: 2015, *Philosophical Transactions of the Royal Society of London Series A* **373**, 20140265

Woltjer, L.: 1958, *Proceedings of the National Academy of Science* **44**, 489

Xia, C., Keppens, R., and Guo, Y.: 2014, *Astrophys. J.* **780**, 130

Zweibel, E. G. and Yamada, M.: 2009, *Ann. Rev. Astron. Astrophys.* **47**, 291

Publications attached with the thesis

1. *On the role of topological complexity in spontaneous development of current sheets*, **Sanjay Kumar**, R. Bhattacharyya, and P. K. Smolarkiewicz, Physics of Plasmas, **22**, 082903 (2015).

2. *Continuous development of current sheets near and away from magnetic nulls*, **Sanjay Kumar** and R. Bhattacharyya, Physics of Plasmas, **23**, 044501 (2016).

On the role of topological complexity in spontaneous development of current sheets

Sanjay Kumar,[1] R. Bhattacharyya,[1] and P. K. Smolarkiewicz[2]
[1]Udaipur Solar Observatory, Physical Research Laboratory, Dewali, Bari Road, Udaipur-313001, India
[2]European Centre for Medium-Range Weather Forecasts, Reading RG2 9AX, United Kingdom

(Received 12 May 2015; accepted 30 July 2015; published online 24 August 2015)

The computations presented in this work aim to asses the importance of field line interlacing on spontaneous development of current sheets. From Parker's magnetostatic theorem, such development of current sheets is inevitable in a topologically complex magnetofluid, with infinite electrical conductivity, at equilibrium. Relevant initial value problems are constructed by superposition of two untwisted component fields, each component field being represented by a pair of global magnetic flux surface. The intensity of field line interlacing is then specified by the relative amplitude of the two superposed fields. The computations are performed by varying this relative amplitude. Also to have a direct visualization of current sheet formation, we follow the evolution of flux surfaces instead of the vector magnetic field. An important finding of this paper is in the demonstration that initial field lines having intense interlacing tend to develop current sheets which are distributed throughout the computational domain with no preference for topologically favorable sites like magnetic nulls or field reversal layers. The onsets of these current sheets are attributed to favorable contortions of magnetic flux surfaces where two oppositely directed parts of the same field line or different field lines come to close proximity. However, for less intensely interlaced field lines, the simulations indicate development of current sheets at sites only where the magnetic topology is favorable. These current sheets originate as two sets of anti-parallel complimentary field lines press onto each other.
[http://dx.doi.org/10.1063/1.4928883]

I. INTRODUCTION

According to Parker's magnetostatic theorem,[1–4] formation of tangential discontinuities, or current sheets (CSs), is inevitable in an equilibrium magnetofluid with infinite electrical conductivity and complex magnetic topology. This development of CSs is attributed to a general failure of magnetic field in achieving force balance everywhere and simultaneously preserving its topology, while remaining spatially continuous. Such CSs also develop in a magnetofluid undergoing topology preserving evolution toward an equilibrium, if the topology is complex. This requirement of topological complexity in onset of CSs is inherent to the magnetostatic theorem. In its skeletal form, the theorem utilizes relaxation of a magnetofluid with infinite electrical conductivity and low plasma β to obtain a terminal magnetic field $\mathbf{B}$ satisfying

$$\nabla \times \mathbf{B} = \alpha(\mathbf{r})\mathbf{B}, \tag{1}$$

where $\alpha(\mathbf{r})$ is a scalar function of position and represents magnetic circulation per unit flux.[3] The solenoidality of $\mathbf{B}$ further restricts $\alpha(\mathbf{r})$ to obey

$$\mathbf{B} \cdot \nabla\alpha(\mathbf{r}) = 0, \tag{2}$$

resulting in the stringent condition that the magnetic circulation per unit flux for each magnetic field line (MFL) is constant along that MFL. It is then expected that different MFLs located at the neighborhood of a given field line will be wrapped around it. An extension of this wrapping to every MFL leads to interlaced field lines, which we identify as a measure of topological complexity. From (1), it is straightforward to identify this interlacing with a non-zero field-aligned current quantified by $\mathbf{J} \cdot \mathbf{B}$, where $\mathbf{J} = \nabla \times \mathbf{B}$ is the total volume current density. Further arguments establish these MFLs satisfying (1) to have opposite chiralities at different locations and thereby violate the constancy of $\alpha(\mathbf{r})$ along a field line. The magnetostatic theorem provides a circumvention of this violation by generating CSs across which the magnetic field is discontinuous. Notably, the ubiquity of (2) associates a connotation of spontaneity to the development of these CSs.

Such spontaneous development of CSs is also intuitive in an evolving magnetofluid with infinite electrical conductivity where the Alfvèn's flux-freezing theorem[5] is satisfied and MFLs at every instant are tied to fluid parcels. The evolution of a surface generated by the loci of these field lines, a magnetic flux surface (MFS), is then identical in motion to a fluid surface identified by the fluid parcels to which these MFLs are tied. Under forcing, this fluid surface along with the corresponding MFS contorts, and develops CSs if the contortion is favorable.[9] In high Reynolds number ($R_M = vL/\eta$, in usual notations) magnetofluids like astrophysical plasmas, the CSs are natural sites where the magnetofluid gets locally diffusive because of a reduction in characteristic length L. The MFLs across a CS then undergo magnetic reconnection (MR), generating mass outflow and heat.[4] After reconnection, the condition of flux-freezing is restored, resulting in an expunge of reconnected MFLs frozen to the mass outflow. These reconnected field lines push onto other MFLs and may create secondary CSs which lead to further reconnections. In a recent numerical demonstration,[6] this formation of secondary CSs and subsequent reconnections were identified as a possible cause for generating various magnetic structures, some duplicating magnetic antics of the Sun. The process of secondary CS development and their decay through MRs is then expected to be continued—intermittent in space and time—until the magnetic energy achieves an allowable lower bound. In Taylor's theory of single-fluid relaxation, this lower bound of the magnetic energy is determined by an approximate preservation of magnetic helicity,[7] leading to a terminal state characterized by (1) but with a constant α. More general magnetohydrodynamic relaxation theories, of which the Taylor relaxation is a special case, can be formulated by using two-fluid MHD equations. The details can be found in Ref. 8 and references therein. These two complementary processes, the development of CSs and the following relaxation through MRs, may account for dynamically shaping up the magnetic topology of high R_M magnetofluids.

With the above scenario in mind, it is important to assess the role of magnetic topology, quantified by the intensity of field line interlacing, in determining potential sites for MRs through formation of CSs. In a recent numerical work[9] these sites of CSs are found to be away from any two or three dimensional magnetic nulls with contortions of MFSs being responsible for their development. While, in another set of numerical experiments,[10,11] the locations of CS formation are identified to be either at the immediate neighborhood of magnetic nulls or across magnetic field reversal layers. Since development of CSs at favorable locations lacks the notion of spontaneity, it is then indicative that formation of CSs away from either the nulls or field-reversal layers is in better agreement with the magnetostatic theorem. Thus, a plausibility is to divide numerical demonstrations of CS formation into two broad categories. The first one consists of the CSs developing at the favorable locations, and the other of CSs distributed throughout the computational domain with no apparent preference for location. Against the above backdrop, the objective is to relate intensity of interlacing with properties of developing CSs within the scope of the above two categories.

To achieve this objective, we track viscous relaxation of an incompressible, thermally homogeneous magnetofluid with infinite electrical conductivity, as it successfully demonstrates CS formation in diverse magnetic topologies with different boundary conditions. The dynamics is determined by the MHD Navier-Stokes equations

$$\rho_0\left(\frac{\partial \mathbf{v}}{\partial t}+(\mathbf{v}\cdot\nabla)\mathbf{v}\right)=\mu_0\nabla^2\mathbf{v}+\frac{1}{4\pi}(\nabla\times\mathbf{B})\times\mathbf{B}-\nabla p, \tag{3}$$

$$\nabla\cdot\mathbf{v}=0, \tag{4}$$

$$\frac{\partial \mathbf{B}}{\partial t}=\nabla\times(\mathbf{v}\times\mathbf{B}), \tag{5}$$

$$\nabla\cdot\mathbf{B}=0, \tag{6}$$

in standard notations, where ρ_0 and μ_0 are uniform density and coefficient of viscosity respectively. For simplification, we consider only the systems periodic in all three Cartesian co-ordinates. From an initial nonequilibrium, this magnetofluid is allowed to relax toward a terminal state by converting magnetic energy W_M to kinetic energy W_K via

$$\frac{dW_K}{dt}=\int\frac{1}{4\pi}[(\nabla\times\mathbf{B})\times\mathbf{B}]\cdot\mathbf{v}\,d^3x-\int\mu_0|\nabla\times\mathbf{v}|^2\,d^3x, \tag{7}$$

$$\frac{dW_M}{dt}=-\int\frac{1}{4\pi}[(\nabla\times\mathbf{B})\times\mathbf{B}]\cdot\mathbf{v}\,d^3x, \tag{8}$$

$$\frac{dW_T}{dt}=-\int\mu_0|\nabla\times\mathbf{v}|^2\,d^3x, \tag{9}$$

the integrals being over a full period. Since the Lorentz force is conservative, the kinetic energy is dissipated via viscous drag. In absence of magnetic diffusivity, the condition of flux-freezing holds and the end state is expected to be in magnetostatic equilibrium, identical in magnetic topology to the initial state. The magnetostatic theorem then demands spontaneous development of CSs in the terminal state if the initial magnetic field is topologically complex, which we ensure by constructing relevant initial value problems (IVPs).

We organize the paper in the following order. In Section II, we introduce the relevant IVPs, while numerical model is discussed in Section III. Section IV is dedicated to results and discussions. In Section V, we summarize these results and highlight the important findings.

II. INITIAL VALUE PROBLEM

The initial value problem is constructed by realizing that a magnetic field with non-interlaced field lines can be written as[10,14]

$$\mathbf{B}_1=W(\psi_1,\phi_1)\nabla\psi_1\times\nabla\phi_1, \tag{10}$$

where ψ_1 and ϕ_1 are two scalar functions of position, known as Euler Potentials (EPs)[12,13] and the amplitude W is an explicit function of ψ_1 and ϕ_1. The solenoidality of $\mathbf{B}_1$ is evident from the above expression. Because the field aligned current $\mathbf{J}_1\cdot\mathbf{B}_1=0$, the field lines of $\mathbf{B}_1$ are closed curves. In addition, with conditions $\mathbf{B}_1\cdot\nabla\psi_1=\mathbf{B}_1\cdot\nabla\phi_1=0$ being satisfied, level sets of ψ_1 and ϕ_1 are global MFSs, the intersections of which generate magnetic field lines. It is noteworthy that $\mathbf{B}_1$, in general, has a nonzero $\mathbf{J}_1$ and hence, although untwisted, is not a potential field. Interlaced field lines are generated by superposing $\mathbf{B}_1$ with another $\mathbf{B}_2$, represented by a separate pair of EPs $\{\psi_2,\phi_2\}$ and having an amplitude W_2. The superposed field $\mathbf{B}$ is given by

$$\mathbf{B}=\mathbf{B}_1+\epsilon_0\mathbf{B}_2, \tag{11}$$

$$=(\nabla\psi_1\times\nabla\phi_1)+\epsilon_0(\nabla\psi_2\times\nabla\phi_2), \tag{12}$$

where the amplitudes $W_1=W_2=1$ and the constant ϵ_0 is related to the intensity of interlacing. Notably, a representation of any magnetic field by superposition of two untwisted or non-interlaced component fields is not general enough, and at least three such component fields are required to represent an arbitrary magnetic field; cf. recent review.[14] Our specific choice (11) of two component fields for the purpose of superposition is based only on having a single parameter ϵ_0 to alter the intensity of interlacing. Based on our previous work,[9] we select the following EPs:

$$\psi_1(x,y,z) = a_0 \cos x \sin z, \tag{13}$$

$$\phi_1(x,y,z) = a_0 \cos y, \tag{14}$$

and

$$\psi_2(x,y,z) = a_0 \sin x \sin y, \tag{15}$$

$$\phi_2(x,y,z) = -a_0 \cos z, \tag{16}$$

with an amplitude a_0 and defined in an uniform triply periodic Cartesian domain of period 2π. Figures 1(a) and 1(b) illustrate the level sets of the above EPs in pairs, (ψ_1, ϕ_1) and (ψ_2, ϕ_2), respectively, for $a_0 = 1$, with ψ-constant surfaces in color grey and ϕ-constant surfaces in color red. The closed lines generated by intersection of the two surfaces are MFLs which are untwisted, as can easily be verified from their appearances. To further facilitate visualization, we overlay Figure 1 with $y = \pi$ plane depicted in color green. Also, in this and subsequent figures, the arrows in colors red, green, and blue depict the directions x, y, and z, respectively.

From (12), the initial component fields $\mathbf{H}_1 = \{H_{1x}, H_{1y}, H_{1z}\}$ and $\mathbf{H}_2 = \{H_{2x}, H_{2y}, H_{2z}\}$ are

$$H_{1x} = a_0^2 \cos x \sin y \cos z, \tag{17}$$

$$H_{1y} = 0, \tag{18}$$

$$H_{1z} = a_0^2 \sin x \sin y \sin z, \tag{19}$$

and

$$H_{2x} = a_0^2 \sin x \cos y \sin z, \tag{20}$$

$$H_{2y} = -a_0^2 \cos x \sin y \sin z, \tag{21}$$

$$H_{2z} = 0. \tag{22}$$

The superposed field $\mathbf{H} = \{H_x, H_y, H_z\}$ is

$$H_x = a_0^2(\cos x \sin y \cos z + \epsilon_0 \sin x \cos y \sin z), \tag{23}$$

$$H_y = -a_0^2(\epsilon_0 \cos x \sin y \sin z), \tag{24}$$

$$H_z = a_0^2(\sin x \sin y \sin z). \tag{25}$$

The Lorentz force exerted by $\mathbf{H}$ is

$$L_x = a_0^4\left[(\epsilon_0^2 - 1)\sin 2x \sin^2 y \sin^2 z - \left(\frac{\epsilon_0}{4}\right)\cos 2x \sin 2y \sin 2z\right], \tag{26}$$

$$\begin{aligned} L_y = a_0^4\Bigg[&\left(\epsilon_0^2 - \frac{1}{2}\right)\sin^2 x \sin 2y \sin^2 z \\ &- \left(\frac{\epsilon_0}{4}\right)\sin 2x \cos 2y \sin 2z \\ &-\left(\frac{1}{2}\right)\cos^2 x \sin 2y \cos^2 z\Bigg], \end{aligned} \tag{27}$$

$$\begin{aligned} L_z = -a_0^4\Bigg[&\left(\frac{\epsilon_0^2}{2} - 1\right)\cos^2 x \sin^2 y \sin 2z \\ &+ \left(\frac{\epsilon_0}{4}\right)\sin 2x \sin 2y \cos 2z \\ &+\left(\frac{\epsilon_0^2}{2}\right)\sin^2 x \cos^2 y \sin 2z\Bigg]. \end{aligned} \tag{28}$$

Noting the initial Lorentz force to be a function of ϵ_0, the amplitude a_0 is adjusted to perform computations with initial fields having different ϵ_0 but identical magnitude of average Lorentz force.

The field-aligned current density and the global magnetic helicity for $\mathbf{H}$ are

$$\begin{aligned} (\nabla \times \mathbf{H}) \cdot \mathbf{H} = a_0^4 \epsilon_0(&\sin^2 x \cos^2 y \sin^2 z \\ &+ \cos^2 x \sin^2 y \cos^2 z + 2\sin^2 y \sin^2 z), \end{aligned} \tag{29}$$

$$K_M = 2a_0^4 \epsilon_0 \pi^3, \tag{30}$$

which reveal that they are directly proportional to ϵ_0. The global magnetic helicity is calculated here using the classical expression

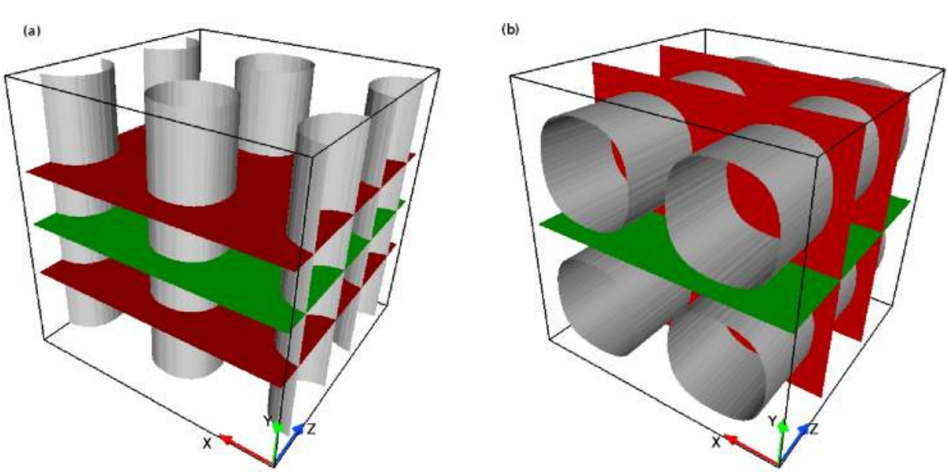

FIG. 1. Panel (a) depicts initial Euler surfaces $\psi_1 = \pm 0.5$ in grey and $\phi_1 = -0.35$ in red. Panel (b) depicts initial Euler surfaces $\psi_2 = \pm 0.1$ in grey and $\phi_2 = 0.15$ in red. The surface in green marks the $y = \pi$ plane.

$$K_M = \int \mathbf{A} \cdot \mathbf{H} dV, \tag{31}$$

with $\mathbf{A}$ as vector potential, the integral being over a full period, and a constant gauge. Discussions on K_M for more general cases can be found in Refs. 15 and 16. The global magnetic helicity is a measure of interlinkages between MFLs and, hence, is explicitly related to interlacing of field lines. The direct proportionality to ϵ_0 in (29) and (30) is affirmative of an increase in interlacing, hence making MFLs of $\mathbf{H}$ more topologically complex. The above inference can further be validated from Figure 2 which visually clarifies an increase of interlacing in MFLs with ascending values of ϵ_0.

To facilitate presentation, in the following, we discuss the topology of $\mathbf{H}$ in relation to ϵ_0. In Figure 3, we plot MFLs of $\mathbf{H}$ for four separate values: $\epsilon_0 = \{0.1, 0.3, 0.5, 0.7\}$ in the vicinity of $y = \pi$ plane. Features evident in this figure are helical MFLs for $\epsilon_0 = 0.1$, and the deviation of MFLs from this helical structure with an increase of ϵ_0 culminating into MFLs is depicted in panels (b)–(d). To explain these features, we revert to Equations (23)–(25) and note that for $\epsilon_0 = 0$, the field lines of $\mathbf{H}$ are closed disjoint curves tangential to y-constant planes (since the component H_y is zero). For any other ϵ_0, the component field $\mathbf{H}_2$ provides a nonzero H_y resulting in lifting up MFLs of $\mathbf{H}$ out of the y constant planes. In addition, a nonzero ϵ_0 contributes to the component H_x. The net result is then a deformation of MFLs in directions both perpendicular and parallel to y-constant planes. For a small value of ϵ_0, this deformation is also small, resulting in helical field lines with projections on y-constant planes similar in geometry to the closed curves of $\epsilon_0 = 0$. Larger values of ϵ_0 deform field lines more, leading to MFLs depicted in panels (b)–(d). A first order Taylor expansion of Equations (23)–(25) near the $y = \pi$ plane for constant x and z yields

$$H_x = -a_0^2 \epsilon_0 \sin x_0 \sin z_0 - a_0^2 (y - \pi) \cos x_0 \cos z_0, \tag{32}$$

$$H_y = a_0^2 \epsilon_0 (y - \pi) \cos x_0 \sin z_0, \tag{33}$$

$$H_z = -a_0^2 (y - \pi) \sin x_0 \sin z_0, \tag{34}$$

evincing H_y and H_z to flip sign across the $y = \pi$ plane. However, for $\epsilon_0 \neq 0$, H_x flips sign at $y = \pi - y_1$, where y_1 satisfies the condition

$$y_1 > \frac{\epsilon_0 \sin x_0 \sin z_0}{\cos x_0 \cos z_0}. \tag{35}$$

A pair of oppositely directed MFLs across $y = \pi$ plane are shifted by y_1, which in turn increases with ϵ_0 (Fig. 3), rendering an initial $\mathbf{H}$ with larger ϵ_0 less favorable to develop CSs.

Further insight into topology of the initial field is gained by constructing its skeleton in terms of magnetic nulls, since these are the sites where development of CSs is expected. To illustrate the nulls, following Ref. 11, we employ the condition $\mathbf{H} \equiv \{H_x, H_y, H_z\} = 0$ in a Gaussian construct

$$\chi(x, y, z) = \exp\left[-\sum_{i=x,y,z} \frac{(H_i(x, y, z) - H_0)^2}{d_0}\right], \tag{36}$$

where $\sqrt{d_0}$ determines width of the Gaussian and H_0 represents a particular isovalue of $H_x, H_y, \text{and}\, H_z$. By choosing $H_0 \approx 0$ and a small d_0, the function $\chi(x, y, z) \neq 0$ only if

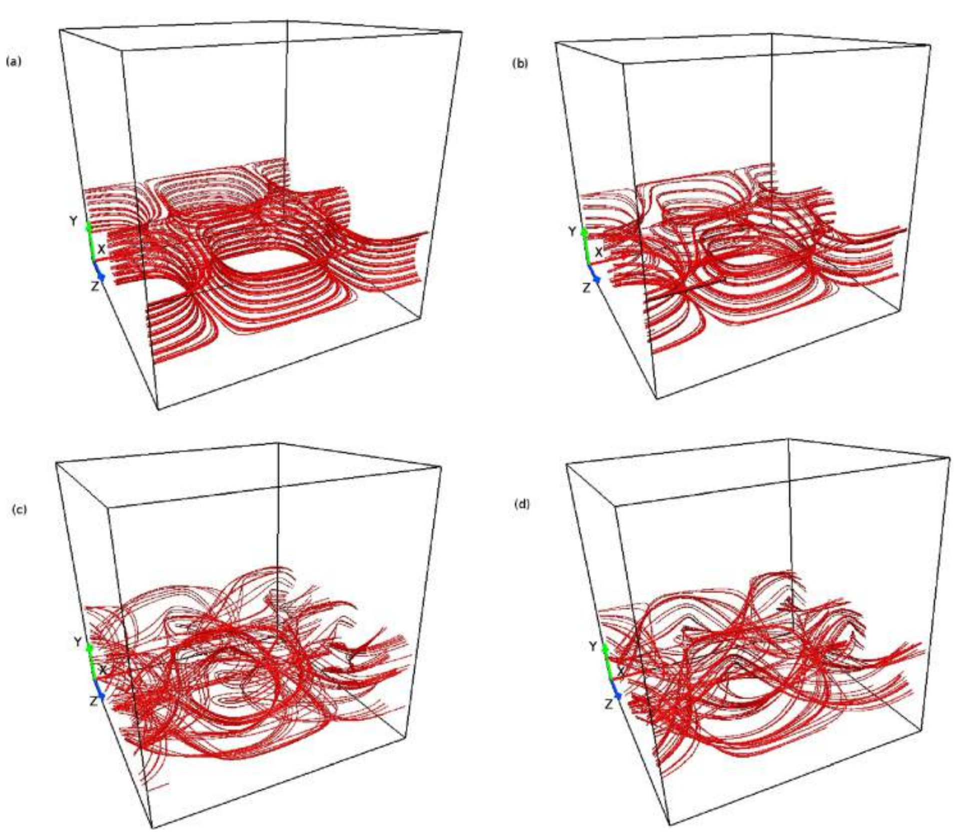

FIG. 2. Panels (a), (b), (c), and (d) illustrate magnetic field lines of the initial field $\mathbf{H}$ for $\epsilon_0 = 0.1, 0.3, 0.5$, and 0.7, respectively. Notably, the field lines are becoming more interlaced as ϵ_0 increases.

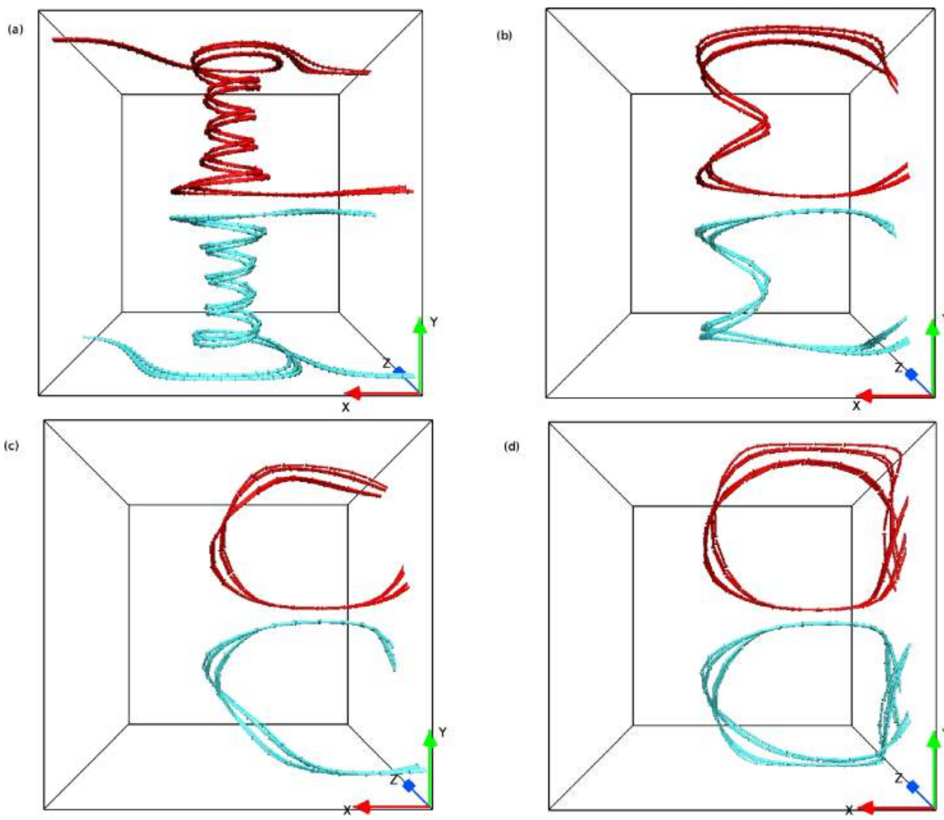

FIG. 3. Panels (a), (b), (c), and (d) show field lines of H for $\epsilon_0 = 0.1$, $0.3, 0.5$, and 0.7, respectively. These field lines are plotted in close proximity of the $y = \pi$ plane and with $z \in \{0, \pi\}$. The figure indicates the field lines to be helical for $\epsilon_0 = 0.1$, while for larger ϵ_0, the field lines deviate from this helical structure. Importantly, the distance between two anti-parallel field lines located across the $y = \pi$ plane increases with ϵ_0.

$H_i \approx H_0$ for each i. The three dimensional (3D) nulls are the points where the three isosurfaces $H_x = H_0, H_y = H_0$, $H_z = H_0$ intersect. It should be noted that at the immediate vicinity of a 3D null all the three components of magnetic field is nonzero. Similarly, a two dimensional (2D) null in a 3D coordinate space can be described as a line of intersection between H_0 isosurfaces of two nonzero magnetic field components while the third component is trivially zero at this line. Using the above technique, in Figure 4, we have depicted nulls of $\mathbf{H}$ for $\epsilon_0 = 0.5$ by selecting parameters $H_0 = 0.01$ and $d_0 = 0.05$. The accuracy of the depiction can easily be verified from the analytical expression of $\mathbf{H}$ in Equations (23)–(25). Figure 4 straightaway confirms only the presence of 2D nulls in the form of lines and a complete absence of 3D nulls. Similar results (not shown) are obtained for the other ϵ_0 values.

To further identify the 2D nulls, we expand components of $\mathbf{H}$ in a Taylor series in the immediate vicinity of $x = \pi/2, z = \pi$ for a constant y to get

$$H_x = a_0^2 \left(x - \frac{\pi}{2} \right) \sin y_0 - a_0^2 (z - \pi) \epsilon_0 \cos y_0, \qquad (37)$$

$$H_y = 0, \qquad (38)$$

$$H_z = -a_0^2 (z - \pi) \sin y_0. \qquad (39)$$

Notably, the non-zero components H_x and H_z have point antisymmetry about co-ordinates $x = \pi/2, z = \pi$ along the y-line rendering every point on it to be a X-type neutral point. The MFLs near two such neutral points are shown in the inset (Fig. 4). Similarly, the z-line (extending in z-direction) is also X-type neutral line. Moreover, the Taylor series

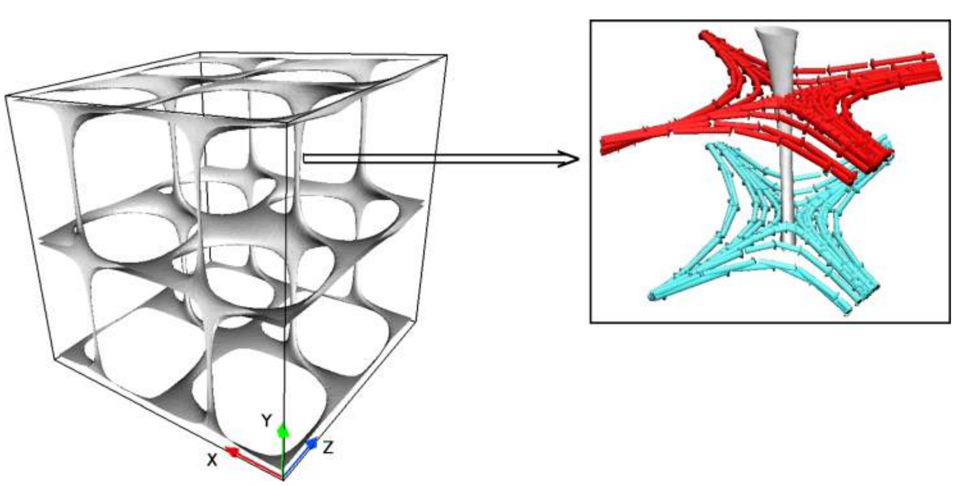

FIG. 4. The figure demonstrates the magnetic nulls by isosurfaces of $\chi(x, y, z)$, defined in (36), with parameter $H_0 = 0.01$ and $d_0 = 0.05$, for $\epsilon_0 = 0.5$. The presence of 2D nulls and complete absence of 3D nulls is evident from the figure. The field topologies near the neutral line located at $x = \pi/2$, $z = \pi$ is depicted in the inset, which correspond to X-type nulls.

expansion of components field in the immediate neighborhood of $y = \pi, z = \pi$ for a constant x yields

$$H_x = a_0^2(y-\pi)\cos x_0 - a_0^2(z-\pi)\epsilon_0 \sin x_0, \quad (40)$$

$$H_y = 0, \quad (41)$$

$$H_z = 0, \quad (42)$$

thus confirming the line along the x-axis with co-ordinates $y = z = \pi$ to be a neutral line.

III. NUMERICAL MODEL

Under the condition of flux freezing, the time evolution of the EPs $\psi_i, \phi_i\,(i = 1, 2)$ is governed by simple advection equations[9,10]

$$\frac{d\psi_i}{dt} = 0, \quad (43)$$

$$\frac{d\phi_i}{dt} = 0, \quad (44)$$

implying

$$\frac{\partial\psi_i}{\partial t} + \mathbf{v}\cdot\nabla\psi_i = 0, \quad (45)$$

$$\frac{\partial\phi_i}{\partial t} + \mathbf{v}\cdot\nabla\phi_i = 0. \quad (46)$$

Any numerical calculation utilizing advection of MFSs requires satisfaction of the flux-freezing condition to a high fidelity. The computational requirement is then a minimization of numerically generated dissipation and dispersion errors. Such a minimization is a signature of a class of inherently nonlinear "high-resolution" transport methods that conserve field extrema along flow trajectories while ensuring higher order accuracy away from steep gradients in the advected fields. For our calculations, we adapt the MHD version[17] of the well established general-purpose hydrodynamic model EULAG predominantly used in atmospheric and climate research.[18,19]

For completeness, here we summarize only the crucial features of the EP based MHD version of the EULAG; the details are in Ref. 10. This model is based on the spatio-temporally second order accurate nonoscillatory forward-in-time (NFT) advection scheme MPDATA (Multidimensional Positive Definite Advection Transport Algorithm).[19] A feature important to MPDATA and relevant to our calculations is its proven dissipative property which is intermittent and adaptive to generation of under-resolved scales in field variables for a fixed grid resolution. As the CS develops, the magnetic field gradient increases unboundedly and a fixed grid resolution becomes insufficient in presence of these high gradients. The MPDATA then removes these under-resolved scales by generating a locally effective residual dissipation of the second order, sufficient to maintain solution monotonicity. These intermittency and adaptiveness are effective in implicit large-eddy simulation (ILES) that mimics the action of explicit subgrid-scale turbulence models, whenever the concerned advective field is under-resolved.[20] Utilizing this ILES scheme, Ghizaru and co-workers have successfully simulated regular solar cycles,[21] while rotational torsional oscillations in a global solar dynamo were characterized and analyzed.[22] The present understanding along with open questions on modeling the solar dynamo are summarized in Reference 23. Furthermore, in the recent works,[6,11] this ILES mode was successfully used to obtain numerically induced MRs that lead to secondary CSs. In the present computations, we follow evolution of MFSs until onsets of such MRs to ensure satisfaction of the flux-freezing to a high fidelity.

IV. RESULTS AND DISCUSSIONS

The results are presented for numerical computations carried out with zero initial velocity and ϵ_0 in the range of $\{0.1, 0.7\}$, in steps of 0.1. The computational grid has uniform resolution of 128^3 and corresponds to a physical volume of $(2\pi)^3$. The coefficient of viscosity and the mass density are set to $\mu_0 = 0.008$ and $\rho_0 = 1$, respectively. When released from an initial non-equilibrium state, the dynamics develops because of an imbalance between the Lorentz force and the pressure gradient with zero initial value. The resulting increase in velocity gets arrested by viscous drag and the magnetofluid relaxes toward a quasi-steady state while preserving its magnetic topology. For a general understanding of this viscous relaxation, Figure 5 plots the histories of kinetic and magnetic energies for $\epsilon_0 = 0.1$, normalized to the initial total (magnetic + kinetic) energy. The development of the peak in kinetic energy centered at $t = 20s$ is due to the viscous arrest. The quasi-steady phase of the evolution is in the temporal range $t \in \{60s, 120s\}$ and is characterized by an almost constant kinetic energy, while the change in magnetic energy is restricted to 13% of its total variation. For

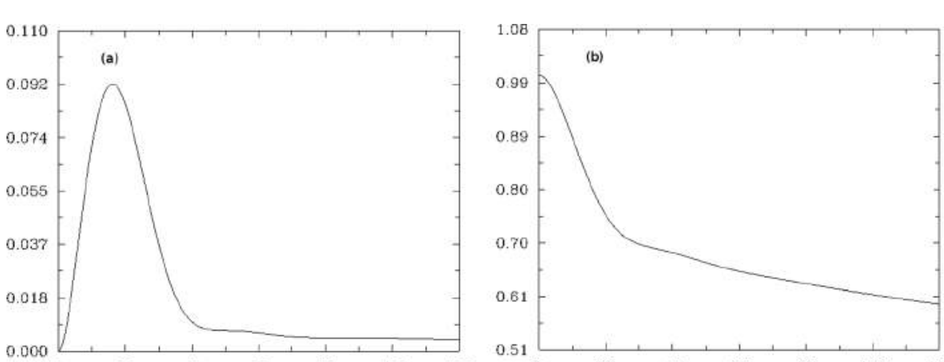

FIG. 5. Time evolution of normalized kinetic and magnetic energies for $\epsilon_0 = 0.1$ (panels (a) and (b)). The normalization is done with the initial total energy. The plots highlight the initial peak in kinetic energy and the quasi-steady phase of the evolution.

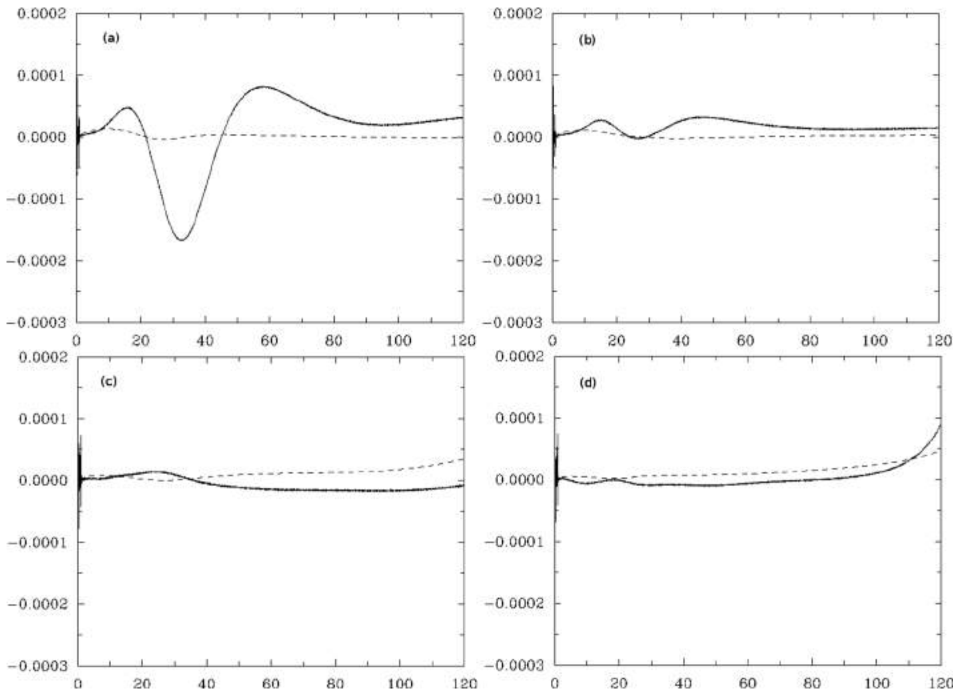

FIG. 6. Panels (a)–(d) illustrate deviations of normalized kinetic (dashed) and magnetic (solid) energy rates from their analytical values during computations with $\epsilon_0 = 0.1, 0.3, 0.5$, and 0.7, respectively. The normalization is with respect to the initial total energy. The plots document an almost accurate maintenance of the energy rates.

other values of ϵ_0, the magnetic and kinetic energy curves show the same qualitative behavior but with different timing and amplitudes (not shown).

The accuracy of computations is assessed in Figure 6 displaying numerical deviations of normalized kinetic (dashed line) and magnetic (solid line) energy rates from their analytical values in (7) and (8). The displayed deviations are for different ϵ_0 values: $\epsilon_0 = 0.1, 0.3, 0.5$, and 0.7, which we have selected as the representative cases. The plots confirm the numerical accuracy to be maintained with acceptable precision; the maximal deviation being 0.0002 (panel (d)). This accurate maintenance of energy rates denies any possibility of numerical MRs and, hence, confirms the preservation of magnetic topology throughout the computations.

The overall tendency to form CSs can be established from panels (a) and (b) of Figure 7, plotting the evolution of average total current density $\langle|\mathbf{J}|\rangle$ and maximal value of $|\mathbf{J}|$, respectively. We denote the latter by $J_{\max}$, and the current densities in the plots are normalized to their initial values. Notable is their tendency to increase, albeit without monotonicity, from the respective initial values. Because for every ϵ_0 the average component current density $\langle|\mathbf{J}_2|\rangle = \langle|\nabla \times \mathbf{H}_2|\rangle$ shows a monotonous increase, and the scalar product $\langle \mathbf{J}_1 \cdot \mathbf{J}_2\rangle$ (where $\mathbf{J}_1 = \nabla \times \mathbf{H}_1$) remains negative (cf. panels (a) and (b) of Fig. 8) throughout evolution, this lack of monotonicity in $\langle|\mathbf{J}|\rangle$ is exclusively due to contribution from the $\langle|\mathbf{J}_1|\rangle$ (panel (c), Fig. 8). Similar analysis (not shown) yields contributions from the corresponding maximum $|\mathbf{J}_1|$ to be responsible for the lack of monotonicity in $J_{\max}$.

Additional computations are performed for different uniform grid resolutions varying from 96^3 to 160^3 in steps of 16^3, with $\epsilon_0 = 0.1$ and $\epsilon_0 = 0.5$ as the representative cases. The resulting plots (Fig. 9) document scaling of $J_{\max}$ with resolution, which points in favor of CS formations.[24] Moreover, the scaling is stronger for $\epsilon_0 = 0.1$, where the $y = \pi$ plane is favorable for CS formation. In contrast, for $\epsilon_0 = 0.5$, with no apparent favorable location for CS formation, the scaling is weaker. Such comparative scaling is a signature of scenarios where CSs develop at three dimensional magnetic nulls against CSs developing away from the nulls.[25–27]

To identify and locate onset of CSs, in the following, we further analyze the four cases separately. The analyses are for the computations with 128^3 grid resolution where we follow appearances and geometries of the isosurface of $|\mathbf{J}|$,

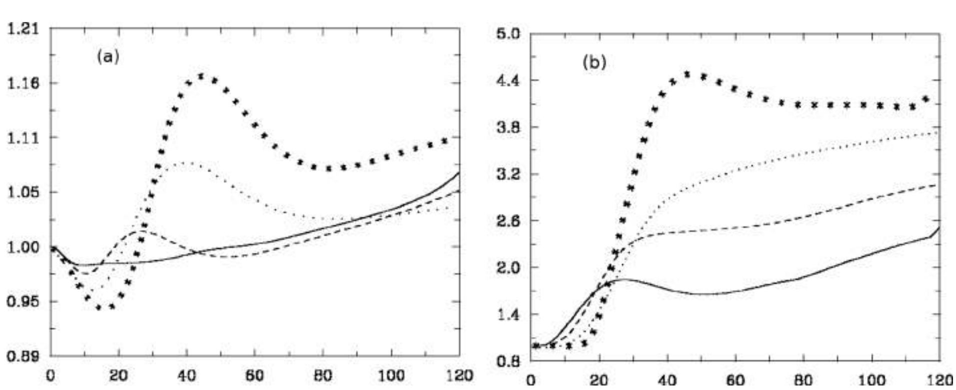

FIG. 7. Panels (a) and (b) show time evolution of normalized $\langle|\mathbf{J}|\rangle$ and $J_{\max}$, respectively, for $\epsilon_0 = 0.1$ (starred line), 0.3 (dotted line), 0.5 (dashed line), and 0.7 (solid line). The overall increase in current densities with time suggests development of CSs.

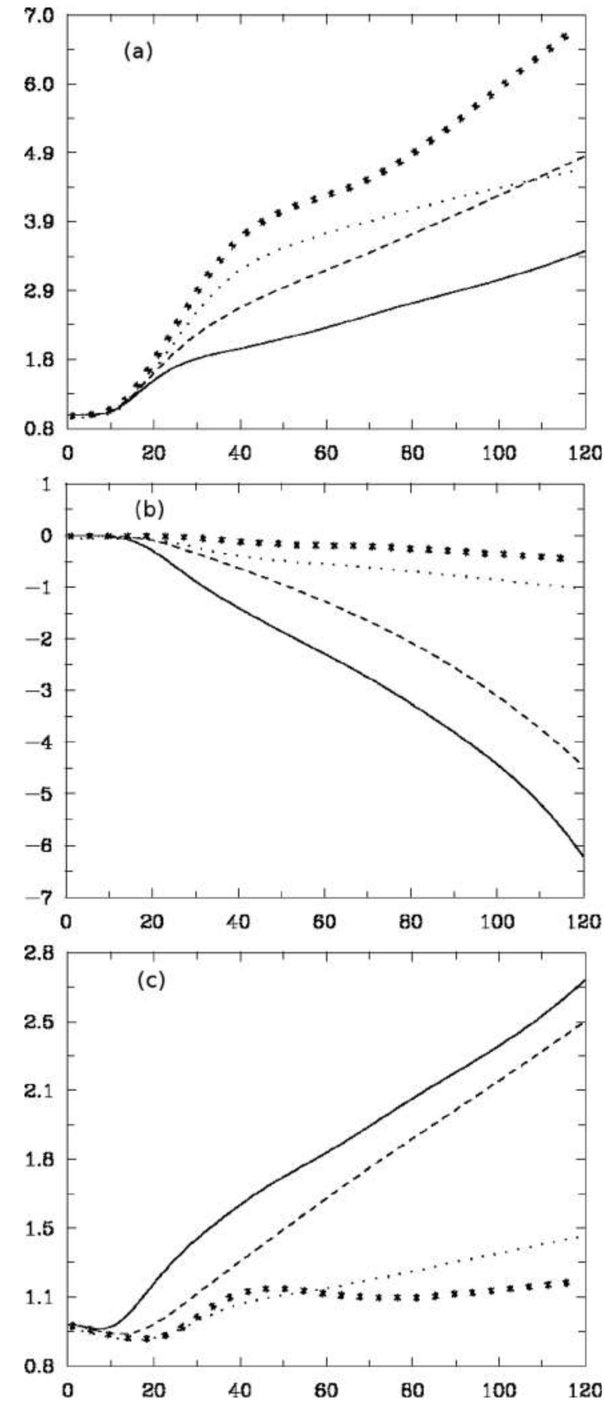

FIG. 8. Panels (a), (b), and (c) illustrate time evolution of $\langle|\mathbf{J}_2|\rangle$, $\langle\mathbf{J}_1\cdot\mathbf{J}_2\rangle$, and $\langle|\mathbf{J}_1|\rangle$, respectively, for $\epsilon_0 = 0.1$ (starred line), 0.3 (dotted line), 0.5 (dashed line), and 0.7 (solid line). The current densities are normalized to their initial values.

referred hereafter as $J - 50$, with an isovalue which is 50% of maximum $|\mathbf{J}|$ for each ϵ_0. Also, to facilitate the general understanding, we overlay these isosurfaces with magnetic nulls.

A. Case (I) ϵ_0=0.1

The evolution of the corresponding $J - 50$ surfaces overlaid with magnetic nulls is illustrated in Figure 10. Based on their shape, these surfaces can be classified into two geometrically distinct categories: the open surfaces appearing at the $y = \pi$ plane and the elongated closed surfaces distributed sparsely in the volume. Evident from the MFL evolution depicted in Figure 11, the open surfaces are the CSs developed by two antiparallel complimentary field lines approaching toward the $y = \pi$ plane. Additionally, the figure identifies generation of the closed $J - 50$ surfaces to an increase in the local number density of parallel field lines, resulting in an increase in $|\mathbf{H}|$ and hence $|\mathbf{J}|$. A sharpening of field gradient playing no role in the generation, the closed surfaces do not qualify as CSs.

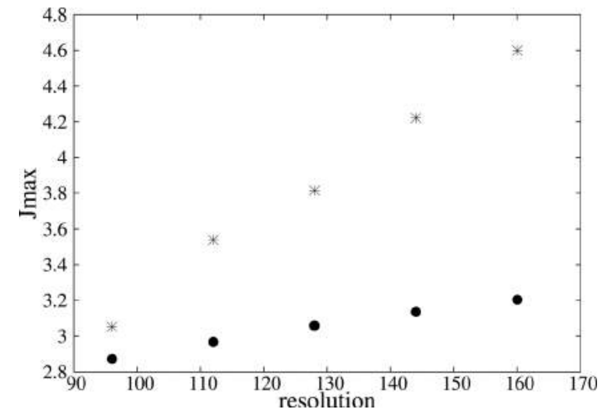

FIG. 9. The plot of $J_{\max}$ against grid resolution for $\epsilon_0 = 0.1$ (stars) and $\epsilon_0 = 0.5$ (dots). The monotonous increase of $J_{\max}$ with resolution confirms the development of CSs for both the ϵ_0 values. Also, the plot documents a stronger scaling with resolution for the case $\epsilon_0 = 0.1$.

B. Case (II) ϵ_0=0.3

To complement results of Case I, here, we analyze $J - 50$ surfaces for computation with $\epsilon_0 = 0.3$. In Figure 12, we illustrate the history of $J - 50$ surfaces overlaid with magnetic nulls. It is evident from the figure that most of the $J - 50$ surfaces are elongated closed structures similar to the case of $\epsilon_0 = 0.1$. In addition, development of localized current layers at the $y = \pi$ plane is noted. Like the previous case, here also an enhancement in density of parallel MFLs is responsible for a local increase in magnitude of $\mathbf{J}$, leading to the formation of these closed current surfaces. More importantly, Figure 12 indicates a delay in the generation of CSs in comparison to the earlier case. This is expected since the initial topology of field lines for larger ϵ_0 is less favorable and, hence, two oppositely directed MFLs require additional push to onset the $J - 50$ surfaces. Also, the spatial extension of these CSs is lesser compared to the case I.

C. Case (III) ϵ_0=0.5

With $\epsilon_0 = 0.5$, the initial favorable topology around $y = \pi$ plane is almost destroyed and the MFLs are interlaced everywhere (panel (c), Fig. 2). The appearances of $J - 50$ surface (overlaid with magnetic nulls) are depicted in Figure 13. The $J - 50$ surfaces start to appear around $t = 32s$ and in their initial phase of evolution are closed surfaces, suggesting a localized increase in $|\mathbf{H}|$. With time, these closed surfaces become increasingly open; generating CSs in the form of helices extended along the y direction and

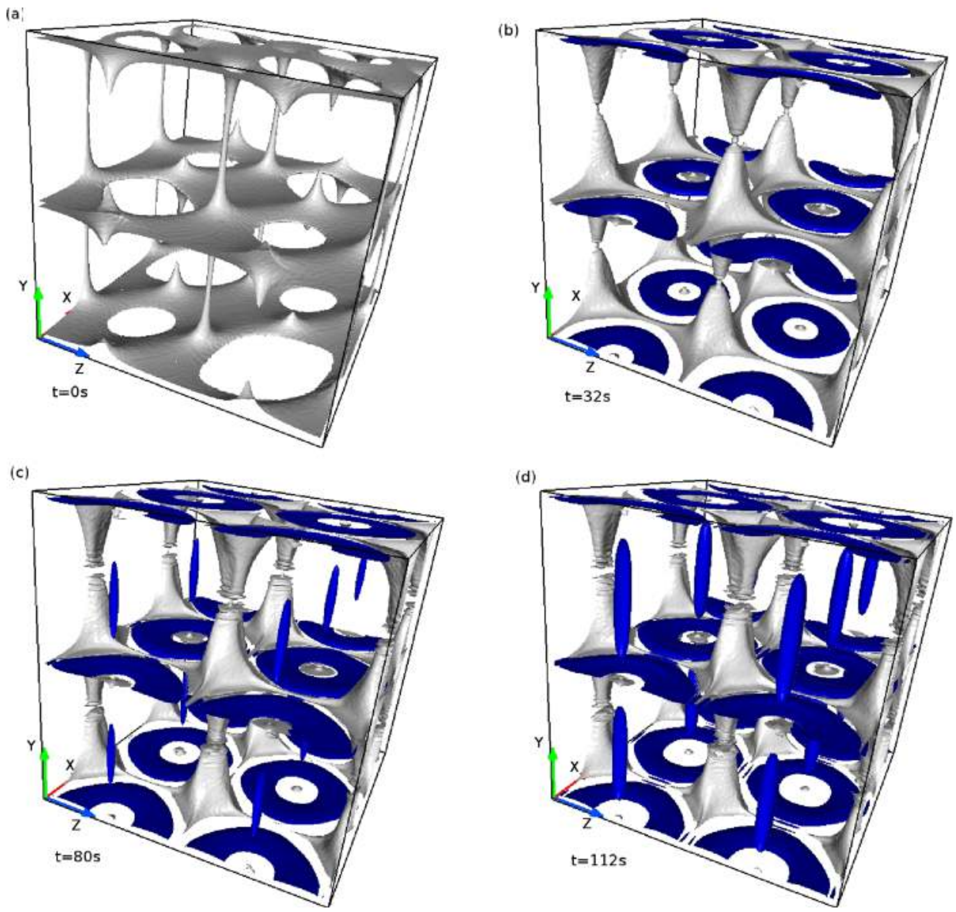

FIG. 10. Evolution of the isosurface $J-50$ (in blue), having an isovalue which is 50% of the maximum $|\mathbf{J}|$ for $\epsilon_0 = 0.1$. The figure is further overlaid with magnetic nulls (in grey). Noteworthy is the development of CSs at $y = \pi$ plane, where they are generally expected because of the presence of favorable field line topology. The figure also shows the generation of closed elongated $J-50$ surfaces.

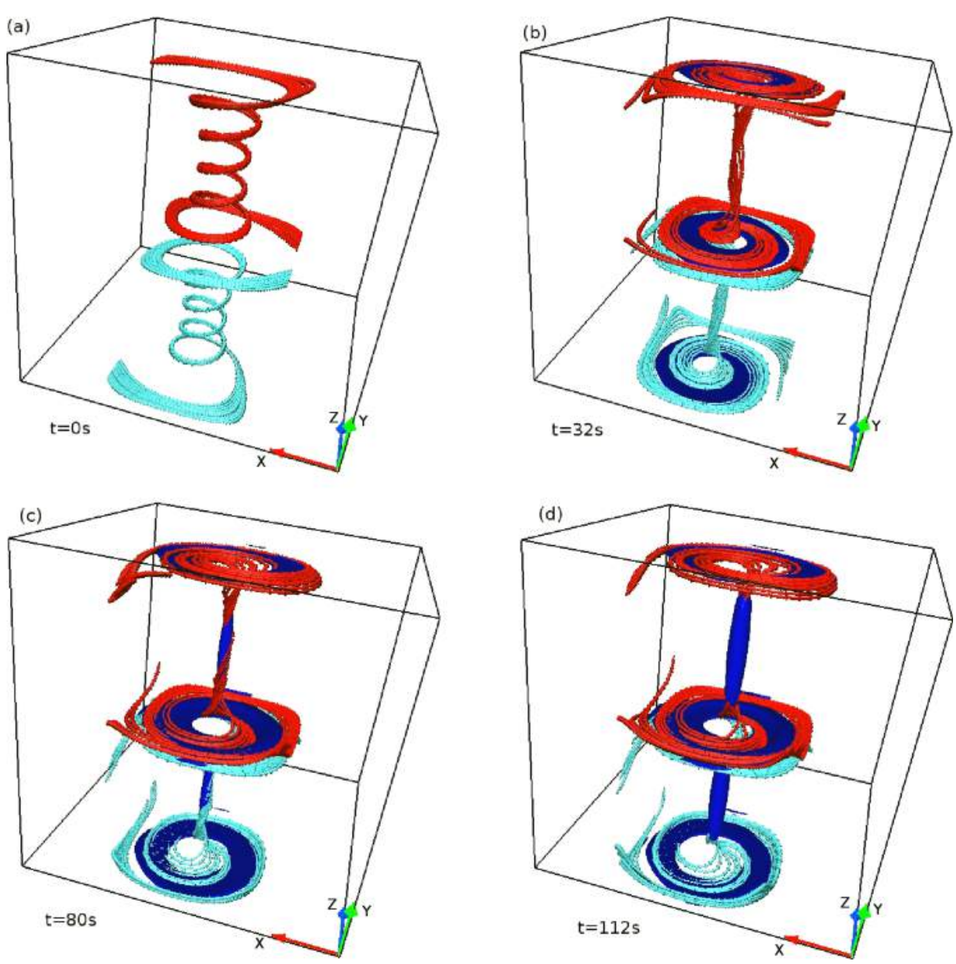

FIG. 11. History of two complementary sets of oppositely directed MFLs of the $\mathbf{H}$ along with $J-50$ surfaces (in blue) for $\epsilon_0 = 0.1$. The plots confirm development of CSs at the $y = \pi$ plane as two oppositely directed field lines approach each other. The figure also relates the closed $J-50$ surfaces to an increase in parallel field lines density, implying their onset does not indicate CS formation.

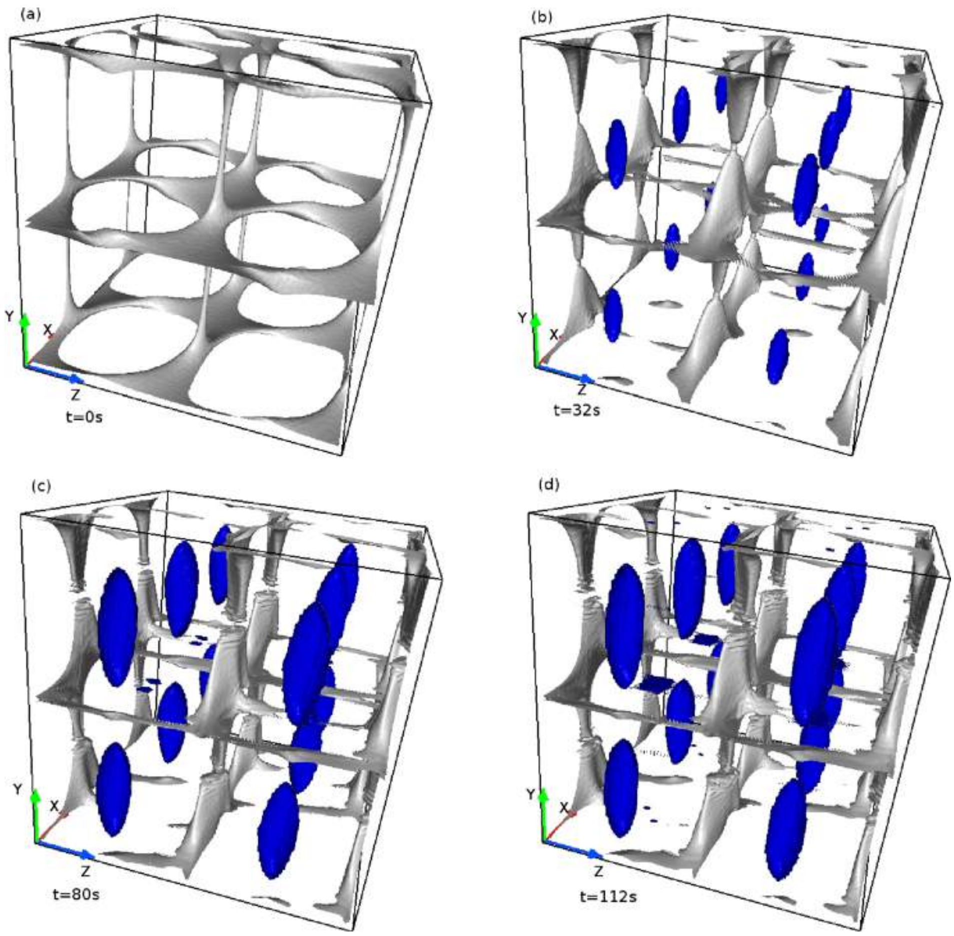

FIG. 12. Time sequence of the isosurface $J - 50$ (in blue) overlaid with magnetic nulls (in grey), for $\epsilon_0 = 0.3$. The plots illustrate the appearances of closed elongated current structures along with CSs located at the $y = \pi$ plane.

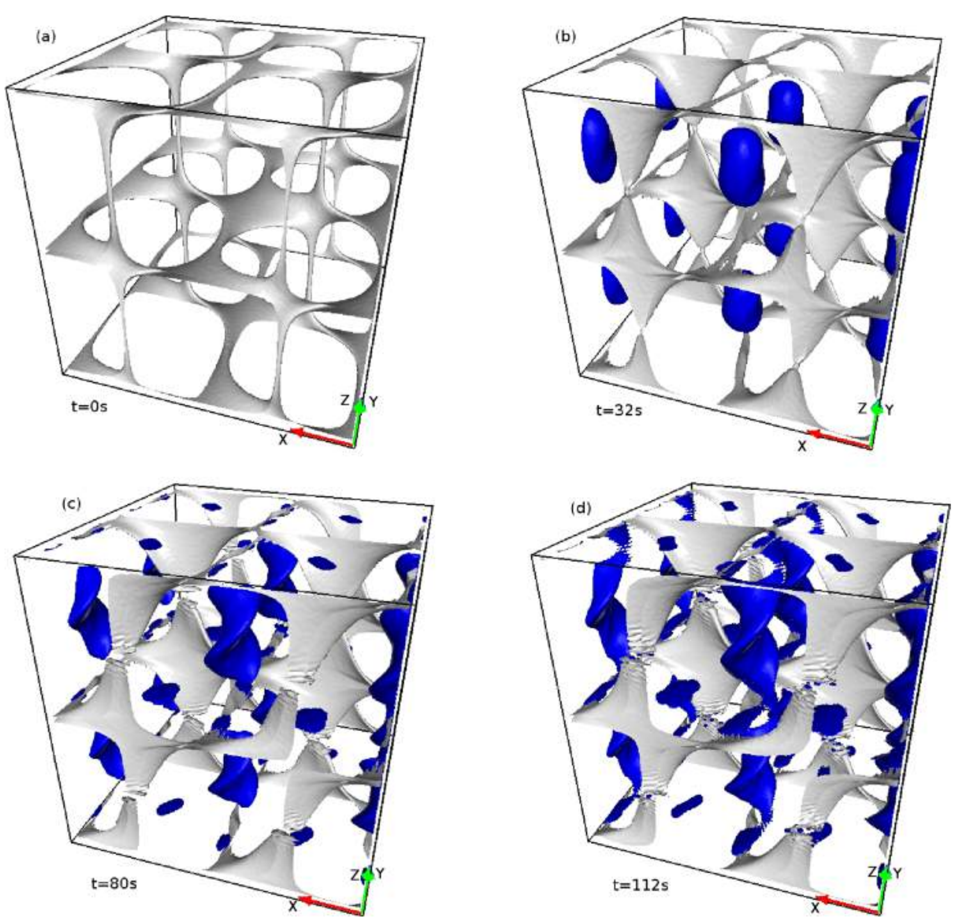

FIG. 13. Evolution of the surface $J - 50$ (in blue) overlaid with magnetic nulls (in grey), for $\epsilon_0 = 0.5$. Noteworthy is the development of CSs away from the nulls.

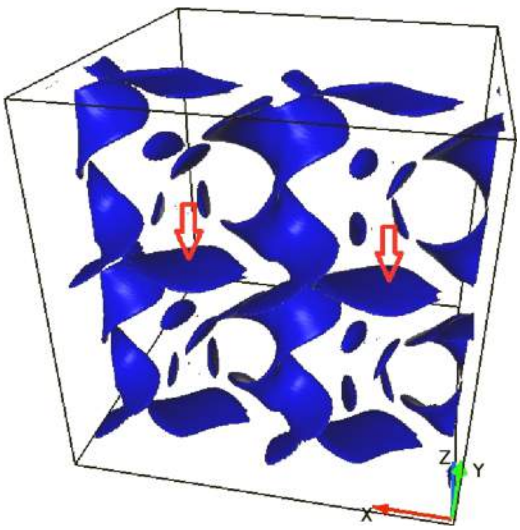

FIG. 14. Appearance of $J_1 - 40$ surfaces at $t = 112s$ for $\epsilon_0 = 0.5$, plotted in the half computational domain with $z \in \{0, \pi\}$. The $J_1 - 40$ surfaces are comprised of helices extended along the y axis and patches (marked by downward arrows) located at the $y = \pi$ plane.

patches located at the $y = \pi$ plane. Importantly, these CSs are located away from the magnetic nulls.

To understand this development of CSs away from the magnetic nulls, the time evolution of appropriate Euler surfaces and selected isosurfaces of $|\mathbf{J}_1|$ and $|\mathbf{J}_2|$ is explored in the following. Considering the negative contribution from $\mathbf{J}_1 \cdot \mathbf{J}_2$, we set the optimal isovalues to 40% of the maximum of $|\mathbf{J}_1|$ or $|\mathbf{J}_2|$, depending on the component current density under consideration. These isosurfaces are nomenclatured as $J_1 - 40$ and $J_2 - 40$ surfaces, respectively. The Figure 14 illustrates a snapshot of $J_1 - 40$ surfaces at the instant $t = 112s$, displayed in the half computational domain $z \in \{0, \pi\}$. Notably, the $J_1 - 40$ surfaces are also in the forms of helices and patches (marked by downward arrows), structurally similar and co-located to the $J - 50$ surfaces. This structural similarity and co-located appearance ascertains the $J_1 - 40$ surfaces to be major contributors toward the development of $J - 50$ surfaces. The helical $J_1 - 40$ surfaces originate from favorable contortions of $\psi_1 -$constant Euler surfaces, evident from Figure 15. However, the patches are due to contortions of $\phi_1 -$ constant Euler surfaces near the $y = \pi$ plane (cf. Figure 16). Identical contortions of $\psi_2 -$constant and $\phi_2 -$constant Euler surfaces generate the corresponding $J_2 - 40$ surfaces (not shown).

D. Case (IV) ϵ_0=0.7

In this case, the initial MFLs are interlaced more strongly (panel (d), Fig. 2). To complement the findings in Case (III), in Figure 17, we depict appearances of $J - 50$ surface. Evidently, these surfaces are initially closed and hence are due to local enhancements in $|\mathbf{H}|$. Later in their evolution, these surfaces become open and morphed into CSs. In comparison to the previous case, these CSs are distributed more extensively in the computational domain and, hence, signify that more intensely interlaced field lines produce CSs with lesser preference for locations, a finding which is in conformity with the magnetostatic theorem.

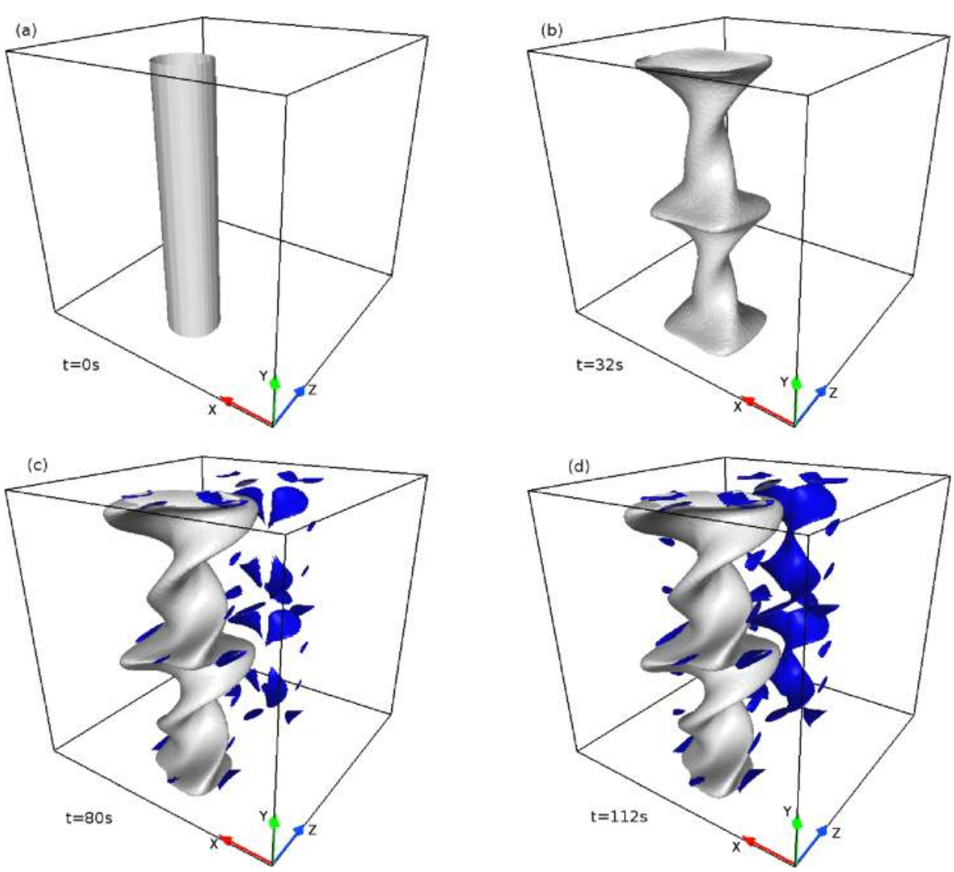

FIG. 15. Evolution of Euler surface $\psi_1 = -0.65$ (in grey) overlaid with the $J_1 - 40$ surface (in blue), for $\epsilon_0 = 0.5$. For better visualization, the evolution is shown in the subdomain $x \in \{\frac{2\pi}{3}, \frac{4\pi}{3}\}$. Noteworthy, the $J_1 - 40$ surface is co-located with the contortion of $\psi_1 = -0.65$ surface, inferring the causality between them.

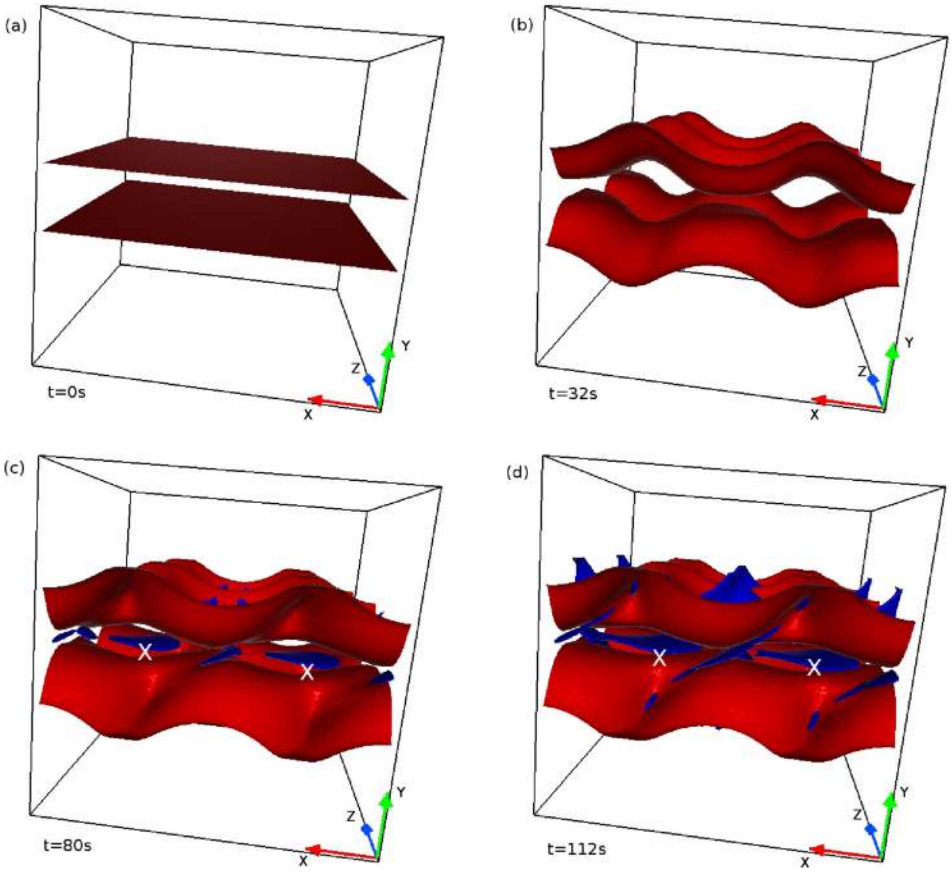

FIG. 16. Time profile of Euler surfaces $\phi_1 = -0.60$ (in red) overlaid with the surface $J_1 - 40$ (in blue) for $\epsilon_0 = 0.5$, plotted in a selected portion of the computational domain. The two Euler surfaces depicted in the figure reside on two opposite sides of the $y = \pi$ plane. The figure identifies the development of current patches (marked by X) to favorable contortions of ϕ_1.

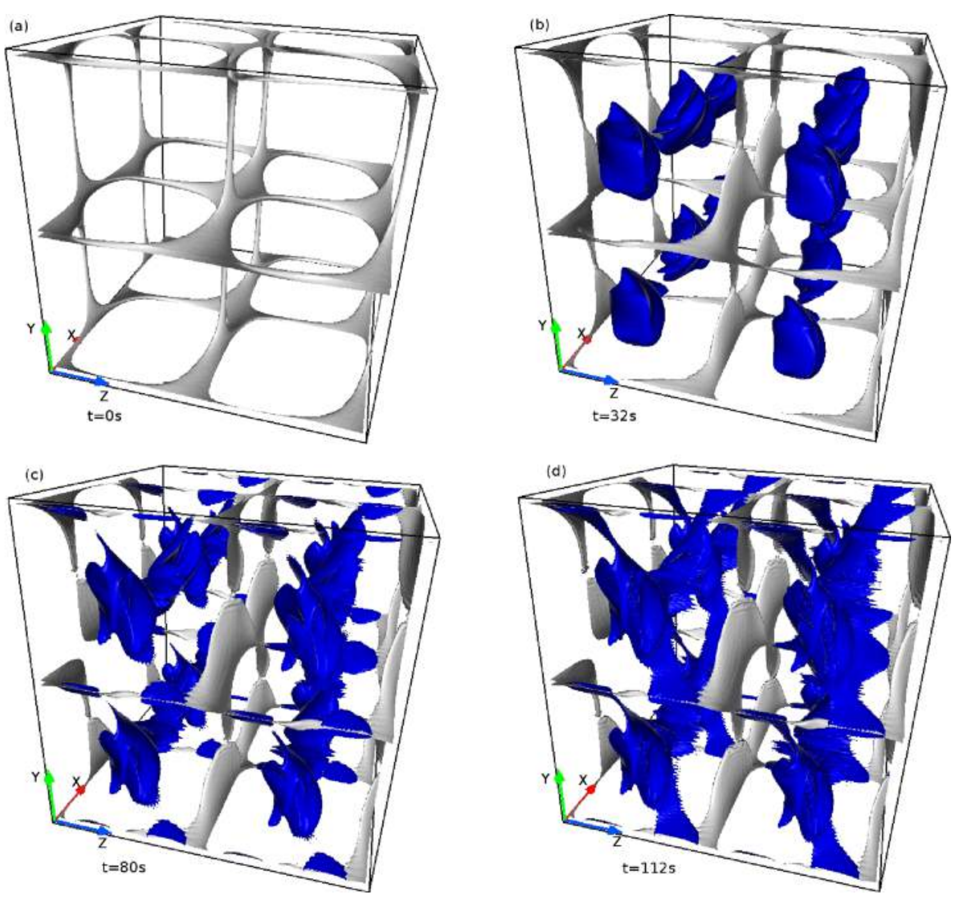

FIG. 17. Development of the surface $J - 50$ (in blue) overlaid with magnetic nulls (in grey), for $\epsilon_0 = 0.7$. The figure substantiates onset of CSs which are away from magnetic nulls and the $y = \pi$ plane. Furthermore, these CSs are distributed throughout the computation volume.

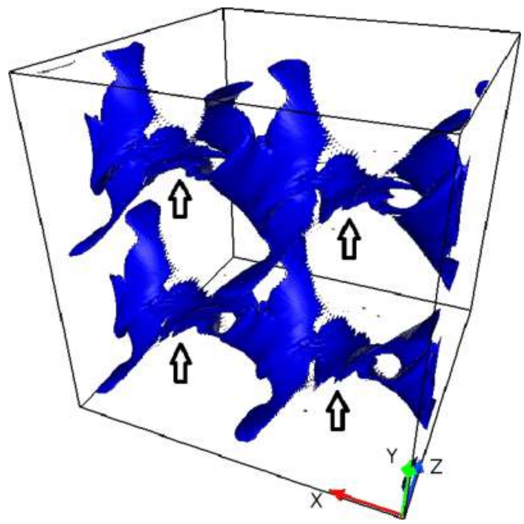

FIG. 18. A snapshot of the $J-50$ surfaces at $t=112s$, for $\epsilon_0=0.7$. The surfaces are plotted in the half computational domain with $z \in \{0,\pi\}$. From the figure, evident are the helical CSs extending along the y axis and the current patches (marked by upward arrows) tangential to y-constant planes.

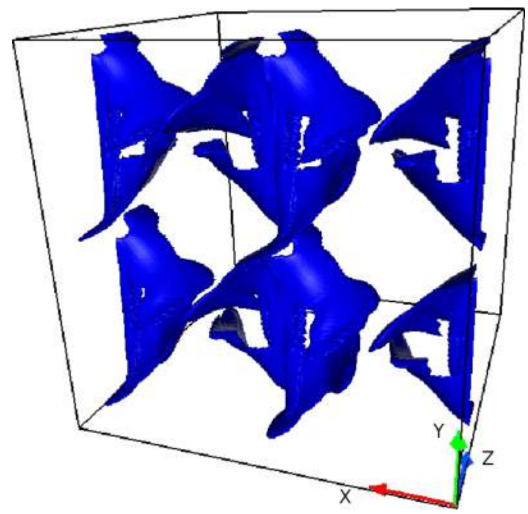

FIG. 19. Appearances of J_1-40 surface at $t=112s$ for $\epsilon_0=0.7$, depicted in the half computational domain with $z \in \{0,\pi\}$. The J_1-40 surfaces are elongated along the y axis.

Figure 18 shows the $J-50$ surfaces at $t=112s$, plotted in the half computational domain. Like the previous case, these $J-50$ surfaces can also be classified into helices and patches (marked by the upward arrows). To explain their origin, in Figure 19, we illustrate the corresponding J_1-40 surface at the instant $t=112s$. The figure confirms, the helical $J-50$ surfaces owe their origin to a development of J_1-40 surfaces. Further, Figure 20 relates the onset of these J_1-40 surfaces to contortions of ψ_1- constant Euler surfaces. The development of the patches is attributed to J_2-40 surfaces, as suggested by Figure 21 that depicts evolution of a single J_2-40 surface located at the immediate vicinity of a patch. The figure is overlaid with evolution of ϕ_2- constant Euler surfaces co-located to the J_2-40 surface. From the figure, it is clear that the onset of J_2-40 surfaces is due to contortions of the ϕ_2- constant Euler surface.

In view of the above discussion, the comparative scaling documented in Figure 9 can now be put into its proper perspective. The intensity of CSs developing at favorable locations (cases I and II) have stronger scaling with resolution than the intensity of CSs that develop in absence of favorable

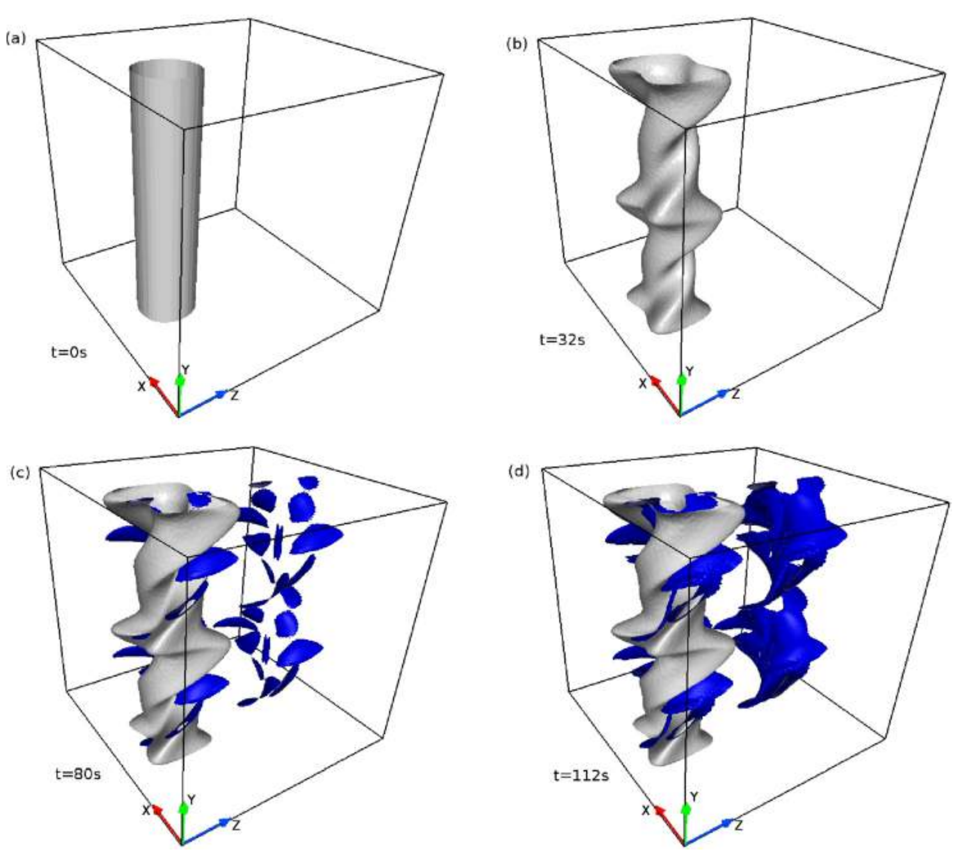

FIG. 20. Evolution of Euler surfaces $\psi_1=-0.60$ (in grey) overplotted with the surface J_1-40 (in blue) for $\epsilon_0=0.7$, shown in the computational domain with $x \in \left\{\frac{2\pi}{3},\frac{4\pi}{3}\right\}$. The figure indicates contortions of ψ_1-constant Euler surfaces to be responsible for onset of the helical J_1-40 surfaces.

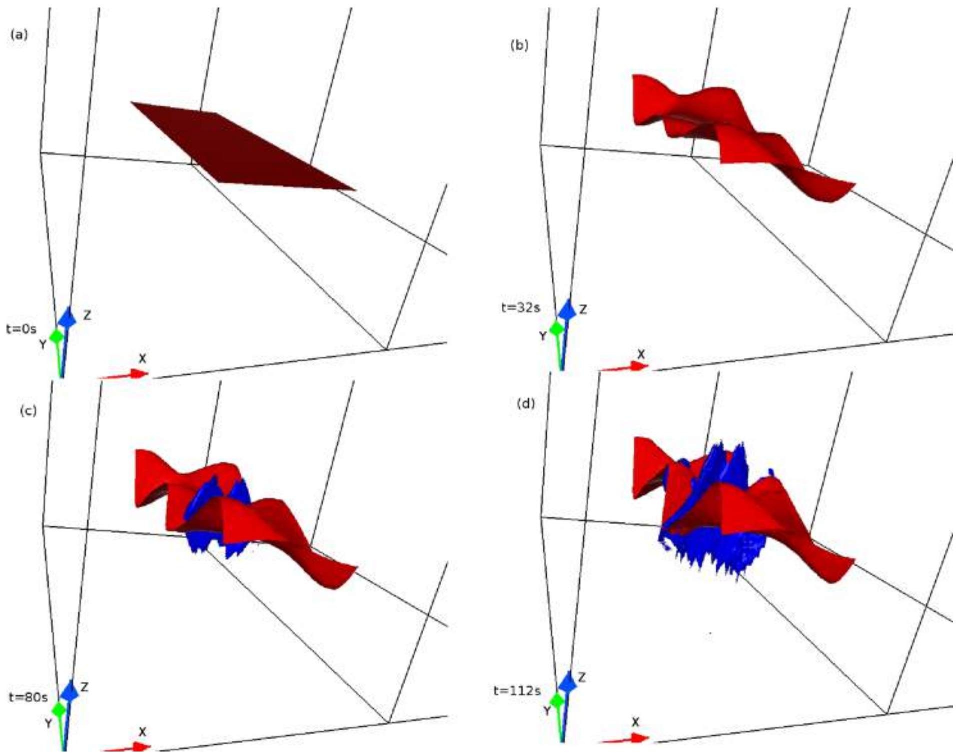

FIG. 21. Evolution of Euler surfaces $\phi_2 = 0.05$ (in red) overlaid with the surface $J_2 - 40$ (in blue) for $\epsilon_0 = 0.7$. The figure indicates, contortions of the ϕ_2-constant surfaces are responsible for developing the patches of $J_2 - 40$ tangential to y-constant planes.

locations (cases III and IV). In a recent work, Craig and Effenberger[25] found similar comparative scaling in the scenario of CS formation at 3D nulls against CS formation at quasi-separatrix layers (QSLs). The QSLs are regions where the magnetic connectivity between a pair of boundaries changes drastically.[28] Along with separators.[29,30] QSLs are known to be the sites, away from nulls, where CSs can develop.[25,31] It is then imperative to seek QSLs in **H** and their relation to CS formation.

In Figure 22, we plot MFLs at the immediate vicinity of a helical CS for $\epsilon_0 = 0.5$. The plots are for instants $t = 0s$ and $t = 112s$. The figure documents the connectivity of two sets of MFLs (in colors red and cyan) connecting plane C with planes D and E. The different connectivities of the two sets are evident from the figure. With CS (marked in color blue) being co-located with the layer where the connectivity changes, existence of QSL structures containing the CS is suggested. A comparison between the two instants further reports MFLs to get more helical with development of the CS, indicating causality between the favorable contortions and the dynamics of QSLs—an important problem that demands separate work.

V. SUMMARY

In this work, we assess the importance of complexity in magnetic topology on development of CSs. The initial magnetic field is constructed by superposing two untwisted fields, where each field is represented by a pair of global magnetic flux surfaces. The magnetic field lines of the superposed field are interlaced and the intensity of interlacing increases with the relative amplitude ϵ_0 of the component fields. The particular initial field used here enables us to divide the magnetic topology into two broad categories: one

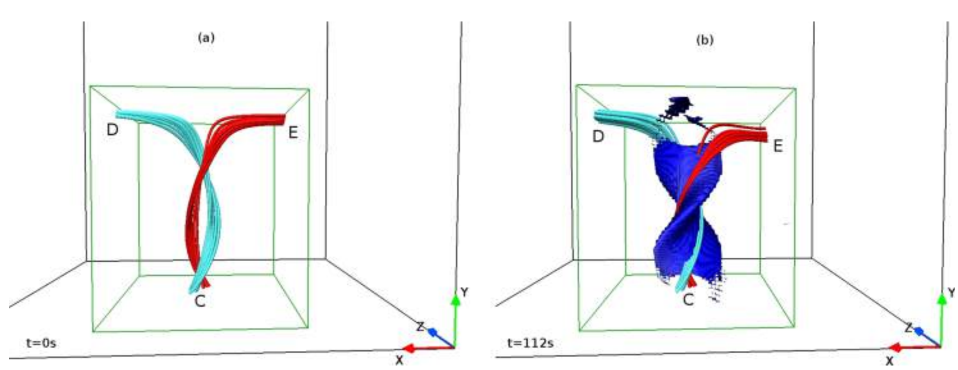

FIG. 22. Two sets of MFLs (colored red and cyan) of the **H** overlaid with the $J - 50$ surfaces (in blue) at $t = 0s$ and $t = 112s$, for $\epsilon_0 = 0.5$. The bifurcation of the MFLs, with the red set connecting the planes C and E and the cyan set connecting the planes C and D, documents a change in field line connectivity. The appearances of CS (in blue) co-located to the layers, across which the MFLs bifurcate, suggest the presence of QSL structures in **H**. Additionally, the MFLs at $t = 112s$ (with the CS fully develop) are more helical compared to the MFLs at $t = 0s$ (in absence of CS), indicating a causal connection between the favorable contortions and the dynamics of QSLs.

with favorable MFL geometry having complementary field lines directed anti-parallel to each other across the $y = \pi$ plane; and the other with interlaced field lines without any such favorable geometry. The numerical computations are performed in a triply periodic uniform Cartesian grid and simulate the viscous relaxation of an incompressible, thermally homogeneous magnetofluid with infinite electrical conductivity. Moreover, to get a direct visualization of CS formation, we advect magnetic flux surfaces instead of the more traditional vector magnetic field.

The numerical precision in preservation of the initial magnetic topology is ensured by the second-order-accuracy of non-oscillatory advection scheme MPDATA. The overall tendency to form CSs is confirmed by the history of component average current densities for different ϵ_0. To identify the locations of CSs in the computation domain and obtain a detail understanding, we analyze the evolution of isosurfaces of total current density having sufficiently high value. For smaller ϵ_0 (i.e., for $\epsilon_0 = 0.1$ and 0.3), the analyses establish generation of CSs at the $y = \pi$ plane which is location favorable to CS development. With an increase of ϵ_0, this favorable topology of field lines gets destroyed. For larger ϵ_0 (i.e., for $\epsilon_0 = 0.5$ and 0.7), additional CSs appear which are located away from the $y = \pi$ plane and the magnetic nulls. Further analysis identifies the origin of these CSs to favorable contortions of co-located magnetic flux surfaces.

Noteworthy are the insights gained on the relation between the intensity of interlacing and the onset of CSs. We have demonstrated that a magnetic field with less interlacing develops CSs at locations where such development is topologically favorable. Also, these CSs are localized at the immediate neighborhood of the favorable location. In contrast, for more interlaced field lines, the CSs develop away from magnetic nulls or any such topologically favorable sites. Further, the CSs being distributed throughout the volume with spatial extensions that increase with intensity of interlacing, their development supports the magnetostatic theorem to its full generality. The onset of CSs are further found to be near possible QSLs and related to their dynamics.

Altogether, the computations reported here and in Refs. 6 and 9–11 substantiate and extend the magnetostatic theorem by relating the intensity of MFL interlacing to the spatial distribution of CSs and identifying MFS contortions as the rationale behind the onset of CSs away from the favorable locations. The contortions are related to possible QSL structures, which provide a basis to extend the EP based computations to the solar corona. Combined with the scenario of secondary CS development which, in general, increases the topological complexity, the findings of this paper point toward the ubiquity of CSs in a high R_M magnetofluid. To relate this ubiquity to observation, it is crucial to include field line topologies similar to the coronal loops along with physical MRs, and this warrants a separate study.

ACKNOWLEDGMENTS

The simulations are performed using the High Performance Computing (HPC) cluster and the 100 TF cluster Vikram-100 at Physical Research Laboratory, India. We also wish to acknowledge the visualisation software VAPOR (www.vapor.ucar.edu), for generating relevant graphics. P.K.S. is supported by funding received from the European Research Council under the European Union's Seventh Framework Programme (FP7/2012/ERC Grant Agreement No. 320375). The authors also sincerely thank an anonymous reviewer for providing specific suggestions to enhance the presentation as well as to raise the academic content of the paper.

[1]E. N. Parker, Astronphys. J. **174**, 499 (1972).
[2]E. N. Parker, Astrophys. J. **330**, 474 (1988).
[3]E. N. Parker, Plasma Phys. Controlled Fusion **54**, 124028 (2012).
[4]E. N. Parker, *Spontaneous Current Sheets Formation in Magnetic Fields* (Oxford University Press, New York, 1994).
[5]E. R. Priest, *Solar Magnetohydrodynamics* (Reidel, Dordrecht, 1982).
[6]D. Kumar, R. Bhattacharyya, and P. K. Smolarkiewicz, Phys. Plasmas **22**, 012902 (2015).
[7]J. B. Taylor, Phys. Rev. Lett. **33**, 1139 (1974).
[8]D. Kumar and R. Bhattacharyya, Phys. Plasmas **18**, 084506 (2011).
[9]S. Kumar, R. Bhattacharyya, and P. K. Smolarkiewicz, Phys. Plasmas **21**, 052904 (2014).
[10]R. Bhattacharyya, B. C. Low, and P. K. Smolarkiewicz, Phys. Plasmas **17**, 112901 (2010).
[11]D. Kumar, R. Bhattacharyya, and P. K. Smolarkiewicz, Phys. Plasmas **20**, 112903 (2013).
[12]D. P. Stern, J. Geophys. Res. **72**, 3995, doi:10.1029/JZ072i015p03995 (1967).
[13]D. P. Stern, Am. J. Phys. **38**, 494 (1970).
[14]B. C. Low, Sci. Chin.-Phys. Mech. Astron. **58**, 015201 (2015).
[15]B. C. Low, Phys. Plasmas **18**, 052901 (2011).
[16]M. A. Berger, J. Geophys. Res. **102**, 2637, doi:10.1029/96JA01896 (1997).
[17]P. K. Smolarkiewicz and P. Charbonneau, J. Comput. Phys. **236**, 608 (2013).
[18]J. M. Prusa, P. K. Smolarkiewicz, and A. A. Wyszogrodzki, Comput. Fluids **37**, 1193 (2008).
[19]P. K. Smolarkiewicz, Int. J. Numer. Methods Fluids **50**, 1123 (2006).
[20]L. G. Margolin, W. J. Rider, and F. F. Grinstein, J. Turbul. **7**, N15 (2006).
[21]M. Ghizaru, P. Charbonneau, and P. K. Smolarkiewicz, Astrophys. J. Lett. **715**, L133 (2010).
[22]P. Beaudoin, P. Charbonneau, E. Racine, and P. K. Smolarkiewicz, Sol. Phys. **282**, 335 (2013).
[23]P. Charbonneau and P. K. Smolarkiewicz, Science **340**, 42 (2013).
[24]C. Mellor, C. L. Gerrard, K. Galsgaard, A. W. Hood, and E. R. Priest, Sol. Phys. **227**, 39 (2005).
[25]I. J. D. Craig and F. Effenberger, Astrophys. J. **795**, 129 (2014).
[26]I. J. D. Craig and D. I. Pontin, Astrophys. J. **788**, 177 (2014).
[27]A. L. Wilmot-Smith, Philos. Trans. R. Soc. A **373**, 20140265 (2015).
[28]E. R. Priest and P. Démoulin, J. Geophys. Res. **100**, 23443, doi:10.1029/95JA02740 (1995).
[29]K. Galsgaard and Å. Nordlund, J. Geophys. Res. **102**, 231, doi:10.1029/96JA02680 (1997).
[30]J. E. H. Stevenson, C. E. Parnell, E. R. Priest, and A. L. Haynes, Astron. Astrophys. **573**, A44 (2015).
[31]G. Aulanier, E. Pariat, and P. Démoulin, Astron. Astrophys. **444**, 961 (2005).

PHYSICS OF PLASMAS 23, 044501 (2016)

Continuous development of current sheets near and away from magnetic nulls

Sanjay Kumar and R. Bhattacharyya
Udaipur Solar Observatory, Physical Research Laboratory, Dewali, Bari Road, Udaipur 313001, India

(Received 8 February 2016; accepted 23 March 2016; published online 7 April 2016)

The presented computations compare the strength of current sheets which develop near and away from the magnetic nulls. To ensure the spontaneous generation of current sheets, the computations are performed congruently with Parker's magnetostatic theorem. The simulations evince current sheets near two dimensional and three dimensional magnetic nulls as well as away from them. An important finding of this work is in the demonstration of comparative scaling of peak current density with numerical resolution, for these different types of current sheets. The results document current sheets near two dimensional magnetic nulls to have larger strength while exhibiting a stronger scaling than the current sheets close to three dimensional magnetic nulls or away from any magnetic null. The comparative scaling points to a scenario where the magnetic topology near a developing current sheet is important for energetics of the subsequent reconnection.
[http://dx.doi.org/10.1063/1.4945634]

Magnetic reconnection (MR) is crucial for energy releases in astrophysical plasmas where the magnetofluid is characterized by large magnetic Reynolds number ($R_M = vL/\eta$, in usual notations). Notably, the large R_M-fluids satisfy the Alfvèn theorem of flux-freezing[1] whereas MR requires the magnetofluid to be diffusive. The diffusive limit can be achieved by a reduction in L, the length over which the magnetic field varies. In an evolving magnetofluid, a potential site for reconnection, i.e., the location at which L is small enough to initiate reconnection, can either pre-exist in the form of two dimensional (2D) and three dimensional (3D) magnetic nulls or get spontaneously generated by the evolution. In the latter, the tangential component of the magnetic field is discontinuous across a surface of intense volume current density ($\mathbf{J}$), known in the literature as a current sheet (CS).[2] Recent simulations,[3,4] congruent with Parker's magnetostatic theorem,[2,5–7] attribute generation of such CSs to favorable contortions of magnetic flux surfaces (MFSs) which bring non-parallel magnetic field lines (MFLs) to close proximity. In contrast to other simulations[8,9] that support the development of CSs localized at pre-existing topologically favorable sites like magnetic nulls and field-reversal layers, the contortions, and the corresponding CSs, were found to be away from such favorable sites and distributed throughout the computational volume. If allowed, these volume-distributed CSs would decay through reconnections, leading to energy release throughout the volume—a scenario supportive of Parker's nanoflare model for solar coronal heating.[2] Notably, energy release in nanoflares is expected to be small ($\approx 10^{23} - 10^{25}$ ergs)[2,10] whereas eruptive events, like flares and coronal mass ejections (CMEs) happening in Sun, are characterized by larger energy release ($\approx 10^{32}$ ergs).[1,2] Standardly, the underlying mechanism for the eruptive events is also magnetic reconnections occurring across CSs.[11] Since $|\mathbf{J}|$ of the involved CS is a measure of energy released in reconnection,[12] it is of fundamental interest to compare $|\mathbf{J}|$ for CSs near the pre-existing nulls against those which develop throughout the volume and their governing dynamics.

Toward achieving the above comparison in an unified framework, we numerically simulate viscous relaxation of an incompressible, thermally homogeneous magnetofluid with infinite electrical conductivity.[3,8,9,13] The relaxation being in harmony with the magnetostatic theorem is proven to spontaneously develop CSs. The simulations are performed by using the numerical model EULAG-MHD.[14] Relevantly, the model advection scheme[15] produces locally adaptive residual dissipation in response to generation of under-resolved scales in field variables to effectively regularize these scales,[16,17] in the spirit of implicit large eddy simulation (ILES) subgrid-scale turbulence models.[18]

Further, as a suitable initial magnetic field, we reconsider the magnetic field $\mathbf{H}$ used in our previous work,[3] as it successfully manifests the distributed CSs in the presence of 2D (X-type) and 3D magnetic nulls; see Ref. 3 for details. In Ref. 3, $\mathbf{H}$ was represented in terms of MFSs to directly visualize physical process responsible for spontaneous development of CSs. This approach provided important insights about the definitive process, which leads to the origin of such CSs. But the MFS representation being only valid until CS formation, the dissipation of these CSs and resultant dynamics around unperturbed magnetic nulls could not be explored. In order to elucidate the subsequent evolution, instead of flux-surface, here we advect vector magnetic field. Importantly, the simulations reported rely on the proven ILES mode of EULAG-MHD in regularizing the under-resolved scales through onset of MRs, concurrent and collocated with developing CSs.[9]

The computations are performed on the $128 \times 128 \times 256$ grid resolving the domain $[0, 2\pi] \times [0, 2\pi] \times [0, 6\pi]$, respectively, in x, y, and z. The coefficient of viscosity and the mass density are set to 0.0045 and 1, respectively.

To develop an overall understanding of the simulated viscous relaxation, in Figure 1, we plot the time profile of the normalized kinetic energy. As the initial Lorentz force pushes the magnetofluid from rest, kinetic energy rises at the

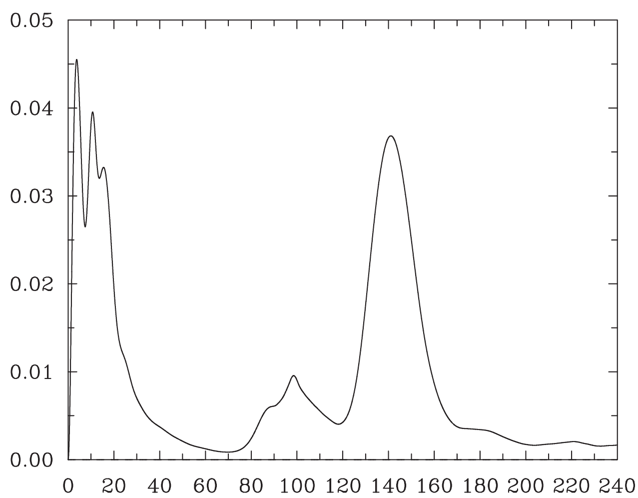

FIG. 1. The evolution of kinetic energy, normalized to initial total (kinetic + magnetic) energy. The five distinct peaks at $t = 4\,$s, $t = 12\,$s, $t = 20\,$s, $t = 100\,$s, and $t = 140\,$s are evident.

expense of magnetic energy and this rise gets arrested by viscosity, resulting in the peak of kinetic energy appearing at $t = 4\,$s. Also to be noted is the existence of four more distinct peaks centered at $t = 12\,$s, $t = 20\,$s, $t = 100\,$s, and $t = 140\,$s in the kinetic energy curve.

To identify and locate the onset of CSs, in Figure 2, we display isosurfaces of $|\mathbf{J}|$ with an isovalue which is 40% of maximum current density $|\mathbf{J}|_{\max}$ at the instant $t = 8\,$s. The appearances of isosurfaces (overlaid with magnetic nulls) show the development of CSs away from the nulls and distributed throughout the volume, confirming the results of Ref. 3. The consequent MRs generate flow which is dissipated by viscous drag, explaining the peak in kinetic energy at $t = 12\,$s. Figure 3 shows the evolution of MFLs in the neighborhoods of the X-type nulls located at $(x, y, z) = (\pi, \pi, 2.64\pi), (\pi, \pi, 3\pi)$, and $(\pi, \pi, 3.36\pi)$. Noticeably, the MFLs in $z = 3\pi$ plane become concave toward the point $(x, y, z) = (\pi, \pi, 3\pi)$, generating a void depleted of MFLs (marked by R in panel (b)). Consequently, parts of two complementary anti-parallel MFLs from the opposite sides of the $z = 3\pi$ plane are dragged (along z) into this void and develop a CS. The scenario is in general agreement with Parker's optical analogy.[19–21] The decay of this CS and the corresponding viscous arrest leads to the kinetic energy peak at $t = 20\,$s. Also, the X-type nulls reappear after the decay (not shown).

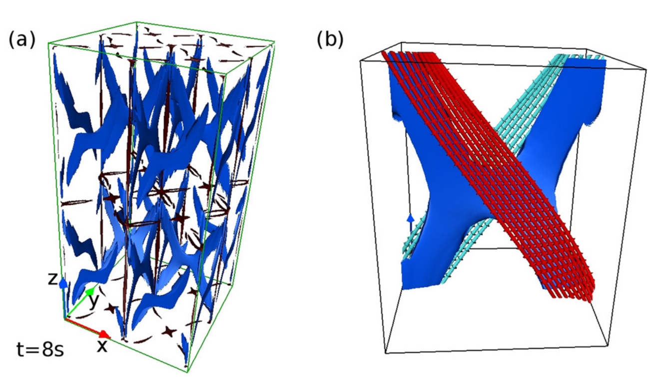

FIG. 2. Panel (a) shows isosurfaces of $|\mathbf{J}|$ (in blue) having a magnitude of 40% of the $|\mathbf{J}|_{\max}$ at $t = 8\,$s. The panel is overplotted with magnetic nulls (in color maroon), highlighting formation of CSs away from nulls and distributed throughout the computational volume. Panel (b) shows MFLs in the locality of such a CS. Noticeably, the MFLs across the CS are misaligned by an angle around 90°.

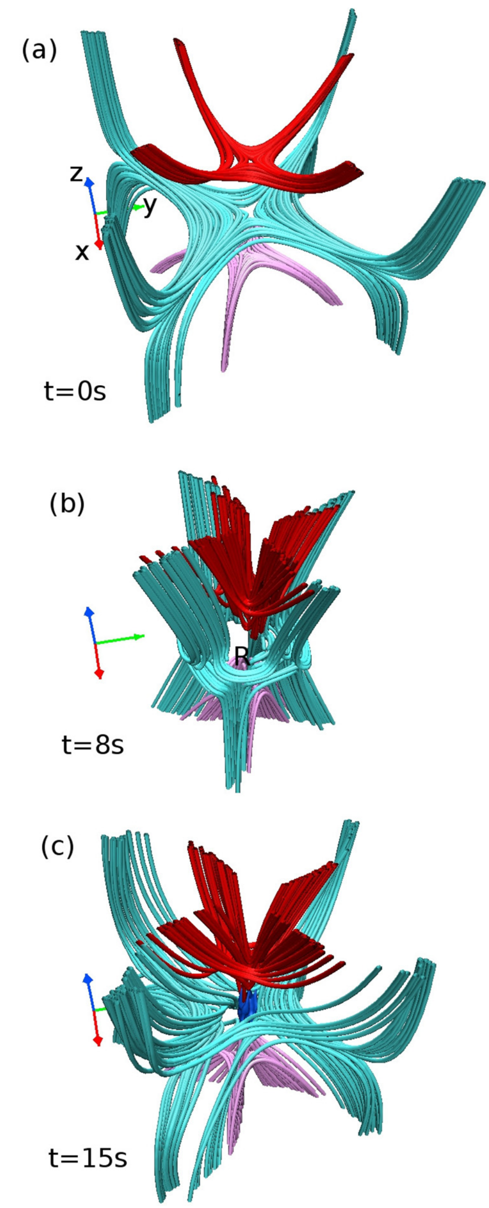

FIG. 3. Evolution of MFLs in neighborhoods of X-type nulls situated at $(x, y, z) = (\pi, \pi, 2.64\pi)$, $(\pi, \pi, 3\pi)$, and $(\pi, \pi, 3.36\pi)$, depicted in colors magenta, cyan, and red, respectively. The plots are overlaid with $|\mathbf{J}|$ isosurface (in blue) at 40% of its maximum in the neighborhoods. Important are the emergence of MFLs depleted zone in $z = 3\pi$ plane (symbolized by R in panel (b)) and consequent CS formation (panel (c)).

To explore the subsequent dynamics, in Figure 4, we illustrate the evolution in the neighborhood of an X-type null, which is situated at $(x, y, z) = (\pi, \pi, 3\pi/2)$. Notably, the X-type null gets squashed and generates an extended CS along with two Y-type nulls at $t = 83\,$s. Figure 5 shows time profile of MFLs in the vicinity of a 3D null. Important is the loss of fan and spine structures central to a 3D null. The collapse brings non-parallel MFLs in close proximity, resulting in CSs at $t = 90\,$s. The collective decay of CSs, near X-type

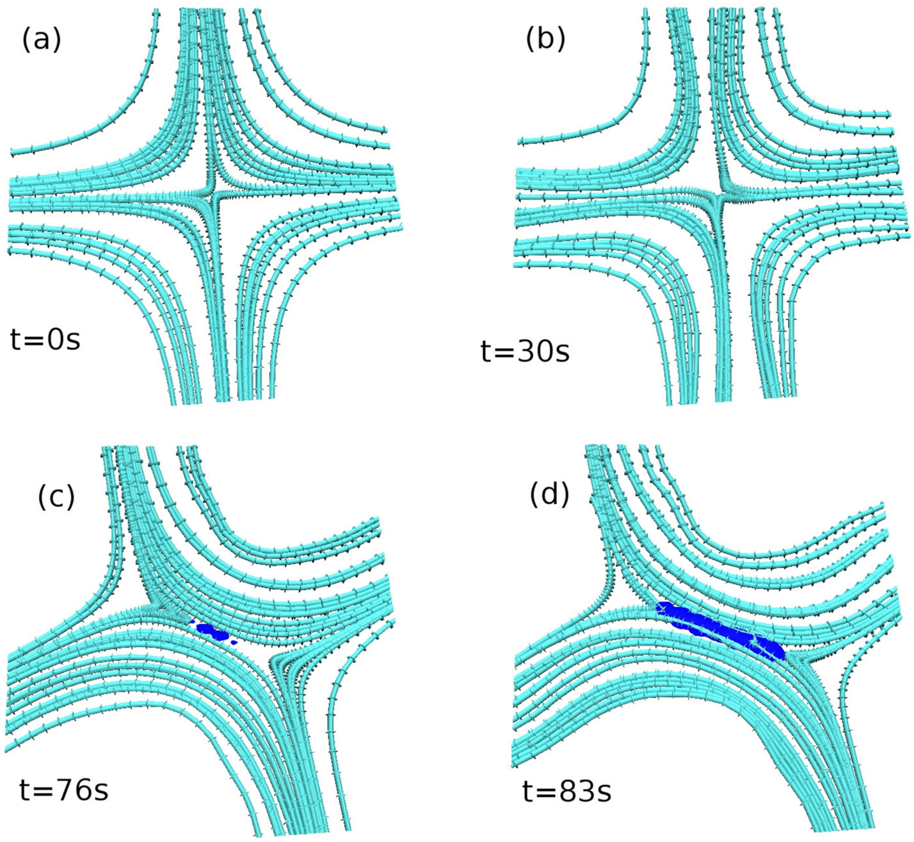

FIG. 4. History of MFLs in the vicinity of an X-type null situated at $(x, y, z) = (\pi, \pi, 3\pi/2)$, overplotted with isosurface of $|\mathbf{J}|$ at 40% of $|\mathbf{J}|_{\max}$ in the vicinity. Noteworthy is the generation of an extended CS along with two Y-type nulls.

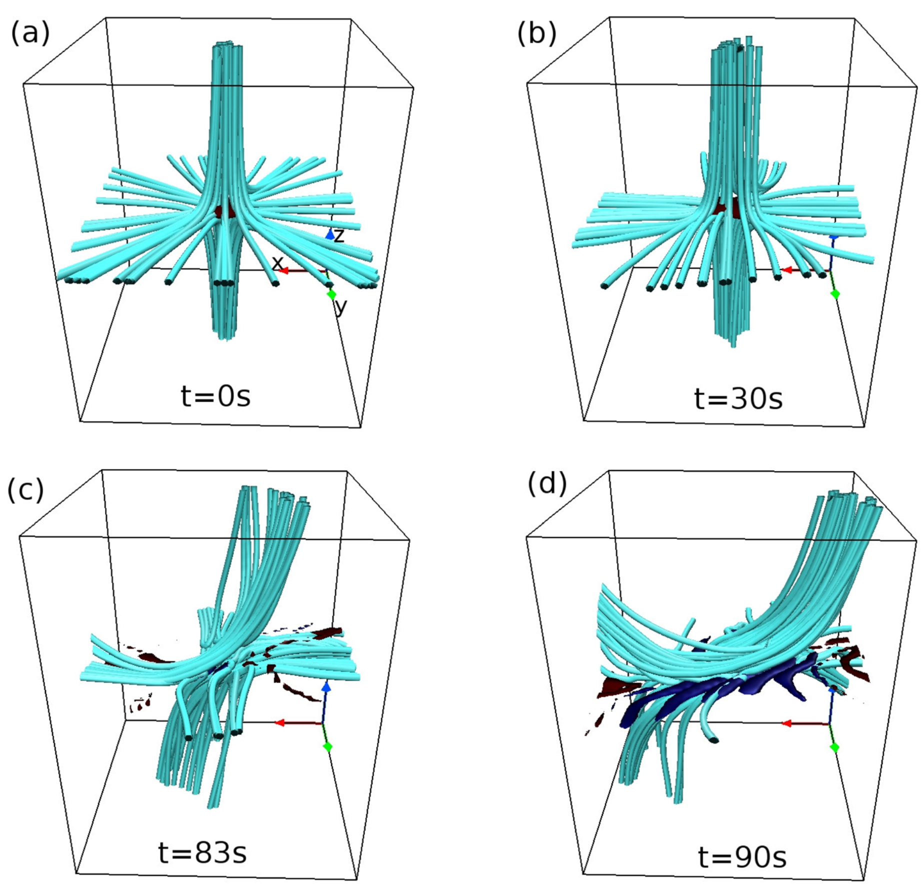

FIG. 5. Time sequence of MFLs in the immediate neighborhood of a representative 3D magnetic null situated at $(x, y, z) = (\pi/2, \pi/2, 3\pi)$ in their important phases of evolution. The plots are further overlaid with current density isosurfaces (in blue) at 40% of its maximum value in the neighborhood. Noticeable is the development of CSs by the collapse of fan and spine structures of the 3D null.

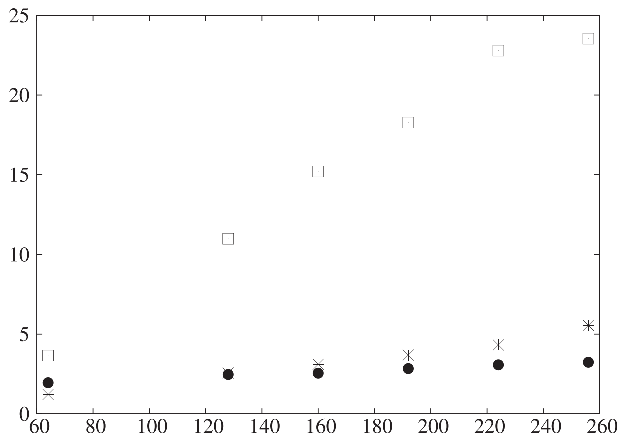

FIG. 6. Scaling of $|\mathbf{J}|_{\max}$ with resolution, for the CSs near the 2D nulls at $t = 83$ s (squares), the 3D nulls at $t = 90$ s (stars), and away from these nulls at $t = 8$ s (dots). The abscissa is grid resolution along z whereas the ordinate is $|\mathbf{J}|_{\max}$. The plot illustrates a strongest scaling for the CSs near the 2D nulls.

and 3D nulls, engenders the kinetic energy peak at $t = 100$ s. With all 2D and 3D nulls destroyed, the subsequent relaxation ranging from $t \in \{120\,\mathrm{s}, 240\,\mathrm{s}\}$ develops the next generation of distributed CSs (not shown), having geometry similar to the ones which appear at $t = 8$ s (Fig. 2) but with different spatial distribution. Such a spontaneous development of CSs in the absence of any topologically favorable sites further supports the magnetostatic theorem. The decay of these distributed CSs explain the last peak in kinetic energy at $t = 140$ s.

Based on the above analysis, the CSs can be broadly classified into three categories. The first one corresponds to the distributed CSs that develop away from the nulls or in absence of the nulls (Fig. 2). The second consists of the CSs originating around the 2D nulls (Figs. 3 and 4). The CSs created by the collapse of 3D nulls fall into the third category (Fig. 5). To explore the features associated with these three types of CSs, we carry-out additional computations on different sized grids—$32 \times 32 \times 64$, $64 \times 64 \times 128$, $80 \times 80 \times 160$, $96 \times 96 \times 192$, and $112 \times 112 \times 224$. Figure 6 documents scaling of peak current density $|\mathbf{J}|_{\max}$ with resolution, for the CSs depicted in Figures 2, 4, and 5 as the representative cases. The figure confirms that the CSs near the 2D nulls have strongest scaling compared to the CSs near the 3D nulls or the distributed ones. In addition, the figure also reveals the $|\mathbf{J}|_{\max}$ to be larger for the CSs around 2D nulls than the other types of CSs. This difference in $|\mathbf{J}|_{\max}$ can be attributed to the angle by which the MFLs are misaligned across a CS. For instance, the MFLs are misaligned by the angle $180°$ for a CS around the 2D null (panel (d), Fig. 4). The angle is much less than $180°$ for a CS which generates away from the nulls (panel (b), Fig. 2).

Succinctly, the paper investigates dynamics and strength of CSs near and away from the 2D and 3D nulls for a given initial magnetic field. Importantly, the simulations demonstrate a complete collapse of fan and spine structures of the 3D nulls which enables pressing of non-parallel MFLs to generate CSs. Notably, compared to CSs near the 3D nulls or which are volume-distributed, the maximum current density near the 2D nulls is found to be largest for a given resolution and show strongest scaling with resolution. With the smallest resolvable scale being fixed for a given computation, scaling seems to be related to the amount of anti-parallel field lines which are pushed together to generate a CS and hence depends on magnetic topology around the current sheet. The strongest scaling physically signifies the reconnections near the 2D nulls to be faster[12] and energetically more explosive than the ones near the volume-distributed CSs—a scenario congruent with the energetics of eruptive events and possible nano-flares, occurring at the solar corona.

The simulations are performed using the 100 TF cluster Vikram-100 at Physical Research Laboratory, India. We acknowledge the visualisation software VAPOR (www.vapor.ucar.edu), for generating relevant graphics. The authors are thankful to Dr. P. K. Smolarkiewicz for many fruitful discussions and an anonymous referee for comments and suggestions which enhance the quality of the paper.

[1]E. R. Priest, *Magnetohydrodynamics of the Sun* (Cambridge University Press, 2014).
[2]E. N. Parker, *Spontaneous Current Sheets Formation in Magnetic Fields* (Oxford University Press, 1994).
[3]S. Kumar, R. Bhattacharyya, and P. K. Smolarkiewicz, Phys. Plasmas **21**, 052904 (2014).
[4]S. Kumar, R. Bhattacharyya, and P. K. Smolarkiewicz, Phys. Plasmas **22**, 082903 (2015).
[5]E. N. Parker, Astrophys. J. **174**, 499 (1972).
[6]E. N. Parker, Astrophys. J. **330**, 474 (1988).
[7]E. N. Parker, Plasma Phys. Controlled Fusion **54**, 124028 (2012).
[8]R. Bhattacharyya, B. C. Low, and P. K. Smolarkiewicz, Phys. Plasmas **17**, 112901 (2010).
[9]D. Kumar, R. Bhattacharyya, and P. K. Smolarkiewicz, Phys. Plasmas **20**, 112903 (2013).
[10]R. A. Kopp and G. Poletto, Astrophys. J. **418**, 496 (1993).
[11]M. J. Aschwanden, *Physics of the Solar Corona* (Springer, Berlin, 2004).
[12]I. J. D. Craig and Y. E. Litvinenko, Phys. Plasmas **12**, 032301 (2005).
[13]D. Kumar, R. Bhattacharyya, and P. K. Smolarkiewicz, Phys. Plasmas **22**, 012902 (2015).
[14]P. K. Smolarkiewicz and P. Charbonneau, J. Comput. Phys. **236**, 608 (2013).
[15]P. K. Smolarkiewicz, Int. J. Numer. Methods Fluids **50**, 1123 (2006).
[16]M. Ghizaru, P. Charbonneau, and P. K. Smolarkiewicz, Astrophys. J. Lett. **715**, L133 (2010).
[17]P. Beaudoin, P. Charbonneau, E. Racine, and P. K. Smolarkiewicz, Sol. Phys. **282**, 335 (2013).
[18]L. G. Margolin, W. J. Rider, and F. F. Grinstein, J. Turbul. **7**, N15 (2006).
[19]E. N. Parker, Geophys. Astrophys. Fluid Dyn. **45**, 169 (1989).
[20]E. N. Parker, Geophys. Astrophys. Fluid Dyn. **46**, 105 (1989).
[21]E. N. Parker, Geophys. Astrophys. Fluid Dyn. **50**, 229 (1990).